



Elaboration of a new sensor based on molecularly imprinted polymers for the detection of molecules in physiological fluids

Hélène Marie

► To cite this version:

Hélène Marie. Elaboration of a new sensor based on molecularly imprinted polymers for the detection of molecules in physiological fluids. Other [cs.OH]. Université de Technologie de Compiègne, 2013. English. NNT : 2013COMP2128 . tel-00977390

HAL Id: tel-00977390

<https://theses.hal.science/tel-00977390>

Submitted on 11 Apr 2014

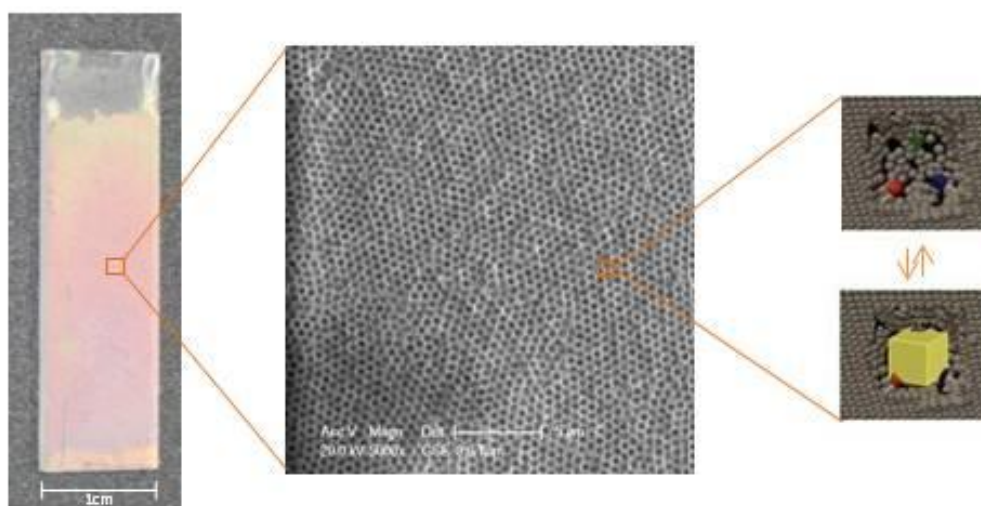
HAL is a multi-disciplinary open access archive for the deposit and dissemination of scientific research documents, whether they are published or not. The documents may come from teaching and research institutions in France or abroad, or from public or private research centers.

L'archive ouverte pluridisciplinaire **HAL**, est destinée au dépôt et à la diffusion de documents scientifiques de niveau recherche, publiés ou non, émanant des établissements d'enseignement et de recherche français ou étrangers, des laboratoires publics ou privés.

Par **Hélène MARIE**

Elaboration of a new sensor based on molecularly imprinted polymers for the detection of molecules in physiological fluids

Thèse présentée
pour l'obtention du grade
de Docteur de l'UTC



Soutenue le 19 décembre 2013
Spécialité : Biotechnologie

D2128



Elaboration of a new sensor based on Molecularly Imprinted Polymers for the detection of molecules in physiological fluids

by

Hélène MARIE

A thesis presented for graduation of
Docteur de l'Université de Technologie de Compiègne
Biotechnologie

Thesis supervised by Prof. Karsten Haupt and Dr. Gilles Marchand

Disputation on December 19th, 2013, in front of a jury composed of:

Valérie Pichon, Pr.	Ecole Supérieure de Physique Chimie Industrielles, Paris	Reviewer
Sabine Szunerits, Pr.	Institut de Recherche Interdisciplinaire, Lille	Reviewer
Frédéric Mallard, Dr.	bioMérieux, Grenoble	Examiner
Daniel Thomas, Pr.	Université de Technologie de Compiègne	Examiner
Gilles Marchand, Dr.	CEA Leti, Grenoble	Supervisor
Karsten Haupt, Pr.	Université de Technologie de Compiègne	Supervisor

Remerciements

Mes premiers remerciements s'adressent aux membres du jury qui ont accepté de lire avec soin ce manuscrit et de juger ce travail. Je remercie Sabine Szunerits et Valérie Pichon d'avoir accepté d'être les rapporteurs. Merci également à Frédéric Mallard et Daniel Thomas d'avoir participé avec enthousiasme au jury de cette thèse.

Je remercie Karsten d'avoir dirigé cette thèse, et ce malgré la distance et la difficulté inhérente à faire de moi une vraie « MIPiste ».

A Gilles, j'adresse ma gratitude pour m'avoir accordé sa confiance pendant ces trois années. Tu as souvent pensé ne pas me consacrer beaucoup de temps mais j'y ai vu avant tout l'autonomie qu'il me fallait, la latitude nécessaire aux essais incertains, tout en ayant la sécurité de savoir la porte de ton bureau toujours ouverte. Porte poussée de nombreuses fois pour y trouver des réponses et discussions scientifiques pertinentes ! Merci.

Pierre et Séverine ont su, chacun à leur façon, s'impliquer dans l'encadrement de cette thèse. Merci d'avoir en particulier assuré un soutien régulier à mon retour de l'épisode "genou" et à la préparation express de Boston. Merci Séverine pour ton écoute rassurante et Pierre ton positivisme scientifique, j'ai pu rebondir plusieurs fois grâce à vous deux.

Plusieurs collaborations scientifiques ont eu lieu pendant cette thèse.

Un premier remerciement va à Mathieu Dupoy qui m'a ouvert les portes de son placard d'opticien, trouvé une salle et un marbre, qui a pris le temps de me mettre sur les bons rails (d'optique !) et qui s'est intéressé, tout le temps, à mes manips et mes résultats. Mathieu, tu as été un sacré repère, merci. Les bancs optiques sont d'ailleurs nés de deux sujets d'encadrement initiés par "papa" Mathieu: un sujet de TIPE et un sujet du BTS photonique d'Argouges, je remercie les élèves concernés et leurs professeurs.

Je souhaite ensuite remercier les membres du CEA Liten qui m'ont permis d'accéder à la technologie Boostream (M. Plissonnier, P. Fugier) et ont œuvré pour fabriquer les opales, de façon efficace et quantitative, un très grand merci à Olivier Dellea et Juliette Lostys.

Les études RMN ont vu le jour grâce à la gentillesse et l'efficacité d'Elise Prost de l'UTC. Qualités partagées par sa collègue de bureau Claire Rossi, qui a apporté une contribution fondamentale au plan d'expériences cortisol. Merci à toutes les deux.

Puisqu'on est dans la thématique plan d'expériences, je remercie aussi chaleureusement Dominique Lauro et lui donne la mention spéciale « broyage vigoureux ». Merci Dom !

Amélie et MEB ne riment pas mais l'un ne fonctionne pas sans l'autre, donc merci Amélie pour toutes les belles images.

Enfin, merci à Thomas Bordy pour les coups de main techniques (superbe dip-coating automa-

tisé) et, plus personnellement, pour le sauvetage héroïque à Chamrousse.

Le labo de la travée 105 a vu passer de bons moments et je remercie tous ses cohabitants. J'ai aussi très largement apprécié les moments passés en salle blanche et la compagnie de tous ses membres. Une étude très sérieuse montre que les chercheurs sont les plus gros buveurs de café au monde, je crois que l'étude devrait aussi montrer que les chimistes sont de bons pâtissiers, des gourmands, et que le café de notre open-space a la palme des plus savoureux macarons (Séverine), madeleines (Guillaume), cannelés (Marjo), tartenplan (David) et j'en passe. . .

Il n'est pas de thèse sans jolies rencontres, professionnelles ou amicales, et j'ai eu la chance d'en faire un grand nombre. A toute l'équipe de sam, joyeuse bande qui a su rendre ces trois ans formidables, j'adresse mes remerciements les plus tendres, les plus lacrimaux et chaudycapesque. Emilie, Mélanie, Régis, Vincent, Adeline, vous avez été extraordinaires. Mention paillettes à Emilie et Mélanie. Merci mes amis.

Merci à Guillaume, pour les nocturnes, les portages de boîte à gants, la gentillesse sans limite et le cat-sitting. Tu m'as appris qu'il n'y avait pas de mur sans porte! Merci à Marjorie, ton joli sourire, ta bonne humeur et merci pour tous ces bons moments ensemble. Merci à Marina, pour les cafés, déjeuners et Macdo partagés à Compiègne. A mon fidèle Etienne et son tel, mille merci.

Merci enfin à l'ensemble des doctorants, post-docs, stagiaires, croisés pendant ces trois ans ; Juliette (béquille-share), Carole et Laure-Hélène, David, Louise (et la relecture assidue de l'anglais, merci), Jonathan (les discussions autour de la centrifugeuse ! Et le soutien plan d'exp immuable), Marie (Pimprenelle) et Zoé (le sourire magique).

Enfin, il reste l'inébranlable soutien familial pour lequel aucun mot n'est suffisant. A mes deux parents, j'adresse des remerciements plein de tendresse, pour cette thèse et toutes les années post-bac, pour les permanences téléphoniques, leur confiance et tout ce qu'ils sont. Vincent et Mathilde ont toujours tout suivi, mine de rien, je suis fière d'eux et redevable de beaucoup. Merci aussi à Papy et Mamie, tant pour les week-ends à Corrençon que pour l'hébergement 5* pendant la rédaction et leur éternelle bienveillance.

Thomas, que l'anecdote suivante illustre ton inconditionnel et fondamental soutien : alors que euphorique, un soir, je racontais avoir obtenu des premiers clichés MEB d'une opale inverse, tu as sereinement traduit à l'ami présent « MEB : Microscope Electronique à Balayage, elle en parle souvent, j'ai vérifié sur Google la signification ». Merci mon Tom.

Merci à vous qui lirez ou feuillerez ce manuscrit, j'espère que vous y trouverez l'information recherchée, que vous y verrez tout ce que j'ai aimé et sinon que vous serez indulgents...

Pour finir, je dédie ce manuscrit et le travail qu'il contient à l'homme le meilleur qu'il m'ait été donné de connaître, source de confiance en l'avenir, Jean Main.

Abstract

This thesis aimed at elaborating an optical sensor to detect molecules in a biological fluid. Two steroids and a xenobiotic were identified as biomarkers released in some body fluids: cyproterone acetate, cortisol and 2,4-dichlorophenoxyacetic acid respectively.

On one hand, detection was performed by Molecularly Imprinted Polymers (MIPs). These tailor-made synthetic receptors display numerous qualities that foster their integration in sensors. MIPs were therefore developed against the targeted analytes. Formulation optimization was led thanks to experimental designs.

On the other hand, optical transduction was made possible thanks to the structuring of a polymer into a photonic crystal. Opals were manufactured with a new process suitable for large scales and were used to mold MIPs in inverse opals. Thus, submicron structures of the polymer are responsible for the color of the sensor. A change of color is triggered by the recognition of the analyte by the polymer (upon swelling). Polymers studied displayed sufficient swelling observed by spectrophotometry.

Finally, the work of this thesis consisted in elaborating polymer formulations and their integration in a sensor so as to detect an analyte with direct, rapid and unobtrusive means.

Key words: Molecularly imprinted polymers, MIPs, steroids, herbicide, biosensor, optical transduction, photonic crystal, body fluids.

Résumé

Ce travail de thèse avait pour objectif l'élaboration d'un capteur optique pour la détection directe de molécules d'intérêt dans un fluide biologique. Deux stéroïdes et un xéniobiotique (herbicide) ont été choisis en tant que biomarqueurs apparaissant dans des fluides corporels: respectivement l'acétate de cyprotérone, le cortisol et l'acide 2,4-dichlorophénoxyacétique.

La partie détection, d'une part, est assurée par les polymères à empreintes moléculaires (MIPs, de l'anglais *Molecularly Imprinted Polymers*). Ces récepteurs synthétiques sur mesure présentent en effet de nombreuses qualités pour l'intégration dans un capteur. Des polymères à empreintes moléculaires ont ainsi été développés pour les analytes visés. L'optimisation des formulations de polymère a été basée sur des plans d'expériences.

La transduction optique, d'autre part, est basée sur la structuration du polymère sous la forme d'un cristal photonique. Des opales ont été fabriquées avec un procédé industrialisable pour permettre la mise en forme du MIP en opale inverse. Ainsi structuré à l'échelle submicronique, le matériau présente une couleur susceptible d'évoluer lors de la détection de l'analyte, et ce, grâce à un changement de conformation (gonflement). Les formulations polymères étudiées ont généré des gonflements réduits mais visibles en spectrophotométrie.

Le travail rapporté dans cette thèse consiste donc en l'élaboration de polymères à empreintes moléculaires et leur intégration dans un capteur afin de détecter un analyte de façon directe, rapide et ne nécessitant que des équipements transportables, voire portables.

Mots clés: Polymères à empreintes moléculaires, MIPs, stéroïde, pesticide, capteur, transduction optique, cristal photonique, fluides corporels.

Contents

Remerciements	3
Abstract	6
Resume	7
Acronymes	15
Introduction	17
 I Bibliography: wearable sensors, molecularly imprinted polymers and optical transduction	 19
1 Interest of body fluids for monitoring the physiological state	21
1.1 Wearable sensors	21
1.1.1 Sensing devices	22
1.1.2 Integration of the sensors	23
1.2 Body fluids	25
1.3 Biomarkers in physiological fluids, with particular focus on steroids	29
 2 Molecularly imprinted polymers and their use in chemical sensors	 33
2.1 Molecular imprinting	33
2.1.1 Molecular recognition and principle of molecular imprinting	33
2.1.2 Characterization of the polymers	35
2.2 Imprinting effect: influencing factors and optimizations	40
2.2.1 Functional monomers	40
2.2.2 Cross-linking monomers	41
2.2.3 Solvent	42
2.2.4 Polymerization conditions	43

2.2.5	Formulation optimization	43
2.3	MIPs as sensitive layers in optical sensors	44
2.3.1	Fluorescence as transduction method for MIP sensors	45
2.3.2	Generation of an optical signal by a specific chemical reaction	46
2.3.3	Surface Plasmon Resonance	46
2.3.4	Infrared and Raman spectroscopy	47
2.3.5	Refractometry	48
3	Photonic crystals: an original way of transduction	51
3.1	Definition	51
3.2	Sensors based on photonic crystals	52
3.2.1	Ions and pH sensors	53
3.2.2	Vapor or solvent sensors	55
3.2.3	Temperature sensors	55
3.2.4	Biosensors	56
3.3	MIPs and photonic crystals	58
4	Scope of this thesis	65
II	A molecularly imprinted polymer for cyproterone acetate	77
1	Cyproterone acetate	79
1.1	Biological action	79
1.2	Monitoring CPA	81
2	Elaboration of MIPs formulations for cyproterone acetate	83
2.1	Development of a preliminary MIP for cyproterone acetate	83
2.2	NMR study	88
2.2.1	Structure of cyproterone acetate	89
2.2.2	Job's plot	89
2.3	Conclusion	94
3	Optimization of cyproterone acetate imprinting by experimental design	95
3.1	Design of experiments	95
3.2	Approach and choice of the input factors	97
3.3	Laboratory implementation	99
3.4	Results	100

3.5	Critical review and conclusion	102
III Towards the detection of cortisol and adrenaline, two stress biomarkers		107
1	Understanding the stress mechanisms and its detection methods	109
1.1	Stress definition, causes and consequences	109
1.2	Hormonal secretions triggered by stress	110
1.2.1	Adrenaline	110
1.2.2	Cortisol	111
1.3	Stress monitoring	113
2	Elaboration of MIPs formulations for adrenaline	115
3	Elaboration of MIP formulation for cortisol	117
3.1	Development of a preliminary MIP for cortisol	117
3.2	NMR studies	123
3.3	Conclusion	128
4	Optimization of the MIP for cortisol: use of a design of experiments	129
4.1	Doehlert design of experiments	129
4.2	Characterizations	131
4.2.1	Affinity responses	131
4.2.2	Porosity responses	137
4.2.3	Correlations between porosity and affinity responses	142
4.3	Validation of the study	143
5	Conclusion	145
IV Elaboration of an optical biosensor		149
1	Towards a new optical sensor	151
2	Opal formation	153
2.1	Bead synthesis	154
2.2	Evaporation	155
2.3	Dip-coating	157
2.4	Boostream [®] equipment	158

3	Inverse opal synthesis	161
3.1	Sandwich	161
3.2	Spin-coating	164
3.3	Dip-coating	165
4	Opals and inverse opals characterization	169
4.1	Diffraction figure and evaluation of $n_{grating}$	169
4.1.1	Opals	170
4.1.2	Inverse opals	173
4.2	Spectrophotometry and evaluation of n_{eff}	174
4.2.1	Opals	174
4.2.2	Inverse opals	178
5	Sensing with inverse opals and MIPs	181
5.1	Imprinting 2,4-dichlorophenoxyacetic acid	181
5.2	Diffraction studies	183
5.3	Spectrophotometry studies	186
5.4	Conclusion	187
	APPENDICES	197
A	Materials	197
A.1	Chemicals	197
A.2	Equipments	200
B	Protocols	203
B.1	Polymer bulk	203
B.1.1	Synthesis	203
B.1.2	Binding evaluation	203
B.1.3	Porosity measurements	204
B.1.4	Designs of experiments	204
B.2	NMR ^1H and ^{13}C	205
B.3	Silica spheres	205
B.3.1	Synthesis	205
B.3.2	Evaluation of the silica particles diameter	205
B.4	Opals	205
B.5	Inverse opals	206

B.5.1	Polymer synthesis	206
B.5.2	Beads dissolution	206
B.5.3	Characterizations	207
C	Cyproterone acetate, cortisol and 2,4-dichlorophenoxyacetic acid dosage by HPLC	209
D	Job plot - method of continuous variations	211
E	Formulations of polymers for the CPA design of experiments	215
F	Binding assays isotherm for polymers of the cortisol design of experiments	225
G	BET measurements: isotherms of N₂ adsorption and desorption for polymers of the cortisol design of experiments	227

List of Tables

1	Chemical groups of hormones and their characteristics.	30
2	A possible classification of steroids.	30
3	List of several widely used functional monomers.	41
4	List of several widely used cross-linking monomers.	42
5	Templates, formulations, conditions of preparation of imprinted polymers in inverse opal sensors and shift of the Bragg's peak reported in literature.	59
6	Formulations used to obtain CPA imprinted polymers	84
7	Binding parameters recorded for polymers imprinted and evaluated in toluene	87
8	Input parameters, and their levels, evaluated in the CPA-design of experiments . . .	98
9	List of conditions used to synthesize cortisol imprinted polymers reported in literature	118
10	Formulations used to obtain cortisol imprinted polymers	119
11	Formulations of cortisol imprinted polymers following a Doehlert design of experiments	131
12	Binding parameters measured for the polymers synthesized according to the design of experiments	133
13	Normalized coefficients of the polynomial responses calculated for the design of experiments	133
14	Porosity parameters measured for the polymers synthesized according to the design of experiments.	139
15	Normalized coefficients of the polynomial responses calculated for the porosity of polymers from the design of experiments.	140
16	Parameters for the binding affinity of the polymers prior (M_{co6}) and after (M_{co21}) optimization and the predicted values.	144
17	Silica beads formulations and size characterization.	155
18	Formulation of a 2,4-D imprinted polymers.	181
19	Chemical products used in the thesis.	199
20	Solvents used in the thesis.	200
21	Equipments used in the thesis.	201
23	Formulations of polymers for the CPA DOE.	215

List of Figures

1	<i>Le malade imaginaire</i> , Daumier, 1863.	21
2	Schematic representation of wearable sensors use	22
3	Chest straps are replaced for women by integrated heart rate monitors in bras. . . .	24
4	Flexible electronic module connected with conductive yarn by embroidery	24
5	Epidermal Electronic System on skin, undeformed, compressed and stretched	25
6	Body fluids which can be used for molecule sensing.	25
7	Picture of the iBGStar [®] , a new glucometer commercialized by Sanofi Aventis.	26
8	Schematic representation of apocrine and eccrine glands.	27
9	Sweat patch Pharmchek [®]	27
10	Chemical representation of gonane, the skeleton of steroids.	30
11	Chemical structure of cholesterol, the biological precursor of all steroids.	31
12	Chemical structures of steroids studied	31
13	Molecular recognition, the basis of imprinting	34
14	Principles of molecular imprinting	34
15	SEM images of different shapes for the polymers	35
16	Theoretical representation of binding isotherms	37
17	Job's plot for 2,4-dichlorophenoxyacetic acid	38
18	Schematic representation of a sensor	45
19	Competitive binding of bisphenol A and bisphenol-A labelled with a gold nanoparticle on MIP nanoparticles grafted on a SPR substrate	47
20	Diffraction of light waves by a periodic structure	48
21	Square-grating MIP	48
22	One dimension periodicity for polymer grating, obtained by holography	49
23	A photonic crystal in the butterfly wings	51
24	Schematic representation of one-, two- and three-dimensionnal photonic crystals . . .	52
25	Photonic sensors are developed in 1, 2, or 3 dimensions and with several possible struc- tures.	53
26	A stack of block copolymer photonic gel film and the tuning mechanism	54

27	Response of an inverse opal sensor for sequential stimuli of temperature and pH . . .	56
28	Cross-section of a photonic-crystal fiber	56
29	Structure of a 1D-photonic crystal sensor and detection of a biomolecule	57
30	Shift of the Bragg's peak upon recognition of atrazine by a molecularly imprinted photonic polymer	58
31	Opal formation described in literature	62
32	Inverse opal formation described in literature	63
33	A planar defect inserted in an opal and its inverse opal	64
34	Schematic representation of the sensor	66
35	General articulation of the chapters in the manuscript	67
36	Chemical structure of cyproterone acetate.	79
37	Chemical structure of testosterone.	80
38	Molecular mechanism of action of androgens and CPA	81
39	Chemical structure of 15 β -hydroxycyproterone acetate.	81
40	Calibration curve for CPA dosage by HPLC	85
41	Binding assays of CPA in acetonitrile to M _{cpa} 2, N _{cpa} 2	86
42	Binding assay of CPA in toluene to M _{cpa} 5, N _{cpa} 5	87
43	Binding assays of CPA in toluene to M _{cpa} 5 – 7 – 8 – 9, N _{cpa} 5 – 7 – 8 – 9	88
44	Chemical structure of cyproterone acetate with numbered carbon atoms.	89
45	NMR HSQC for cyproterone acetate	90
46	NMR spectra of CPA in toluene-d8 and a mixture of CPA and MAA	92
48	Representative Job's plot for the interaction between H4-, H7- and H24-CPA and MAA in toluene.	92
47	Superposition of NMR spectra with different ratio of CPA/MAA	93
49	Block diagram representatiing a design of experiments	96
50	Comparison of actual versus predicted response	97
51	Washing steps of the polymer performed in a 96-well filtration plate.	100
52	Responses of the DOE plotted according to the solvent used	101
53	Results predicted by the model against results obtained for the responses	102
54	Response stages of the body induced by a stressor.	110
55	Physiological reactions in the adrenal glands induced by stressors.	111
56	Chemical structure of adrenaline.	111
57	Chemical structure of cortisol.	112
58	Circadian rythm of the cortisol secretion	112
59	Evolution of adrenaline concentration, cortisol concentration and heart rate during the trial	113

60	Chemical structure of adrenochrome.	116
61	Calibration curve for cortisol dosage by HPLC	120
62	Binding assay with leaching of cortisol	121
63	Evolution of cortisol concentration in supernatants along with the washings	121
64	Binding assay of cortisol with M _{co} 6 and N _{co} 6 in dichloromethane	122
65	Study of the influence of the polymerization temperature on the binding assay of cortisol in dichloromethane	123
66	Chemical structure of cortisol with numbered carbons atoms	124
67	NMR spectra of cortisol in CD ₂ Cl ₂ and a mixture of cortisol and MAA	124
68	Superposition of NMR spectra with different ratio of cortisol/MAA	126
69	Representative Job's plot for the interaction between H21-cortisol and MAA in CD ₂ Cl ₂	127
70	Representative Job's plot for the interaction between H4-cortisol and MAA in CD ₂ Cl ₂	127
71	Schematic representation of a 2 and 3 factors Doehlert design.	130
72	Adsorption isotherms of M _{co} 12, M _{co} 9, M _{co} 14	132
73	Plot of the response B _{max} as a function of MAA and EDMA ratios	134
74	Evolution of B _{max} versus the cross-linking density for polymers of the Doehlert design.	135
75	Plot of the response IF as a function of MAA and EDMA ratios	135
76	Plot of the response K ₅₀ as a function of MAA and EDMA ratios	136
77	SEM images of a poly(MAA-co-EDMA)	137
78	Adsorption and desorption isotherms of N ₂	138
79	Plot of the specific area as a function of EDMA and MAA molar ratios	139
80	Plot of the pore volume as a function of EDMA and MAA molar ratios	141
81	Plot of the pore size as a function of EDMA and MAA molar ratios	141
82	Evolution of the pore size against the cross-linking density for polymers of the Doehlert design.	142
83	Evolution of the imprinting factor against the difference between NIPs and MIPs specific area for the polymers of the Doehlert design.	142
84	Evolution of B _{max} against the pore size for the polymers of the Doehlert design . . .	143
85	Binding isotherm of cortisol for the first polymer developed and the optimized formula- tion	144
86	Principles of a sensor based on an imprinted polymeric inverse opal.	151
87	Natural opals	153
88	SEM image of synthesized silica beads	155
89	Opal synthesis by evaporation	156
90	Imitation opals synthesized by evaporation	157
91	SEM image of an opal deposited by dip-coating	158

92	The Boostream [®] equipment	159
93	Pictures of a monolayer of 1 μ m silica beads deposited by the Boostream [®] equipment	159
94	5 layers of silica beads, deposited by the Boostream [®] equipment	160
95	Schematic representation of inverse opal formation by "sandwich"	162
96	Picture of an inverse opal on a PMMA substrate made by "sandwich"	162
97	SEM images of inverse opals made by the "sandwich" technique.	163
98	AFM image of an inverse opal fabricated by the "sandwich" technique	163
99	Schematic representation of inverse opal formation by spin-coating	164
100	Picture of an inverse opal on a PMMA substrate made by spin-coating	164
101	SEM images of inverse opals, made by spin-coating.	165
102	Inverse opal formation by dip-coating	166
103	Picture of the dip-coating equipment	166
104	Pictures of inverse opal obtained by dip-coating	167
105	SEM images of inverse opals, made by one dip-coating	167
106	SEM images of inverse opals, made by two dip-coatings	168
107	Diffraction of light by a monolayer of 1 μ m silica spheres.	169
108	Schema of an opal stack	170
109	Figure of diffraction for 5 layers of 1 μ m particles	170
110	A new detector support for 3D measurements of diffraction intensities	171
111	Evaluation of the refractive efficiency of an opal with 1 μ m silica spheres	172
112	Evaluation of the refractive efficiency of an opal with 500 nm silica spheres	172
113	Evaluation of the refractive efficiency of an inverse opal built from 1 μ m silica spheres	173
114	Schematic representation of d and d_{111} for opals	174
115	Reflection of white light by an opal for different angles of incidence	175
116	The developed optical bench for angle resolved spectroscopy	175
117	Transmission and reflection spectra for an opal with 5 layers of 300 nm beads	176
118	Spectrophotometric study of an opal with 5 layers of 300nm beads	176
119	A reflection spectrum for an opal displaying Fabry-Perot interferences	177
120	A Fabry-Perot cavity	177
121	Reflection spectra for opals with 5 and 10 layers of beads	178
122	Spectrophotometric study of an inverse opal made from 5 layers of 300 nm beads	179
123	The chemical structure of 2,4-dichlorophenoxyacetic acid.	181
124	Calibration curve for 2,4-D dosage by HPLC	182
125	Binding isotherm of 2,4-dichlorophenoxyacetic acid	182
126	Optical bench for the diffraction monitoring	184
127	Picture and schematic representation of the sample holder.	184

128	Relative diffraction efficiency as a function of time after solvent injection.	185
129	Washing the inverse opal with a dropwise system.	186
130	Reflection spectra for NIP and MIP inverse opals before and after incubation with 2,4-D	187
131	Picture of the developed optical bench for angle resolved spectroscopy.	207

Acronymes

2,4-D	2,4-Dichlorophenoxyacetic acid
4-vp	4-vinylpyridine
AA	Acrylic Acid
ABDV	2,2'-Azo-Bis-(2,4-DimethylValeronitrile)
AFM	Atomic Force Microscopy
AIBN	Azo-bis-IsoButyroNitrile
AM	AcrylaMide
ANOVA	ANalysis Of VAriance
BET	Brunauer-Emmett-Teller method
BJH	Barret-Joyner-Halenda method
BMa	Benzyl Methacrylic acid
BMA	Benzyl MethacrylAte
B_{max}	Maximum of bound molecule to the polymer in a binding assay
CL%	Cross-linking density
CPA	CyProterone Acetate
DNA	DeoxyriboNucleic Acid
DOE(s)	Design(s) Of Experiments
DSC	Differential Scanning Calorimetry
DVB	DiVinylBenzene
EDMA	Ethylene glycol DiMethacrylAte
fcc	face centred cubic lattice
FDA	Food and Drug Administration
GPS	Global Positioning System
GC/MS	Gas Chromatograph/Mass Spectrometer
hCG	human Chorionic Gonadotropin

HEMA	2-HydroxyEthyl Methacrylate
HPA	Hypothalamo-Pituitary-Adrenal
HPLC	High Performance Liquid Chromatography
HPLC	High Performance Liquid Chromatography tandem Mass
MS/MS	Spectroscopy
HSQC	Heteronuclear Single Quantum Correlation
IF	Imprinting Factor
IR	InfraRed
IUPAC	International Union of Pure and Applied Chemistry
K ₅₀	Concentration of polymer at half the absorption of analyte
LCST	Low Critical Solution Temperature
LED	Light Emitting Diode
MAA	MethAcrylic Acid
MbAAm	N,N'-Methylene-bis-AcrylAmide
MIP(s)	Molecularly Imprinted Polymer(s)
MOO	Multi Objective Optimization
NIP(s)	Non Imprinted Polymer(s), reference control for the MIP
NIPAm	N-IsoPropylAcrylamide
NMR	Nuclear Magnetic Resonance spectroscopy
PBG	Photonic Band Gap
PDI	PolyDIspersity
PMMA	PolyMethylMethAcrylate
PS	PolyStyrene
SEM	Scanning Electron Microscope
SERS	Surface Enhanced Raman Scattering
SPR	Surface Plasmon Resonance
TEOS	TetraEthylOrthoSilicate
TFMAA	TriFluoroMethylAcrylic Acid
THF	TetraHydroFuran
TRIM	Trimethylolpropane trimethacrylate
UV	UltraViolet

Introduction

Physiological fluids offer a rich matrix of biological components containing a lot of information (biomarkers). Researches on these fluids and their constituents are opening new opportunities for biochemical sensors.

Recognition of a biological molecule by a receptor is the result of specific interactions. Natural systems provide dozens of receptors with different properties and at several scales. Some of these receptors, such as antibodies, are used as sensitive layers in sensors. They provide high selectivity to the sensors but display many drawbacks. Indeed, they are often expensive, unstable during storage and difficult to anchor on a transducer. For that reason, the advent of synthetic receptors is considered as a promising alternative. Among the latter, Molecularly Imprinted Polymers (MIPs) position as tailor-made receptors with substantial advantages. In a context of biomimicry, they offer good selectivity and stability, may be produced in large amounts and may be used as recognition elements in sensors.

Once an analyte is detected by a sensitive layer, the sensor should transduce the detection into a measurable signal (by electrochemistry, conductometry, optics *etc.*). This is the role of transducers. Among all transducing possibilities, label-free techniques are direct methods which drew scientists attention. It is the case, for example, of photonic crystals, structured materials that can be used to transduce a detection into an optical signal.

Biosensing is at the frontier between biology, chemistry and physics. Thus, it requires a wide variety of expertises and a multidiscipline approach. Understanding and knowledge of the biological matrix should be combined with chemical detection and physical transduction in the sensor. Intersections should be defined to articulate all these competences.

In this context, the Department of Micro-Technologies for Biology and Healthcare of CEA Leti (Grenoble, France) aims at creating and developing new technologies and innovative solutions for life sciences, healthcare, environment and chemistry, that will further improve diagnosis and treatment, and create market opportunities for industrial partners. Its laboratory of Material and Chemistry Interface develops sensors in these fields. In order to elaborate a sensor with a new type of detection layer, a collaboration was set with the research group for Biomimetic and Nanostructured Functional Materials of Compiègne University of Technology (France), headed by Prof. K. Haupt, the supervisor of this thesis. This laboratory declines competencies in molecular imprinting known worldwide. Thanks to this collaboration, a sensor which combines MIPs and an optical transduction was elaborated.

In this thesis, we worked on the elaboration of an original sensor based on MIPs. Their development and the study of their properties took place in Compiègne University of Technology. In CEA Leti, the sensor was developed and polymers were optimized. The innovative environment of Grenoble accounted for several collaborations in order to improve and characterize the sensor.

A literature review is led in chapter I. After introducing wearable sensors and the interest of physiological fluids, MIPs are emphasized with their ability to be used in sensors. This chapter ends on the introduction of photonic crystals as transducers which can be combined to MIPs.

The manuscript is then devoted to the elaboration and study of MIPs for two steroid molecules. Cyproterone acetate is a synthetic steroid whose study and imprinting is described in chapter II, whereas cortisol is a steroid hormone studied in chapter III. In these chapters, interactions in liquid phase are studied and a multivariate analysis is used to optimize MIPs formulations.

The last chapter is dedicated to the sensor's creation and characterization. The latter is the assembly of several units, *i.e.* the integration of the sensitive layer to the selected transducer. Further tests were performed to prove the concept.

CHAPTER I

Bibliography: wearable sensors,
molecularly imprinted polymers and
optical transduction

1 Interest of body fluids for monitoring the physiological state

External signs of health or fatigue have been interpreted for centuries and our cultural heritage reveals the role of physicians through ages. We may refer to the caricature by Moliere of physicians of the 17th century (*Le malade imaginaire*). In this play, physicians palpate, smell, take the pulse and exaggerate their physical investigation to establish their diagnostic (figure 1). Despite the caricatural aspect of the play, this underlines the importance of physical external parameters to evaluate health of the body. Nowadays, the evaluation of the excess of body temperature by a parent's hand on his child's forehead and the measurement of the pulse frequency are still reflex gestures. However, the advent of sensing technologies and the progresses in medicine gave rise to the development of sensors and their use by medicine's neophytes.



Figure 1: *Le malade imaginaire*, Daumier, 1863.

1.1 Wearable sensors

Wearable sensors originate from the need to constantly monitor physiological or environmental parameters. This technology is commonly used by people doing exercise and being eager to monitor their performances and to control their health. Pedometers and heart rate monitors are well-known examples of such sensors. During the last decades, the progress in wearable systems and the ageing of the population have fostered the development of wearable sensors for patient monitoring. They aim

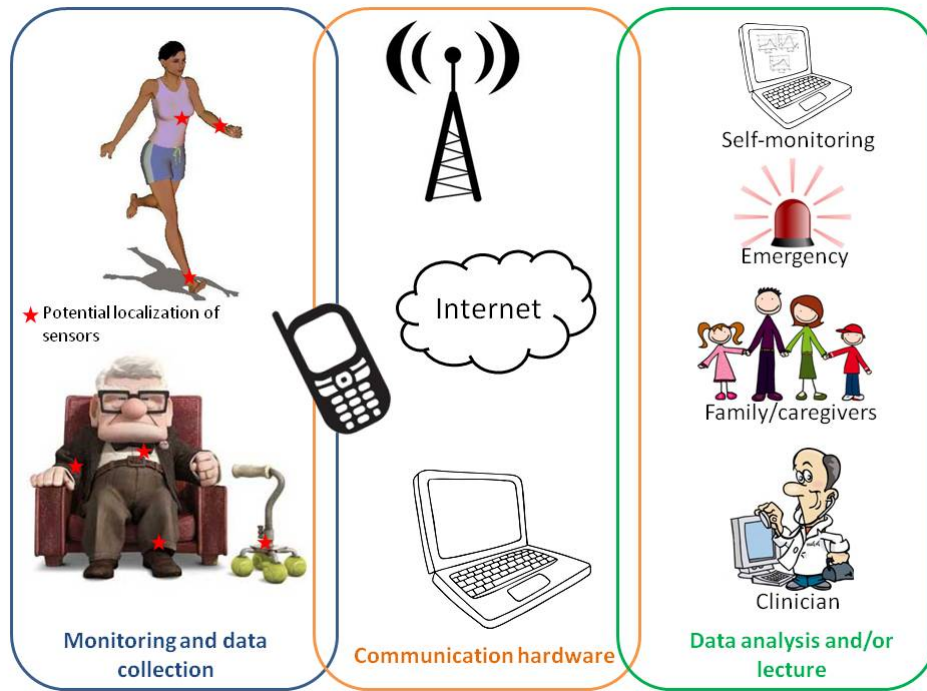


Figure 2: Schematic representation of wearable sensors use. These devices monitor physiological parameters and may communicate the data to a personal software or external centers.

at providing quality of care and preventing rising healthcare costs (by allowing home hospitalization and the earliest detection of symptoms).

The principles of wearable systems are illustrated in figure 2. According to the situation, the sensor can display in real time the data or communicate them to a personal computer or a control center. In the case of sportsmen/women, it is possible, for example, to monitor and register the heart rate frequencies, the speed, the route and its changes of altitude. But wearable sensors can also be useful for elderly and/or sick people. Physiological and physical data are transmitted to control centers thanks to a wireless network. The analyses of the data can trigger an emergency intervention (in case of a fall or cardiac arrest for example). The data are also accessible to a clinician for a daily care and thus wearable sensors register in the *connected health* technology.

In the last years, many developments of devices were reported in the literature. Most often, they integrate all the components of the sensor (power supply, communication antenna) and optimize the transmission of the data and their users interface [1].

1.1.1 Sensing devices

Heart rate monitors are personal monitoring devices used largely by performers in various physical exercises. Medical devices performing a similar function are nowadays used to monitor the cardiac activity of sick people in daily living conditions [2]. Long-term monitoring of heart rate can allow

the capture of rarely occurring events, yet relevant for diagnostics. Additionally, accelerometers are commercialized as part of the motion-sensing technologies. The devices are able to monitor and analyze human motion and may, for example, detect the fall of an elderly person [3]. They could also be useful for patients with motor disorders and help determine new symptoms. In particular, patients with Parkinson's disease need an appropriate medication according to the evolution of the symptoms. Finally, wearable sensors may also include GPS (Global Positioning System), pedometers and breathing rate monitors to complete the possibilities of physiological monitoring.

All these sensors are worn on the body and communicate with a base station. This could be a computer located in a close environment or a data logger worn by the subject. Indeed, several devices provide real-time, on-board monitoring of physical parameters. However, more detailed information is possible with storage and analyses of the data. That's why data analysis may be performed by a software and data loggers (such as cell phones) are used as a gateway for remote access to the subject's data.

Data may be analyzed by diverse algorithms to facilitate their study. The algorithms are specifically designed to treat the data and manage artifacts. Moreover, they may also help to improve sportsmen/women trainings, to improve medical treatments, enhance early detection and thus mitigate risks [4]. For example, Berckmans and coll. worked on an algorithm which monitors different heart rate responses to training intensities of cyclists [5]. The real-time model could be used to calculate the needed intensity during training in order to acquire the optimal training effect for an individual at any given moment.

1.1.2 Integration of the sensors

Sensors should be comfortable and discrete in order to gain interest in the market. A possibility is to integrate the devices in textile or to reduce their sizes, in order to integrate them in daily life accessories (glasses, watch, rings *etc.*).

Substantial progresses were made in electronic textiles (e-textiles). These are clothes with integrated sensors. Also called smart clothing, they contain sensors integrating novel fiber materials, a wireless transmitter and a power supply. Comfort, washability and time resistance are the main issues of this technology. Some sensors are already integrated in commercialized clothes. Runners routinely use heart rate monitors as a chest strap and a watch. Recently, the latter have been integrated in sports bra (figure 3).

Integration in textiles is also fostered by the advent of smart connectivity and soft electronics. Thus, Reichl and coll. developed a flexible electronic module that can be connected to conductive yarns and be integrated in textile [6] (figure 4). This enables an interconnection between sensors, batteries and textile keyboards.

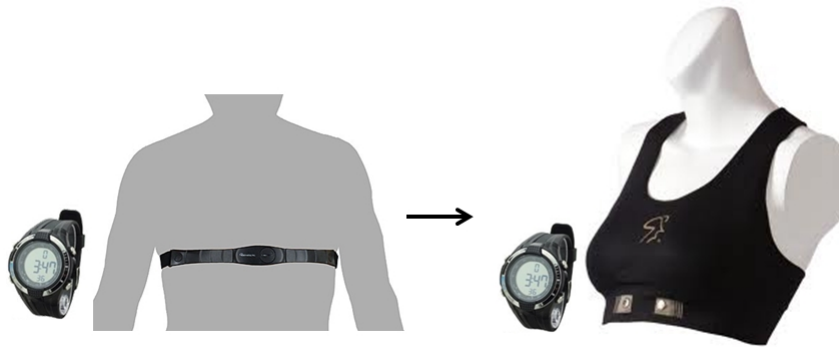


Figure 3: Chest straps are replaced for women by integrated heart rate monitors in bras.

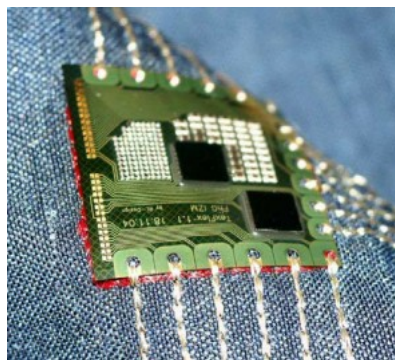


Figure 4: Flexible electronic module connected with conductive yarn by embroidery, figure issued from [6].

An example of a complete sensor with a specific goal and integrated in clothes is given by the European project ProeTEX. This project developed garments for firemen which detect several physical parameters [7]. The inner garment is used to monitor the breathing rate and the body temperature. Breathing rate can be evaluated either by the 5 electrodes measuring the thoracic impedance or a piezoresistive textile. The outer garment is used for the power supply, the communication antenna and accelerometers monitoring the movements. The sensor is able to communicate with a central unit and it can alert support.

Another challenge is to miniaturize sensors to integrate them easily or make them the least inconvenient. If not integrated in clothes, they could be directly worn on the body. Rogers and coll. proposed a very thin epidermic electronic system ($7\mu\text{m}$) that resists to strain (figure 5) and can be transferred to the skin by a system like temporary tattoo [8]. The device measures electroencephalograms, electrocardiograms and electromyograms. Temperature sensors and LEDs for further chemical detection could soon be integrated in the device as well. Materials and mechanics presented in this article focus on small integrated circuits with high performance for physiological measurements. Rings and earrings are other original carriers used respectively by Asada *et al.* and Guang-Zhong *et al.* to monitor heart rate [9],[10]. Last but not least, STMicroelectronics and Sen-

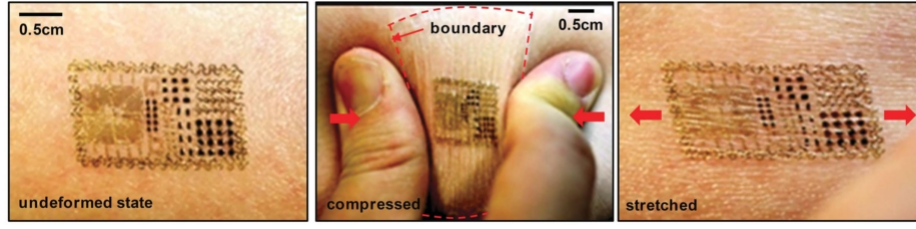


Figure 5: Epidermal Electronic System on skin, undeformed, compressed and stretched. Figure issued from [8].

sioned developed a smart contact lens with embedded wireless sensor to achieve earlier diagnostic of glaucoma thanks to pressure monitoring [11], [12].

Despite the growing interest in wearable sensors, most of them only measure physical parameters. Measurements are thus global and don't bring all the answers necessary for diagnostic. Only a few chemical sensors are described monitoring biomarkers in body fluids whereas they contain very rich information about the physiological state of an individual.

1.2 Body fluids

Body fluids are liquids contained in the organism and the main component of these fluids is water. A human being is generally composed of 50-60 % of water. Two thirds are located in intracellular fluids and the other third is found in the extracellular fluids which are interstitial fluids and blood plasma. Flowing liquids transport of molecules within the body. They overpass diffusion and provide the body with the required molecules and eliminate waste. They also protect from the outer world. For example, the eyes are protected with a thin layer of tears, the nose is coated with mucus and the mouth with saliva. Many of these fluids reflect the body state and could be used to diagnose, manage and assess disease or homeostasis disorders (figure 6).

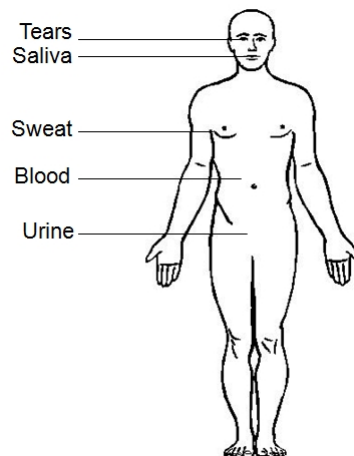


Figure 6: Body fluids which can be used for molecule sensing.

Blood is the main fluid used for diagnosis. Indeed, its composition is stable during long periods and reliable for analyses, and moreover it reflects the state of the whole body. Thus, the blood enables biochemical analyses (small molecules and ions), molecular profiles and cellular evaluations *via* different tools of *in vitro* diagnostic. For example, the human Chorionic Gonadotropin (hCG), a hormone marker of pregnancy, can be detected and dosed in blood in local analysis laboratories. Other blood tests need to be performed daily (or more) and this is the case of glucose dosing. Diabetics have to measure their level of glucose several times a day. The widespread method is to prick the finger with a lancet to obtain a drop of blood. The drop is then collected on a test-strip and inserted in a glucose-meter. On the strip, the glucose is oxidized by an enzyme (oxidoreductase) and the electrons are transferred to a mediator molecule. Finally, the mediator transfers the electrons to an electrode (electrochemical measurement) or to an indicator molecule (photometric measurement). Nowadays, although these tests become faster and need less blood volume [13], they are still rather uncomfortable and invasive. The periodicity of the tests does not allow measurements in laboratories and requires devices for home testing. Among the devices developed, Sanofi Aventis launched a hightech product called iBGStar[®] (figure 7) which enables the connection of the glucometer to an iPhone and thus the glucose monitoring and analyses in a few seconds with the display of the result.

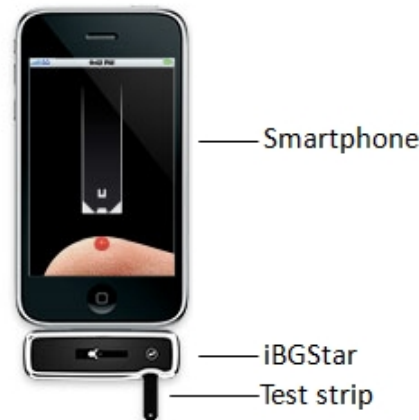


Figure 7: Picture of the iBGStar[®], a new glucometer commercialized by Sanofi Aventis.

Testing glucose in blood will still be necessary during the next decades as no cure for diabetes seems to be emerging. Nevertheless, non invasive measurements, using other body fluids (sweat, saliva, tears or urine), are under investigations to replace current devices. This may reduce pain and, in some cases, enable real-time monitoring. We will now consider these fluids in more detail, keeping glucose as a guideline for discussion.

Sweat is a physiological fluid that has attracted the attention during the past decades. Sweating induces the thermoregulation of the body. It is also triggered by emotions (stress, pain) and spicy food. Sweat is secreted by two types of glands: apocrine and eccrine (figure 8). Eccrine glands are

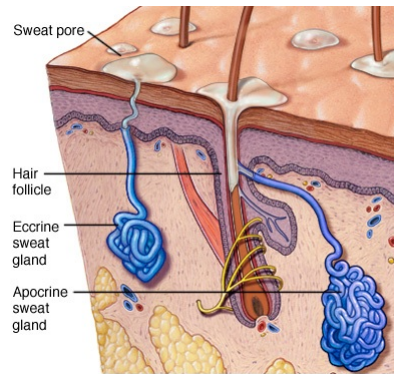


Figure 8: Schematic representation of apocrine and eccrine glands.

spread on the entire skin surface. They are responsible for body thermoregulation and are regulated by the hypothalamus. Apocrine glands are located in specific areas such as axillae.

Sweat is an isotonic ultra filtrate of plasma (excretion glands are in contact with blood capillaries): it represents the composition of blood and thus may be used for biomarkers analyses. When primary secretion passes the duct, several ions are reabsorbed and excreted sweat becomes hypotonic. When the sweat flow rate is high, it passes faster through the duct and a more concentrated sweat is produced [14]. Finally, ions, small molecules (such as sodium, chloride, potassium, urea, lactate) are found in the ultra filtrate thanks to hydrostatic pressure. There are also organic and inorganic compounds [15], including exogenous substances (heavy metals, pesticides, drugs *etc.*).

This is why sweat analysis is used to detect drug consumption [16].

For example, PharmChem developed a patch to detect drugs of abuse in sweat, during a large window of detection (up to 10 days) [17]. They highlight that in sweat both the parent drug and the drug metabolites can be detected, which reinforces the test. The patch can not be substituted (figure 9) because it possesses a bar code and can not be replaced if peeled off. It is used as drug consumption evidence and has been upheld in federal and state courts. After removal of the patch, the collected analytes are solubilized and analyzed by GC/MS in laboratories. Detection of cocaine, opiates and amphetamines can be achieved with a sensitivity of 10 ng/mL.



Figure 9: Sweat patch Pharmchek®.

On the other hand, real-time analysis of sweat is currently used to prevent dehydration. This application was addressed by the European project Biotex which aimed at monitoring physiological parameters in sweat during daily activities [18]. Scientists developed a biochemical sensor integrated in the textile that collects sweat and transports it to several sensing units. They analyzed in real time the sweat for its pH, sodium concentration and conductivity and demonstrated a correlation

between the evolution of these parameters and the modification of the subject’s physiology during an effort [19], [20].

Real-time monitoring of sweat composition can also be focused on organic molecules. Here again the example of glucose can be cited. Indeed, a recent study showed that glucose level in sweat is correlated to blood level [21]. Furthermore, a watch evaluating glucose in sweat was developed in the last decade (GlucoWatch®). In this device, detection of glucose is enabled by applying a low current on the skin surface in order to extract glucose molecules by reverse iontophoresis. The device was approved by the U.S. Food and Drug Administration (FDA) but later disappeared from the market. The reasons of this failure rely on the long warm-up time, the necessity to calibrate it with finger pricks and its lack of robustness. According to the numerous articles devoted to this watch on the internet, there is a high probability that a device with better finishing touches and fewer disadvantages would conquer the diabetic population.

Saliva is a gland secretion. It contains serum molecules carried there by passive diffusion and ultra-filtration. The advantage of saliva for molecule sensing is the ease of sampling and storage. In particular, when a control is required, the sampling is simple and non invasive. Nevertheless, the analytes are in low concentration and contamination is always possible. Several molecules can already be tested in saliva such as antibodies and hormones. Lipid soluble hormones for example reach saliva and their level can represent the free-hormone level in serum [22]. Basic exogenous drugs have also been observed: they arrive in oral fluids by passive diffusion. Glucose is also measurable in saliva [23]. For example, the Endocrinology and Metabolism Research Institute of Tehran University of Medical Sciences developed a prototype able to measure glucose in saliva. Although not commercialized yet, this was the first prototype whose sensitivity was satisfactory.

Tears are a complex biological fluid. It is the extracellular fluid wetting the eye surface and is basically a diluted proteins and salt solution. The composition of this fluid is useful to discover biomarkers of eye diseases, such as proteins related to the Alzheimer’s disease [24]. The glucose level in tears is correlated to its plasma level [25]. This property is exploited by Noviosense, a young start-up which developed a device for glucose monitoring in an eyelid [26]. The detection is similar to blood test-strip but the electrochemical cell is very small and the signal is converted into a radiofrequency signal that transmits information to a phone or similar device. Tears are of particular interest as the fluid is renewed at each eye blinking, enabling real-time data monitoring.

Urine is also a very interesting fluid for molecules sensing. It is composed of water, certain electrolytes, and various waste products that are filtered out of the blood system by the kidneys. The filtration of blood to form urine takes place in the nephrons. Soluble wastes are excreted primarily by urine. It is mainly constituted of urea (formed to eliminate ammonia), ions, organic and inorganic compounds. Concerning glucose, a Japanese corporation (Tanita) developed a urine glucose-meter that works well for self-monitoring glucose [27]. Detection is amperometric and the

sensor is used like a pregnancy test. On the other hand, urine is an important source of biomarkers since the protein population (containing hundreds of different molecules) can be rather different between disease and control samples. However, the selection of biomarker candidates is difficult and time consuming. To solve this issue, Gao and coll. recently built a database of all repertoriated protein biomarkers in urine. This tool is very useful to compare the works and results of dozens of researchers [28].

We described above several physiological fluids in which some molecules can be measured. With the common example of glucose, we demonstrated that organic molecules can be monitored in other media than blood [29]. We also underlined the existence of different sensors that enable a real-time, non-invasive and self-monitoring of a chemical parameter. Thus, several biomarkers can be monitored in physiological fluids.

1.3 Biomarkers in physiological fluids, with particular focus on steroids

Biomarkers are indicators of a physiological state, which is why these biomolecules are used to diagnose and classify diseases. The identification of biomarkers has been and is still a big challenge [30]. They are very often discovered by chance. The metabolites and peptides found in body fluids can be collected outside the body after crossing diseased tissues and therefore reflect the body condition. Thus, body fluids are studied for new biomarker identification. The progress of separation methods and proteomics (coupled with mass spectrometry) resulted in a large increase in the number of known biomarkers [31]. Among these, lots of hormones were identified.

Hormones are small molecules secreted by the body. They can sometimes be used as biomarkers for certain diseases. For example, among many soluble proteins and cell markers, hormone activity in breast cancer is under investigation [30]. They seem to play a role in the risk of cancer development and progression. Hormones act normally as a chemical signal for control and regulation of the physiological state. These chemical messengers are secreted by cells of the endocrine system into the extracellular fluid and activate target cells. They can be divided into three categories according to their chemical functions: polypeptides, steroid hormones and amine hormones. Categories of hormones and their properties are given in table 1. We will mainly work in this thesis on steroids (hormones and synthetic) and evocate the case of epinephrine, an amine hormone.

Steroids are a class of organic compounds that are widely found in plants, animals and fungi. The term steroid includes both steroid hormones and synthetic steroids. These compounds present a tetracyclic hydrocarbon skeleton. The skeleton molecule is gonane, with 17 carbons (figure 10). They vary by the functional groups attached to the ring core, which defines their parent ring, and the oxidation state of the rings. Small chemical variations can produce enormous hydrophilic differences

Polypeptides	Steroid hormones	Amine hormones
<ul style="list-style-type: none"> - Water soluble - Can be transported in blood - Delivered to cells thanks to vesicle packaging 	<ul style="list-style-type: none"> - Derivatives from cholesterol - Lipid soluble - Pass easily the cell membranes - Bound to carrier proteins in blood 	<ul style="list-style-type: none"> - Derivatives of the aminoacid tyrosine - Either water or lipid-soluble
ex: Insulin (51 amino acids)	ex: Testosterone, cortisol	ex: Thyroxin, epinephrine

Table 1: Chemical groups of hormones and their characteristics.

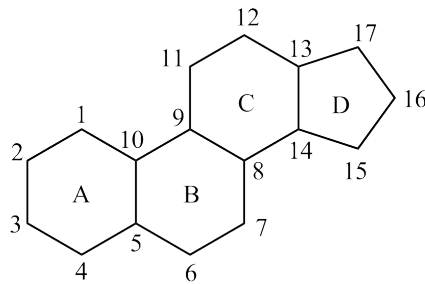


Figure 10: Chemical representation of gonane, the skeleton of steroids.

and thus, lead to differences in their actions.

Steroids can be divided into several categories (table 2). They are either classified according to their number of carbons or by the name of their tropic peptides (each steroid possesses its own stimulatory peptide, called "tropic").

The steroid cholesterol is the most recognized member of these organic compounds (figure 11). It is also the only precursor of the biogenesis of steroids, called "steroidogenesis". Steroid hormones are produced either in the adrenal cortex, testis, ovary or some peripheral tissues. They circulate in blood thanks to protein carriers and can pass through the cell membrane and bind to steroid hormone receptors.

The metabolism of steroid hormones takes place in the liver, on free molecules. It mainly consists in rendering the molecules more hydrophilic to eliminate them in urine. In common slang, the term

Number of carbons	Parent ring structure	Steroid class
C18	Estrane	Estrogens
C19	Androstranes	Androgens
C21	Pregnane	Progestins Glucocorticoids Mineralocorticoids
C24	Cholane	Bile acids
C27	Cholestane	Vitamin D steroids

Table 2: A possible classification of steroids.

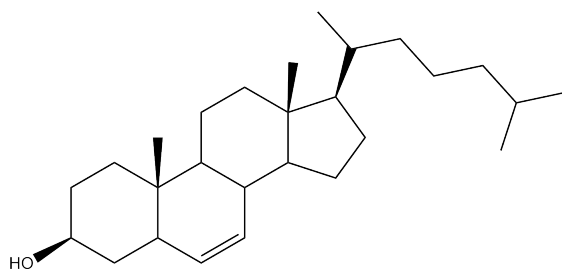


Figure 11: Chemical structure of cholesterol, the biological precursor of all steroids.

steroid often refers to anabolic androgenic steroids, classified as drugs. Some athletes take them to increase muscle mass, strength and resistance to long training sessions. These molecules are chemically related to testosterone. Most of the molecules used are exogenous (synthesized) and a few are endogenous. In this manuscript, we will rather focus on two different steroids: hydrocortisone and cyproterone acetate (figure 12), which are the targets of the developed sensors. Hydrocortisone also known as cortisol is a steroid hormone, a glucocorticoid related to stress and inflammation. Cyproterone acetate is an androgen synthetic steroid, often prescribed after a prostate cancer.

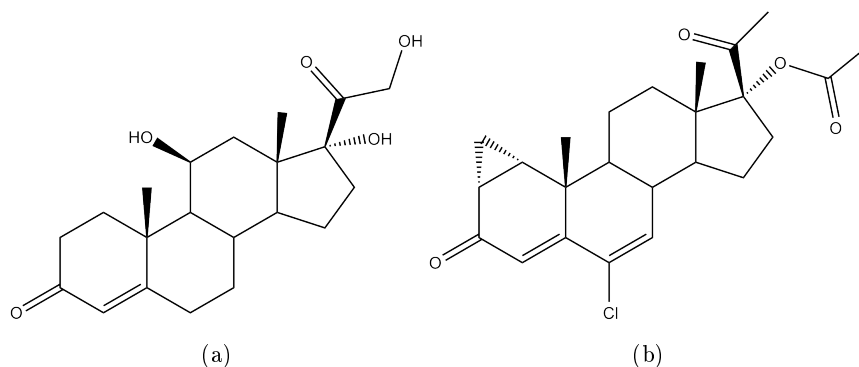


Figure 12: Chemical structures of steroids studied in this manuscript: (a) cortisol and (b) cyproterone acetate.

We underlined here that steroids are an interesting class of molecules, which could be used as biomarkers. In particular, cortisol is a biomarker whose secretion is related to stress and can be paralyzing in critical situations. Cyproterone acetate is a medicine whose delivery quantity should be controlled. These steroids are respectively a natural and a synthetic steroid and their detection by a wearable sensor would be interesting, since they can also be secreted and monitored in other media than blood. That's why, in this thesis, these two molecules will be studied more deeply and detected by molecularly imprinted polymers.

2 Molecularly imprinted polymers and their use in chemical sensors

Molecular imprinting is a technique allowing to generate biomimetic synthetic receptors. It consists in producing binding sites in synthetic polymers, using a templating process at the molecular level. Molecularly Imprinted Polymers (MIPs) exhibit selective binding of the template used during their fabrication. They are generally more robust, more stable and cheaper than their biological counterparts. These materials have been used in a wide range of applications (chromatography, sensors, solid phase extraction, synthesis and catalysis, drug delivery and others) requiring dedicated approaches to optimize the polymers according to their use.

2.1 Molecular imprinting

2.1.1 Molecular recognition and principle of molecular imprinting

Molecular recognition refers to specific interactions between two molecules, called host and guest, which exhibit a molecular complementarity. The involved interactions include ionic and weak interactions (electrostatic, hydrogen bonds, Van der Waals, hydrophobic interactions and $\pi-\pi$ stacking). To visualize such an interaction, Fischer proposed in 1890 the "lock and key" model (in the case of enzyme/substrate) [32] (figure 13a). This model then gave rise then to stereocomplementarity. Later, Pauling discovered the complementary in "shape" between antibody and antigen [33] (figure 13b). Nowadays one of the strongest non-covalent recognition pairs in nature is the complex of streptavidin and biotin (figure 13c).

In addition to biological recognition pairs, synthetic systems have raised great interest during the past decades. One of them is molecularly imprinted polymers. These materials (figure 13d) reproduce the natural molecular recognition phenomena occurring in nature, and are thus referred to biomimetics, the study and mimicry of biological systems. The first example of molecular imprinting in organic polymers was reported by Wulff and coll. in the early 1970s [35]. They had a template molecule covalently modified with vinyl functions. After polymerization of this polymerizable tem-

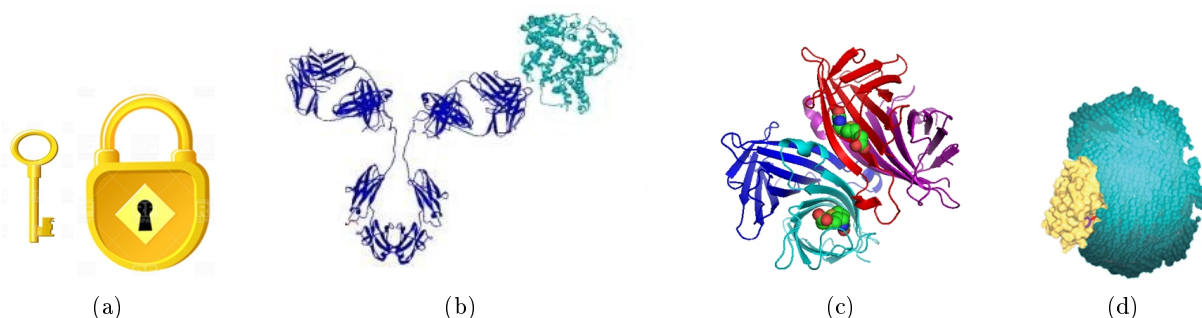


Figure 13: Molecular recognition. (a) The lock-and-key model introduced by Fischer, (b) an antigen linked to an antibody, (c) the complex streptavidin-biotin, and (d) the schematic representation of a molecularly imprinted polymer with its target, the protein trypsin [34].

plate with a cross-linker, they hydrolyzed the bonds, releasing the template, and leading to cavities capable of recognizing and binding the template. This technique is known as "covalent imprinting". A decade later, Mosbach *et al.* introduced "non-covalent molecular imprinting" consisting in polymerizing monomers previously complexed with a template molecule *via* non-covalent interactions [36]. Nowadays, this general approach is most widely used. The principles of molecular imprinting are represented in figure 14.

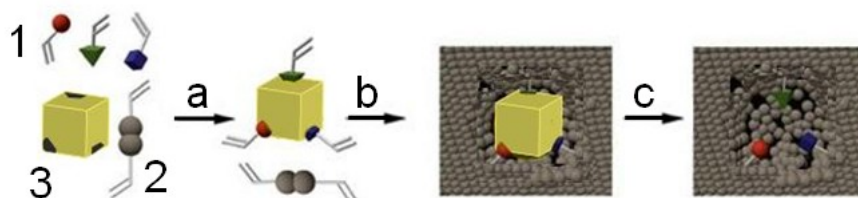


Figure 14: Principles of molecular imprinting. 1: functional monomers, 2: cross-linker, 3: template, a: complex formation, b: polymerization and c: extraction of the template leaving a binding site. Figure issued from [37].

In the non covalent approach, the template molecule self-assembles to form a complex with functional monomers *via* weak interactions governed by equilibria. A cross-linker is introduced at high molar ratio with respect to the functional monomers to cross-link the polymer. Other important ingredients is a solvent playing at the same time the role of a porogen, and an initiator of (in most cases) the radical polymerization. After polymerization, a highly cross-linked and porous polymeric matrix is obtained and the template molecule can be extracted by several washing steps with suitable solvents. Cavities are formed in the polymer, complementary in size and shape of the template. Chemical functions are located in the cavities and enable a selective rebinding of the molecule (with single or multiple point interactions). Cavities are the chemical and physical imprint of the molecule, giving the name of Molecularly Imprinted Polymers to the studied polymers. A

particular attention should be paid to the extraction of the template from the polymeric matrix. The successive washing steps often employ a solvent containing a competitor, like acetic acid, to break the interactions between template and polymer (such as hydrogen bonds). If some template remains in the cavities, this could later lead to "template bleeding", which may be a problem for the specific application the material is intended for, in particular affinity solid-phase extraction (SPE) for trace analysis. A solution to avoid problems with template bleeding is to use a "dummy template": a different molecule that closely resembles the target molecule to be recognized serves as the template. If some template leaching occurs, the template can be easily distinguished from the target molecule during the chromatographic quantification step (*e.g.* by HPLC MS/MS) following SPE. For example, epitestosterone was used as a template to generate a MIP recognizing testosterone [38].

One considerable advantage of polymers is that they can be synthesized with different shapes (figure 15). Historically, MIPs have been synthesized by bulk polymerization followed by mechanical grinding of the monolith to obtain small, irregularly shaped particles. Precipitation polymerization directly yields nanobeads of uniform size [39]. Other examples are polymer films that can be made by different manners like spin-coating [40] or bottom-up synthesis with immobilized initiators [41]. It is also possible to generate microdots [42], nanostructures like surface-bound filaments [43] or even soluble MIP microgels [34].

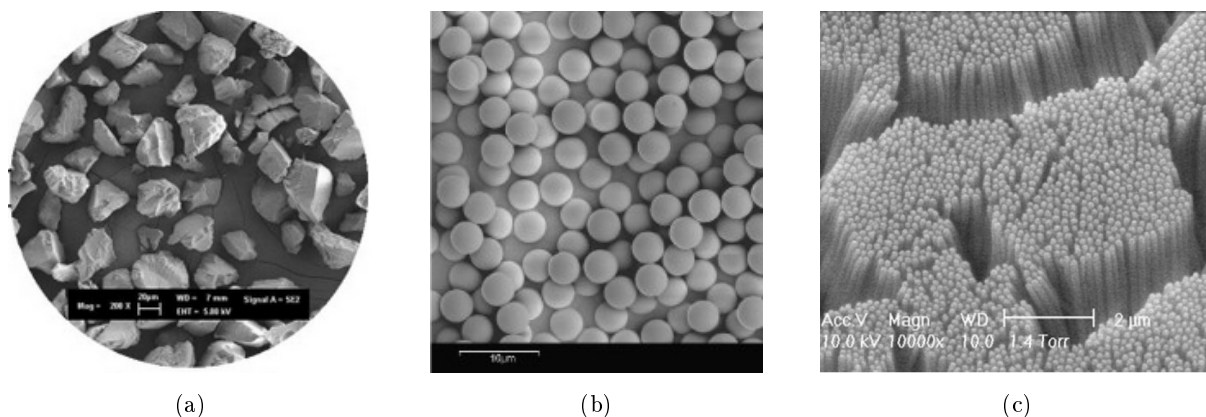


Figure 15: SEM images of different shapes for the polymers: (a) grounded bulk , (b) nanospheres and (c) molded nanofilaments. Figures issued from [44], [39] and [43].

2.1.2 Characterization of the polymers

Once synthesized, the polymers must be characterized. The first step is usually to prove the formation of imprints although polymer morphology studies, for example porosimetry, as well as nano-metrics analysis by microscopic methods, are also important.

If the imprinting has been successful, then the polymer will have a specific binding capacity with a certain affinity for the template. A non imprinted reference (NIP) is often synthesized to evaluate the non specific adsorption (the NIP having the same formulation as the MIP but the template is not introduced in the precursor mixture), although great care should be taken as the NIP is often not the appropriate control and can only provide an indication of the extent and type of non specific interactions that can be expected. In fact, most of the monomers' functional groups that are available for non specific binding in the NIP will be situated in specific binding sites in the case of MIPs.

A binding test, often performed under equilibrium conditions, reveals the binding of the template to the polymer's specific binding sites. For this test, a constant concentration of polymer is introduced (same number of binding sites) in a constant volume of solvent containing different concentrations of template. The concentrations of either bound or free templates in solution are monitored. It is then possible to fit the data with a suitable binding isotherm equation. The first choice of an isotherm model would be the basic Langmuir model derived from the expressions of the equilibria involved (one or two classes of binding site with respect to affinities). However, MIPs tend to contain a more heterogeneous population of binding sites, and the Langmuir-Freundlich isotherm is often more appropriate [45]. This model is a function that correlates free and bound molecule concentrations, for homogeneous and heterogeneous systems, with three fitting coefficients (see equation 2.1, where N_t is the number of binding sites, K_0 is the median binding affinity, m is the heterogeneity index and F and B respectively the concentrations of free and bound templates in solution). It can simulate both Langmuir and Freundlich behaviors and can be used for all concentration variations.

$$B = \frac{N_t K_0^m F^m}{1 + K_0^m F^m} \quad (2.1)$$

Alternatively, it is possible to vary the amount of polymer and keep the template concentration constant at a low level. With a higher concentration of polymer, the number of binding sites available increases and less template stays in solution. Figure 16 represents a binding isotherm with a constant amount of template and an increasing concentration of polymer. The non specific binding is represented by the NIP. This technique of binding test is used in this manuscript. It enables a direct comparison between the MIP and the NIP and allows for relative evaluation of the association constants.

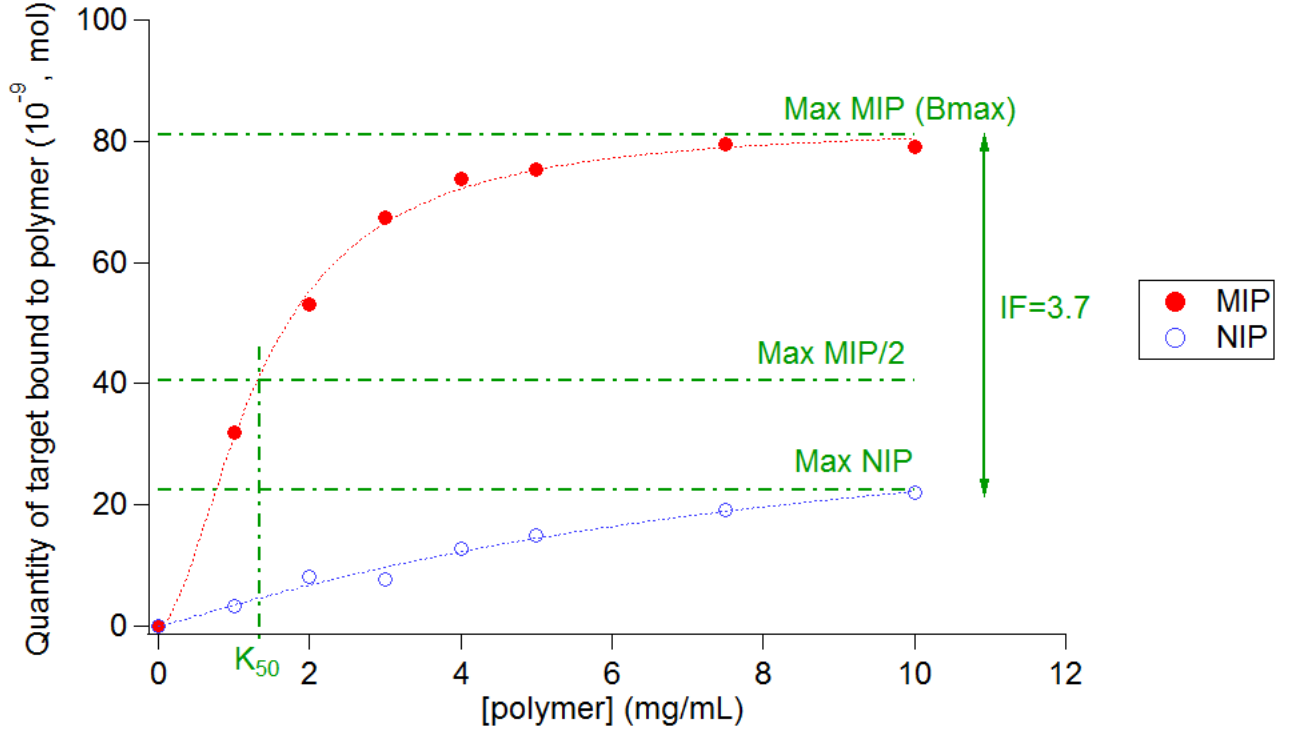


Figure 16: Theoretical representation of binding isotherms and the determination of K_{50} and the imprinting factor (IF) for a polymer concentration of 10 mg/mL.

From the binding data, fitted with a Langmuir-Freundlich isotherm, several parameters can be extracted.

- K_{50} is a binding affinity parameter that can be extracted from this plot. It corresponds to the concentration of polymer where 50% of the analyte is adsorbed. This parameter leads evaluation of polymer affinity: the smaller is K_{50} , the better is the affinity of the MIP towards its template.
- Another parameter is the maximum of template bound to polymer, B_{max} , which refers to the polymer capacity.
- The imprinting factor (IF) is the binding to the MIP versus binding to the NIP for a given polymer concentration. This definition will be used in this thesis, although there are many other possible ways to define an imprinting factor. In any case, IF should only be used for a general indication of the success of imprinting, or to compare different MIPs, keeping in mind that it is associated with the same shortcomings as the NIP itself, as outlined above.

Several physical measurements can be done to characterize the polymers, in order to optimize their formulation or understand the theoretical aspects lying behind the technology. Thus, spectroscopic measurements provide information on molecular interactions and can be useful for the study

of the complex formation before polymerization or the molecular recognition due to the imprinting process. A change in the template's environment will indeed modify the vibrations and any weak-interaction will also modify the local magnetic field. Among the spectroscopic measurements, we can quote Nuclear Magnetic Resonance spectroscopy (NMR), infrared (IR) or Raman spectroscopy.

NMR spectroscopy can also be used to determine the interactions between the template molecules and the monomers in the precursor mixture, before the synthesis of MIP. Thus, Job's plot [46] results from the monitoring of a chemical shift as a function of the molecules concentrations. For example, starting from a successful formulation of MIP [47], this approach was used to determine the stoichiometry of the complex between the herbicide 2,4-dichlorophenoxyacetic acid (2,4-D) and the functional monomer 4-vinylpyridine [48]. Job's plot is represented in figure 17a. The maximum of the plot is obtained for a molar ratio of 0.5, which means that the interaction is 1:1 for the complex 2,4-D:monomer. The publication also underlines the interaction of two more monomers in $\pi - \pi$ stacking. Finally, the authors assume the formation of a complex with three monomers for one molecule of 2,4-D (figure 17b). This technique will be used and discussed in more detail in chapters II and III.

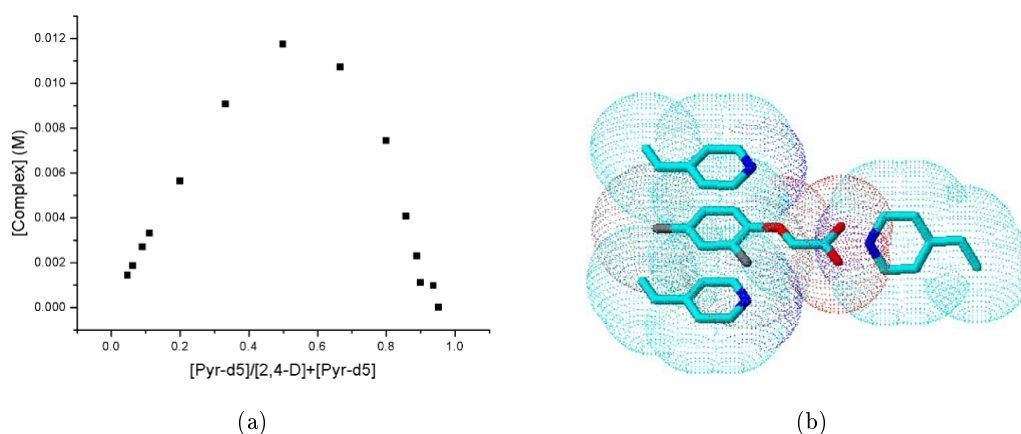


Figure 17: Study of the complex 2,4-D and 4-vinylpyridine. (a) Job's plot and (b) Proposed conformation of the complex 1:3. Figure from [48].

Once the polymer is synthesized, solid state NMR can provide information on the solid polymer. With this technique, it is possible to show the binding of analytes to the polymer, if interactions are very strong. Sellergren and coll. studied the imprinting of 9-ethyladenine by solid state NMR spectroscopy [49]. The measurements gave information on the different types of binding sites. Unfortunately, solid state NMR is not sufficient to monitor the binding of the template because this is a transfer from the solvent to the solid. That's why they combined solid state NMR to a suspended-state analysis.

UV spectroscopic analysis is an interesting tool to study the self-assembly of monomers and tem-

plates in the precursor mixture. Nicholls and coll. performed a titration of methacrylic acid with a dipeptid and proved that this technique could be useful for the optimization of the monomer/template ratios [50].

Infrared spectroscopy is a vibrational spectroscopy that can be used to study intra and inter-molecular hydrogen bonding [51]. When a complex is formed in the precursor mixture, the intensity of the stretching vibrations of amino-, hydroxyl- or carbonyl- groups is correlated to the complex concentration (relative measurements are then allowed). Moreover, the structure of the complex influences the vibrational spectrum. The observed frequency shift is even higher when the hydrogen-bonding is strong. With infrared spectroscopy, Stidham and coll. characterized the host-guest complex [52]. With these data, they could establish a relationship between some vibration intensities and the binding constant, and subsequently measured it before and after polymerization of their MIP films.

Finally, isothermal titration calorimetry can be used to perform a thermodynamic analysis of the MIP-template interaction and to extract the binding constant as well as the contribution by the enthalpy and entropy terms [53].

Other physico-chemical characterizations of the polymers itself that can be performed are thermogravimetric analyses or differential scanning calorimetry (DSC). DSC studies also detects the complete or incomplete polymerization (pendant double bonds) [54], [55]. Thermogravimetric analyses showed that MIPs have a high thermal stability with generally no mass loss under 200 °C [56]. Nicholls and coll. studied the theophylline imprinted polymer and its thermal resistance. They observed that the polymers displayed no loss of affinity for the template while heating up to 150 °C. Moreover, after incubation in HCl (1-10M) and NH₃ (5-25%) during 24 hours, no change of the polymer behavior was noticed.

Finally, porosity measurements are employed to qualify the polymers. Pore size and surface area studies on the polymers can be provided by Brunauer-Emmett-Teller analysis (BET) [57]. The adsorption isotherms usually show that the polymers are dominated by mesoporous structures. Differences of morphology were observed for the polymers, according to the used solvent and the ratios of functional monomer and crosslinker [58]. For example, Rix and coll. studied morphology differences according to the interactions involved and assumed that $\pi - \pi$ stacking confines the polymer network growth [59]. They also observed that solvents providing a poor polymer chain solubility resulted in higher surface areas.

In conclusion, molecular imprinting is a vast field in which chemical and physical characterization is essential for the comprehension of the mechanisms involved. The main problem is often the empirical determination of MIP formulations, resulting in poor specificity and the compromises that have to be made in the context of a particular application of the materials, for example when

the MIP has to be interfaced with a transducer in a chemical sensor. In the next section, we will consider the main factors influencing the imprinting effect and how MIPs can be integrated in some optical sensors.

2.2 Imprinting effect: influencing factors and optimizations

In this section, we will describe several factors which influence the quality of the imprinting in polymers. We will particularly focus on the constituents of the polymer and explore their influence as it is known so far. This will drive the discussion to the current techniques employed to optimize the formulation of MIPs.

2.2.1 Functional monomers

The monomers have to be carefully chosen as they should form a stable complex, with strong interactions with the template. The monomers can interact with the template thanks to their functional groups. For example, basic functional groups tend to interact with monomers bearing acidic functional groups. A classification of common monomers according to their level of acidity/basicity is given in table 3.

Methacrylic acid is a widespread monomer. Its carboxylic acid group can establish hydrogen bonds as a donor and as an acceptor, and in an appropriate solvent it can establish an electrostatic bond with a basic group. For some basic templates, more acidic monomers may be preferred. For example, trifluoromethacrylic acid gives a better affinity for nicotine than methacrylic acid [60]. The two basic functional groups of nicotine present more affinity for the carboxylic acid and its electron-withdrawing effect due to the trifluoromethyl group. Another example is the sulfonic acid-based monomers [61]. In case of an acidic template, basic monomers are favored. This is the case for 2,4-dichlorophenoxyacetic acid which presents a high affinity for the 4-vinylpyridine functional monomer [47]. On the other hand, the charge density of the monomer may have an influence on the template rebinding, as shown by Kofinas and coll. The authors studied the influence of cationic and anionic monomers on the rebinding of a protein [62] and they showed that the results strongly depended on the template.

Molecular modeling of the template-monomer complex can greatly facilitate the choice of the monomer. However, rather than choosing a monomer -from the long list of commercially available ones-, it is sometimes necessary to create more favorable interactions. That's why another strategy consists in synthesizing new functional monomers based on structural features of the template. Thus, Ersoz and coll. imprinted L-histidine *via* a metal-chelating monomer. Indeed, they synthesized this monomer by considering the ability of histidine to chelate metal ions [63].

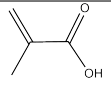
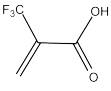
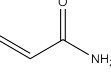
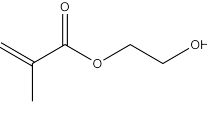
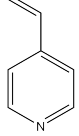
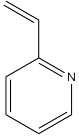
Class	Name	Chemical structure
Acidic monomers	Methacrylic acid (MAA)	
	Trifluoromethylacrylic acid (TFMAA)	
Neutral monomers	Acrylamide (AM)	
	2-Hydroxyethyl methacrylate (HEMA)	
Alkaline monomers	4-Vinylpyridine (4-vp)	
	2-Vinylpyridine (2-vp)	

Table 3: List of several widely used functional monomers.

Otherwise, if several and different types of interactions are possible with the template, it is possible to combine different monomers. This can, however, give rise to monomer/monomer interactions, at the expense of imprinting effect.

Finally, taking into account the equilibria involved, to enhance the formation of the complex template-monomer, often an excess of functional monomer needs to be applied. This may result however in increased non-specific binding sites since some of the monomers will be randomly distributed in the material.

2.2.2 Cross-linking monomers

The cross-linking density has to be optimized for each polymer because the selectivity of the polymer is effectively influenced by the molar amount and the kind of cross-linker (common cross-linkers are listed in table 4). Moreover, since the cross-linker represents the mayor component of a MIP, it also determines some physico-chemical properties of the material, like hydrophobicity/hydrophilicity. MIPs have to be rather rigid to preserve the structure of the cavity but on the other hand, a certain flexibility facilitates release and uptake of the template. Cross-linkers can have two or more polymerizable bonds, bifunctional monomers leading to polymers less rigid than trifunctional monomers. Ethylene glycol dimethacrylate has two polymerizable bonds and has been used extensively in molecular imprinting. To obtain even less rigid polymers, it can be replaced by triethylene

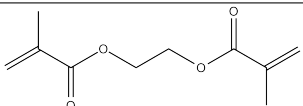
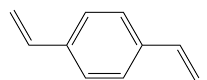
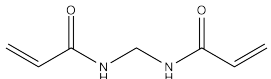
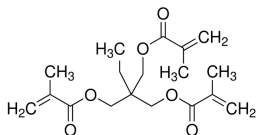
Type	Name	Chemical structure
Bifunctional	Ethylene glycol dimethacrylate (EDMA)	
	Divinylbenzene (DVB)	
	Methylene-bis-acrylamide (MbAAm)	
Trifunctional	Trimethylolpropane trimethacrylate (TRIM)	

Table 4: List of several widely used cross-linking monomers.

glycol dimethacrylate which possesses a longer linker between polymerizable moieties.

2.2.3 Solvent

The solvent should solvate all the components in the precursor mixture and be inert for the polymerization. It acts as a porogen and therefore has a considerable effect on the polymer morphology. The porous MIP structure leads to high inner surface area and gives easier access to the imprinted cavities. It facilitates both desorption of the template and analyte binding. Since different solvents swell network polymers differently, usually, the same solvent is used for polymerization and re-binding studies. Indeed, it has been proven that maintaining the same conditions for these stages enhances the recognition [64]. Another aspect is that some polymerization conditions lead to evaporation of the solvent and thus the solvent does not fulfill its function of a porogen. In this case, solvents with a lower vapor pressure can be used, or porosity can be introduced by a sacrificial polymeric porogen. For example, Haupt and coll. synthesized polymer films by spin-coating, with a low volatility solvent and a linear poly(vinyl acetate) as porogen [40]. They controlled thickness and morphology of the polymer thanks to the porogen concentration and the evaporation of the solvent no longer led to an absence of porosity. The intrinsic properties of the solvent govern the strength of the interactions in the self-assembly process during imprinting. Using a polar protic solvent may disrupt the non covalent interactions between template and functional monomer, resulting in randomly distributed monomers in the polymer, and therefore in non-specific binding. That's why imprinting in aqueous conditions is still a challenge although some attempts have been successful [47]. On the other hand, some MIPs prepared in organic solvents have demonstrated a good recognition in aqueous solvents [65].

2.2.4 Polymerization conditions

Polymerizations are initiated either thermally or photochemically by UV irradiation. In this context, the template should be resistant to the initiation step and should not undergo a photo/thermoreaction or degradation. Common initiators are azo-bis-isobutyronitrile (AIBN) and 2,2'-azo-bis-(2,4-dimethyl valeronitrile) (ABDV).

If the complex is formed with electrostatic interactions and hydrogen bonding, then performing a photopolymerization at a lower temperature will favor the complex formation. Hydrophobic interactions will be enhanced by increasing the temperature due to a favorable entropy term. Photopolymerization is often preferred when it can be favorably associated to the photostructuring of the final material [66].

2.2.5 Formulation optimization

First trials for a MIP synthesis are driven by the experience of the research. Otherwise, several options are possible.

- Trial and error, combinatorial libraries

This method is an empirical way to find a formulation for the imprinted polymer. For a particular template, several functional monomers and different relative ratios are tested. The nature and quantity of cross-linker are also modified. The porogen volume is a fluctuant parameter too. Finally, all the polymers synthesized are tested in batch rebinding studies. This approach is time-consuming and cost effective but it is still common [67]. It can be sped up by synthesizing combinatorial libraries of MIPs, if possible in parallel. MIPs can be synthesized in small amounts and be evaluated *in situ* [68]. It allows for the determination of the best polymer formulation. Sellergren and coll. chose two screening steps: the dosage of template release after polymerization (a complete release of the template during the first washing step means no affinity) followed by a comparison between the MIP and NIP. Recently, Baggiani *et al.* highlighted the connection between NIP and MIP affinity for the template [69]. They assumed that the functional monomer should be a good ligand for the analyte and that imprinting will then enhance the selectivity. This study showed that the affinity of a template for a library of reference polymers can be tested and the best-binding NIP should produce a MIP with a good binding ability. This lowers the cost of the combinatorial libraries because a library can be tested for several analytes.

- Molecular modeling

Molecular modeling is a thermodynamic calculation which predicts interactions between a library of monomers and the template by energy minimization. However, the modeling usually takes into account the template and the functional monomer but neglects the cross-linker and solvent effects (although these can be incorporated in the model), assuming that if with the chosen conditions

a complex is strong enough it will enhance recognition properties in the polymer. This technique reduces time and material consumption as only the monomers with the highest binding scores will be used to actually synthesized MIPs. Also, information on the stoichiometry of the complex is accessible. For example, Turner and coll. developed with this approach a synthetic receptor for microcystin-LR [70].

- Design of experiments

The application of mathematical and statistical methods for optimizing a polymer formulation and extracting relevant information is more and more used for MIP synthesis, in particular when optimizing a MIP for a given application. Designs of experiments give simultaneously the individual and interactive effects of factors that could affect some output responses. Several approaches exist (full factorial, fractional factorial, response surface designs *etc.*). Well chosen experimental designs maximize the amount of obtained information for a limited amount of experiments. With this approach, it is then possible to optimize a MIP formulation. Kunath *et al.* used a full factorial experimental design combined with a multi-objective optimization approach to optimize the imprinting of glucuronic acid [71]. They chose the degree of cross-linking, the molar equivalent of monomer to template and the initiator concentrations as input variables and binding parameters as output responses. The analysis of the data gave a formulation for an optimized polymer with a 6 times lower K_{50} , a B_{max} 40% higher and an imprinting factor 1.3 times higher as compared to the starting formulation. A similar approach was chosen in this thesis to optimize MIP formulations.

2.3 MIPs as sensitive layers in optical sensors

A sensor is a device that measures a variable and converts it into a readable signal. Chemical sensors are able to detect and quantify atoms or molecules. They are composed of a recognition element and a transducer (figure 18). The transducer translates the binding signal of the target into a readable output signal. It can be based on optical, electrochemical, or acoustic measurements, or measure the heat of interaction. We define here optical sensors as sensors from which the output signal is an optical signal (color, fluorescence *etc.*), in this manuscript, we will only focus on the latter. Optical methods, particularly label-free approaches, are attractive because they can easily be integrated in sensors, are compact, cheap, light, non destructive and give fast output responses.

Optical sensors based on MIPs emerged naturally due to all the progress in optical analytical techniques. Recent research opened the possibilities for chemical sensors to be interfaced with optics with satisfying sensitivities. Concerning MIPs, they may be integrated in optical sensors thanks to a covalent linkage of the polymer to an optical transducer.

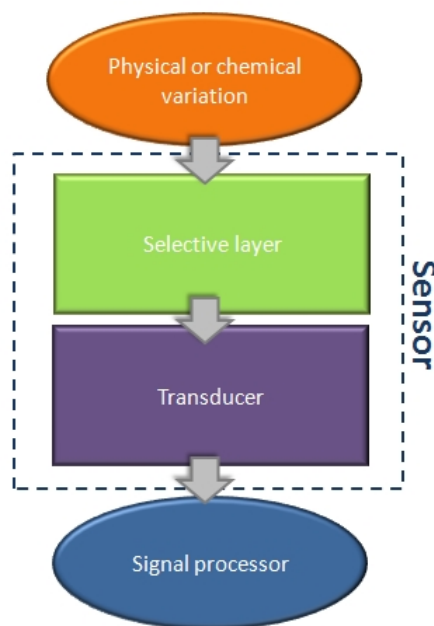


Figure 18: Schematic representation of a sensor.

2.3.1 Fluorescence as transduction method for MIP sensors

Several cases can be distinguished according to the origin of the fluorescence.

- The template can be fluorescent. While it binds to the polymer, the material becomes more and more fluorescent. The integration in a sensor requires a fluorescence reading that is often done spectroscopically, for example *via* an optical fiber. This is the solution adopted by Mosbach and coll. for the detection of dansyl-phenylalanine [72]. Problems encountered in this particular example were that the polymer was not completely template-free, resulting in a fluorescent background signal. It is also difficult to attach MIPs for the fluorescence reading. Some people immobilize the template in cells and measure the fluorescence with an optical fiber on a spot inside the cell. The MIP can be glued to the fiber with an intermediate polymer but the latter can change the selectivity and sensitivity of the sensor. Fernandez-Gutierrez and coworkers proposed the use of super-paramagnetic hybrid nanoparticles [73]. In this work, the magnetic MIP is coupled to an optical fiber with a magnetic separator and the detection of 1-naphtylamine is possible thanks to its intrinsic fluorescence.

- If the template can be functionalized by a fluorophore, then it is possible to use a competitive or displacement approach. Binding of the non-labeled analyte to the polymer results in a decrease in binding of the labeled analyte due to competition, and thus in a decrease in fluorescence [74].

- Finally, the fluorescence can be intrinsic to the polymer by using fluorescent monomers. The binding event would either quench the fluorescence, enhance the fluorescence, or displace the maximum emission wavelength. Takeuchi and coll. recently proposed to synthesize a fluorescent monomer

that would be used for the detection of proteins [75]. They used a monomer with a l-hydroxyproline structure conjugated with a dansyl structure. The fluorescence changes seem to appear only for specific binding events.

2.3.2 Generation of an optical signal by a specific chemical reaction

Reaction of the analyte with the polymer or with a chromogenic reagent can form a colored adduct that enables the detection of the analyte. Considering this, Hong and coll. fabricated a microfluidic biochip for the optical detection of propofol (an anesthetic agent) [76]. The imprinted polymer and its reference were directly polymerized in the microfluidic chambers. After extraction from the sample by the MIP, propofol can react with a color reagent. The microfluidic chamber is embedded between a diode and a photodetector and this enables the monitoring of the transmittance which is a function of the propofol concentration. This sensor is compact, cheap, needs small sample volumes and gives a fast response (around one minute).

The sensors described above are dependent of a specific optical property of the analyte, of a label, or of a monomer introduced in the polymer. However, this may be a drawback as it can result in quenching, short shelf-life due to photobleaching, and background fluorescence. The next techniques described below, allow optical detection while avoiding chromophores.

2.3.3 Surface Plasmon Resonance

Surface plasmon resonance (SPR) is commonly used for the detection of components adsorption on metal surfaces. The chip surface is covered with a layer of metal (often gold) and the latter can be functionalized with recognition elements. The detection is based on the propagation of electromagnetic waves on the metal surface. The oscillations of the evanescent waves are very sensitive to any change at the boundaries and reflectivity measurements, study of the resonance angle or spectroscopy can be used to detect the molecule adsorption. SPR biosensors are an interesting label-free platform which can couple many different surfaces to several functionalizations [77].

Major issues with SPR measurement rely on the investigation thickness since the wave amplitude decreases exponentially with the distance to the surface. Films of polymer should be really thin [78]. In order to improve the sensitivity of the method, nanoparticles of polymer can be grafted on the metal surface. This is the solution recently adopted by Denizli and coll. for chloramphenicol imprinted nanoparticles (52 nm of diameter) on a gold surface. They could then detect 40 ng of the target in 1 kg of honey [79]. It is also possible to enhance the effect with metallic nanoparticles embedded in the polymer. Sugimoto and coll. imprinted a gel with adrenaline and gold nanoparticles embedded in the polymer [80]. The shift in the plasmon band upon molecular recognition encouraged

them to graft the polymer on a gold surface [81]. They imprinted dopamine, a molecule similar to adrenaline. The sensor chip showed a shift in the SPR angle correlated with dopamine concentration and enhanced by the combination of gold nanoparticles and gold surface.

More recently, Takeuchi and coll. developed a sensor for bisphenol A [82]. The sensor is made of gold and silver parallel bands on which MIP nanoparticles are grafted (figure 19). The reflectivity spectra are obtained for both gold and silver layers and a competition takes place between free bisphenol A and bisphenol A labelled with gold nanoparticles. This results in the specific detection of bisphenol A.

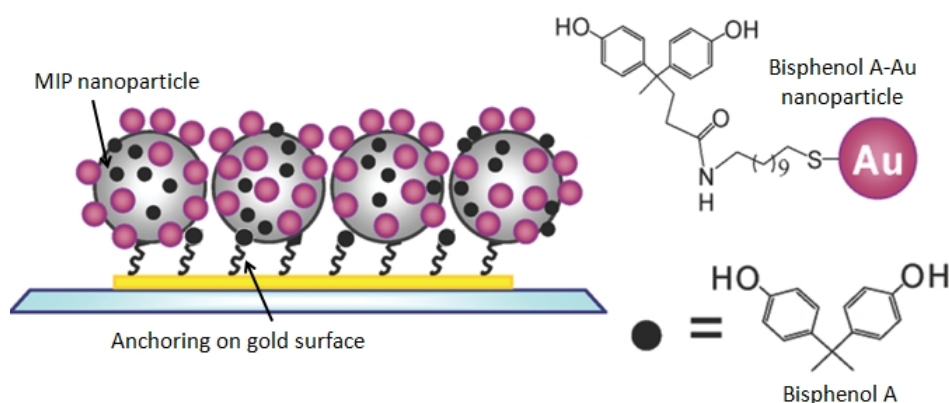


Figure 19: Competitive binding of bisphenol A and bisphenol-A labelled with a gold nanoparticle on MIP nanoparticles grafted on a SPR substrate. Figure issued from [82].

2.3.4 Infrared and Raman spectroscopy

Infrared spectroscopy with evanescent wave techniques can be coupled to MIPs to realize selective sensors. A first study was performed by Haupt and coll. with the model analyte 2,4-dichlorophenoxyacetic acid [83]. Detection limits were down to $2.9 \mu\text{M}$ but they highlighted the necessity to make films with a uniform thickness, thinner than $5 \mu\text{m}$. IR spectroscopy provides the chemical fingerprint, and thus a signal with a higher information content, and therefore enables the discrimination between several molecules by the study of different characteristic absorption bands.

Similarly, Raman spectroscopy focuses on the vibrational energy levels of molecules and can distinguish molecules *via* their characteristic Raman bands. Raman effect occurs when a photon interacts with the vibrational energy levels of a molecule and is scattered. Surface-Enhanced Raman Scattering (SERS) conjugates Raman scattering of a molecule with the close proximity of a nanostructured surface metal acting as a nano-antenna. This may result in enhanced Raman signal. Raman spectroscopy has been used for MIP readout but results with higher sensitivity were obtained by SERS. Kantarovich and coll. deposited small drops of MIP for S-propanolol on a gold-coated SERS-active surface. The SERS measurements clearly showed peaks related to propanolol in the MIP that can be used for analyte's quantification [84].

2.3.5 Refractometry

Finally, a last approach consists in shaping MIPs to form a periodical structure with interesting optical characteristics. The period of the structure accounts for the diffraction of light, and the monitoring of the diffraction wavelengths or intensity can be used for transduction.

If d is the periodical spacing of the structure, then the diffraction regime is observed for $\lambda \approx d$, where λ is the wavelength of the light source. According to the Bragg law, constructive interferences are observed for $\lambda \leq 2d$ (figure 20).

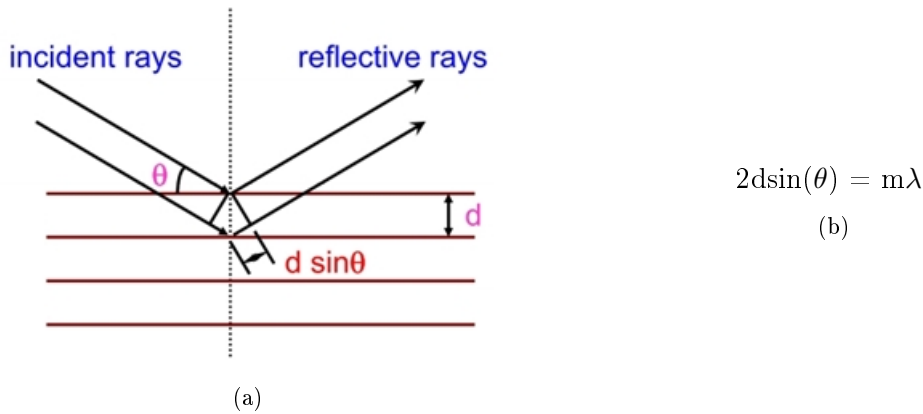


Figure 20: Diffraction of light waves by a periodic structure (a) schema of the interferences, (b) the Bragg law, where θ is the angle of light incidence, d is the periodical spacing, λ is the wavelength of the light source and m an integer, the diffraction order.

Moreno-Bondi and coworkers developed a periodic polymer for the detection of enrofloxacin [85], [86]. The polymer is synthesized with a square-grating mold with a periodicity of 6 or 12 μm (figure 21). They observed a diffraction figure using a He-Ne gas laser ($\lambda = 632.8 \text{ nm}$).

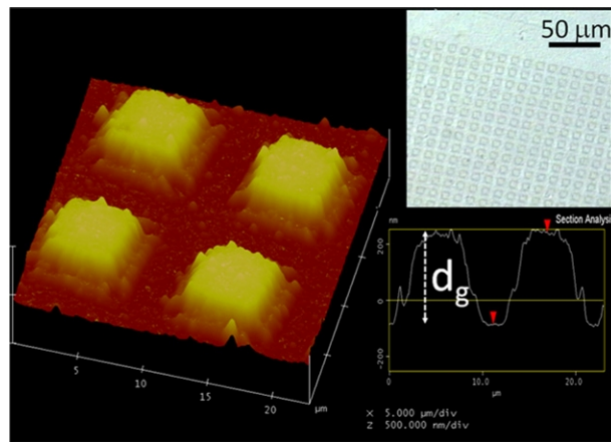


Figure 21: Square-grating MIP, Atomic Force Microscopy (AFM) and optical microscope images. Figure issued from [86].

A diffraction study allowed them to monitor the binding of their analyte to their structured

MIP. Indeed, with a thin grating (thickness of the polymer is smaller than the laser wavelength), the diffraction efficiency η is a useful and simple tool. The diffraction efficiency is the ratio of the first order intensity to the total intensity ($\eta = \frac{I_1}{I_{tot}} \approx \frac{I_1}{I_0}$ since $I_1 < I_0$ in thin gratings) and is proportional to the square of the grating thickness and of the surrounding refractive index (equation 2.2, where e is the grating thickness, $\Delta n = n_{grating} - n_{medium}$ and C a dimensionless constant).

$$\eta = C \left(\frac{e \Delta n}{\lambda} \right)^2 \quad (2.2)$$

Using equation 2.2, it is possible to measure the refractive index of the polymer. The authors dipped the polymer in different solvents and measured the diffraction efficiency. The linear plot of $\sqrt{\eta}$ as a function of n_{medium} gives the $n_{grating}$ value. Then, a binding test can be performed and the evolution of the diffraction efficiency is measured. The molecule recognition is accompanied by an increase in the optical thickness of the grating (thickness and/or refraction index) and thus a change in the diffraction efficiency. As a result, the MIP showed a good recognition for enrofloxacin, while the reference polymer had a constant diffraction efficiency. This device is a selective label-free optical sensor.

In the previous case, the periodicity was in two dimensions and was obtained by molding. It is also possible to generate one dimensional periodicity, in a polymer in the form of fringes for example. Fuchs *et al.* synthesized such structures with light interferences of two laser beams using a holographic approach [66]. Figure 22a represents the photostructuring of a polymer film by two interfering laser beams. In figure 22b, the characterization by diffraction is represented. The MIP was imprinted for testosterone and showed good recognition properties with a detection limit of $1\mu\text{M}$, but only 5% of evolution of the diffraction efficiency for $100\mu\text{M}$ of analyte.

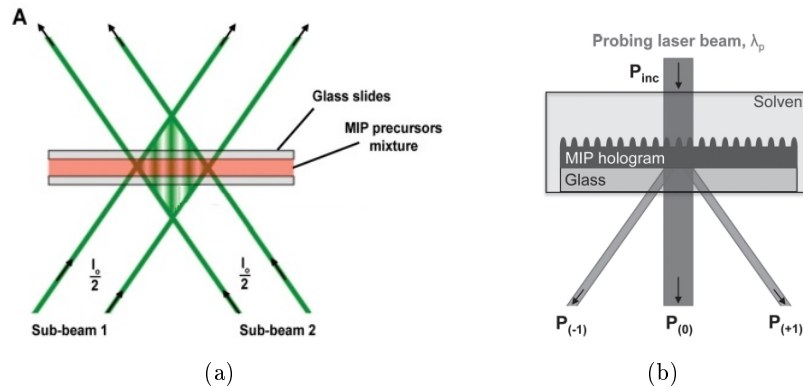


Figure 22: One dimension periodicity for polymer grating, obtained by holography. (a) Polymer synthesis by light interferences and (b) characterization of the polymer by diffraction. Figures issued from [66].

For all these sensing possibilities, several platforms could be used, from the optical fiber to the

planar waveguide. The sensitivity of optical sensors is often determined by the transducer design. Its fundamental aim is to maximize the concentration of light where the measured variable changes. In this context, photonic crystals are very good candidates for optical sensing. They are described in the next section.

3 Photonic crystals: an original way of transduction

Colors can result from chemical or physical properties. Pigments absorb or reflect certain light frequencies as a result of their chemical composition. In other cases, the iridescence of some colorful creatures is due to physical properties. They wear microstructures made of materials with periodical holes or bumps for which physical properties (size, refraction index, period) determine a reflected color. This phenomenon instigates, for example, the color of butterflies wings (figure 23).

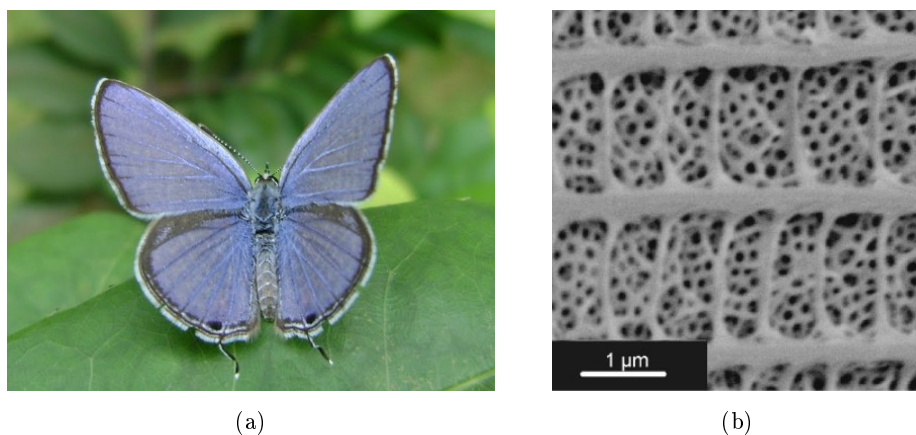


Figure 23: (a) The Lycaenid butterfly and (b) a SEM image of its wings.

3.1 Definition

Photonic crystals are the optical analogues of the electronic propagation within atomic and molecular crystals. They were discovered by Yablonovitch and John independently in the 80s [87], [88]. They are microstructured materials in which the dielectric function is spatially periodical. The field associated with light is a vector and respects Maxwell's equations [89] (equation 3.1).

$$\nabla \cdot \mathbf{B} = 0 \quad \nabla \times \mathbf{E} + \frac{\partial \mathbf{B}}{\partial t} = 0 \quad \nabla \cdot \mathbf{D} = \rho \quad \nabla \times \mathbf{H} - \frac{\partial \mathbf{D}}{\partial t} = \mathbf{J} \quad (3.1)$$

where \mathbf{E} and \mathbf{H} are the macroscopic electric and magnetic fields, \mathbf{D} and \mathbf{B} are the displacement and magnetic induction fields and ρ and \mathbf{J} are the free charge and current densities.

If the materials have sufficiently different refraction indices and do not absorb too much light, then the refractions and reflections of light produce phenomena of interest. Thus, when light is incident on a periodic structure, it is reflected from each interface. Under certain conditions, the waves interfere constructively and the reflected wavelength is missing in transmission. The range of wavelengths at which it happens is called the photonic stop band. If the stop band is the same in all directions and for both polarization states of light, then it is referred to as Photonic BandGap (PBG) [89]. Within this frequency, light is not capable of propagating in the structure. The position of this bandgap can be modulated either by changing the refractive index and/or the periodicity of the photonic crystal structure. The materials can be periodic along one or more axes, and photonic crystals are featured by the number of periodicity directions (figure 24).

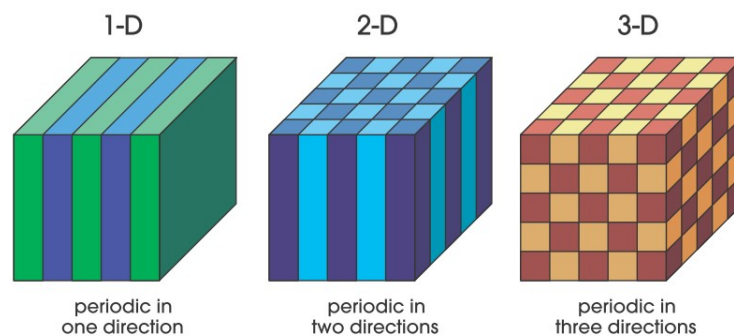


Figure 24: Schematic representation of one-, two- and three-dimensionnal photonic crystals. Colors represent materials with different dielectric constants. Figure issued from [89].

Photonic crystals have a wide range of applications. With this technology, scientists hope to be able to control light propagation: perfect reflection for determined frequencies, propagation in certain directions, confinement in specified volumes. In this thesis, we aim at using photonic crystals as transducers in a sensor.

3.2 Sensors based on photonic crystals

Photonic crystals have been developed for chemical sensing thanks to the variation of their optical properties correlated to a change in their environment. The reaction of the target molecule with the sensor results in a physicochemical change of the sensor, such as the refractive index or the crystal lattice. The measured variables are often the variation of the wavelength of the peak reflectance and/or its intensity, either as a function of time or space [90]. Photonic sensors represent a **novel label-free platform**. The confined electromagnetic field within the structure provides high sensitivity and a very good spatial resolution.

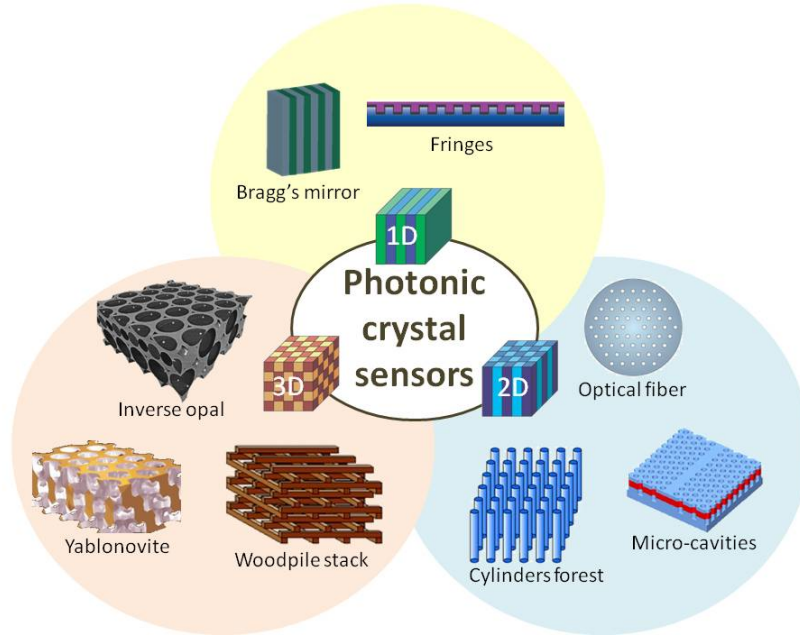


Figure 25: Photonic sensors are developed in 1, 2, or 3 dimensions and with several possible structures.

Photonic crystal sensors were developed with 1, 2 or 3 directions of periodicity (figure 25). Their color may be tuned by several external stimuli that we propose to present non exhaustively in the next paragraphs, along with the introduction of the classical photonic crystals.

3.2.1 Ions and pH sensors

Bragg's mirror

The most famous photonic crystal is the one dimensional crystal called the Bragg mirror. Layers of different refractive indices alternate and form a multilamellar stack. The refractive index varies periodically in one direction and the material is homogeneous in the other two dimensions. The choice of the thickness and the refractive index of the dielectric layers gives specific properties of reflectivity to the multilamellar stack. Different wavelengths of light are then reflected with a high intensity. Layers can be successively formed by evaporation, dip/spin-coating, sputtering or phase separation in polymer. Two types of sensors may be distinguished, according to the localization of the detection. Either, the detection is achieved inside the layers or it is due to the superior adlayer (grafted with receptors for example).

Detection inside the layers of a Bragg's mirror is often correlated with the swelling properties of the stack so as to tune color by an external stimulus. Thomas and coll. synthesized a block copolymer stack of glassy block layers and polyelectrolyte block gels [91]. The polyelectrolyte layers are able to swell according to the salt concentration in solution and with an intensity depending

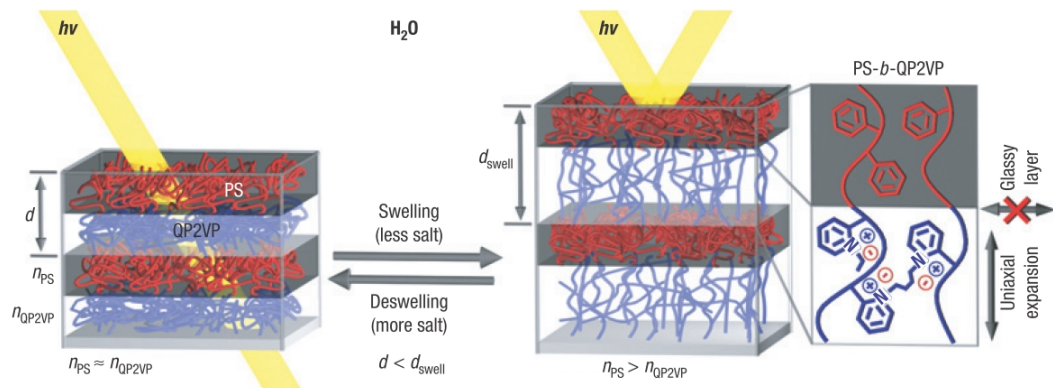


Figure 26: A stack of block copolymer photonic gel film and the tuning mechanism. Swelling/deswelling of the polyelectrolyte layers shift the wavelengths reflected by the stopband. Figure issued from [91].

on their cross-linking degree. The glassy layers do not swell and constraint the polyelectrolytes to swell only in one direction (figure 26). The authors observed a large reversible shift of the stop band (around 1250 nm for NH_4Cl concentrations from 2.5 M to 0 M).

Fringes

Substrates structured with fringes display parallel bands whose height alternates from low to high. The structure is periodical in 1 dimension and the detection is mainly achieved on the surface of the structure. Fringes may be obtained by molding of a master or by interference photolithography (holography).

Polymeric fringes can be manufactured by holography thanks to two coherent laser beams (incident and reflected) which interfere on a substrate where photosensitive monomers polymerize. Thus, the pattern of the interference fringes is fixed in the polymer film. In certain conditions, the holographic photonic crystal reflects a visible wavelength under white light illumination. Any change of the fringes interspacing generates a visible change in the color of the film. Thus, pH sensing can be achieved with the use of ionizable monomers [92]. The functional groups of the hydrogel are ionizable and cause the grating to swell as a result of electrostatic and osmotic forces. While the polymer swells, longer wavelengths are reflected and hence the pH of the surrounding solution can be monitored. In this article, the diffracted wavelength shifted of 175 nm for a pH variation of 2.5.

If not based on the intrinsic properties of the polymer, sensing can be achieved by functionalization of the structured polymer. This is the case, for example, of the detection of specific ions by functionalization of the polymer by crown-ether [93]. Li^+ , Na^+ and K^+ were detected selectively with a maximum wavelength shift of 200 nm, corresponding to an ion concentration of 33 mM.

3.2.2 Vapor or solvent sensors

Opals

Home-made opals are multilayers of colloids arranged either in a face centred cubic (fcc) or hexagonal compact lattice. Beads with a diameter in the range of 150-1000 nm can be used but only periods of 150-350 nm have a stop band in the visible region of the spectrum. Beads are commonly in silica but polystyrene and poly(methyl methacrylate) are possible alternatives (to avoid the use of hydrofluoric acid for example).

Rao and coll. made an opal of polystyrene beads (331 nm diameter) [94]. They monitored the shift of the Bragg diffraction peak according to the surrounding solvent and demonstrated that the structure was able to differentiate different alcohols such as methanol, ethanol and butanol. They also underlined the potential complementarity in the study of several Bragg planes.

1D Bragg's mirror composed of two alternating mesoporous layers of SiO₂ and TiO₂ was studied by Ozin and coll. for solvent detection [95]. The stack was fabricated by spin-coating and the reflected color was tuned by various solvents. The mirror displayed different responses, even for solvents with close refractive indices (*n*-hexane $n = 1.375$ and 2-propanol $n = 1.377$).

3.2.3 Temperature sensors

Inverse opals

Inverse opals are the inverted-opal structure. The photonic matrix is filled with a dielectric material and beads (mostly silica but sometimes polystyrene -PS- or poly(methyl methacrylate) -PMMA-) are subsequently removed. Inverse opals can present a complete photonic bandgap. However, this requires a high refractive index contrast. Several sensors have been developed with the structure of inverse opal as a transducer. They possess large voids due to their inner structure and this provides a great surface area, more potential interaction sites and a great access of the analyte to the recognition sites.

Some temperature detectors are based on polymers, thanks to reversible swelling and shrinking induced by temperature variation. Recently, a hydrogel was polymerized in the voids of a polystyrene opal [96]. The polystyrene beads had a diameter of 220 nm and were dissolved in tetrahydrofuran (THF) after polymerization of the hydrogel. Monomers include N-isopropylacrylamide (NIPAm) and acrylic acid (AA), used for the detection. Poly(NIPAm) is a well-known polymer having a thermoresponsive volume transition. The polymer has a low critical solution temperature (LCST) at 32 °C. Below this temperature the gel swells, and is compatible with water, whereas at higher temperatures the hydrophobic effects predominate and the gel collapses. This property is used for

temperature sensing. Moreover, acrylic acid is pH-responsive thanks to the acidic functions. The obtained sensor showed a maximum absorbance at 497 nm at ambient temperature and in a buffer (pH = 1.5). With a change of temperature or pH, the maximum of absorbance shifts (figure 27) and the variations induced by the stimuli are reversible. The authors also underlined the rapid response of the sensor with a kinetic study.

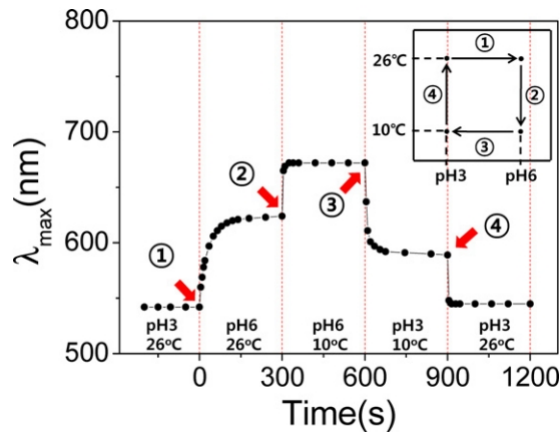


Figure 27: Response of an inverse opal sensor for sequential stimuli of temperature and pH. Figure issued from [96].

Asher and coll. developed directly poly(NIPAm) colloidal particles self-assembled into an opal. The particles were swollen at low temperature (10 °C, 350 nm diameter) and shrunk at high temperature (40 °C, 125 nm diameter).

3.2.4 Biosensors

Optical fibers

The optical fibers are characterized by a plurality of air holes running along the silica, polymer or glassy fiber. The optical properties are defined by the geometry, the size and the relative positions of the holes. Figure 28 represents an example of cross-section of a photonic-crystal fiber. Some photonic crystal fibers are already commercialized.

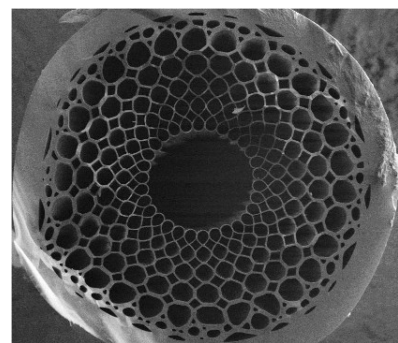


Figure 28: SEM image of the cross-section of a photonic-crystal fiber.

The high specific area of the fibers offers numerous sites for detection. In most cases, photonic fibers are functionalized with a probe molecule. Nowadays, the trend is to integrate the photonic

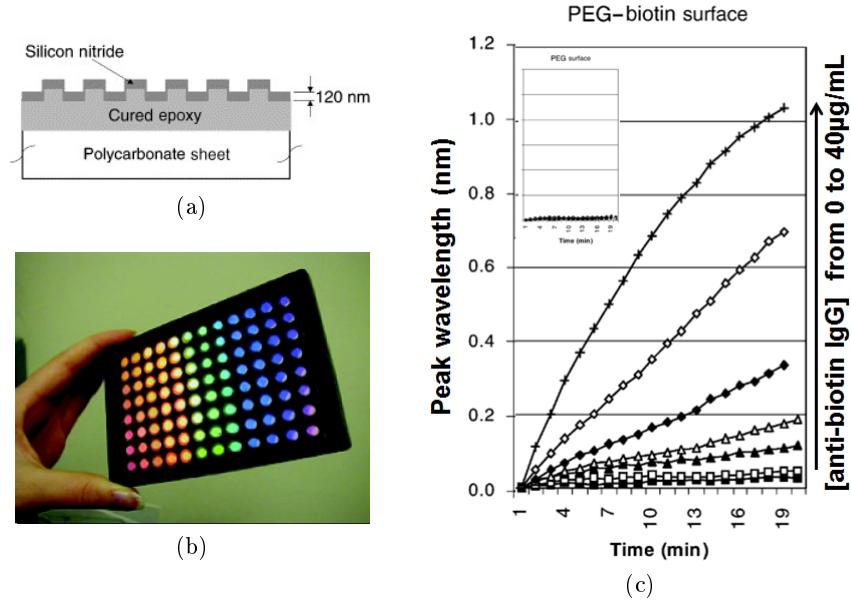


Figure 29: A 1D-photonic crystal sensor, (a) photonic structure, (b) picture of the sensors embedded in a 96-well microplate and (c) detection of different concentrations of anti-biotin IgG, onset is a reference control. Figures issued from [98] and [99].

fibers in devices. Thus, Geschke and coll. developed a microstructured optical fiber incorporated in a biochip [97]. The fiber is functionalized to selectively capture a single stranded DNA string. They immobilized the complementary string on the surface of the holes. The characterization of the sensor is led by absorbance spectroscopy and the DNA is captured selectively. This integrated optical fiber in a sensor could be used to real-time monitor DNA hybridation or antigen/antibody complexation.

Hugh and coll. worked with fringes made by a replica from a silicon master wafer (figure 29a). In this study, the sensor was manufactured with 9mm diameter circular gratings, arranged side by side to get the pattern of a 96-well microtiter plate. Thus, the gratings close a bottom-less microtiter plate (figure 29b) and are further functionalized with biotin molecules. The analysis of streptavidin binding is done column by column on the plate thanks to 8 optical fibers. The minimum shift detected is 0.003 nm which corresponds to a sensitivity limit of 0.61 nM (figure 29c).

We introduced several photonic sensors used for different applications. Many of the devices for biological sensing display a good sensitivity and were developed for the streptavidin/biotin complex. This complex is a good candidate to test sensors thanks to the strong interactions between the two molecules, and the possibility to anchor biotin on substrates. However, biosensors have good perspectives only if selectivity and stability are achieved, and it is often difficult to anchor biomolecules like antibodies on surfaces. That's why we believe that molecularly imprinted polymers may be an interesting choice as the recognition elements in biosensors.

3.3 MIPs and photonic crystals

We will now focus on photonic crystals biosensors with MIPs. Indeed, these sensors can enable a direct detection of the analyte *via* a change of polymer conformation upon target molecule recognition. When the polymer is structured as a photonic crystal, the detection of the analyte is enabled by an optical variation of the sensor.

The first possibility is to imprint polymeric particles and form an opal lattice. This was investigated by Guo *et al.* [100]. They imprinted Bisphenol A in poly(methyl methacrylate) and studied the Bragg's shift of the opal upon target recognition. This approach is simple but the access to the imprinted cavities is not easy because of the low specific area. That's why the great majority of teams working in this field have focused on inverse opals. Indeed, these structures have a high specific area and the access to the imprints is greatly favored.

Li and coll. were the first to elaborate a MIP photonic sensor and further developed the sensor for several analytes. They built an opal with silica spheres, and molded an inverse opal with an imprinted polymer. The imprinted templates are atrazine [101], L-dopamine [102], a protein [103], cholic acid [101] and alkaloids [104]. As compared to usual bulk MIPs, the inverse opals developed by this team are not very cross-linked, which enables the polymer to swell but decreases the selectivity of the polymer. For the herbicide atrazine, cross-linker and template were equimolar and they observed a shift of the absorption maximum up to 60 nm (figure 30), for atrazine concentrations between 10^{-11} and 10^{-6} M.

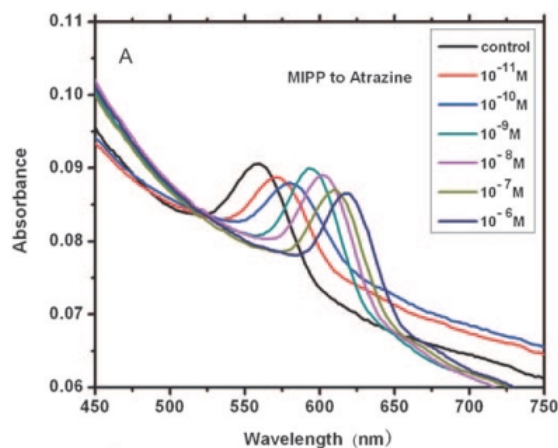


Figure 30: Shift of the Bragg's peak upon recognition of atrazine by a molecularly imprinted photonic polymer. Figure issued from [101].

After these first photonic sensors based on MIPs, several other attempts were described in the literature. The applied strategies are summarized in table 5.

Table 5: Templates, formulations, conditions of preparation of imprinted polymers in inverse opal sensors and shift of the Bragg's peak reported in literature.

Ref.	Template	Monomers and their molar ratio compared to template	Beads	Opal formation	Inverse opal formation	$\Delta\lambda$ nm
[102]	L-3,4-dihydroxy phenylalanine	MAA/EDMA 4.6/1	Silica spheres 186 nm	Evaporation	Sandwich glass-opal-PMMA	80 nm for 10 mM
[101]	Cholic acid	MAA/EDMA 3/2 or 6 or 13				30 nm for 0.1 μ M
[105]	Atrazine	MAA/EDMA 4/1				150 nm for 1 μ M
[104]	Theophylline	MAA/EDMA 24/4.2	Silica spheres 150-400 nm			45 nm for 1 mM
[103]	Bovine serum albumin	MAA/EDMA ratio unknown	Silica spheres diameter unknown			25 nm for 0.15 mM
[106]	3-pyridine carboxamide	AA/AM/MbAAm ratio unknown	PS spheres 237 nm	Evaporation	Capillarity	150 nm for an aqueous solution of 4%

Refs.	Template	Monomers and their molar ratio compared to template	Beads	Opal formation	Inverse opal formation	$\Delta\lambda$ nm
[107]	Chloramphenicol	MAA/EDMA 5/1.2	Silica spheres 300 nm	Evaporation	Sandwich glass-opal-PMMA	reflection intensity decrease of 70% for 3 μ M
[108]	Tetracycline	AM/AA/MbAAm 2800/1266/40	Polystyrene spheres 200 nm	Evaporation	Capillarity	160 nm for 0.25 μ M
[109]	L-pyroglutamic acid	AM/MAA/MbAAm 40/4/1	Polystyrene spheres 209 nm			90 nm for 0.5 mM
[110]	L-Phenylalanine	Maleic anhydride modified β -cyclodextrin/ AA/MbAAm 4/0.2/6.5	Polystyrene spheres			100 nm for 0.1 mM
[111]	Atropine	MAA/EDMA 5/1	Silica spheres 220 nm	Evaporation	Sandwich glass-opal-PMMA	183 nm for 3.5 μ M
[112]	Ketamine	MAA/EDMA 5/0.6	Silica spheres 220 nm			80 nm for 3.6 μ M

Refs.	Template	Monomers and their molar ratio compared to template	Beads	Opal formation	Inverse opal formation	$\Delta\lambda$ nm
[113]	Methyl phosphonic acid	HEMA/NIPAm/EDMA/MbAAm 10/10/1.5/0.5	PMMA spheres 280 nm	Evaporation	Capillarity	reflection intensity decrease of 20% for 25 μ M
[114]	Glucose	4-ethylene phenylboronic acid/HEMA/NIPAm/MbAAm 1/1/8.8/1.5				155 nm for 20 mM
[115]	Cholesterol	MAA/EDMA 4/1.5	Silica spheres 240 nm	Evaporation	Sandwich glass-opal-PMMA	20 nm for 0.1 μ M
[116]	Vanillin	MAA/EDMA 4/1.2	199, 235, 270, 305 nm			45 nm for 1 mM
[117]	Bisphenol A	MAA/EDMA 26.5/1.8	Silica spheres 280 and 265 nm	Langmuir-Blodgett (5layers)	Sandwich glass-opal-PMMA	75 nm for 10 μ M

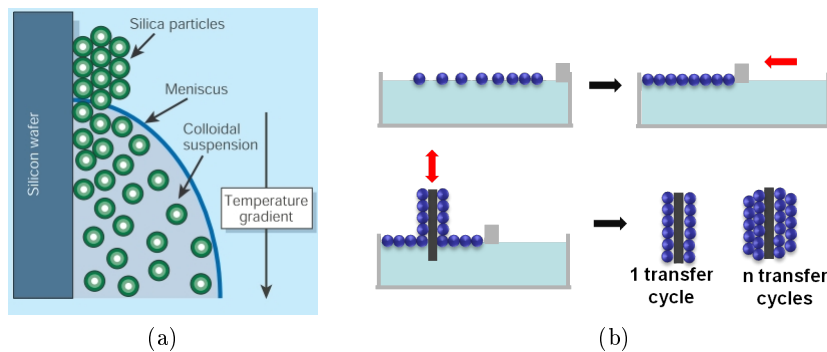


Figure 31: Opal formation described in literature: (a) by vertical deposit , (b) by Langmuir-Blodgett. Figures issued from [118] and [119].

Several observations can be extracted from table 5. First, there are several ways to make opals and inverse opals. Opals are mainly synthesized by vertical deposition: a substrate is placed vertically in a colloidal suspension and while the solvent evaporates, the meniscus delivers a close packed lattice on the substrate (figure 31a). Some parameters can be varied to optimize the opal, such as surrounding vibrations and temperature (homogeneous or with a gradient to sustain agitation and avoid sedimentation). It is also possible to use the Langmuir-Blodgett technique (figure 31b). The opal is then prepared by a layer-by-layer technique, leading to uniform thin films. The particles can be made of different materials, but silica spheres are common and can be easily dissolved by hydrofluoric acid for inverse opals synthesis. Some alternatives were found with polystyrene and PMMA (non cross-linked polymeric particles) that can easily be dissolved in toluene, THF or dimethyl sulfoxide, which is convenient when the substrate does not resist hydrofluoric acid treatment.

To obtain inverse opals, several techniques are employed (table 5). Most of the inverse opals are prepared with the "sandwich" technique (figure 32a). With this technique, opals on glass substrates are infiltrated by the polymerization precursor mixture. A cover substrate in PMMA is then placed on top of the opal and polymerization is launched. After polymer synthesis, the silica spheres are dissolved in hydrofluoric acid, which is accompanied by a dissolution of the oxide layer of glass and thus an inverse opal is obtained on the PMMA substrate. The second approach is by capillarity (figure 32b). The precursor mixture is infiltrated into the colloidal crystal mold by a capillarity-attraction-induced method. The substrate may be inclined by a 10-20° angle and the interstitial space between the spheres is filled with the solution because of gravity and capillary effects.

Once the sensor is prepared and the template is extracted from the MIP, the sensor performances can be evaluated. Detection of the analyte by the sensor is monitored by color change of the inverse opal or intensity of the reflectance. This optical change is induced by a physico-chemical variation of the polymer, in particularly by swelling/shrinking. The recognition of the target by the MIP induces a change of conformation of the polymer chains, the solvent uptake leads to swelling of the matrix.

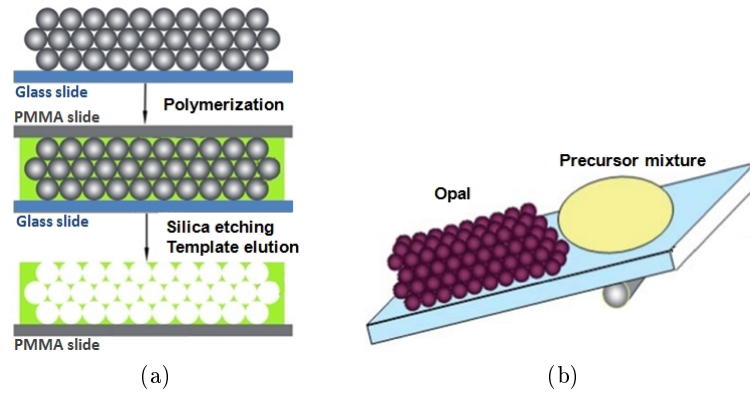


Figure 32: Inverse opal formation described in literature: (a) Sandwich between glass and PMMA, (b) capillarity infiltration. Figures issued from [111] and [108].

The swelling ability of the MIP is directly controlled by its cross-linking density. As underlined in the previous section, a high quantity of cross-linker leads to a too rigid polymer whereas a low quantity does not maintain a good recognition. This effect was highlighted with an experimental design applied to the molecularly imprinted photonic films [120]. While imprinting creatinine, Li and coll. explored the impact of molar ratios of the functional monomer, the cross-linker and volume of solvent on sensing properties. The modeled response of the design is the ratio of the Bragg shift of the photonic MIP to the Bragg shift of the photonic NIP treated with the same concentration of analyte. The higher the ratio, the better is the imprinting effect. The cross-linker ratio is not surprisingly the dominant factor of the design and an optimum appears in the predictions. In the examples quoted in table 5, the cross-linker molar ratio compared to the template varies between 0.5 and 6.5. These are very low values compared to bulk polymers (usually between 20 - 50) and this enables wavelength shifts of the Bragg diffraction peak between 25 and 183 nm.

Mangeney and coll. further developed this type of sensors by introducing a planar defect in the opal [121]. Similarly to doping of semiconductors, the introduction of well-defined defects into photonic crystals is a powerful tool to enhance the performances of the devices [122], [123]. In this article, the authors inserted a layer of beads with a different size into an opal with the Langmuir-Blodgett technique. A layer of 390 nm spheres was embedded between 5 layers of 280 nm spheres on both sides (figure 33). The sensitivity of the sensor was enhanced compared to an inverse opal made from 10 layers of 280 nm spheres because the default layer widens the photonic stop-band of the sensor. For a concentration of template of 1 mM, the Bragg peak shift was about 7 nm for the classic device and came up to 15 nm for the defect-containing MIP.

This literature review underlined the growing number of sensors based on photonic crystals and particularly on the combination of photonic crystals and MIPs. Imprinted inverse opals are polymerized in the interspaces of a colloidal crystal and form a new type of sensor. The majority

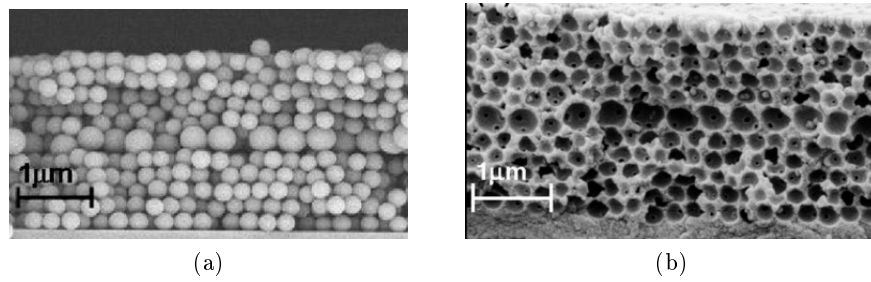


Figure 33: SEM images of (a) a planar defect inserted in an opal and (b) its inverse opal. Figure from [121].

of the devices are biosensors and are particularly driven by environment and health requirements. Molecularly imprinted polymers state as synthetic receptors and enable a selective, cheap and stable detection by the sensor. In many publications, people imagine to use the sensor as a colored strip for common detection of analytes. However, the main drawback to this evolution is the preparation of the device, still restricted to laboratory scale.

4 Scope of this thesis

Various aspects were introduced in this literature review. First, the discussion focused on wearable sensors and the advent of more performing and complete sensors for sports performers as well as for a sick or elderly population. Indeed, the progress in communication and sensing technologies gave birth to numerous physical sensors. However, monitoring of physical parameters is not sufficient and would gain high interest by being completed with biochemical information. Thus, over the last decade, new sensors were turned towards detection and quantification of biomarkers. The work presented in this thesis corresponds well with this tendency to develop these new types of sensors.

The detection of molecules by sensors may be achieved by different techniques. First, the anchoring of biological receptor molecules (such as antibodies, enzymes, or DNA) is possible and offers a very good specificity. However, some molecules cannot be easily grafted and other may not be stable and may be denatured. Moreover, biological receptors are often expensive. On the other hand, it is also possible to use polymers with properties like hydrophilicity, polarity or other intrinsic properties that enable the binding of certain analytes. This is the case for example of polymers functionalized with crown ethers or for hydrogels with ionizable groups. Unfortunately this technique is restricted to a few types of molecules and is largely unspecific. In this context, MIPs are a potential alternative, offering the stability of synthetic polymers and good recognition abilities. Over the past years, MIPs were used as sensitive layers in many types of sensors and display numerous advantages. Thus, we chose this polymeric approach in the thesis to elaborate a sensor.

Concerning the transducer, to associate a means of optical detection to the sensor that has the potential to be easy of use and transportable, we reviewed diverse approaches combined with MIPs. Label dependent transduction and sensors that need heavy instrumentation for the analyses were discarded, whereas optical detection based on diffraction and refraction seemed promising. Thus, photonic crystals, appeared to possess the required advantages. Indeed, it is a label free approach, with the possibility of real-time monitoring.

The experimental work presented in this manuscript will be articulated around three chapters, schematically represented in figure 35. The sensor being based on molecularly imprinted polymers, two chapters are devoted to the development of MIPs formulation targetting two steroids of interest, cypoterone acetate and cortisol, their optimization and characterizations. The elaboration of the

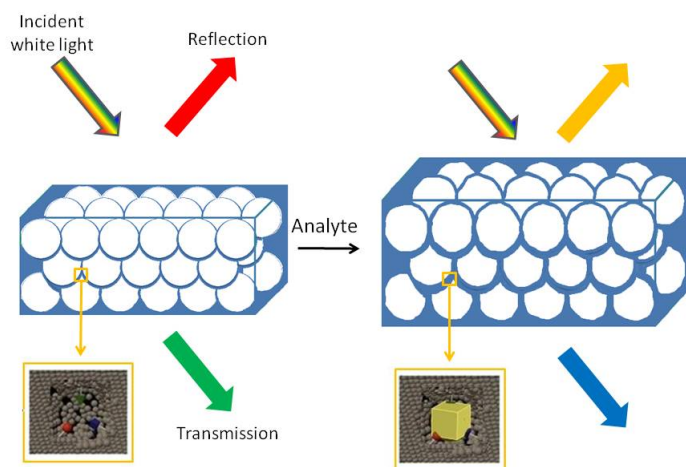


Figure 34: Schematic representation of the sensor, the optical transduction is obtained by a structuration of the MIP.

sensor is then described in the last chapter, where MIPs are structured into inverse opal allowing to obtain a color change upon analyte recognition (figure 34). A first proof of concept will be described with a model molecule in aqueous media (not in real sample) but the principles of the sensor can be widened for many other compounds.

The development of photonic crystal sensors with molecularly imprinted polymers has the potential to change the landscape of health monitoring and to enable new diagnostic capabilities, in particular when used to monitor physiological states with a non invasive approach. These visions are the bottomline of the work presented here.

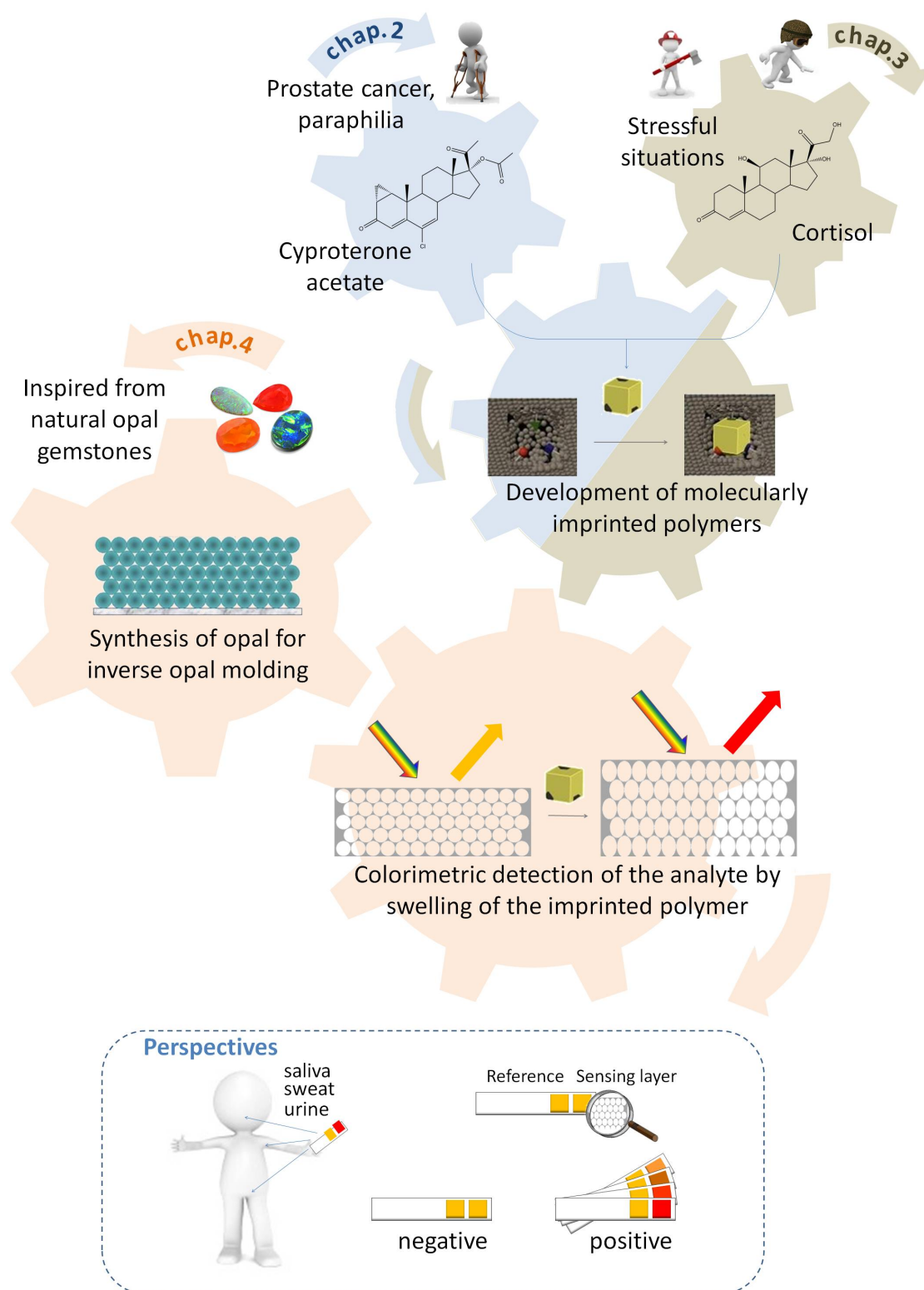


Figure 35: General articulation of the chapters in the manuscript.

Bibliography

- [1] P. Bonato, "Wearable Sensors and Systems," *IEEE Engineering in Medicine and Biology Magazine*, vol. 29, no. 3, pp. 25–36, 2010.
- [2] P. S. Kumar, S. Oh, H. Kwon, P. Rai, V. K. Varadan, and H. Medical, "Smart Real-time Cardiac Diagnostic Sensor Systems for Football Players and Soldiers under Intense Physical Training," *Proceedings of SPIE*, vol. 8691, pp. 1–6, 2013.
- [3] C. Wong, Z. Zhang, R. Kwasnicki, J. Liu, and G.-z. Yang, "Motion Reconstruction From Sparse Accelerometer Data Using PLSR," *Ninth International Conference on Wearable and Implantable Body Sensor Networks*, pp. 178–183, 2012.
- [4] B. Eskofier, P. Kugler, D. Melzer, and P. Kuehner, "Embedded Classification of the Perceived Fatigue State of Runners: Towards a Body Sensor Network for Assessing the Fatigue State during Running," in *2012 Ninth International Conference on Wearable and Implantable Body Sensor Networks*, pp. 113–117, IEEE, May 2012.
- [5] J. Lefever, F. Jansen, J.-M. Aerts, and D. Berckmans, "Real-Time Monitoring of the Heart Rate Response to Power Output for Cyclists," in *2010 International Conference on Body Sensor Networks*, pp. 76–79, IEEE, June 2010.
- [6] T. Linz, C. Kallmayer, R. Aschenbrenner, and H. Reichl, "Embroidering Electrical Interconnects with Conductive Yarn for The Integration of Flexible Electronic Modules into Fabric," in *Ninth IEEE International Symposium on Wearable Computers (ISWC'05)*, pp. 86–91, Ieee, 2005.
- [7] D. Curone, E. L. Secco, A. Tognetti, G. Loriga, G. Dudnik, M. Risatti, R. Whyte, A. Bonfiglio, and G. Magenes, "Smart garments for emergency operators: the ProeTEX project.," *IEEE transactions on information technology in biomedicine : a publication of the IEEE Engineering in Medicine and Biology Society*, vol. 14, pp. 694–701, May 2010.
- [8] D.-H. Kim, N. Lu, R. Ma, Y.-S. Kim, R.-H. Kim, S. Wang, J. Wu, S. M. Won, H. Tao, A. Islam, K. J. Yu, T.-i. Kim, R. Chowdhury, M. Ying, L. Xu, M. Li, H.-J. Chung, H. Keum, M. McCormick, P. Liu, Y.-W. Zhang, F. G. Omenetto, Y. Huang, T. Coleman, and J. a. Rogers, "Epidermal electronics," *Science (New York, N.Y.)*, vol. 333, pp. 838–43, Aug. 2011.
- [9] P. A. Shaltis, A. Reisner, and H. H. Asada, "Wearable, cuff-less PPG-based blood pressure monitor with novel height sensor.," *Conference proceedings : Annual International Conference of the IEEE Engineering in Medicine and Biology Society. IEEE Engineering in Medicine and Biology Society. Conference*, vol. 1, pp. 908–11, Jan. 2006.
- [10] J. A. Patterson, D. C. McIlwraith, and G.-Z. Yang, "A Flexible, Low Noise Reflective PPG Sensor Platform for Ear-Worn Heart Rate Monitoring," in *2009 Sixth International Workshop on Wearable and Implantable Body Sensor Networks*, pp. 286–291, IEEE, June 2009.
- [11] STMicroelectronics, "'Smart' Contact Lens with Embedded Wireless Sensor Promises Earlier Diagnosis and Optimized Treatment of Glaucoma."

- [12] Sensimed, "<http://www.sensimed.ch/>."
- [13] J. Hönes, P. Müller, and N. Surridge, "The Technology Behind Glucose Meters: Test Strips," *Diabetes Technology & Therapeutics*, vol. 10, pp. S-10-S-26, June 2008.
- [14] K. M. Shamsuddin, S. Yanagimoto, T. Kuwahara, Y. Zhang, C. Nomura, and N. Kondo, "Changes in the index of sweat ion concentration with increasing sweat during passive heat stress in humans," *European journal of applied physiology*, vol. 94, pp. 292-7, June 2005.
- [15] A. G. R. Whitehouse, "The Dissolved Constituents of Human Sweat," 1935.
- [16] S. L. Kacinko, A. J. Barnes, E. W. Schwilke, E. J. Cone, E. T. Moolchan, and M. a. Huestis, "Disposition of cocaine and its metabolites in human sweat after controlled cocaine administration.," *Clinical chemistry*, vol. 51, pp. 2085-94, Nov. 2005.
- [17] PharmChem, "<http://www.pharmchem.com/>."
- [18] Biotex, "<http://www.smartex.it/index.php/en/research/projects/european-projects/biotex>."
- [19] D. Morris, B. Schazmann, Y. Wu, S. Coyle, S. Brady, C. Fay, J. Hayes, K. T. Lau, G. Wallace, and D. Diamond, "Wearable technology for bio-chemical analysis of body fluids during exercise.," *Conference proceedings : ... Annual International Conference of the IEEE Engineering in Medicine and Biology Society. IEEE Engineering in Medicine and Biology Society. Conference*, vol. 2008, pp. 5741-4, Jan. 2008.
- [20] S. Coyle, K.-T. Lau, N. Moyna, D. O'Gorman, D. Diamond, F. Di Francesco, D. Costanzo, P. Salvo, M. G. Trivella, D. E. De Rossi, N. Taccini, R. Paradiso, J.-A. Porchet, A. Ridolfi, J. Luprano, C. Chuzel, T. Lanier, F. Revol-Cavalier, S. Schoumacker, V. Mourier, I. Chartier, R. Convert, H. De-Moncuit, and C. Bini, "BIOTEX-biosensing textiles for personalised healthcare management.," *IEEE transactions on information technology in biomedicine : a publication of the IEEE Engineering in Medicine and Biology Society*, vol. 14, pp. 364-70, Mar. 2010.
- [21] J. Moyer, D. Wilson, I. Finkelshtein, B. Wong, and R. Potts, "Correlation between sweat glucose and blood glucose in subjects with diabetes.," *Diabetes technology & therapeutics*, vol. 14, pp. 398-402, May 2012.
- [22] E. Kaufman and I. B. Lamster, "the Diagnostic Applications of Saliva- a Review," *Critical Reviews in Oral Biology & Medicine*, vol. 13, pp. 197-212, Mar. 2002.
- [23] S. Amer, M. Yousuf, P. Q. Siddiqui, and J. Alam, "Salivary glucose concentrations in patients with diabetes mellitus-a minimally invasive technique for monitoring blood glucose levels.," *Pakistan journal of pharmaceutical sciences*, vol. 14, pp. 33-7, Jan. 2001.
- [24] S. Frost, R. N. Martins, and Y. Kanagasalingam, "Ocular biomarkers for early detection of Alzheimer's disease.," *Journal of Alzheimer's disease : JAD*, vol. 22, pp. 1-16, Jan. 2010.
- [25] Q. Yan, B. Peng, G. Su, B. E. Cohan, T. C. Major, and M. E. Meyerhoff, "Measurement of tear glucose levels with amperometric glucose biosensor/capillary tube configuration.," *Analytical chemistry*, vol. 83, pp. 8341-6, Nov. 2011.
- [26] Noviosense, "<http://noviosense.com/>."
- [27] M. Miyashita, N. Ito, S. Ikeda, T. Murayama, K. Oguma, and J. Kimura, "Development of urine glucose meter based on micro-planer amperometric biosensor and its clinical application for self-monitoring of urine glucose.," *Biosensors & bioelectronics*, vol. 24, pp. 1336-40, Jan. 2009.
- [28] C. Shao, M. Li, X. Li, L. Wei, L. Zhu, F. Yang, L. Jia, Y. Mu, J. Wang, Z. Guo, D. Zhang, J. Yin, Z. Wang, W. Sun, Z. Zhang, and Y. Gao, "A tool for biomarker discovery in the urinary proteome: a manually curated human and animal urine protein biomarker database.," *Molecular & cellular proteomics : MCP*, vol. 10, p. M111.010975, Nov. 2011.
- [29] J. C. Claussen, A. Kumar, D. B. Jaroch, M. H. Khawaja, A. B. Hibbard, D. M. Porterfield, and T. S. Fisher, "Nanostructuring Platinum Nanoparticles on Multilayered Graphene Petal Nanosheets for Electrochemical

- Biosensing,” *Advanced Functional Materials*, vol. 22, pp. 3399–3405, Aug. 2012.
- [30] S. S. K. Tang and G. P. H. Gui, “Biomarkers in the diagnosis of primary and recurrent breast cancer,” *Biomarkers in medicine*, vol. 6, pp. 567–85, Oct. 2012.
- [31] R. Aebersold and M. Mann, “Mass spectrometry-based proteomics,” *Nature*, vol. 422, pp. 198–207, Mar. 2003.
- [32] E. Fischer, “Einfluss der Configuration auf die Wirkung der Enzyme,” *Berichte der deutschen chemischen Gesellschaft*, vol. 27, no. 3, pp. 2985–2993, 1894.
- [33] L. Pauling, “A theory of the structure and process of formation of antibodies,” *Journal of the American Chemical Society*, vol. 62, no. 10, pp. 2643–2657, 1940.
- [34] A. Cutivet, C. Schembri, J. Kovensky, and K. Haupt, “Molecularly imprinted microgels as enzyme inhibitors,” *Journal of the American Chemical Society*, vol. 131, pp. 14699–702, Oct. 2009.
- [35] G. Wulff and A. Sarhan, “The use of polymers with enzyme-analogous structures for the resolution of racemates,” *Angewandte Chemie International Edition*, vol. 11, no. 4, p. 341, 1972.
- [36] R. Arshady and K. Mosbach, “Synthesis of substrate-selective polymers by host-guest polymerization,” *Die Makromolekulare Chemie*, vol. 182, no. 2, pp. 687–692, 1981.
- [37] K. Haupt, “Imprinted polymers-tailor-made mimics of antibodies and receptors,” *Chemical communications (Cambridge, England)*, pp. 171–8, Jan. 2003.
- [38] B. Tse Sum Bui, F. Merlier, and K. Haupt, “Toward the use of a molecularly imprinted polymer in doping analysis: selective preconcentration and analysis of testosterone and epitestosterone in human urine,” *Analytical chemistry*, vol. 82, pp. 4420–7, June 2010.
- [39] A. Beltran, R. M. Marcé, P. A. G. Cormack, and F. Borrull, “Synthesis by precipitation polymerisation of molecularly imprinted polymer microspheres for the selective extraction of carbamazepine and oxcarbazepine from human urine,” *Journal of chromatography. A*, vol. 1216, pp. 2248–53, Mar. 2009.
- [40] R. H. Schmidt, K. Mosbach, and K. Haupt, “A Simple Method for Spin-Coating Molecularly Imprinted Polymer Films of Controlled Thickness and Porosity,” *Advanced Materials*, vol. 16, no. 8, pp. 719–722, 2004.
- [41] T. Piacham, A. s. Josell, H. Arwin, V. Prachayasittikul, and L. Ye, “Molecularly imprinted polymer thin films on quartz crystal microbalance using a surface bound photo-radical initiator,” *Analytica Chimica Acta*, vol. 536, no. 1, pp. 191–196, 2005.
- [42] K. Kantarovich, I. Tsarfati, L. A. Gheber, K. Haupt, and I. Bar, “Reading microdots of a molecularly imprinted polymer by surface-enhanced Raman spectroscopy,” *Biosensors & bioelectronics*, vol. 26, pp. 809–14, Oct. 2010.
- [43] F. Vandevelde, a. S. Belmont, J. Pantigny, and K. Haupt, “Hierarchically Nanostructured Polymer Films Based on Molecularly Imprinted Surface-Bound Nanofilaments,” *Advanced Materials*, vol. 19, pp. 3717–3720, Nov. 2007.
- [44] T. P. Lee, B. Saad, W. S. Khayoon, and B. Salleh, “Molecularly imprinted polymer as sorbent in micro-solid phase extraction of ochratoxin A in coffee, grape juice and urine,” *Talanta*, vol. 88, pp. 129–35, Jan. 2012.
- [45] R. J. Umpleby, S. C. Baxter, Y. Chen, R. N. Shah, and K. D. Shimizu, “Characterization of molecularly imprinted polymers with the Langmuir-Freundlich isotherm,” *Analytical chemistry*, vol. 73, pp. 4584–91, Oct. 2001.
- [46] P. Job, “Formation and stability of inorganic complexes in solution,” *Ann. Chim.*, vol. 9, pp. 113–203, 1928.
- [47] K. Haupt, A. Dzgoev, and K. Mosbach, “Assay system for the Herbicide 2,4-Dichlorophenoxyacetic Acid Using a Molecularly Imprinted Polymer as an Artificial Recognition Element,” *Analytical chemistry*, vol. 70, no. 3, pp. 628–631, 1998.
- [48] J. O’Mahony, a. Molinelli, K. Nolan, M. R. Smyth, and B. Mizaikoff, “Towards the rational development of molecularly imprinted polymers: ¹H NMR studies on hydrophobicity and ion-pair interactions as driving forces for selectivity,” *Biosensors & bioelectronics*, vol. 20, pp. 1884–93, Mar. 2005.

- [49] U. Skogsberg, C. Meyer, J. Rehbein, G. Fischer, S. Schauff, N. Welsch, K. Albert, A. J. Hall, and B. Sellergren, "A solid-state and suspended-state magic angle spinning nuclear magnetic resonance spectroscopic investigation of a 9-ethyladenine molecularly imprinted polymer," *Polymer*, vol. 48, pp. 229–238, Jan. 2007.
- [50] H. k. S. Andersson and I. A. Nicholls, "Spectroscopic Evaluation of Molecular Imprinting Polymerization Systems," *Bioorganic Chemistry*, vol. 25, pp. 203–211, June 1997.
- [51] K. Nakamoto, M. Margoshes, and R. E. Rundle, "Stretching Frequencies as a function of Distances in Hydrogen Bonds," *Journal of the American Chemical Society*, vol. 77, no. 24, pp. 6480–6486, 1955.
- [52] D. J. Duffy, K. Das, S. L. Hsu, J. Penelle, V. M. Rotello, and H. D. Stidham, "Binding Efficiency and Transport Properties of Molecularly Imprinted Polymer Thin Films," *Journal of the American Chemical Society*, vol. 124, no. 28, pp. 8290–8296, 2002.
- [53] W.-Y. Chen, C.-S. Chen, and F.-Y. Lin, "Molecular recognition in imprinted polymers: thermodynamic investigation of analyte binding using microcalorimetry," *Journal of Chromatography A*, vol. 923, no. 1, pp. 1–6, 2001.
- [54] Z. Li, M. Day, J. Ding, and K. Faid, "Synthesis and Characterization of Functional Methacrylate Copolymers and Their Application in Molecular Imprinting," *Macromolecules*, vol. 38, no. 7, pp. 2620–2625, 2005.
- [55] M. Cela-Pérez, a. Lasagabáster-Latorre, M. Abad-López, J. López-Vilariño, and M. González-Rodríguez, "A study of competitive molecular interaction effects on imprinting of molecularly imprinted polymers," *Vibrational Spectroscopy*, vol. 65, pp. 74–83, Mar. 2013.
- [56] T.-V. Nicolescu, A. Sarbu, M. Ghiurea, and D. Donescu, "Influence of crosslinker / porogen ratio upon imprinted polymer parameters," *U.P.B. Sci. Bull., seriesB*, vol. 73, no. 1, pp. 163–172, 2011.
- [57] J. G. Karlsson, B. Karlsson, I. Andersson, and I. A. Nicholls, "The roles of template complexation and ligand binding conditions on recognition in bupivacaine molecularly imprinted polymers," *The Analyst*, vol. 129, pp. 456–462, 2004.
- [58] J. L. Urraca, M. C. Carbajo, M. J. Torralvo, J. González-Vázquez, G. Orellana, and M. C. Moreno-Bondi, "Effect of the template and functional monomer on the textural properties of molecularly imprinted polymers," *Biosensors & bioelectronics*, vol. 24, pp. 155–61, Oct. 2008.
- [59] M. Kobaisi, M. Tate, C. Rix, T. S. Jakubov, and D. E. Mainwaring, "The effect of molecular imprinting on the pore size distribution of polymers," *Adsorption*, vol. 13, pp. 315–321, Oct. 2007.
- [60] J. Matsui, O. Doblhoff-Dier, and T. Takeuchi, "2-(Trifluoromethyl)acrylic acid: a novel functional monomer in non-covalent molecular imprinting," *Analytica Chimica Acta*, vol. 343, pp. 1–4, May 1997.
- [61] T. A. Sergeyev, H. Matuschewski, S. A. Piletsky, J. Bendig, U. Schedler, and M. Ulbricht, "Molecularly imprinted polymer membranes for substance-selective solid-phase extraction from water by surface photo-grafting polymerization," *Journal of chromatography. A*, vol. 907, pp. 89–99, Jan. 2001.
- [62] D. S. Janiak, O. B. Ayyub, and P. Kofinas, "Effects of Charge Density on the Recognition Properties of Molecularly Imprinted Polymeric Hydrogels," *Macromolecules*, vol. 42, pp. 1703–1709, Mar. 2009.
- [63] A. A. Ozcan, R. Say, A. Denizli, and A. Ersoz, "L -Histidine Imprinted Synthetic Receptor for Biochromatography Applications," *Anal. Chem*, vol. 78, no. 20, pp. 7253–7258, 2006.
- [64] B. Sellergren and K. J. Shea, "Influence of polymer morphology on the ability of imprinted network polymers to resolve enantiomers," *Journal of Chromatography A*, vol. 635, pp. 31–49, Apr. 1993.
- [65] O. Ramstrom, L. Ye, and P. Gustavsson, "Chiral Recognition by Molecularly Imprinted Polymers in Aqueous Media," *Chromatographia*, vol. 48, no. 3/4, pp. 197–202, 1998.
- [66] Y. Fuchs, O. Soppera, A. G. Mayes, and K. Haupt, "Holographic molecularly imprinted polymers for label-free chemical sensing," *Advanced materials (Deerfield Beach, Fla.)*, vol. 25, pp. 566–70, Jan. 2013.
- [67] T. Anirudhan, P. Divya, and J. Nima, "Silylated montmorillonite based molecularly imprinted polymer for the

- selective binding and controlled release of thiamine hydrochloride,” *Reactive and Functional Polymers*, vol. 73, pp. 1144–1155, Aug. 2013.
- [68] F. Lanza and B. Sellergren, “Method for Synthesis and Screening of Large Groups of Molecularly Imprinted Polymers,” *Anal. Chem*, vol. 71, no. 11, pp. 2092–2096, 1999.
- [69] C. Baggiani, C. Giovannoli, L. Anfossi, C. Passini, P. Baravalle, and G. Giraudi, “A connection between the binding properties of imprinted and nonimprinted polymers: a change of perspective in molecular imprinting,” *Journal of the American Chemical Society*, vol. 134, pp. 1513–8, Jan. 2012.
- [70] I. Chianella, M. Lotierzo, S. A. Piletsky, I. E. Tothill, B. Chen, K. Karim, and A. P. F. Turner, “Rational Design of a Polymer Specific for Microcystin-LR Using a Computational Approach,” *Anal. Chem*, vol. 74, no. 6, pp. 1288–1293, 2002.
- [71] S. Kunath, N. Marchyk, K. Haupt, and K.-H. Feller, “Multi-objective optimization and design of experiments as tools to tailor molecularly imprinted polymers specific for glucuronic acid,” *Talanta*, vol. 105, pp. 211–8, Feb. 2013.
- [72] D. Kriz, O. Ramström, A. Svensson, and K. Mosbach, “A biomimetic Sensor Based on a Molecularly Imprinted Polymer as a Recognition Element Combined with Fiber-Optic Detection,” *Analytical chemistry*, vol. 67, no. 13, pp. 2142–2144, 1995.
- [73] A. Valero-Navarro, A. L. Medina-Castillo, J. F. Fernandez-Sanchez, and A. Fernandez-Gutierrez, “Synthesis of a novel polyurethane-based-magnetic imprinted polymer for the selective optical detection of 1-naphthylamine in drinking water,” *Biosensors & bioelectronics*, vol. 26, pp. 4520–5, July 2011.
- [74] J. L. Suarez-Rodriguez and M. E. Diaz-Garcia, “Fluorescent competitive flow-through assay for chloramphenicol using molecularly imprinted polymers,” *Biosensors and Bioelectronics*, vol. 16, pp. 955–961, Dec. 2001.
- [75] Y. Inoue, A. Kuwahara, K. Ohmori, H. Sunayama, T. Ooya, and T. Takeuchi, “Fluorescent molecularly imprinted polymer thin films for specific protein detection prepared with dansyl ethylenediamine-conjugated O-acryloyl l-hydroxyproline,” *Biosensors & bioelectronics*, vol. 48, pp. 113–9, Oct. 2013.
- [76] C.-C. Hong, P.-H. Chang, C.-C. Lin, and C.-L. Hong, “A disposable microfluidic biochip with on-chip molecularly imprinted biosensors for optical detection of anesthetic propofol,” *Biosensors & bioelectronics*, vol. 25, pp. 2058–64, May 2010.
- [77] E. Wijaya, C. Lenaerts, S. Maricot, J. Hastanin, S. Habraken, J.-P. Vilecot, R. Boukherroub, and S. Szunerits, “Surface plasmon resonance-based biosensors: From the development of different SPR structures to novel surface functionalization strategies,” *Current Opinion in Solid State and Materials Science*, vol. 15, no. 5, pp. 208–224, 2011.
- [78] M. Lotierzo, O. Henry, S. Piletsky, I. Tothill, D. Cullen, M. Kania, B. Hock, and A. Turner, “Surface plasmon resonance sensor for domoic acid based on grafted imprinted polymer,” *Biosensors and Bioelectronics*, vol. 20, no. 2, pp. 145–152, 2004.
- [79] M. Kara, L. Uzun, S. Kolayli, and A. Denizli, “Combining molecular imprinted nanoparticles with surface plasmon resonance nanosensor for chloramphenicol detection in honey,” *Journal of Applied Polymer Science*, vol. 129, pp. 2273–2279, Aug. 2013.
- [80] J. Matsui, K. Akamatsu, S. Nishiguchi, D. Miyoshi, H. Nawafune, K. Tamaki, and N. Sugimoto, “Composite of Au nanoparticles and molecularly imprinted polymer as a sensing material,” *Analytical chemistry*, vol. 76, pp. 1310–5, Mar. 2004.
- [81] J. Matsui, K. Akamatsu, N. Hara, D. Miyoshi, H. Nawafune, K. Tamaki, and N. Sugimoto, “SPR Sensor Chip for Detection of Small Molecules Using Molecularly Imprinted Polymer with Embedded Gold Nanoparticles,” *Analytical chemistry*, vol. 77, no. 13, pp. 4282–4285, 2005.
- [82] Y. Taguchi, E. Takano, and T. Takeuchi, “SPR Sensing of Bisphenol A Using Molecularly Imprinted Nanoparti-

- picles Immobilized on Slab Optical Waveguide with Consecutive Parallel Au and Ag deposition Bands Coexistent with Bisphenol A-immobilized Au Nanoparticles,”
- Langmuir*
- , vol. 28, no. 17, pp. 7083–7088, 2012.
- [83] M. Jakusch, M. Janotta, B. Mizaikoff, K. Mosbach, and K. Haupt, “Molecularly Imprinted Polymers and Infrared Evanescent Wave Spectroscopy . A Chemical Sensors Approach,” *Anal. Chem.*, vol. 71, no. 20, pp. 4786–4791, 1999.
- [84] K. Kantarovich, I. Tsarfati, L. A. Gheber, K. Haupt, and I. Bar, “Writing Droplets of Molecularly Imprinted Polymers by Nano Fountain Pen and Detecting Their Molecular Interactions by Surface-Enhanced Raman Scattering,” *Anal. Chem.*, vol. 81, no. 14, pp. 5686–5690, 2009.
- [85] C. a. Barrios, C. Zhenhe, F. Navarro-Villoslada, D. López-Romero, and M. C. Moreno-Bondi, “Molecularly imprinted polymer diffraction grating as label-free optical bio(mimetic)sensor,” *Biosensors & bioelectronics*, vol. 26, pp. 2801–4, Jan. 2011.
- [86] C. Barrios, S. Carrasco, M. Francesca, P. Yurrita, F. Navarro-Villoslada, and M. Moreno-Bondi, “Molecularly imprinted polymer for label-free integrated optical waveguide bio(mimetic)sensors,” *Sensors and Actuators B: Chemical*, vol. 161, pp. 607–614, Jan. 2012.
- [87] E. Yablonovitch, “Inhibited Spontaneous Emission in Solid-State Physics and Electronics,” *Physical Review Letters*, vol. 58, pp. 2059–2062, May 1987.
- [88] S. John, “Strong localization of photons in certain disordered dielectric superlattices,” *Physical Review Letters*, vol. 58, pp. 2486–2489, June 1987.
- [89] J. D. Joannopoulos, S. G. Johnson, J. N. Winn, and R. D. Meade, *Photonic Crystals: Molding the Flow of Light*. Princeton University Press, 2008.
- [90] R. V. Nair and R. Vijaya, “Photonic crystal sensors: An overview,” *Progress in Quantum Electronics*, vol. 34, pp. 89–134, May 2010.
- [91] Y. Kang, J. J. Walsh, T. Gorishnyy, and E. L. Thomas, “Broad-wavelength-range chemically tunable block-copolymer photonic gels,” *Nature materials*, vol. 6, pp. 957–60, Dec. 2007.
- [92] A. J. Marshall, S. Kabilan, J. Blyth, and C. R. Lowe, “Analyte-responsive holograms for (bio)chemical analysis,” *Journal of Physics: Condensed Matter*, vol. 18, pp. S619–S626, May 2006.
- [93] A. G. Mayes, J. Blyth, R. B. Millington, and C. R. Lowe, “Metal Ion-Sensitive Holographic Sensors,” *Analytical Chemistry*, vol. 74, pp. 3649–3657, Aug. 2002.
- [94] K. Shadak Alee, G. Sriram, and D. Narayana Rao, “Spectral and morphological changes of 3D polystyrene photonic crystals with the incorporation of alcohols,” *Optical Materials*, vol. 34, pp. 1077–1081, May 2012.
- [95] S. Y. Choi, M. Mamak, G. Von Freymann, N. Chopra, and G. Ozin, “Mesoporous Bragg Stack Color Tunable Sensors,” *Nano Letters*, vol. 6, no. 11, pp. 2456–2461, 2006.
- [96] J. Shin, S. G. Han, and W. Lee, “Dually tunable inverse opal hydrogel colorimetric sensor with fast and reversible color changes,” *Sensors and Actuators B: Chemical*, vol. 168, pp. 20–26, June 2012.
- [97] L. Rindorf, J. B. Jensen, M. Dufva, L. H. Pedersen, P. E. Høiby, and O. Bang, “Photonic crystal fiber long-period gratings for biochemical sensing,” *Optics Express*, vol. 14, p. 8224, Sept. 2006.
- [98] B. Cunningham, B. Lin, J. Qiu, P. Li, J. Pepper, and B. Hugh, “A plastic colorimetric resonant optical biosensor for multiparallel detection of label-free biochemical interactions,” *Sensors and Actuators B: Chemical*, vol. 85, pp. 219–226, July 2002.
- [99] B. T. Cunningham, P. Li, S. Schulz, B. Lin, C. Baird, J. Gerstenmaier, C. Genick, F. Wang, E. Fine, and L. Laing, “Label-free assays on the BIND system,” *Journal of biomolecular screening*, vol. 9, pp. 481–90, Sept. 2004.
- [100] C. Guo, C. Zhou, N. Sai, B. Ning, M. Liu, H. Chen, and Z. Gao, “Detection of bisphenol A using an opal photonic crystal sensor,” *Sensors and Actuators B: Chemical*, vol. 166–167, pp. 17–23, May 2012.

- [101] Z. Wu, C.-a. Tao, C. Lin, D. Shen, and G. Li, "Label-free colorimetric detection of trace atrazine in aqueous solution by using molecularly imprinted photonic polymers," *Chem. Eur. J.*, vol. 14, pp. 11358–68, Jan. 2008.
 - [102] X. Hu, Q. An, G. Li, S. Tao, and J. Liu, "Imprinted photonic polymers for chiral recognition," *Angewandte Chemie (International ed. in English)*, vol. 45, pp. 8145–8, Dec. 2006.
 - [103] X. Hu, G. Li, J. Huang, D. Zhang, and Y. Qiu, "Construction of Self-Reporting Specific Chemical Sensors with High Sensitivity," *Advanced Materials*, vol. 19, pp. 4327–4332, Dec. 2007.
 - [104] X. Hu, G. Li, M. Li, J. Huang, Y. Li, Y. Gao, and Y. Zhang, "Ultrasensitive Specific Stimulant Assay Based on Molecularly Imprinted Photonic Hydrogels," *Advanced Functional Materials*, vol. 18, pp. 575–583, Feb. 2008.
 - [105] Z. Wu, X. Hu, C.-a. Tao, Y. Li, J. Liu, C. Yang, D. Shen, and G. Li, "Direct and label-free detection of cholic acid based on molecularly imprinted photonic hydrogels," *Journal of Materials Chemistry*, vol. 18, p. 5452, Dec. 2008.
 - [106] Y. Yuan, Z. Li, Y. Liu, J. Gao, Z. Pan, and Y. Liu, "Hydrogel photonic sensor for the detection of 3-pyridinecarboxamide," *Chemistry (Weinheim an der Bergstrasse, Germany)*, vol. 18, pp. 303–9, Jan. 2012.
 - [107] C. Zhou, T. Wang, J. Liu, C. Guo, Y. Peng, J. Bai, M. Liu, J. Dong, N. Gao, B. Ning, and Z. Gao, "Molecularly imprinted photonic polymer as an optical sensor to detect chloramphenicol," *The Analyst*, vol. 137, pp. 4469–74, Oct. 2012.
 - [108] L.-Q. Wang, F.-Y. Lin, and L.-P. Yu, "A molecularly imprinted photonic polymer sensor with high selectivity for tetracyclines analysis in food," *The Analyst*, vol. 137, pp. 3502–9, Aug. 2012.
 - [109] Y.-X. Zhang, P.-Y. Zhao, and L.-P. Yu, "Highly-sensitive and selective colorimetric sensor for amino acids chiral recognition based on molecularly imprinted photonic polymers," *Sensors and Actuators B: Chemical*, vol. 181, pp. 850–857, May 2013.
 - [110] X.-Y. Liu, H.-X. Fang, and L.-P. Yu, "Molecularly imprinted photonic polymer based on β -cyclodextrin for amino acid sensing," *Talanta*, vol. 116, pp. 283–289, Nov. 2013.
 - [111] L. Meng, P. Meng, B. Tang, Q. Zhang, and Y. Wang, "Molecularly imprinted photonic hydrogels for fast screening of atropine in biological samples with high sensitivity," *Forensic Science International*, vol. 231, pp. 6–12, Sept. 2013.
 - [112] L. Meng, P. Meng, Q. Zhang, and Y. Wang, "Fast screening of ketamine in biological samples based on molecularly imprinted photonic hydrogels," *Analytica chimica acta*, vol. 771, pp. 86–94, Apr. 2013.
 - [113] F. Liu, S. Huang, F. Xue, Y. Wang, Z. Meng, and M. Xue, "Detection of organophosphorus compounds using a molecularly imprinted photonic crystal," *Biosensors and Bioelectronics*, vol. 32, no. 1, pp. 273–277, 2012.
 - [114] F. Xue, T.-R. Duan, S.-Y. Huang, Q.-H. Wang, M. Xue, and Z.-H. Meng, "A covalently imprinted photonic crystal for glucose sensing," *Journal of Nanomaterials*, vol. 2013, 2013.
 - [115] J. Li, Z. Zhang, S. Xu, L. Chen, N. Zhou, H. Xiong, and H. Peng, "Label-free colorimetric detection of trace cholesterol based on molecularly imprinted photonic hydrogels," *Journal of Materials Chemistry*, vol. 21, p. 19267, Nov. 2011.
 - [116] H. Peng, S. Wang, Z. Zhang, H. Xiong, J. Li, L. Chen, and Y. Li, "Molecularly Imprinted Photonic Hydrogels as Colorimetric Sensors for Rapid and Label-free Detection of Vanillin," *Journal of Agricultural and Food Chemistry*, vol. 60, pp. 1921–1928, 2012.
 - [117] N. Griffete, H. Frederich, A. Maitre, S. Ravaine, M. M. Chehimi, and C. Mangeney, "Inverse opals of molecularly imprinted hydrogels for the detection of bisphenol A and pH sensing," *Langmuir : the ACS journal of surfaces and colloids*, vol. 28, pp. 1005–12, Jan. 2012.
 - [118] J. D. Joannopoulos, "Self-assembly lights up," *Nature*, vol. 414, pp. 257–8, Nov. 2001.
 - [119] P. Massé and S. Ravaine, "The Langmuir–Blodgett technique: A powerful tool to elaborate multilayer colloidal crystals," *Colloids and Surfaces A: Physicochemical and Engineering Aspects*, vol. 270–271, pp. 148–152, Dec.
-

- 2005.
- [120] D. Xu, W. Zhu, Y. Jiang, X. Li, W. Li, J. Cui, J. Yin, and G. Li, "Rational design of molecularly imprinted photonic films assisted by chemometrics," *Journal of Materials Chemistry*, vol. 22, p. 16572, July 2012.
 - [121] N. Griffete, H. Frederich, A. Maitre, C. Schwob, S. Ravaine, B. Carbonnier, M. M. Chehimi, and C. Mangeney, "Introduction of a planar defect in a molecularly imprinted photonic crystal sensor for the detection of bisphenol A," *Journal of colloid and interface science*, vol. 364, pp. 18–23, 2011.
 - [122] L. Wang, Q. Yan, and X. S. Zhao, "From planar defect in opal to planar defect in inverse opal," *Langmuir : the ACS journal of surfaces and colloids*, vol. 22, pp. 3481–4, Apr. 2006.
 - [123] A. Z. Khokhar, F. Rahman, and N. P. Johnson, "Photonic crystal heterostructures from self-assembled opals," *Applied Physics A*, vol. 102, pp. 281–287, Dec. 2010.

CHAPTER II

A molecularly imprinted polymer for cyproterone acetate

1 Cyproterone acetate

In this chapter, we will develop a MIP for a synthetic steroid and try to optimize its formulation. Cyproterone acetate (CPA) is a synthetic steroid efficient as an antiandrogen (suppressing the action of testosterone in tissues). As a steroid, it possesses a tetracyclic hydrocarbon skeleton (figure 36).

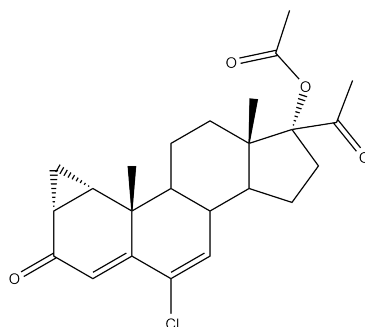


Figure 36: Chemical structure of cyproterone acetate.

1.1 Biological action

CPA was discovered fortuitously, during a research on non-virilizing progestin. The study was focused on progesterone derivatives and among them, CPA was the most potent progestin. Routine tests for the molecule displayed its androgenic properties and since then, many studies were led on this molecule (to understand sexual differentiation for example). Conventional syntheses of CPA start from solasodine which can be extracted from leaves of the tropic plant *Solanum laciniatum*. The general synthesis requires between 14 and 18 steps [1], [2].

Androgens are steroids which possess 19 carbons and are commonly called "male steroids". They stimulate or control the development and maintenance of male characteristics. The dominant androgen is testosterone (figure 37). Androgens are synthesized in the adrenal cortex (covering the adrenal glands). Cells presenting receptors to androgens are involved in the development of male secondary sex characteristics such as deep voice, facial and body hair and increased muscle mass.

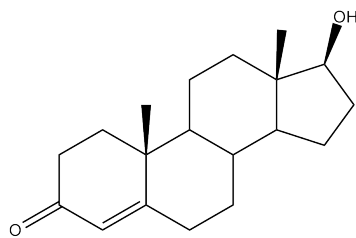


Figure 37: Chemical structure of testosterone.

Antiandrogens prevent androgens from expressing their biological effects on responsive tissues. They inhibit the circulation of androgens by blocking their receptors (figure 38) and suppress their synthesis. Cyproterone acetate is one of the antiandrogen used as a valuable drug in certain pharmaceutical compositions.

Cyproterone acetate is mainly indicated in prostate cancer treatment [4]. It relieves the symptoms caused by a tumor in the prostate gland. Indeed, some tumors need testosterone to grow and cyproterone acetate prevents the testosterone to bind to tumor receptors. The other methods of androgen deprivation in the palliative therapy of metastatic carcinoma include estrogens which have higher side effects. It is also indicated to men suffering of hypersexuality or sexual deviances called paraphilia. CPA inhibits accessory sexual gland function, spermatogenesis and lowers libido. However, important conditions must be met before CPA therapy. The patient must agree to be treated, the treatment should be combined with psychotherapy and the indication should be restricted to those who have or might come into conflict with the law and to patients under severe mental stress as a result of uncontrollable sexual drive. For women, this drug may be used in the treatment of certain dermatological disorders or to treat hirsutism.

Unlike other steroid esters, little of cyproterone acetate is hydrolyzed to cyproterone. The main metabolite is 15 β -hydroxycyproterone acetate [5] (figure 39). The pharmacokinetics are complicated due to its lipophilic nature, however both the oral and intramuscular administrations are equivalent and display a metabolite level below the CPA level until 4 days [6].

Urine analysis shows that cyproterone acetate is excreted almost exclusively in the free form. Approximately 6% of the typically daily dose is excreted in urine. In blood plasma, the relative amount of 15 β -hydroxycyproterone acetate to cyproterone acetate appears more elevated.

Cyproterone acetate orally administered is also found in non negligible concentrations in the milk of lactating women [7].

Thus, cyproterone acetate and its main metabolite are present in several physiological fluids, such as blood plasma, urine and milk. As far as we know, no studies have focused on the detection of CPA in sweat, saliva or tears. However, the skin synthesizes amounts of sexual hormones, thus many androgen receptors are expressed in sebaceous and sweat glands [8] and this rises the probability of CPA to be excreted in sweat.

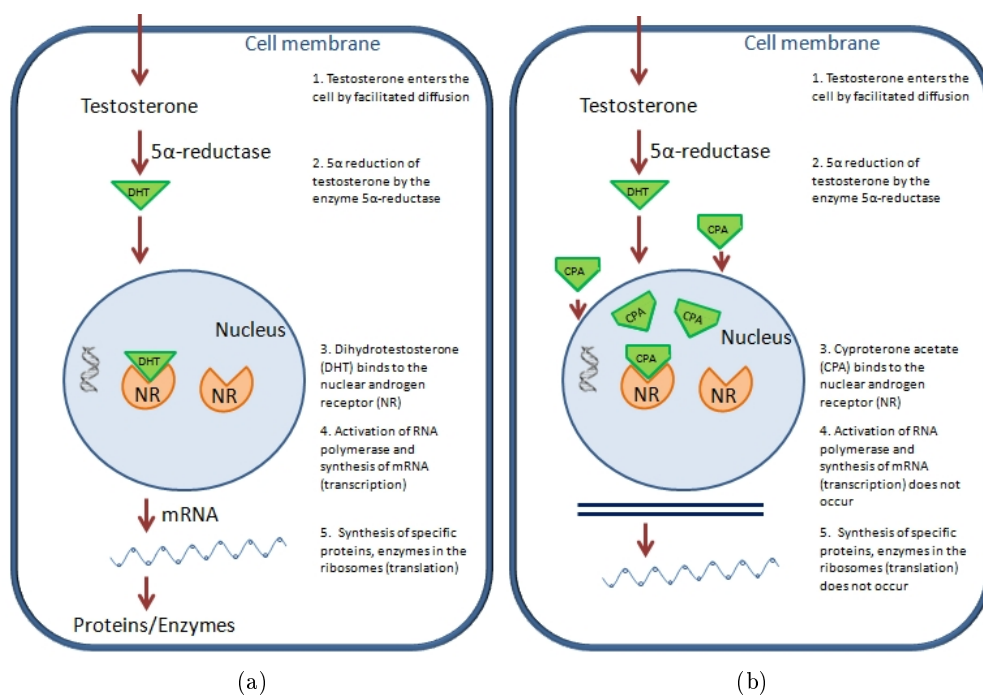


Figure 38: Molecular mechanism of action of (a) androgens and (b) CPA. Figure issued from [3].

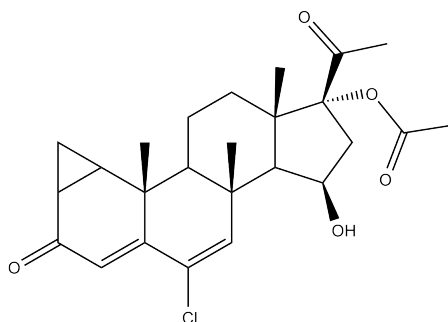


Figure 39: Chemical structure of 15 β -hydroxycyproterone acetate.

1.2 Monitoring CPA

When CPA is prescribed for patients with a prostate cancer, tight monitoring enables the continuous delivery of the appropriate quantity of the drug, which in turn reduces side effects. Moreover, in particular concerning the elderly, any omission of the drug could be detected. Similarly, when prescribed for people with paraphilia, appropriate administration of the medication has to be assured.

Today the standard methods of cyproterone acetate detection and quantification are either by HPLC or by radioimmunoassay [5], [9]. Its detection by a simple colorimetric sensor could be of interest for the reasons mentioned above. Since detection is also possible in sweat or saliva, the use of a sensor would be easy, comfortable and non invasive.

2 Elaboration of MIPs formulations for cyproterone acetate

To elaborate a sensor for cyproterone acetate, we decided to develop a sensing layer with a molecularly imprinted polymer. This section is thus dedicated to the development, the study and the characterization of formulations for cyproterone acetate MIPs.

2.1 Development of a preliminary MIP for cyproterone acetate

To the best of our knowledge, cyproterone acetate has never been imprinted in a polymer. This analyte belongs to the family of steroids, however, even if several steroids were imprinted successfully in polymers, each molecule of this compounds family has its own hydrophilic properties. Since the intrinsic chemical properties of the template largely influence the best polymer formulation, no trial for the transposition of literature’s formulations was led in the work presented below.

First MIPs formulations are summarized in table 6 and protocols are given in appendix B. Non imprinted polymers (NIPs) are not included in the table, but they were prepared exactly as the corresponding MIPs without the template. For M_{cpa1} to M_{cpa5} , the same monomers were kept, with the same molar ratios and the only variable parameter was the solvent. Formulations from M_{cpa6} to M_{cpa9} are trials of optimization.

Polymer	Template	Functional monomer	Cross-linker	Molar ratio ^a	Initiator ^b	Solvent	Polymerization conditions
M _{cpa1}	CPA 0.2 mmol	MAA	EDMA	1/8/25	ABDV 0.2 mol%	Chloroform 1.5 mL	45 °C overnight
M _{cpa2}	CPA 0.2 mmol	MAA	EDMA	1/8/25	ABDV 0.2 mol%	Acetonitrile 1.5 mL	45 °C overnight
M _{cpa3}	CPA 0.2 mmol	MAA	EDMA	1/8/25	ABDV 0.2 mol%	Tetrahydrofuran 1.5 mL	45 °C overnight
M _{cpa4}	CPA 0.2 mmol	MAA	EDMA	1/8/25	ABDV 0.2 mol%	Methanol/Water 4/1 1.5 mL	45 °C overnight
M _{cpa5}	CPA 0.2 mmol	MAA	EDMA	1/8/25	ABDV 0.2 mol%	Toluene 1.5 mL	45 °C overnight
M _{cpa6}	CPA 0.2 mmol	TFMAA	EDMA	1/8/25	AIBN 0.2 mol%	Acetonitrile 1.5 mL	45 °C overnight
M _{cpa7}	CPA 0.2 mmol	MAA	DVB	1/8/25	ABDV 0.2 mol%	Toluene 1.5 mL	45 °C overnight
M _{cpa8}	CPA 0.2 mmol	TFMAA	EDMA	1/8/25	ABDV 0.2 mol%	Toluene 1.5 mL	45 °C overnight
M _{cpa9}	CPA 0.2 mmol	TFMAA	DVB	1/8/25	ABDV 0.2 mol%	Toluene 1.5 mL	45 °C overnight

^a molar ratio of template/functional monomer/cross-linker

^b concentration expressed in molar percentage compared to the polymerizable groups

Table 6: Formulations used to obtain CPA imprinted polymers.

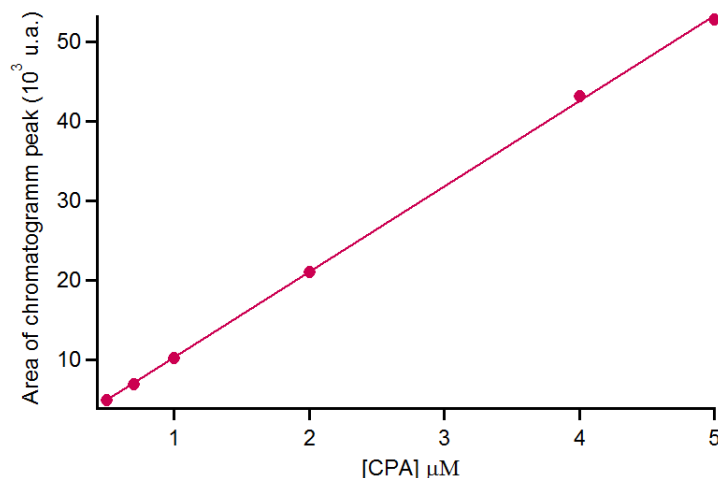


Figure 40: Calibration curve for CPA dosage by HPLC. $R^2 > 0.99$.

After polymerization, all polymers were white bulk monoliths. In order to evaluate their binding properties, an HPLC method to measure CPA concentration in solutions was established (see appendix C for method). The concentration of CPA in solution was determined by measuring the area of the chromatographic peak. Thus, a linear calibration curve was obtained for concentrations from 0.5 to 100 μM (the range 0.5-5 μM is represented in figure 40). This dosage was performed in acetonitrile and was still valuable for ethanol, ethyl acetate, water or a mixture of them. For chloroform, tetrahydrofuran and toluene, the direct quantification by HPLC was not possible. Therefore, a defined volume of sample in these solvents was transferred to a test tube and the solvent evaporated in a centrifuge under vacuum. The same volume of acetonitrile was then added followed by vigorous agitation to dissolve the CPA, and quantification by HPLC was performed. The results were coherent and a linear calibration curve was obtained.

After grinding and washing of the polymers, binding assays were performed with a growing concentration of polymer and a constant concentration of CPA (5 μM). This is the lowest concentration possible for the binding, since 0.5 μM is close to the limit of detection of CPA by HPLC and, with this value, we are close to the range of potential concentrations to be measured by a sensor (CPA concentration in blood plasma is around 100-900 nM).

First binding assays evidenced an issue of CPA leaching from the MIPs. Indeed, after the washing steps (described in appendix B), the supernatants displayed higher concentrations of CPA than the initial 5 μM . This results in binding isotherms with absurd negative quantity of CPA retained by the MIP (figure 41a). This is not visible if the binding test is performed with higher concentrations (figure 41b), although this is not practical since the detection limit would be too high. However, an increase in the number of washing steps seemed to solve the problem, even if some loss of polymer occurred.

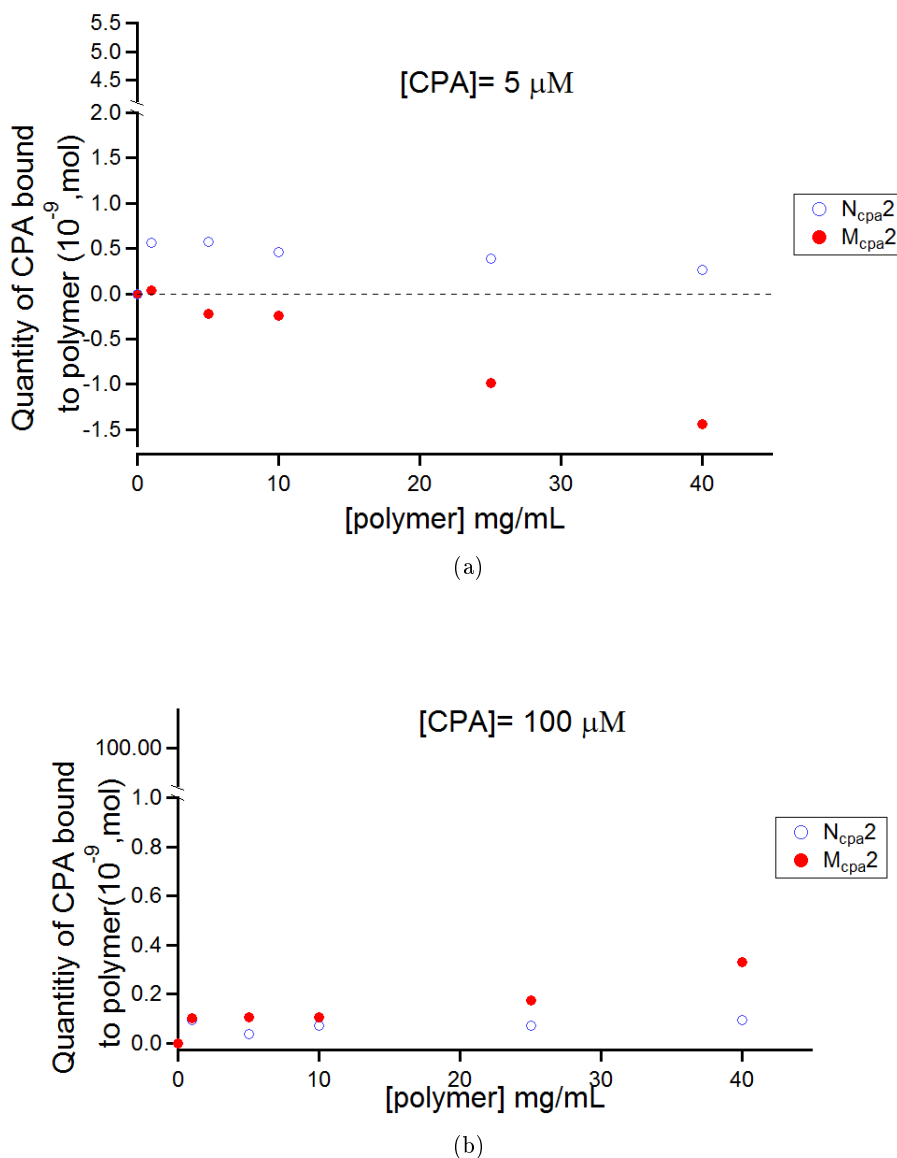


Figure 41: Binding assay of CPA in acetonitrile to M_{cpa2} , N_{cpa2} . (a) $[CPA]=5 \mu M$ and (b) $[CPA]=100 \mu M$.

Binding of CPA was studied ($[CPA]=5 \mu M$), in their solvent of synthesis. No difference of molecular uptake was observed between NIPs and MIPs for M_{cpa1} to M_{cpa4} . M_{cpa6} did not show any binding ability, despite the use of a monomer reputed to be a strong hydrogen bond donor. Imprinting seems to be possible in toluene, however. Indeed, M_{cpa5} bound more CPA than its non imprinted control N_{cpa5} , as represented in figure 42. The MIP K_{50} is about 3.6 mg/mL and for a polymer concentration of 40 mg/mL, $IF = 1.7$.

Thus, toluene seems to enhance imprinting and the recognition of CPA by the polymer. This binding ability was further investigated with the use of trifluoromethylacrylic acid (TFMAA) in M_{cpa8} , since TFMAA is a functional monomer more acid than MAA thanks to the electronegative

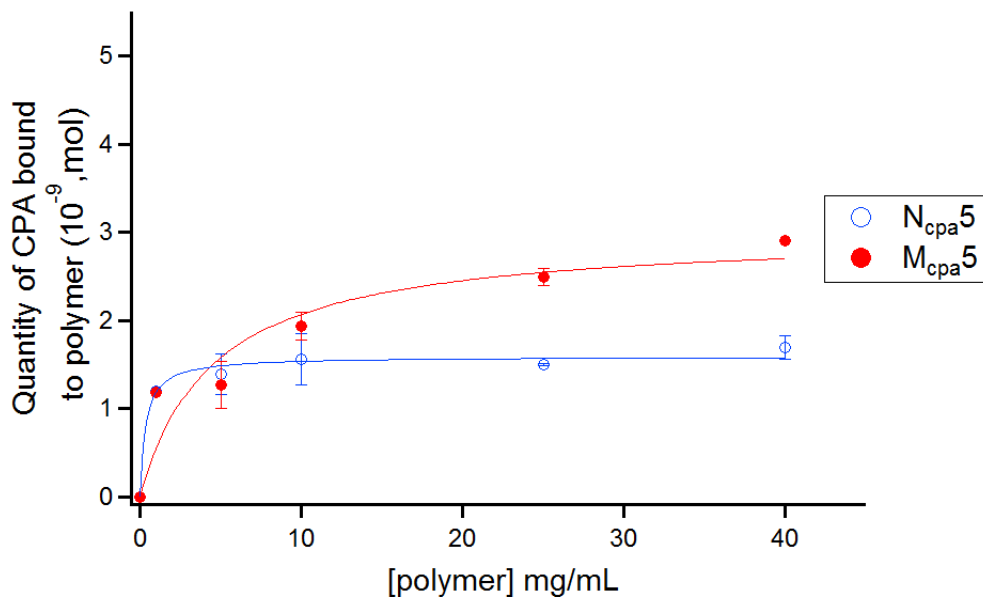


Figure 42: Binding assay of CPA (initial concentration of 5 μ M) in toluene to M_{cpa5} , N_{cpa5} . Error bars represent the standard deviation of two measurements for each of two different samples.

fluorine atoms. Moreover, the cross-linker influence was also evaluated with the replacement of EDMA by divinylbenzene (DVB) in M_{cpa7} . Finally a polymer was also synthesized with both TFMAA and DVB and led to M_{cpa8} . The binding tests of these polymers in toluene are represented in figure 43 and their binding parameters are summarized in table 7.

Polymer	K_{50} (mg/mL)	B_{max} (nmol)	IF
M_{cpa5}	3.6	2.7	1.7
M_{cpa7}	6.2	4.2	2.1
M_{cpa8}	5.4	4.7	1.5
M_{cpa9}	2.2	4.3	1.3

Table 7: Binding parameters recorded for polymers imprinted and evaluated in toluene.

From this study of polymers imprinted in toluene, several tendencies can be distinguished. First, the cross-linker DVB leads to a higher B_{max} than EDMA with MAA. Then, TFMAA generates more unspecific adsorption than MAA (the NIP binds more than 3.1 nmol CPA). The combination of MAA and EDMA (M_{cpa5}) leads to the smallest B_{max} whereas the other MIP formulations bound more than 4 nmol of CPA. So, either TFMAA or DVB are required for a high B_{max} but TFMAA leads to more unspecific adsorption. DVB is a hydrophobic monomer that leads to a polymer more hydrophobic than polymers based on EDMA. CPA may present more affinity for hydrophobic polymers and may enter easily the imprinted cavities. This is confirmed by CPA high solubility in

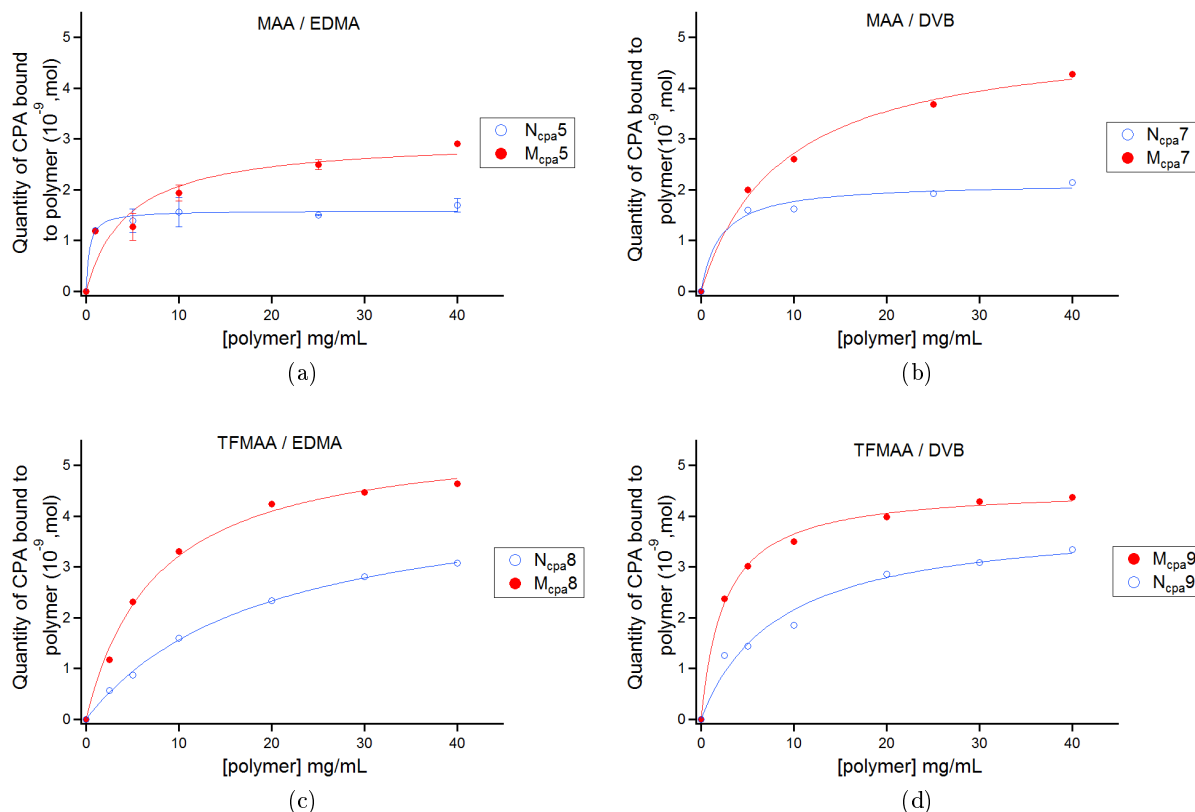


Figure 43: Binding assay of CPA, with $[CPA]=5 \mu M$, in toluene, to (a) M_{cpa5} , N_{cpa5} , (b) M_{cpa7} , N_{cpa7} , (c) M_{cpa8} , N_{cpa8} and (d) M_{cpa9} , N_{cpa9} .

toluene (much higher than in methanol or water). Moreover, the formation of a complex between the functional monomer and CPA probably relies on hydrogen bonding. That's why the use of TFMAA enhances the complex formation thanks to its strong acidity and leads to a good capacity of the MIP. Finally, M_{cpa7} is a good formulation that displays both a high quantity of CPA bound to the polymer and the highest imprinting factor, although its K_{50} is higher than for the other polymers, indicating a somewhat lower affinity. In the next section, spectroscopic measurements are used to confirm the formation of a complex between CPA and an acidic functional monomer, leading thus to the observed imprint in the polymer.

2.2 NMR study

The aim of this section is to prove the formation of a complex between methacrylic acid and cyproterone acetate in the solvent used for polymerization (toluene) thanks to NMR studies associated to a Job's plot.

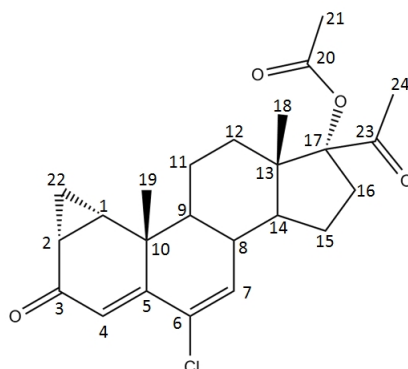


Figure 44: Chemical structure of cyproterone acetate with numbered carbon atoms.

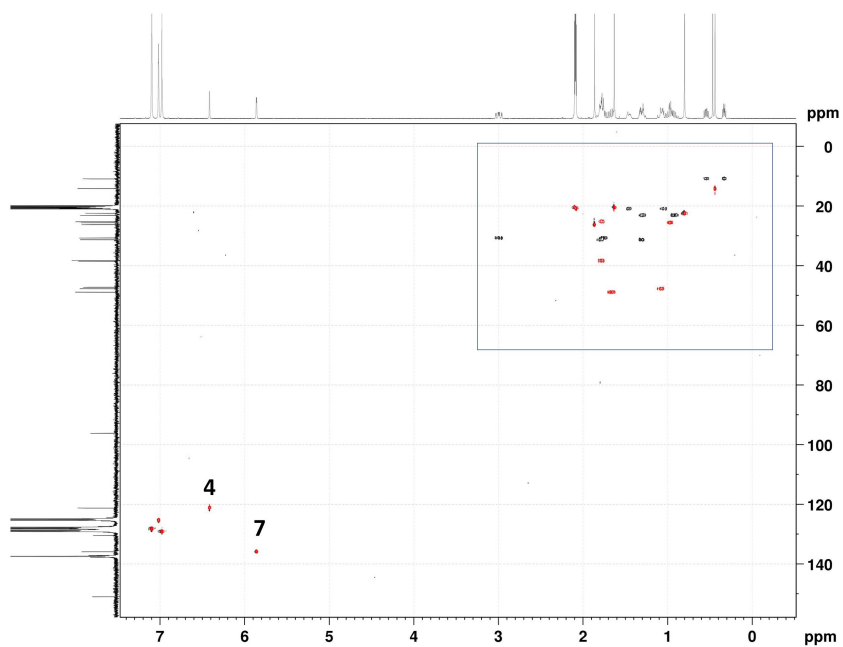
2.2.1 Structure of cyproterone acetate

Cyproterone acetate has a tetracyclic hydrocarbon skeleton and thus, its NMR spectrum is very dense in the chemical shift's interval 0-2 ppm. In order to assign the NMR peaks to the protons, HSQC (Heteronuclear Single Quantum Correlation) was used. This technique relies on a two dimensional NMR spectrum with an axis for the proton and a second axis for a heteronucleus, generally the carbon atom nucleus. The obtained spectrum has a signal for each proton bound to the considered carbon. The HSQC spectrum of cyproterone acetate is given in figure 45. It allowed the determination of the protons peaks for CPA, numbered according to their carbon, as presented in figure 44. This assignment of each peak to its proton(s) is fundamental for the interpretation of the Job's plot performed in the next paragraph.

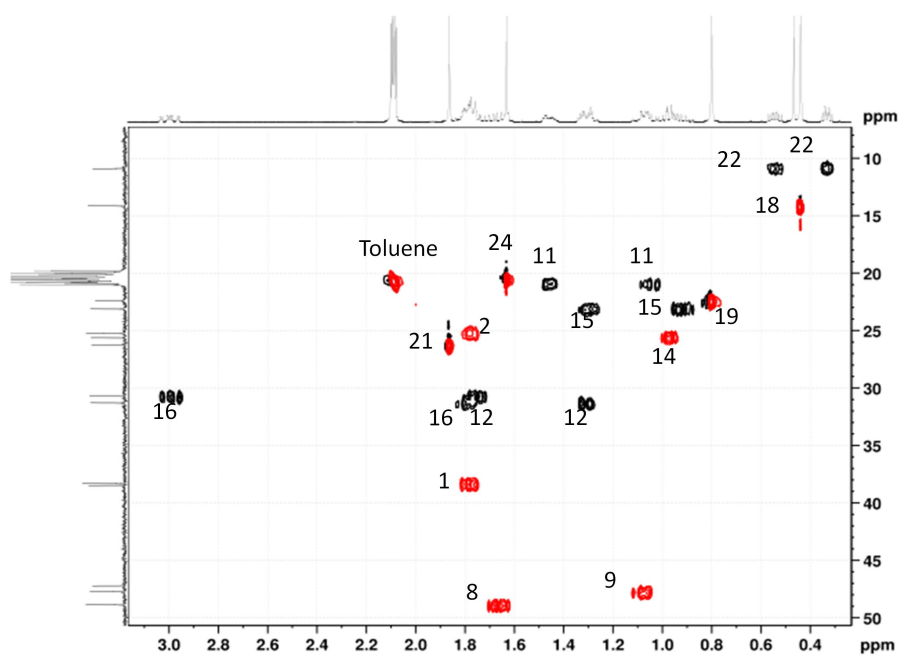
2.2.2 Job's plot

NMR is a technique that enables the study of interactions in liquid phase and thus, the formation of a complex. Indeed, the protons chemical shift depends on the environment of the studied molecule. In case of hydrogen bonding for example, the screening constant of a hydrogen nucleus changes and this leads to additionnal shielding. As the chemical shift of the chosen proton changes, we can correlate it to the initial mole fraction of the reactants. The Job's plot [10], also called method of continuous variations, expresses this correlation and allows determining the stoichiometry of the complex.

The formation of the complex occurs according to the reaction described by equation 2.1. The association constant, K , of the complex gives a correlation between the concentration of the complex at equilibrium and mole fractions of free species. Job showed that when a physical property is linear with the concentration of species, then the evolution of this property from the reference is an



(a)



(b)

Figure 45: NMR HSQC for cyproterone acetate. Red dots represent CH and CH₃, black dots represent CH₂.

extremum at a stoichiometric mixture.



Equation 2.2 gives the relation between the chemical shifts difference Δ ($= \delta_{obs} - \delta_T$ difference between the chemical shifts observed and pure template) and v the molar ratio of CPA in solution when the concentrations of monomer and template in stock solutions are identical (calculations are detailed in appendix D). Note that this equation of the Job's plot is verified if the system is in a fast exchange (no distinction of peaks between the complex and the free molecule), if there is only one complex formed (no other competition) and if there is no chemical reaction between the species.

$$\Delta v = \frac{\Delta^0}{C_{tot}} K (C_T^i v - C_{TM_n}) ((1 - v)C_T^i - nC_{TM_n})^n \quad (2.2)$$

where: Δ is the difference between the chemical shifts observed and the pure template, Δ^0 is the difference between the chemical shifts of the pure complex and the pure template, $v = \chi_T$ the mole fraction of template in solution, K is the association constant, C_{tot} the total concentration of species in solution, C_T^i is the concentration of template in stock solution, C_{TM_n} the equilibrium concentration of the complex.

To trace the Job's plot, stock solutions of CPA and methacrylic acid were prepared in deuterated-toluene, at a concentration of 10 mM. Then, different mole fractions of template and monomer were mixed with fixed final concentration and volume (respectively 1 mM and 700 μ L). For each mole fraction, the chemical shift of chosen protons was monitored. Figure 46 represents the NMR spectrum of CPA and the spectrum of an equimolar mixture of CPA and MAA. We can see that, if a complex is obtained, its peaks and free species peaks are not distinguishable, which means that we have a system in fast exchange and, so, we can trace the Job's plot.

The study was focused on four protons, H4, H7, H24 and H21, all close to groups expected to form hydrogen bonding with MAA. Their signals are fortunately distinguishable on the NMR spectrum. Spectra were obtained at room temperature. Superposition of spectra from 0 to 1 in CPA molar ratio (and thus 1 to 0 in MAA) and zoom in the area of H4, H24 and H7 protons signals are represented in figure 47.

No chemical shift was observed for H21. However, the Job's plot for H4, H7 and H24 are represented in figure 48. The graphs are fitted by equation 2.2 and gives $n_{H4} = 0.75$, $n_{H7} = 1$ and $n_{H24} = 1$. Despite this evaluation of n , we prefer not to make any assumption on the complex stoichiometry since several complexes could occur and this would be out of the Job's area. Nevertheless, the expected shape of the Job's plot was observed and fitted, which confirms the formation of a complex between CPA and MAA in toluene.

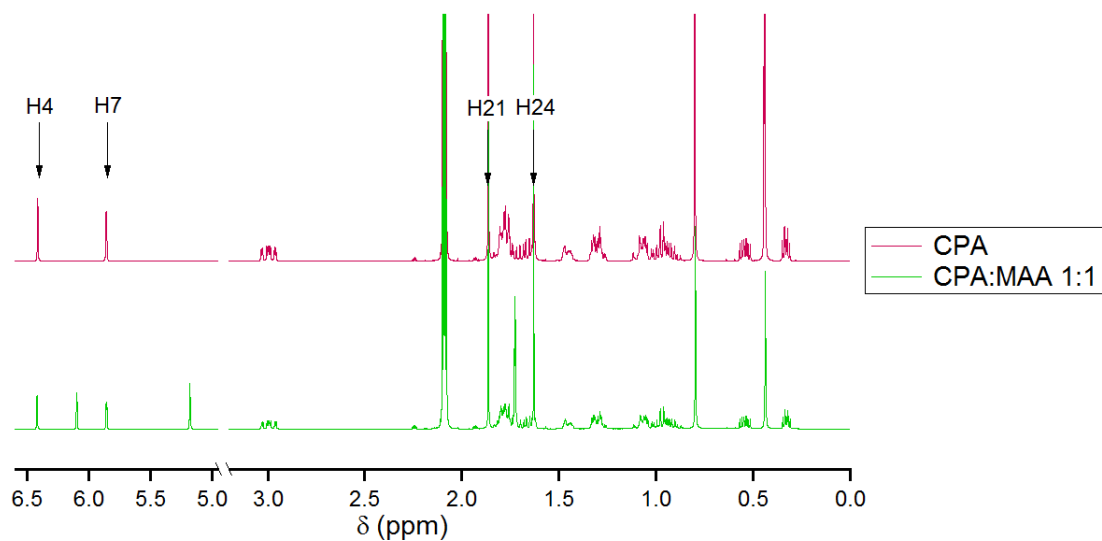


Figure 46: NMR spectra of CPA in toluene- d_8 and a mixture of CPA and MAA, with $\chi_{cpa} = 0.5$. Chemical shifts of the interest protons are pointed out and identified with the number of the supportive carbon.

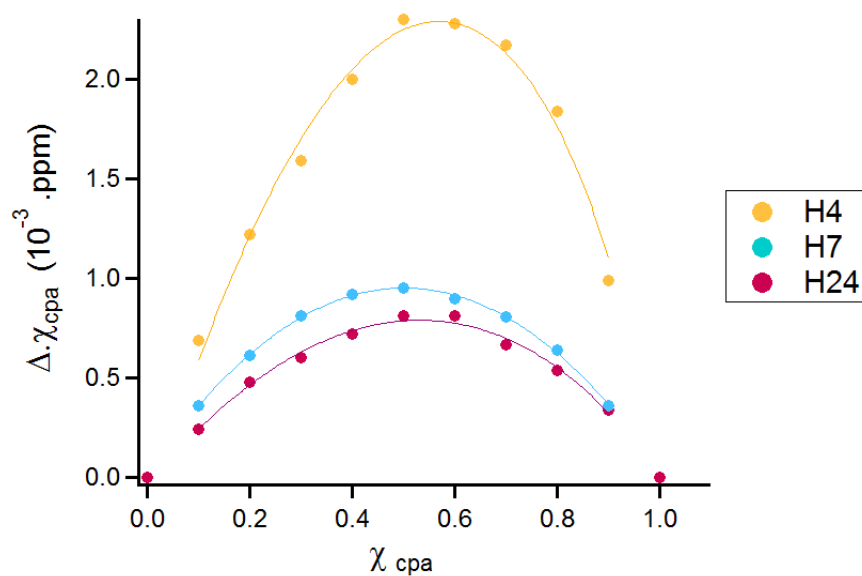


Figure 48: Representative Job's plot for the interaction between H4-, H7- and H24-CPA and MAA in toluene.

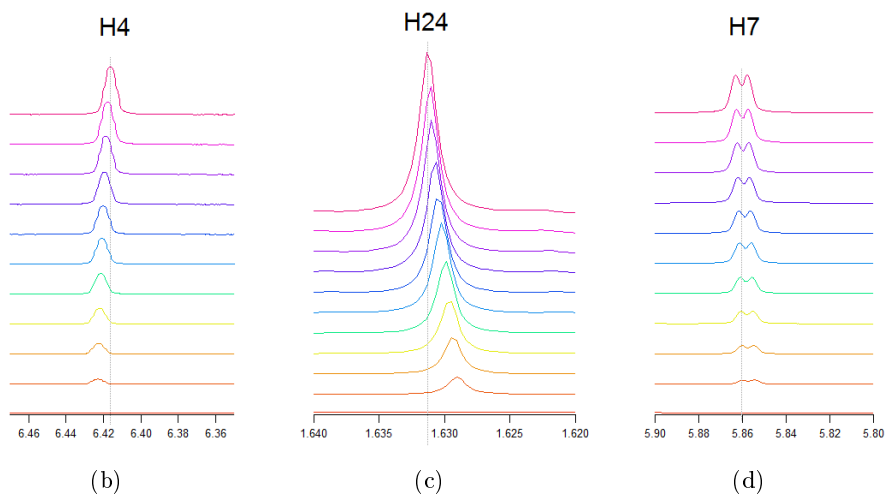
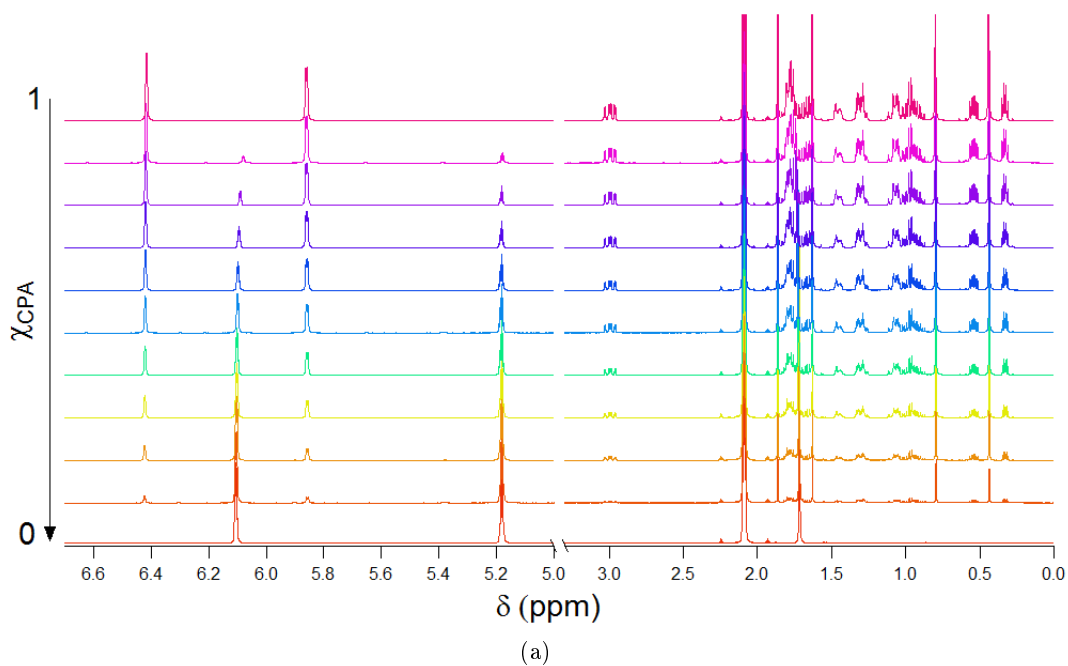


Figure 47: Superposition of NMR spectra with different ratio of CPA/MAA. (a) complete spectra, (b) zoom on H4 signal, (c) zoom on H24 signal and (d) zoom on H7 signal.

2.3 Conclusion

A first MIP was imprinted against CPA in toluene, thanks to an acidic monomer and a hydrophobic cross-linker. The subsequent study of some CPA protons showed that some groups of this steroid interact with MAA in toluene. No deep investigation was led to determine the stoichiometry of the complex as the validity barriers set by the Job's equation are very thin and it is difficult to know if all the hypotheses are still respected. The interactions analyte/monomer, rarely investigated in liquids in the literature, were proved in this study. The imprinting of CPA in toluene with MAA is thus fostered by interactions and the formation of a complex prior to polymerization.

3 Optimization of cypoterone acetate imprinting by experimental design

As described in the previous part, a first MIP was elaborated for CPA and involved interactions studied by NMR spectroscopy. This was used as a starting point in this part to improve the MIPs formulations and to study the formulations with a theoretical approach. To evaluate the influence of several factors and their interdependence, we used a design of experiments. We will first introduce this approach, display its results and finish with a critical review of the study.

3.1 Design of experiments

During the development of a product, numerous phenomena interfere and influence the result(s). In order to predict the result(s) and limit the influence of external parameters, models and software simulations are proposed. The study of all the external parameters and their interactions is often long and expensive. Furthermore, it does not take into account the interferences between parameters. Thus, designs of experiments (DOEs) are statistical approaches that consist in selecting and classifying assays to identify, with a limited cost, the effects of parameters on the result(s). The variables of interest in a DOE are represented in figure 49.

The first step is the identification of the parameters influencing the system, called input factors. They are parameters which can be controlled during experiments. Next, the values for the input parameters should be set, with either a continuous variation (interval) or a discrete variation (a finite number of possibilities). Values attributed to the factors are called levels. A successful DOE requires knowledge of the factors, the ranges of the factors and the appropriate levels to use. A bad evaluation of the factors may completely devalue the usefulness of the DOE.

The output responses are the values measured during the experiments. The responses are then modeled: their values are predicted by a model which is a function of the input parameters (equation 3.1, where n is the number of input factors), the noise and the effect of time are not taken

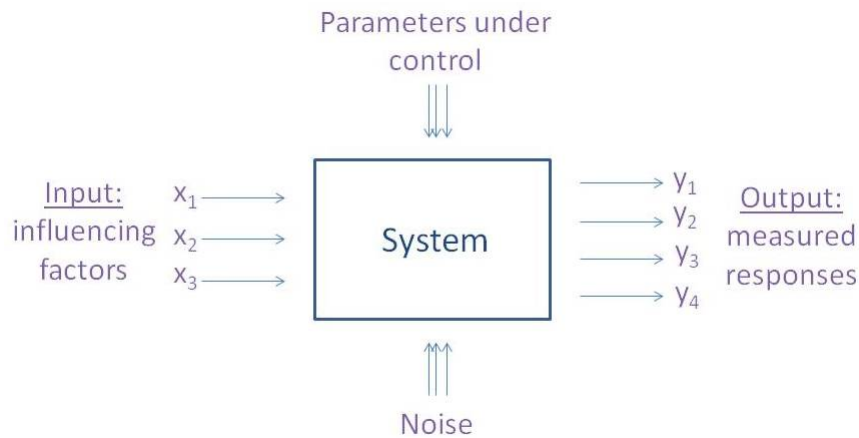


Figure 49: Block diagram representating a design of experiments. Influencing variables are input and responses are output. Some controllable parameters (such as experiment temperature) and uncontrollable parameters (such as climatic conditions) are also inputs. x_i are the inputs of the design and y_j the output responses.

into account.

$$y_j = f(x_1, x_2, \dots, x_n) \quad (3.1)$$

The choice of the response model is the postulate of a function f whose coefficients are identified by the experiments. The simplest models are affine models without or with interactions (equation 3.2 and equation 3.3). Without interactions, the model is very simple but in most cases insufficient because factors often act with an interdependence on the other factors. The interdependence of factors can be expressed by second order terms. It is also possible to use other functions, such as a quadratic one.

$$y_j = \beta_{j0} + \sum_{i=1}^n \beta_{ji} x_i \quad (3.2)$$

$$y_j = \beta_{j0} + \sum_{i=1}^n \beta_{ji} x_i + \sum_{i=1}^{n-1} \sum_{k=i+1}^n \beta_{jik} x_i x_k \quad (3.3)$$

Finally, to identify the model coefficients, a number of assays have to be performed. The assays should be designed in order to be efficient (minimizing the number of assays) and robust (minimizing the impact of measurement and modelization errors). This is the role of experimental designs.

Full factorial designs test all the possible combinations of all input factors. They provide a complete information but require numerous assays. That's why fractional designs, which select several combinations, are preferred. Since they lower the numbers of assays, they also reduce the resulting information and the choice of the design should thus be wise enough to identify the model

coefficients. Numerous designs are described, the most famous are the Taguchi tables. They were created by Taguchi in order to reduce the noise and the measurement errors (instead of trying to eliminate them). The tables are listed and precise the models that they can complete. Optimal designs determine the number of assays n from the number of factors levels and their interactions. A calculation finds the n assays necessary to get the most information. The design of experiments led in the next sections was based on an optimal design.

Once all the assays are performed, the obtained model can be used to simulate the results and thus be used to validate or conceive a response. The analysis of the data is often performed thanks to statistical tools, such as regression analysis and analysis of variance (ANOVA). Then, practical conclusions can be drawn and graphical methods are often useful to present the results. For example, the graph of the values predicted for a response against the actual values should follow the line $y = x$ (figure 50), this would evidence the model ability to predict the response.

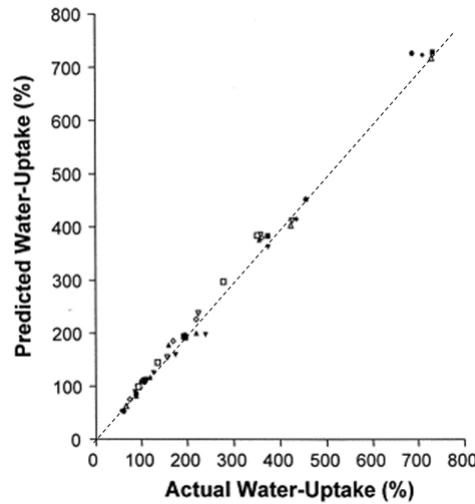


Figure 50: Comparison of actual versus predicted response -water uptake by a polymeric matrix-, the plot shows that the model accurately predicted the response [11].

The objectives of the conception may be an optimization of a performance or a multi-objectives optimization (compromises between robustness and performances). The multi-objectives optimization aims at improving a set of goals concurrently and gives several efficient solutions, based on the model developed by the DOE. Such optimizations will only be used in chapter III.

3.2 Approach and choice of the input factors

Very few papers were published with MIPs optimization by DOEs, although this seems to be a field to explore as the potential of the method is very high, in particular for the often complex conditions and requirements in MIP development. In this thesis, our objective was to develop a sensor for CPA

in a physiological fluid. Thus, it was of high interest to detect the analyte in an aqueous medium and with high selectivity and specificity. After the first synthesis of a MIP imprinted by CPA, we decided to work with an experimental design so as to study the influence of numerous factors on MIPs characteristics and to optimize the formulations.

Due to these very challenging objectives, no influencing parameters should be neglected. Thus, inputs were chosen as continuous, discrete, chemical and physical parameters. The selected parameters and their levels of variation are summarized in table 8.

Solvent	Toluene Ethanol Acetonitrile Ethyl acetate Ethanol/water 4/1 Acetonitrile/water 4/1
Solvent volume	1-5 mL
Polymerization temperature	40-70 °C
Functional monomer	MAA TFMAA BMA (Benzylmethacrylate) MAA/HEMA 1/1
Molar ratio of functional monomer^a	2-12
Cross-linker	EDMA DVB MbAAm
Molar ratio of cross-linker^b	10-50

^a molar ratio of functional monomer compared to template

^b molar ratio of cross-linker compared to template

Table 8: Input parameters, and their levels, evaluated in the CPA-design of experiments.

The solvents were chosen because they solubilize CPA. One solvent is apolar (toluene), two are polar aprotic (acetonitrile and ethyl acetate) and two others are polar protic (ethanol and water).

Thus, the study of imprinting in these solvents would allow an evaluation of the influence of the polarity and the ability to make hydrogen-bonding. Water was used in mixture with other solvents since pure water does not dissolve CPA. The volume of solvents varied between 1 and 5 mL to solubilize the species and influence the porosity of the bulk polymers. Indeed, the volume of solvent directly influences the volume of pores and the structure of the polymer.

The functional monomers were acidic or hydrophobic monomers since these properties seemed interesting in the first MIPs formulations. MAA and TFMAA present a difference in acidity, BMA possesses a phenyl group able to form hydrophobic interactions and the hydrophilic monomer HEMA, mixed with MAA, could bring the ability to a polymer to swell which is interesting for the development of the sensor.

The cross-linkers were chosen as bifunctional, a classic choice for MIPs and which gives polymers less rigid than trifunctional monomers. DVB was used to provide a hydrophobic alternative to EDMA, while MbAAM leads to an acrylamide skeleton of the polymer, and the network of the chains with an intermediate polarity and hydrophilicity is able to swell in polar solvents.

Molar ratios of functional monomers and cross-linkers were varied in ranges common for molecular imprinting [12].

Finally, the temperature of polymerization varied from 40 to 70 °C, an interval to observe the influence of the temperature on the quality and efficiency of imprinting.

The formulations of polymers were calculated with the approach of optimal designs (taking into account all the second-order interactions) and the 110 formulations are given in appendix E.

3.3 Laboratory implementation

The first step consisted in synthesizing all the polymers. For each polymer, CPA was used (except for the NIPs), and the initiator was AIBN. Polymers were synthesized in glass flasks of 4 or 10 mL according to the final volume and polymerized at the chosen temperature in a graphite bath, for 20 hours. When a polymer had not polymerized, a second trial was done and in case of two failures of polymerization, the formulation was abandoned.

Once synthesized, the polymers were manually and mechanically ground. Fifteen successive washing steps were applied to the polymers in the following conditions: five washings with acetonitrile/acetic acid 4/1 (v/v), five washings with acetonitrile/acetic acid 9/1 (v/v) and five washings with acetonitrile. Washed polymers were then dried under vacuum and stored at ambient temperature under normal atmosphere.

Binding tests were performed with 5 and 20 mg/mL of polymer in their solvent of synthesis and with $[CPA] = 5 \mu\text{M}$. The first binding assays displayed a problem of template leaching. Increasing the number of washing steps seemed difficult since the number of washing tubes (centrifuge tubes)

and the number of places on the rotation wheel was limited and thus it would have been terribly time-consuming. On the other hand, we did not want either to rise the CPA concentration to keep close to the sensor application.

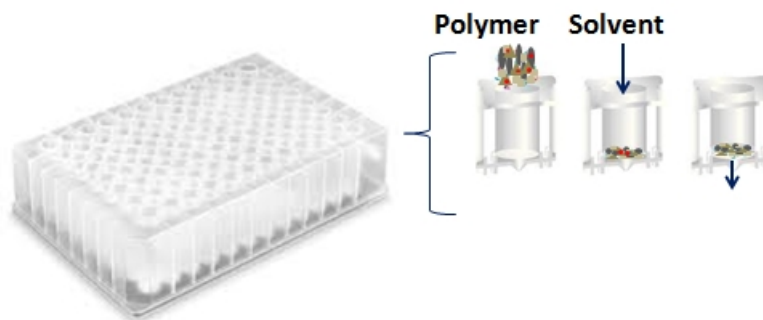


Figure 51: Washing steps of the polymer performed in a 96-well filtration plate.

Confronted to this issue, we considered the possibility to change the protocols. Polymers were all synthesized, so we looked for an opportunity to improve the washing stages. Indeed, we decided to use 96-well filtration plates (figure 51). The wells volume was 2 mL and the filtrating membrane was in teflon ($0.2\ \mu\text{m}$ of mesh). Around 50 mg of polymer were suspended in solvent and deposited in a well. When the 96 wells of the plate were filled, the vacuum manifold was turned on and solvent filtrated off. Subsequent washing steps could be applied to all wells simultaneously. With this technique, the centrifugation time was gained and all the polymers were washed in parallel which reduced considerably the duration of the washings. After dozens of washing steps (40-60), the polymers were recovered in suspension and centrifuged. The supernatants were studied by HPLC to evaluate potential leaching of CPA. If needed, several washings were again performed. Finally, the few milligrams left were weighed and used for binding assays. Unfortunately, for some polymers, it appeared that CPA was really difficult to extract from the MIPs and, for some other polymers, quantities of materials left in the well were not sufficient to perform the binding assay. Thus, for some formulations, we did not achieve to perform the binding tests and get the expected response for the DOE.

3.4 Results

The evaluation of the polymers imprinting was performed *via* binding assays of 5 and 20 mg/mL of polymer, in presence of $5\ \mu\text{M}$ CPA. Thus, the DOE responses were the quantities of CPA bound to the NIP and MIP for 5 and 20 mg/mL : $B_{5,NIP}$, $B_{5,MIP}$, $B_{20,NIP}$ and $B_{20,MIP}$. All values $B_{5,NIP}$ and $B_{20,NIP}$ (for polymers successfully polymerized) were completed in the design. We assumed that if the model displayed any tendencies for the NIP, it would be interesting since the affinity for the

template between NIP and MIP is correlated. Concerning the missing responses, they would affect the robustness of the model but even before the software calculations, we knew that a larger issue was facing us. Indeed, the binding ability of the polymers were extremely low (less than 1 nmol), except for a few formulations (figure 52). For example, in ethanol/water 4/1 a few polymers bound more than 1 nmol of CPA but no imprinting was observed. Toluene is the only solvent in which the polymers display an affinity for CPA.

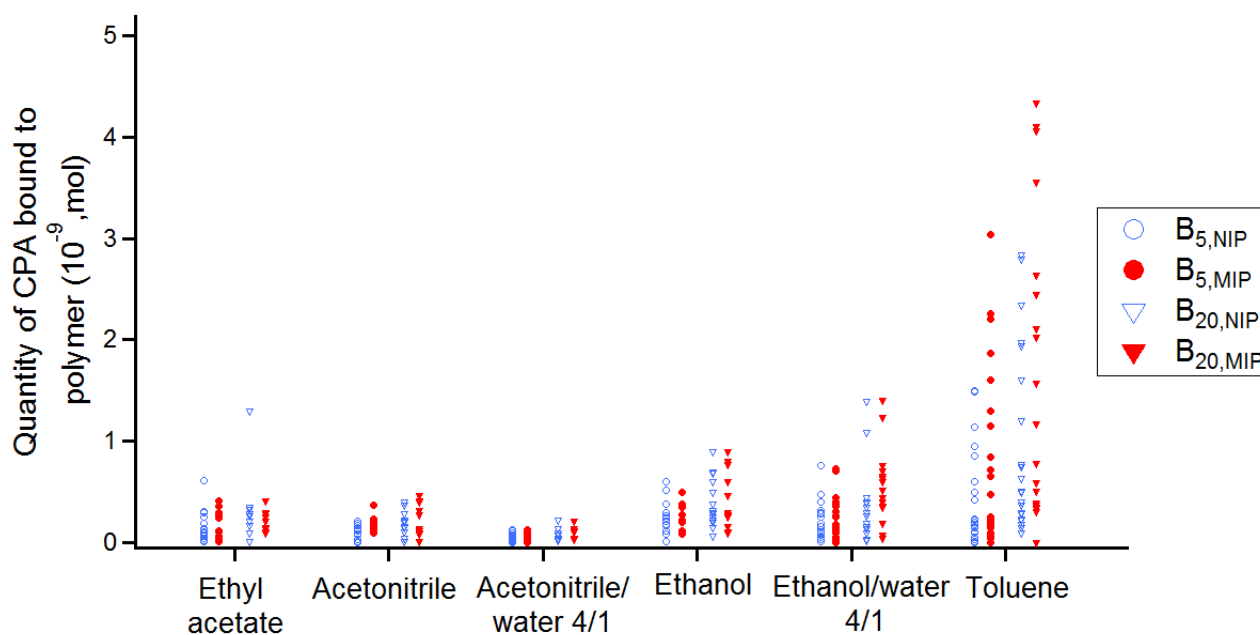


Figure 52: Responses of the DOE -quantity of CPA bound to 5 or 20 mg/mL of polymers- plotted according to the solvent used. In toluene, much more CPA is bound to the polymers than in any other solvent.

The model used to analyze the results of the DOE was quadratic, all interactions of second order were taken into account in the calculation. The results of the model can be evaluated by the graph of predicted responses against obtained responses (figure 53, R^2 is the correlation coefficient and should tend towards 1). Coefficients of correlation for the plots are really under the expected values. Indeed, the model does not fit the high values measured for the binding affinity. These values of the DOE are indeed rare and thus difficult to modelize whereas these responses are the only values of interest. The graphs display what is called a "significant lack-of-fit" and this indicates that this model cannot be used.

However, the results underline obviously the role of the solvent with a significant coefficient value for toluene. A small positive effect is also displayed by the functional monomer TFMAA. The tendencies of the model are thin since five out of six synthesis solvents resulted in barely any affinity for the template and thus the responses are lost in the noise. Factors would be more significant if

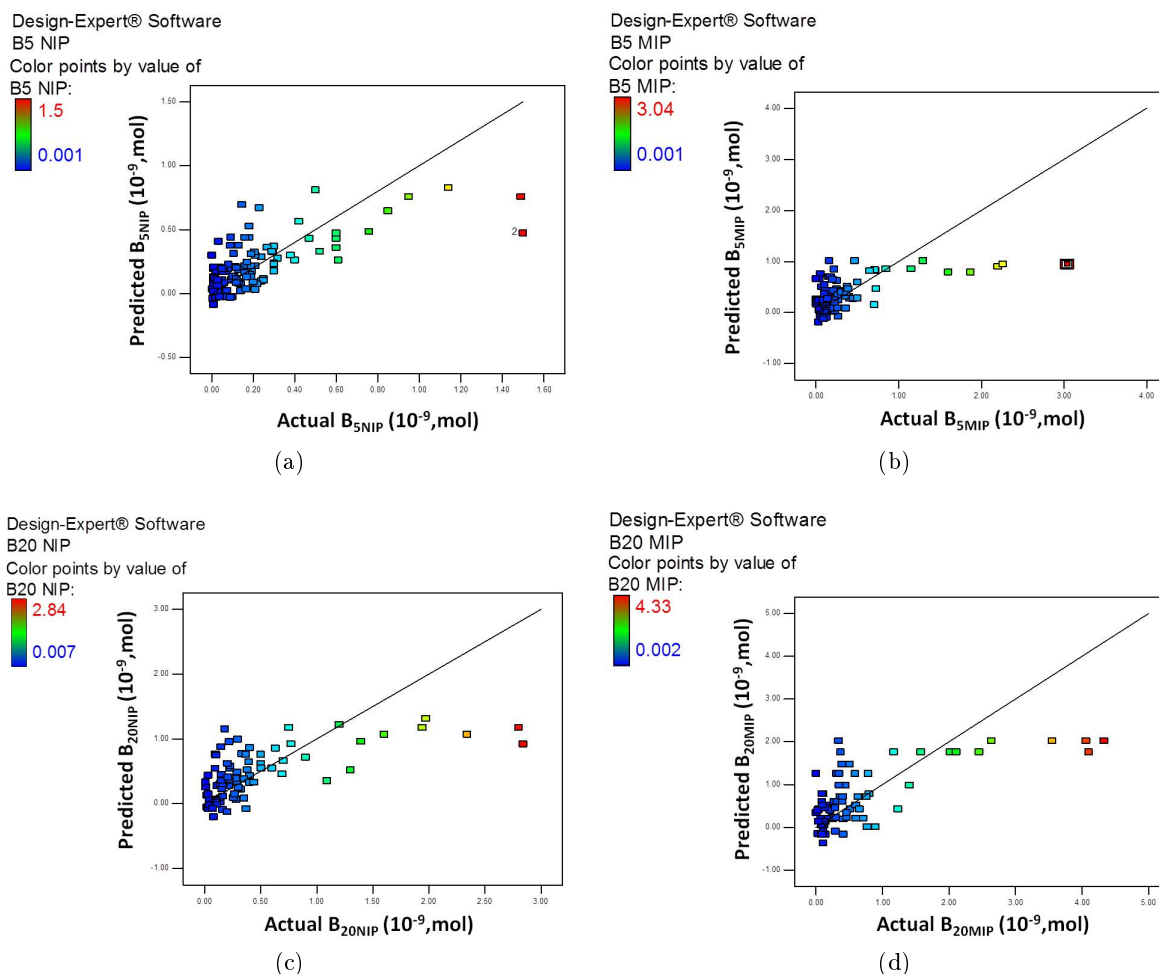


Figure 53: Results predicted by the model against results obtained for the responses: (a) $B_{5,NIP}$ $R^2=0.43$ (b) $B_{5,MIP}$ $R^2=0.35$ (c) $B_{20,NIP}$ $R^2=0.40$ and (d) $B_{20,MIP}$ $R^2=0.47$.

the study was led in toluene only but the results are too scarce in toluene to apply a model for this solvent only.

3.5 Critical review and conclusion

The use of an experimental design for the optimization of CPA MIPs was not successful. Several issues, combined together, led to the model not yielding reliable tendencies. This design was elaborated at the beginning of the thesis, and thus, it is easier today to underline the mistakes that were made.

The objectives of the DOE were : a MIPs theoretical approach for a formulation's optimization and the search for a formulation working in aqueous media. This led to a significant set of experiments.

Concerning the choice of several solvents which resulted in no imprinting effect (in fact, all solvents except toluene) before the DOE, we ran the risk of integrating them in order to find if a formulation could be efficient in aqueous media. However, this generated a high number of experiments and many of them led to insignificant results. Then, this number of polymers in the DOE combined to the required washing steps was clearly an obstacle and increased the time required for the experiments. As Mettas and Guo wrote "it is usually a major mistake to design a single, large, comprehensive experiment at the start of a study" [13]. That's why the experiments should be led sequentially.

If we had to do this work again, we may separate the DOE into different blocks, according to the solvent. Thus, we would lead a complete study in toluene whereas the other solvents would have been eliminated. Time dedicated to the experiments should also be lightened thanks to an approach used with combinatorial libraries [14]. With this approach, the polymers, synthesized in small quantities, can be directly evaluated after polymerization. Indeed, the quantity of template released during the first washing is a first evidence of the polymer affinity for the template (a complete release discards the polymer for further tests). Moreover, it is also possible to synthesize polymers directly in a filtration well plate and avoid the grinding stages. Last change, we would also perform more preliminary experiments before the DOE, to test for example basic monomers.

Bibliography

- [1] D. Buddhasukh, R. Maier, A. Manosroi, J. Manosroi, P. Sripalakit, and R. Werner, "Synthesis of cyproterone acetate," Feb. 2004.
- [2] H. J. Ringold, B. Löken, G. Rosenkranz, and F. Sondheimer, "Steroids. LXXIII.1a The Direct Oppenauer Oxidation of Steroidal Formate Esters. A New Synthesis of 17 α -Hydroxyprogesterone1b," *Journal of the American Chemical Society*, vol. 78, pp. 816–819, May 1956.
- [3] F. Neumann, "The antiandrogen cyproterone acetate: discovery, chemistry, basic pharmacology, clinical use and tool in basic research.," *Experimental and clinical endocrinology*, vol. 102, pp. 1–32, Jan. 1994.
- [4] F. de Jong, P. Reuvers, J. Bolt-de Vries, E. Mulder, J. Blom, and F. Schroeder, "Androgens and androgen-receptors in prostate tissue from patients with benign prostatic hyperplasia: Effects of cyproterone acetate," *The Journal of Steroid Biochemistry and Molecular Biology*, vol. 42, no. 1, pp. 49–55, 1992.
- [5] R. Frith and G. Phillipou, "15-hydroxycyproterone acetate and cyproterone acetate levels in plasma and urine," *Journal of Chromatography*, vol. 338, no. 1, pp. 179–186, 1985.
- [6] J. Huber, R. Zeillinger, J. Schmidt, U. Täuber, W. Kuhn, and J. Spona, "Pharmacokinetics of cyproterone acetate and its main metabolite 15 beta-hydroxy-cyproterone acetate in young healthy women.," *International journal of clinical pharmacology, therapy, and toxicology*, vol. 26, pp. 555–61, Nov. 1988.
- [7] I. Stoppelli, E. Rainer, and M. Hümpel, "Transfer of cyproterone acetate to the milk of lactating women.," *Contraception*, vol. 22, pp. 485–93, Nov. 1980.
- [8] C. Zouboulis, W. Chen, M. Thornton, K. Qin, and R. Rosenfield, "Sexual Hormones in Human Skin," *Hormone and Metabolic Research*, vol. 39, no. 2, pp. 85–95, 2007.
- [9] D. Matějček and V. Kubáň, "High performance liquid chromatography/ion-trap mass spectrometry for separation and simultaneous determination of ethynylestradiol, gestodene, levonorgestrel, cyproterone acetate and desogestrel," *Analytica Chimica Acta*, vol. 588, no. 2, pp. 304–315, 2007.
- [10] P. Job, "Formation and stability of inorganic complexes in solution," *Ann. Chim*, vol. 9, pp. 113–203, 1928.
- [11] N. K. Ebube, G. Owusu-Ababio, and C. M. Adeyeye, "Preformulation studies and characterization of the physicochemical properties of amorphous polymers using artificial neural networks," *International Journal of Pharmaceutics*, vol. 196, no. 1, pp. 27–35, 2000.
- [12] M. Yan and O. Ramstrom, *Molecularly Imprinted Materials Science and Technology*. 2003.
- [13] H. Guo and A. Mettas, "Design of Experiments and Data Analysis," in *Tutorial Notes 2010 AR&MS 2010 Annual RELIABILITY and MAINTAINABILITY Symposium*, 2010.
- [14] F. Lanza and B. Sellergren, "Method for Synthesis and Screening of Large Groups of Molecularly Imprinted Polymers," *Anal. Chem*, vol. 71, no. 11, pp. 2092–2096, 1999.

CHAPTER III

Towards the detection of cortisol and adrenaline, two stress biomarkers

1 Understanding the stress mechanisms and its detection methods

In this chapter, we describe the development of a molecularly imprinted polymer for sensing of the stress markers adrenaline and cortisol. Most of the stress sensors described in literature monitor skin perspiration or conductivity, heart rate and elevated temperature [1],[2]. These are all physical parameters, consequences of adrenaline and cortisol secretion. However, the physical parameters could be induced by other causes than stress such as exercise, fever and others. Thus, it is interesting to detect directly cortisol and adrenaline with a non invasive sensor.

Stress is nowadays a wide concept covering daily environmental changes and chronic diseases. Many efforts are produced by the society to lower psychological pressure and foster welfare. In some cases, however, high levels of stress in harsh conditions can generate bad decisions and lives are involved.

1.1 Stress definition, causes and consequences

Stress often refers to the trigger of a psychological imbalance. It more generally extends to psychological or physical changes that threaten the organism's balance (homeostasis). The first notion of stress was set by H. Selye in the 50's [3]. He defined it as the reaction of the organism to an emergency, such as physical trauma, microbial or predator attack, long exposure to cold *etc.* Under such nocuous conditions, the body reacts *via* intensive secretion of adrenaline, mobilization of a part of the nervous system and secretion of glucocorticoids. This first definition was only based on physiological states, omitting the psychic and immunologic components. It settles though the basis of a stress definition: a general adaptation syndrome, a response of the body to specific stimuli. Besides, we will only focus in this manuscript on the physiological dimension of stress. An event that threatens an individual is called a stressor by Selye. It triggers a three-stage response of the body, as represented in figure 54.

The first stage is a "fight or flight" response [4]: the sympathetic nervous system is activated and **adrenaline** and **cortisol** are two hormones quantitatively secreted in the blood. Next comes

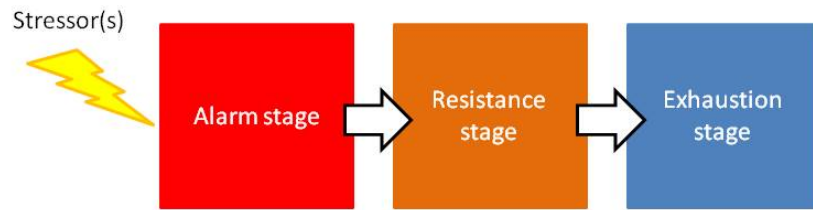


Figure 54: Response stages of the body induced by a stressor.

the resistance stage. The body focuses resources against the stressor, the sympathetic nervous system returns to normal conditions while cortisol and adrenaline are still at high concentration in the blood. The body remains very active (heart rate, blood pressure and breathing increase). If stressors continue and push the body to its limits, resources can be exhausted and disease or death could occur, it's the exhaustion stage. Besides, intensive and prolonged exposure to stressors can lead to chronic stress. It rhymes with a dysregulation of cortisol secretion and high cortisol levels in plasma [5]. Exposure to extreme stressors, in the case of soldiers for example, can lead to mental health disorders (such as post traumatic stress disorders) [6], decreasing dramatically their performances. Generally, soldiers submitted to severe stressors are treated against the consequences to which they are faced. More and more, the army focuses on preventing stress effects, thus working before stressors. The negative effects of extreme stressors are extended to all people working in harsh conditions, such as firemen, people studying earthquakes and others. We therefore think that it is of high interest to real-time monitor stress thanks to reliable sensors: this would enable a control center to monitor stress and maybe call the individual back over the line. This intervention may limit the stress disorders.

We will focus in the next section on the hormonal secretion triggered during the alarm stage of stress and see if they could help to monitor stress.

1.2 Hormonal secretions triggered by stress

As it is resumed in figure 55, a stressor triggers a reaction in the body along two pathways, a nervous way and an endocrinous way. They both act in the adrenal glands, which leads to adrenaline quickly followed by cortisol secretion. Thus, these two hormones are considered as stress biomarkers.

1.2.1 Adrenaline

Epinephrine, also called adrenaline, is a catecholamine hormone derived from tyrosine (figure 56). Indeed, the hormone presents a catechol group and a secondary amine.

The adrenal glands are located at the top of the kidneys. The core of these glands is the adrenal

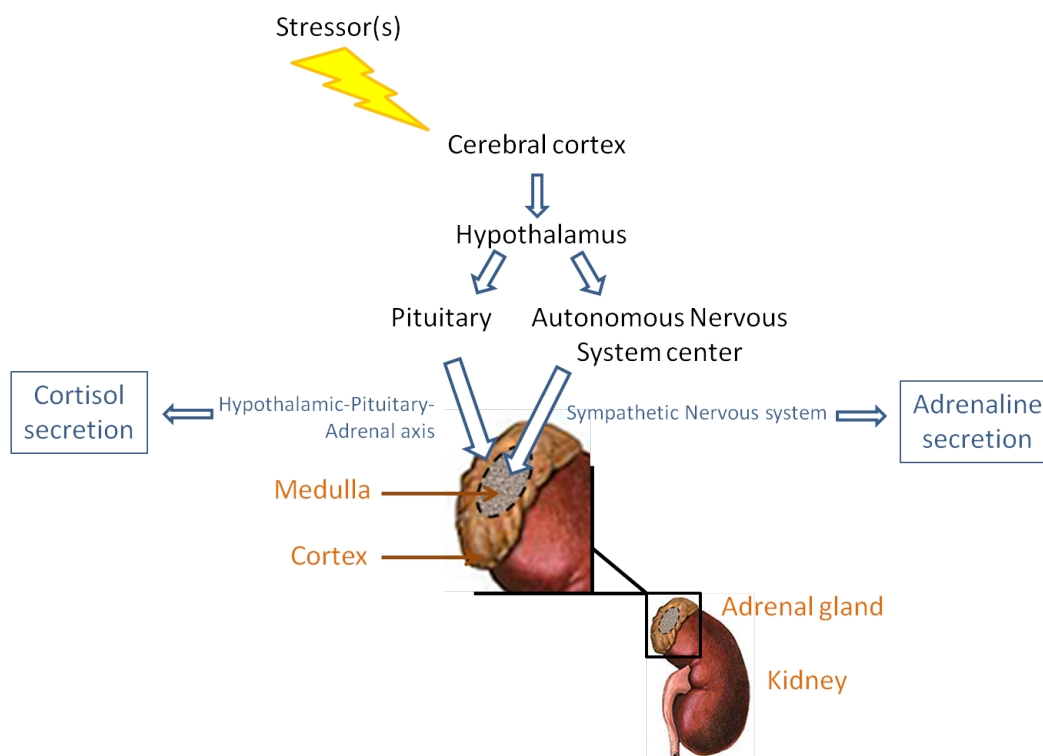


Figure 55: Physiological reactions in the adrenal glands induced by stressors.

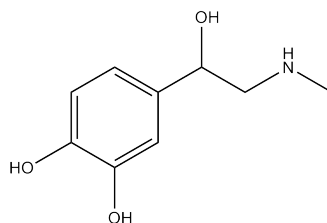


Figure 56: Chemical structure of adrenaline.

medulla which secretes adrenaline. In case of immediate danger, or stressors, the nervous system stimulates the endocrine cells and epinephrine is instantaneously secreted at high concentrations (the blood basal level is 50 ng/L and it can peak up to 700 ng/L). Then, the fight-or-flight response is activated. It consists in raising the heart rate to fuel the muscles, stimulating the release of glucose and driving more blood to the muscles and less to unhelpful organs. These reactions increase the reactivity of the body and therefore help to escape from a dangerous situation. Epinephrine is also used as a treatment for asthma or important allergies thanks to its effect of dilatating the respiratory track.

1.2.2 Cortisol

Hydrocortisone, also known as cortisol, is a steroid hormone that belongs to the glucocorticoids class. As a steroid, it possesses a tetracyclic hydrocarbon skeleton (figure 57).

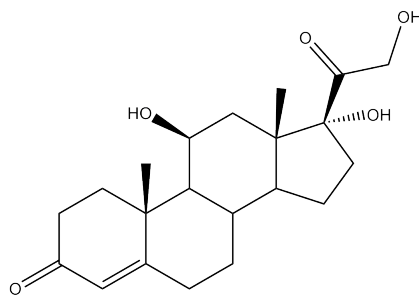


Figure 57: Chemical structure of cortisol.

Cortisol is synthesized and secreted by the adrenal glands. These glands are made of a medulla surrounded by an outer cortex which synthesizes and secretes cortisol. A cortisol secretion triggers glucose release into the blood, the suppression of the immune system, and the metabolism of fat, carbohydrates and proteins: it focuses on the protection of the vital organs. The secretion is regulated by a hormone cascade and cortisol is the final product of the hypothalamo-pituitary-adrenal axis (HPA). In normal conditions, the cascade depends on a circadian rhythm: cortisol is secreted per burst with different amplitudes correlated with the person's activity [7]. The level in blood rises in the early morning hours (with a peak at the awakening) and falls throughout the day (figure 58). The cascade can also integrate information from cognitive processes, emotional and stress reactions.

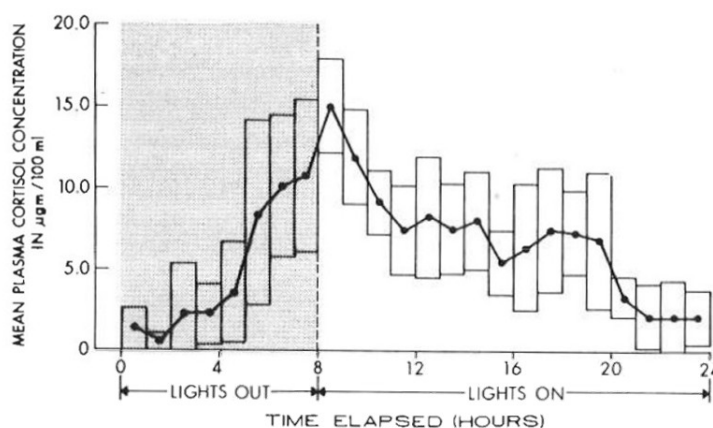


Figure 58: Circadian rhythm of the cortisol secretion, figure issued from [7].

In case of a stressor, the cortisol secretion raises. For example, when subjects were submitted to hyperthermia, their level of cortisol increases from $8 \mu\text{g}/100 \text{ mL}$ of blood-plasma to $28 \mu\text{g}/100 \text{ mL}$, in less than 1,5 h [8]. During this study, the authors noticed that acclimatized subjects did not show any cortisol increase, proving the importance in the experience of the coping strategies.

In case of a chronic stress disease, the HPA axis presents hyperactivity which dysregulates the secretion of cortisol and flattens the circadian curve. The sympathetic nervous system can also be altered. In any case, such dysregulations can damage the immune or cardiovascular system, the

metabolic functions and behaviour.

Monitoring stress is essential for two main reasons:

- if the levels of secreted hormones are too high, this could lead to health damages and generate bad decisions in crucial moments,
- if the secretion of hormones do not lower after the alarm and resistance stages, they can cause stress dysregulations.

Real-time stress monitoring could anticipate these issues.

1.3 Stress monitoring

As underlined in the previous sections, adrenaline and cortisol are stress biomarkers. Adrenaline has a short-term effect while cortisol is secreted later and longer. These two hormones were measured in plasma of parachutists just before, during and after a jump [9]. Schedlowski and coll. collected blood samples, every ten minutes, *via* a catether, and showed an increase in adrenaline levels, correlated with a raised heart rate (figure 59).

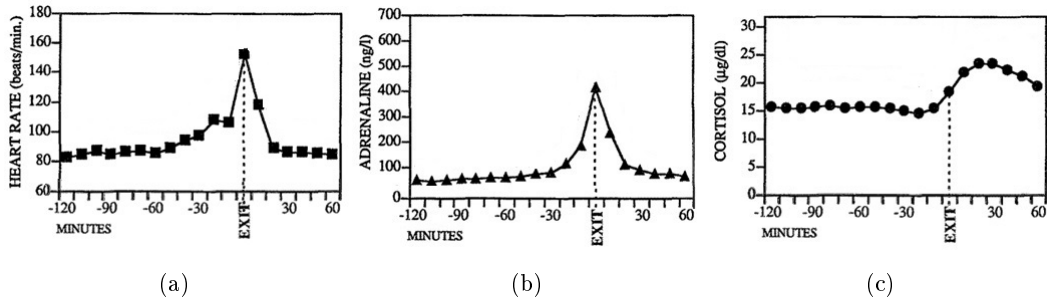


Figure 59: Evolution of heart rate frequencies (a) and plasma levels of (b) adrenaline and (c) cortisol, before, during and after a parachutist jump. Figure from [9].

In this example, as for many other hormones tests, adrenaline and cortisol were dosed in blood-plasma. It is usually based on an immunoassay: an antibody recognizes and binds a specific molecule and a measurable signal is produced in response to the binding (radiation, color change, fluorescence...). The detection of cortisol and adrenaline in plasma is more precise but can be distorted by the sampling technique as the venipuncture can be an additional stressor. Moreover, the invasive measurement in plasma is difficult for real-time monitoring. That's why scientists are interested in measuring cortisol and adrenaline with non invasive techniques in other physiological fluids, such as urina, saliva or sweat.

Measurements of salivary cortisol were proven to be relevant and to reflect the free fraction of cortisol in plasma [10]. Thus, a low level of cortisol during the afternoon is observed in plasma and

saliva for example. Even the pulsatile secretion can be detected [11]. Moreover, it was demonstrated that salivary cortisol is increased in anticipation of, during and after a stressful event [12]. Finally, the influence of daily stressors, less intense than severe stressors, on cortisol salivary level was shown. Adrenaline has never been measured in saliva.

Urinary free adrenaline is correlated to its plasma concentration [13] and can be quantified by HPLC methods [14], [15]. Similarly, urinary free cortisol can be dosed by different liquid chromatography techniques. However, urine still rises difficulties: the participants unease, the storage and transport of samples. Moreover, urinary measures give only an average of secretion between two samplings and do not enable real time monitoring.

Measurements in sweat are more rarely reported in literature. Cortisol was reported in sweat several times [8], [16], [17]. Garcia-Cortes and coll. [18] have developed an electronic nose able to detect adrenaline and cortisol. Thanks to principal component analysis, they managed to distinguish two persons sweat and their activity during sweat collection (inactive or running), unfortunately they do not precise if the analyses proved the presence of both adrenaline and cortisol in sweat. Adrenaline secretion is correlated to sweat induction but, as far as we know, the molecule has not been detected in sweat yet.

Considering this overview of stress chemical sensing, a sensor able to detect adrenaline and cortisol in aqueous media would be interesting. We think that body external fluids are promising media for non invasive, real-time monitoring of physiological parameters. We will focus in the next sections on the use of molecularly imprinted polymers for monitoring adrenaline and cortisol.

2 Elaboration of MIPs formulations for adrenaline

The detection of adrenaline and cortisol may be achieved in a sensor with molecularly imprinted polymers. In this section, we try to synthesize adrenaline imprinted polymers.

A few MIPs for adrenaline have been reported so far. We extended the literature review to catecholamine imprinted polymers and particularly dopamine imprinted polymers [19], [20], [21], [22], because these molecules are close to adrenaline structure.

We used formulations with methacrylic acid, N-isopropylacrylamide, vinylboronic acid, acryloylmorpholine on their own or mixed together. Polymerizations were launched either by heat or UV. All imprinted polymers, with no exception, became orange or yellow and their controls were white. The yellowish molecule formed absorbed at the same wavelength as adrenaline. We studied the degradation of adrenaline by HPLC coupled to mass spectroscopy. After 12h, at 7°C, already 30% of a 1 mM solution of adrenaline had disappeared. We could follow this evolution only by MS, because adrenaline transforms into a molecule that absorbs at the same wavelength and the compounds are difficult to separate by chromatography. To study further the degradation of adrenaline, we sent a sample of adrenaline and the degradation products in water to the analytical systems company Agilent. They performed an analysis by chromatography HPLC MS and MS/MS. They observed four different compounds in solution. The software generated their molecular formulas. Adrenaline was still present but in very small amount. They also observed a molecule that could be adrenochrome (formula $C_9H_9NO_3$, figure 60). This compound could be assessed by fluorescence of the solution observed, and as West underlined, the fluorescence of this compound is temporary [23]. Moreover, the auto-oxidation of adrenaline in adrenochrome was already observed [24]. The two other compounds were $C_{10}H_{13}NO_3$ and $C_{10}H_{11}NO_2$: we are not capable of identifying them to date. An alternative could have been the use of a "dummy template", like ephedrine. This approach was used by Pichon and coll. [25] for solid-phase extraction.

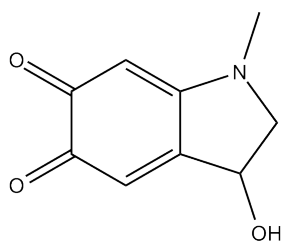


Figure 60: Chemical structure of adrenochrome.

Very quick degradation of adrenaline and its difficulty to be imprinted led us to exclusively work with cortisol imprinted polymers.

3 Elaboration of MIP formulation for cortisol

After the first trials for adrenaline, we aim in this section at finding the best formulation for cortisol's recognition by polymers.

3.1 Development of a preliminary MIP for cortisol

During the last decades, a few papers have reported the molecular imprinting of cortisol. Ramström and coll. have been the first to investigate non covalent imprinting of cortisol [26]. Monomers, their ratios and the solvents used for cortisol imprinting reported in literature are summarized in table 9. Much of the polymers imprinted for cortisol were carried out for chromatographic separation but never in an attempt to develop a sensor. Moreover, the polymers described present low binding capacity; this is supposedly due to a small number of interactions between the steroid and monomers. Some other steroids have been imprinted, cholesterol for example, but as underlined in chapter I, a small chemical variation can produce a big change in hydrophilicity of the molecule. We think that formulations of polymers with these compounds may not be relevant for our case.

Among the publications listed in table 9, Baggiani and coll. worked on a MIP formulation for cortisol [27]. They aimed at synthesizing a matrix able to recognize several steroids, and thus, they used cortisol as a group template. The steroid selectivity could then be used for extraction of molecules from biological samples as a clean-up treatment. The first MIPs imprinted for cortisol used methacrylic acid and ethylene glycol dimethacrylate as monomers in either tetrahydrofuran or chloroform [26], [28], but they enlarged the formulation possibilities. Baggiani and coll. proposed to test a reduced combinatorial approach. First, they settled the molar ratios of template/functional monomer/cross-linker to 1/3/27, and the cross-linker, the solvent and different functional monomers were tested. With the best functional monomer of this first step (best binding abilities of the MIP), they varied the cross-linker, keeping the same solvent. Finally, with the best functional monomer and the best cross-linker, they screened several solvents. The three best formulations are reported in the last line of table 9. Methacrylic acid, one of the most commonly used monomer in

Functional monomer	Cross-linker	Molar ratio ^a	Solvent	Polymerization conditions	Refs
MAA	EDMA	1/10/50	Tetrahydrofuran	UV 4 °C	[26]
MAA	EDMA	1/10/90	Chloroform	UV 4 °C	[28]
HEMA	EDMA	1/28/73	Chloroform	Gamma irradiation from Co ⁶⁰	[29]
AM	EDMA	1/3/27	Chloroform	UV 4 °C	[27]
AM	EDMA	1/3/27	Chloroform	UV 4 °C	
4-vp	EDMA	1/3/27	Chloroform	UV 4 °C	

^a molar ratio of template/functional monomer/cross-linker

Table 9: List of conditions used to synthesize cortisol imprinted polymers reported in literature.

imprinting, is supplanted by acrylamide and 4-vinylpyridine. However, this study sets a hierarchy in the importance of the factors, thus it is possible for example, that a functional monomer is efficient in a solvent different than the one chosen in the first step and this approach would miss this.

We based our first MIP trials on literature specific to the determination of MIP's formulation for cortisol and further extended the tests to some new formulations. Polymers were prepared as specified in table 10. The protocol is given in appendix B. Non imprinted polymers (NIPs) are not included in the table, they were prepared exactly as the corresponding MIPs but without the template.

	Poly- mer	Template	Functional monomer	Cross- linker	Molar ratio^a	Initiator^b	Solvent	Polymerization conditions
[26]	M _{co} 1	Cortisol 0.13 mmol	MAA	EDMA	1/10/50	AIBN 0.5 mol%	THF 2 mL	UV 5 °C overnight
[27]	M _{co} 2	Cortisol 0.14 mmol	AM	EDMA	1/3/27	DMPA 0.24 mol%	Chloroform 1.5 mL	UV 5 °C 30 h
[27]	M _{co} 3	Cortisol 0.14 mmol	AM	EDMA	1/3/27	DMPA 0.24 mol%	Acetonitrile 1.5 mL	UV 5 °C 30 h
inspired from [26]	M _{co} 4	Cortisol 0.14 mmol	MAA	EDMA	1/10/50	AIBN 0.5 mol%	THF 2 mL	50 °C overnight
	M _{co} 5	Cortisol 0.2 mmol	MAA	EDMA	1/8/25	AIBN 0.65 mol%	Methanol 1.5 mL	UV 5 °C overnight
	M _{co} 6	Cortisol 0.2 mmol	MAA	EDMA	1/8/25	AIBN 0.65 mol%	Dichloromethane 1.5 mL	UV, 5 °C, overnight
	M _{co} 7	Cortisol 0.2 mmol	MAA	EDMA	1/8/25	AIBN 0.65 mol%	Dichloromethane 1.5 mL	UV, room temperature, overnight

^a molar ratio of template/functional monomer/cross-linker

^b concentration expressed in molar percentage compared to the polymerizable groups

Table 10: Formulations used to obtain cortisol imprinted polymers.

M_{co}2 and M_{co}3 showed a yellow color after polymerization whereas their control N_{co}2 and N_{co}3 were white. Numerous washings were not sufficient to eliminate this color and a constant intense leaching was observed. We assumed that cortisol had deteriorated. The analyses of the yellowish supernatants by HPLC and mass-spectrometry did not allow the determination of the formed product. Therefore, we did not work further with these polymers.

The other formulations gave white polymers, so we decided to test them for cortisol binding. Beforehand, a method to measure the cortisol concentration in solutions was established (appendix C). The concentration of cortisol in the solution was determined by measuring the area of the chromatogram peak. Thus, a linear calibration curve was obtained for concentrations from 1 to 100 μ M (figure 61).

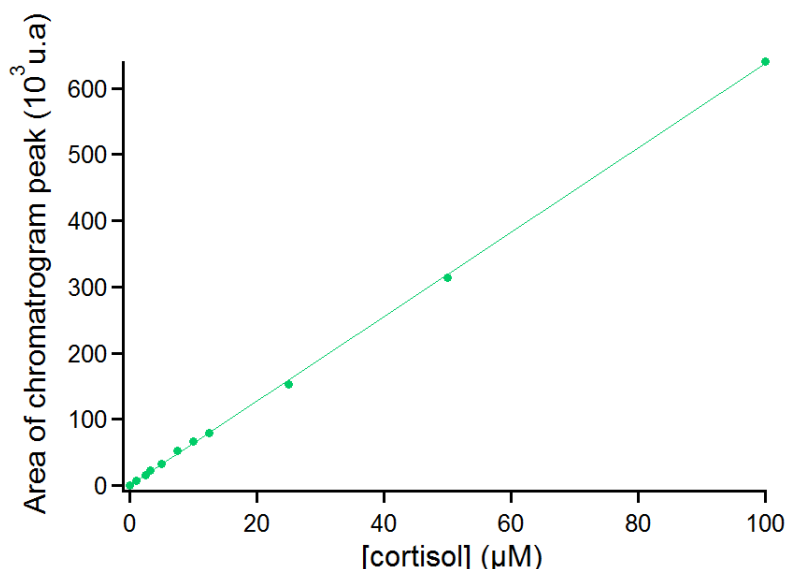


Figure 61: Calibration curve for cortisol dosage by HPLC and UV detector. $R^2 > 0.99$.

After grinding and washing the polymers, binding assays were performed with an increasing concentration of polymer and a constant concentration of cortisol (10 μ M), around ten times the concentration of cortisol in saliva [10] and still easily measurable by HPLC-UV.

The first binding assays rose a particular issue. Indeed, after a dozen of washing steps, the binding isotherms showed a very important leaching of residual template. Large amounts of cortisol were released into the solvent and the amount of cortisol in supernatants overpassed largely the initial amount inserted. As it is observed on figure 62, the concentration of cortisol in solution for the NIP is just below the assay's concentration, and for the MIP, it rises with the concentration of polymer, revealing some leaching.

Whereas teams working with MIPs usually use a determined number of washings, we decided to monitor the cortisol release from polymers. In figure 63, the concentration of cortisol in supernatants is represented along with the number of washings. For M_{co}6, after 18 washings, cortisol concentration

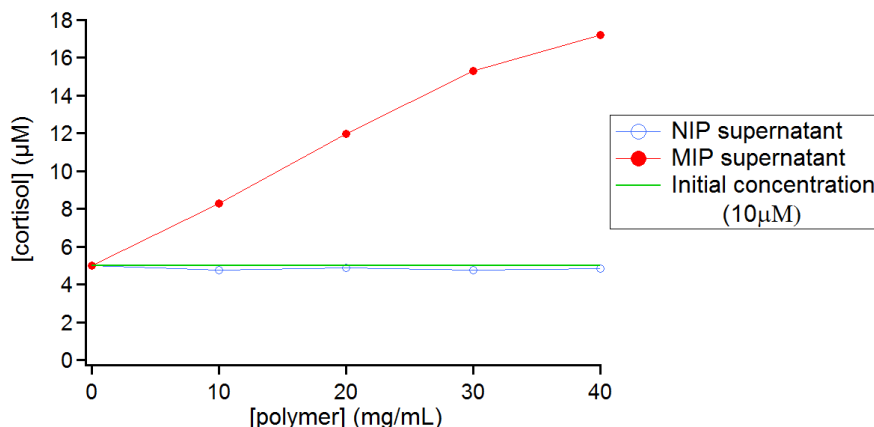


Figure 62: Binding assay with a constant concentration of cortisol ($10 \mu\text{M}$), and a growing concentration of polymer (on the x axis). The amount of cortisol in supernatant is determined through HPLC. This amount rises steadily for MIP supernatants (red), which indicates the leaching of cortisol during incubation.

is still above $1 \mu\text{M}$, whereas this value is reached for M_{co5} . M_{co1} needs more washings, as the cortisol concentration is still above $10 \mu\text{M}$. We also noticed an increase of the concentration for the 11th washing: this often appears when the washing lasts more than an hour (overnight for example). The template is difficult to extract and longer time favors a higher extraction. All binding tests were performed at a concentration of $10 \mu\text{M}$. For all the cortisol MIPs studied in this manuscript, the washing supernatants were finally controlled every 5 washings and the washing was stopped when the supernatants concentrations was under $1 \mu\text{M}$.

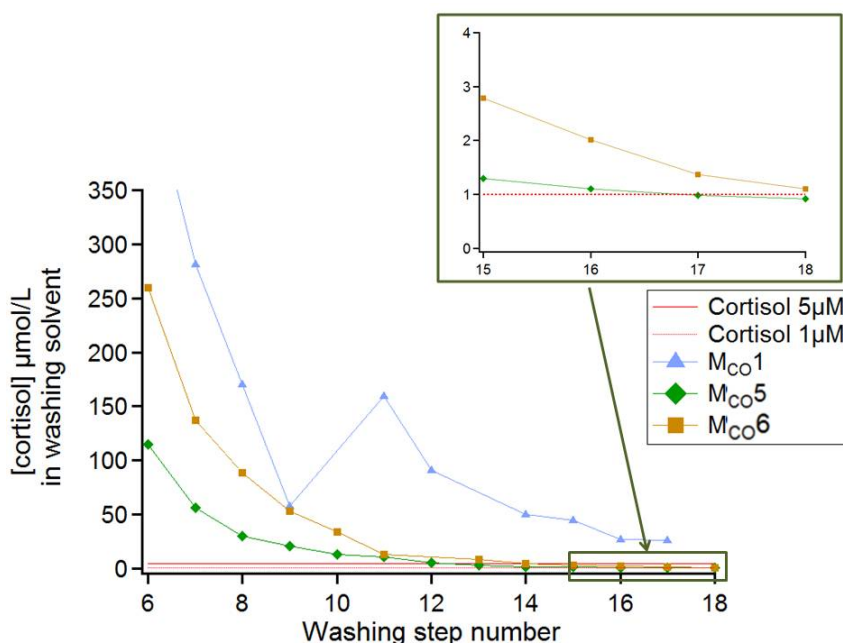


Figure 63: Evolution of cortisol concentration in supernatants along with the washings. Solvents were successively 10 mL of methanol/acetic acid 4/1, 9/1 or pure methanol.

Once the polymers were thoroughly washed, cortisol binding was studied. We observed no difference of molecular uptake between M_{co1} and N_{co1} , M_{co4} and N_{co4} , neither in THF (the polymerization solvent) nor in THF/n-heptane (1/1 in volume) although it is the optimal solvent observed by Ramström and coll. [26].

From these first studies, we assumed that Baggiani's group formulations led to deterioration of cortisol and that the first formulations proposed by Ramström did not show any binding effect. After these failures, we decided to continue the study using methacrylic acid (one of the most commonly used functional monomer) and to test new solvents that were able to solubilize all ingredients:

- methanol as a polar solvent,
- dichloromethane as an alternative to chloroform.

Thus, polymers M_{co5} and M_{co6} were obtained. This time again no molecular uptake by M_{co5} was observed. However, M_{co6} was successfully imprinted. Indeed, M_{co6} bound more cortisol than its non imprinted control N_{co6} as represented in figure 64. The K_{50} is about 7.8 mg/mL, and for a polymer concentration of 40 mg/mL, $IF = 2.7$.

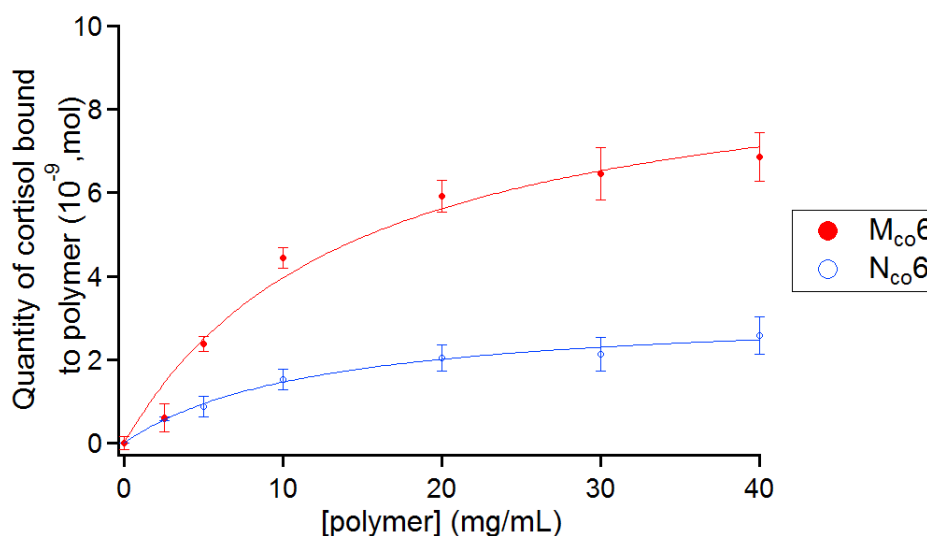


Figure 64: Binding assay of cortisol (initial concentration in solution $10 \mu\text{M}$) in dichloromethane to M_{co6} , N_{co6} . Error bars are the standard deviation for two measurements of two polymers with the same formulation.

We further investigated this formulation by polymerizing M_{co7} at room temperature, in order to study the influence of the temperature. The results show little differences between M_{co6} and M_{co7} (figure 65).

We decided to keep the polymerization temperature at 5°C , so as to promote interactions and to reduce the risks of cortisol deterioration for the next polymers. M_{co6} is thus the formulation retained as a starting point for the thesis.

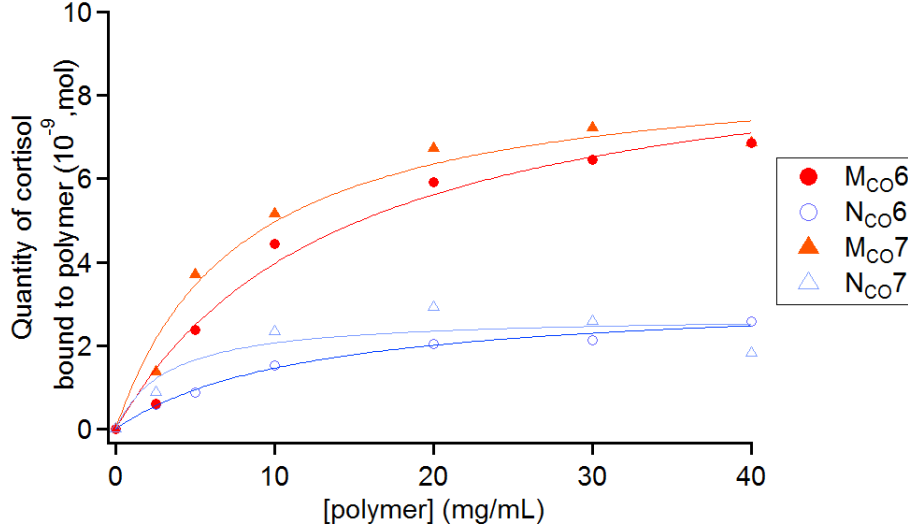


Figure 65: Study of the influence of the polymerization temperature on the binding assay of cortisol (initial concentration in solution 10 μ M) to M_{co6}, N_{co6} and M_{co7}, N_{co7} in dichloromethane, synthesized respectively at 5 °C and room temperature.

3.2 NMR studies

The aim of this section is to prove the formation of a complex between methacrylic acid and cortisol in the solvent used for polymerization (dichloromethane) thanks to NMR studies associated to a Job's plot.

NMR spectroscopy is used to study interactions in liquid phase and in our case, the formation of a complex. As we underlined in chapter II, the formation of the complex (equation 3.1) generates a chemical shift of some protons which can be correlated to the mole fraction of reactants and this is expressed by the Job's plot (equation 3.2).



$$\Delta v = \frac{\Delta^0}{C_{tot}} K (C_T^i v - C_{TM_n}) ((1 - v)C_T^i - nC_{TM_n})^n \quad (3.2)$$

where: Δ is the difference between the chemical shifts observed and the pure template, Δ^0 is the difference between the chemical shifts of the pure complex and the pure template, $v = \chi_T$ the mole fraction of template, K is the association constant, C_{tot} the total concentration of species in solution, C_T^i is the concentration of template in stock solution, C_{TM_n} the equilibrium concentration of the complex.

To trace the Job's plot, stock solutions of cortisol and methacrylic acid were prepared in deuterated-dichloromethane, at a concentration of 10 mM. Then, different mole fractions of tem-

plate and monomer were mixed with fixed final concentration and volume (respectively 1 mM and 700 μ L). For each mole fraction, the chemical shift of chosen protons was monitored.

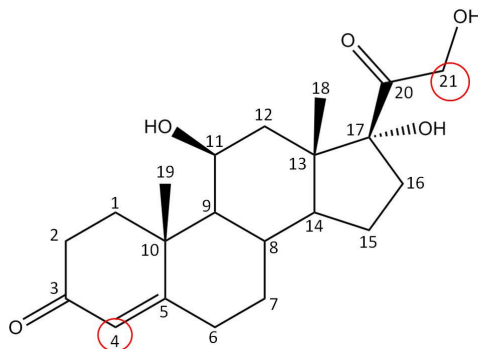


Figure 66: Chemical structure of cortisol with numbered carbon atoms and circled position of interest protons.

Cortisol was studied here as a template (figure 66). Figure 67 represents its NMR spectrum and the spectrum of an equimolar mixture of cortisol and MAA. We can see that peaks of the complex and free species are not distinguishable, which means that, if a complex is formed, we have a system in fast exchange and, therefore, we can trace the Job's plot.

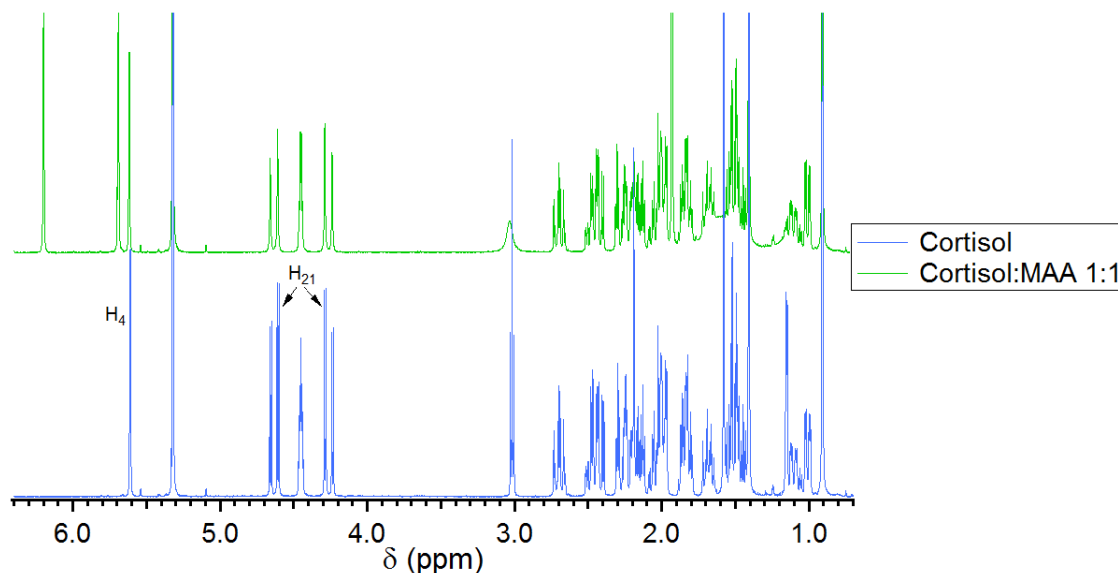


Figure 67: NMR spectra of cortisol in CD_2Cl_2 and a mixture of cortisol and MAA, with $\chi_{cort} = 0.5$. Chemical shift of the protons of interest are pointed out and numbered with the number of the supportive carbon.

The study was focused on three protons, H_4 and H_{21} (figure 66), both close to functions expected to form hydrogen bonding with MAA. Their signals are fortunately distinguishable on the NMR spectrum and not located in the very dense area of peaks. Spectra were obtained at room

temperature and at 5 °C, the polymerization temperature. Superposition of spectra from 0 to 1 in cortisol molar ratio and zoom in the area of H4 and H21 protons signals are represented in figure 68.

This study was mainly focused on H21, two protons located between hydroxyl and cetone groups. They have a different environment and thus are coupled together. When cortisol is alone in solution, a coupling with the neighbouring hydroxyl proton is observed. The double doublets at 4.25 and 4.65 ppm are characteristic of an ABX system, with $^3J_{AX} = ^3J_{BX} = 4.8$ Hz and $^2J_{AB} = 20$ Hz. The hydroxyl signal is a triplet at 2.98 ppm. As soon as MAA is added to cortisol, the hydroxyl signal disappears and the double doublets for H21 become doublets of an AB system, with $^2J_{AB} = 20$ Hz. We suggest that these signal evolutions are first evidence of a hydrogen bonding with MAA.

The Job's plot for H21 is represented in figure 69. As the signal is double doublets, we chose to monitor the average chemical shift of the protons, corresponding to the exact chemical shift of the CH₂ with no coupling. The graph is fitted by equation 2.2 and gives $n = 0.7$. Despite this evaluation of n , no assumption is done on the complex stoichiometry, as several complexes could exist and this would be out of the Job's area. However, we observe the expected shape of the Job's plot and this confirms the formation of a complex.

Figure 70 shows the Job plot for H4. The graph is also the proof of hydrogen bonding between the enone and methacrylic acid. We can also underline the intensity difference between the plots at 5 °C and at room temperature. Equation 2.2 actually shows that the intensity is proportional to the equilibrium constant, whose value depends on the temperature.

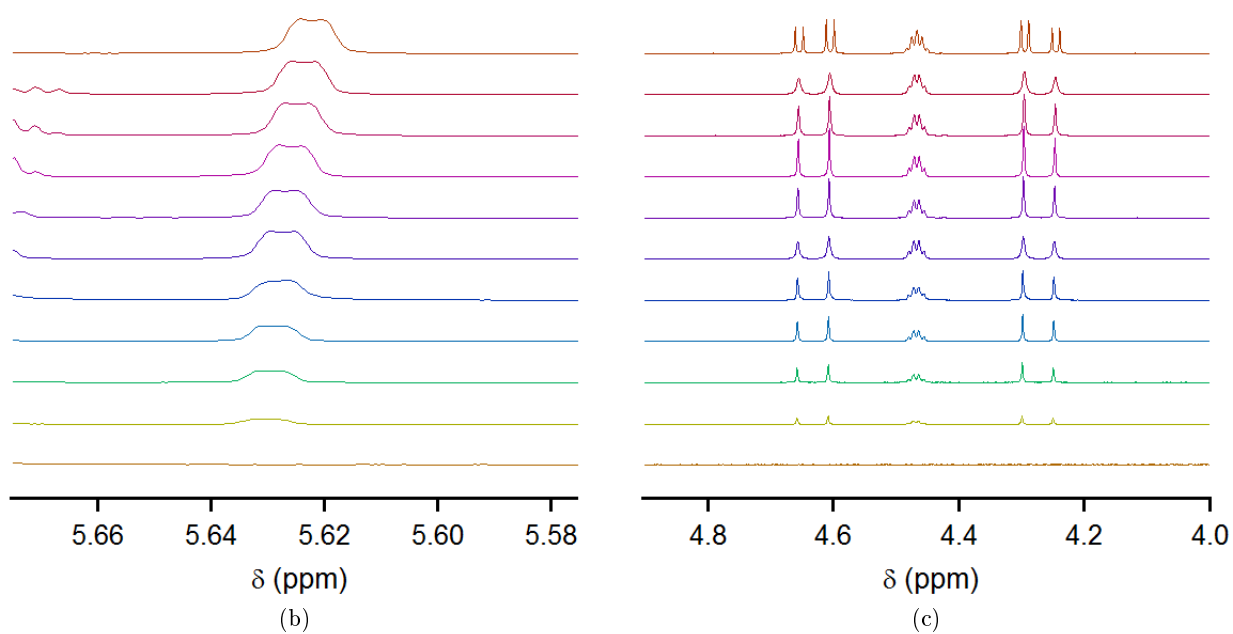
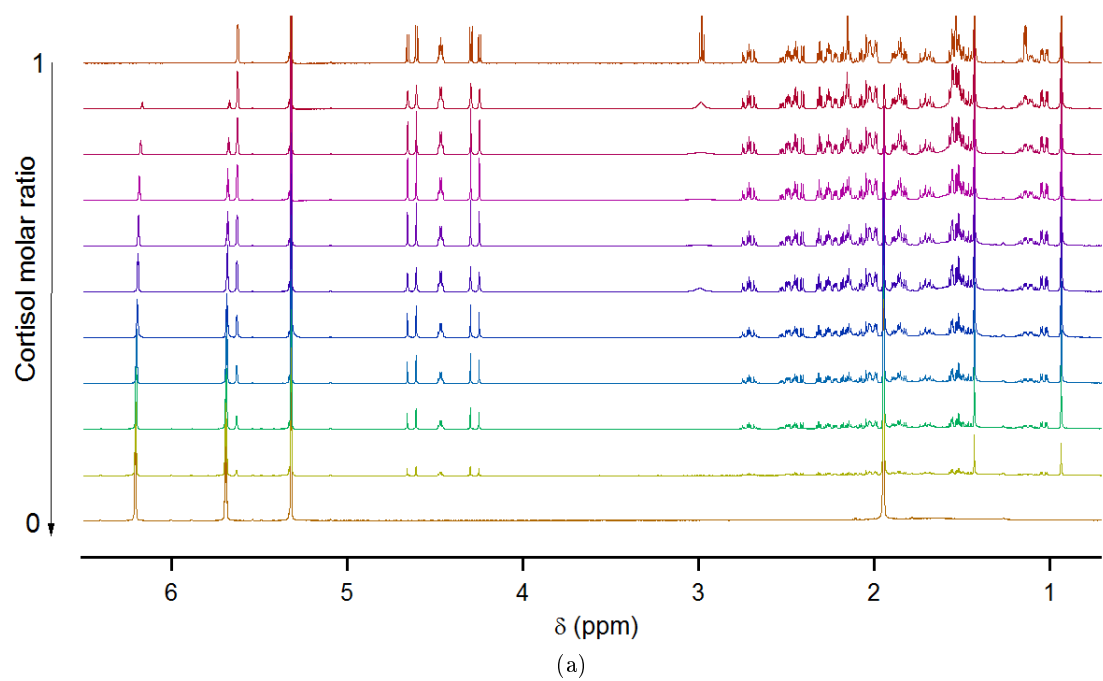


Figure 68: Superposition of NMR spectra with different ratio of cortisol/MAA. (a) Complete spectra, (b) zoom on H4 signal, (c) zoom on H21 signal.

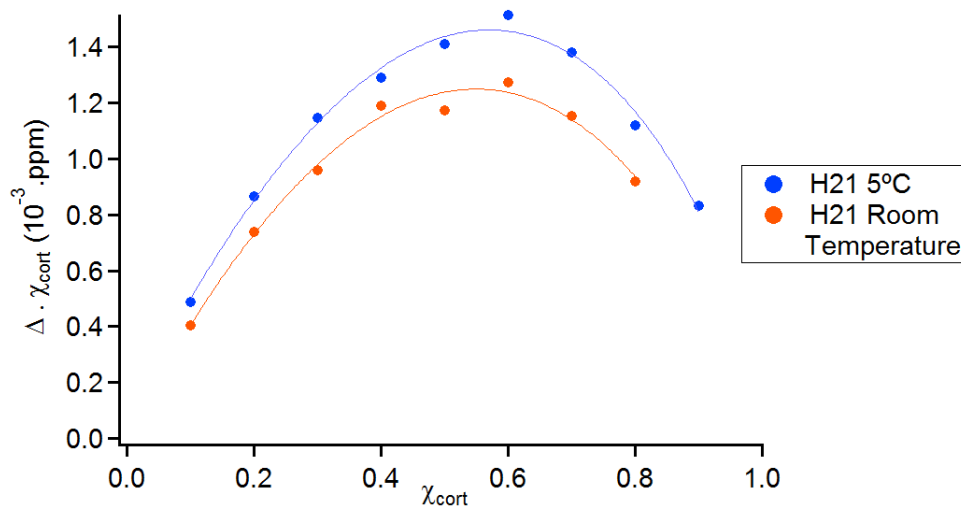


Figure 69: Representative Job's plot for the interaction between H21-cortisol and MAA in dichloromethane.

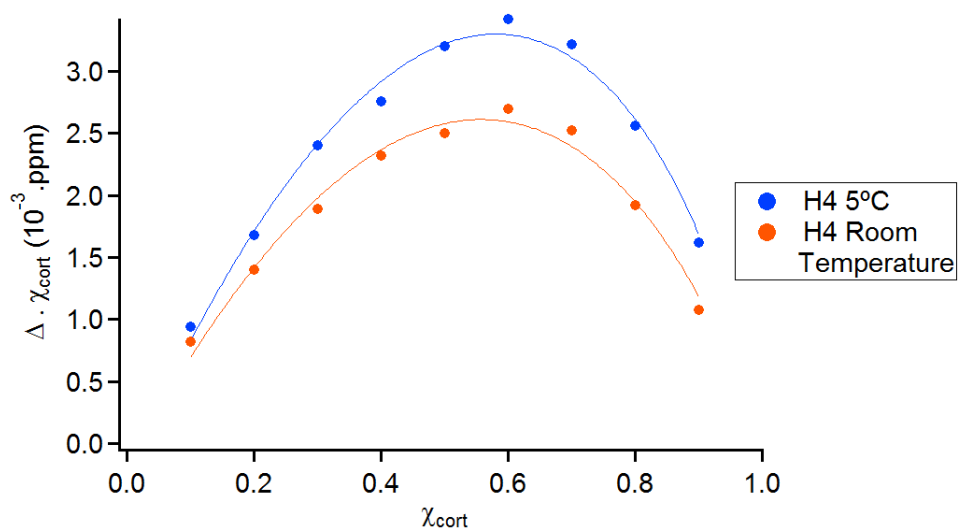


Figure 70: Representative Job's plot for the interaction between H4-cortisol and MAA in dichloromethane.

3.3 Conclusion

The study of these two protons clearly shows an interaction between MAA and cortisol. Other protons could be studied by this method of continuous variation (some signals shift on the superposition of NMR spectra, whereas others don't move at all). We did not investigate further as we only intended to prove the existence of a complex. We did not either work on the stoichiometry as we were not certain that only one complex was formed. Dichloromethane and methacrylic acid are components that favor the imprinting of cortisol and we are comforted in our choice of solvent and functional monomer.

4 Optimization of the MIP for cortisol: use of a design of experiments

A first formulation of polymer imprinted for cortisol was obtained in the previous part. Thus, an optimization can be undertaken. We decided to continue working with MAA, EDMA and dichloromethane, and initiating polymerization with AIBN. To evaluate the influence of several factors and to optimize the amount of components used in the polymer formulations, we chose to use a design of experiments based on the formulation obtained in the previous part.

4.1 Doehlert design of experiments

Designs of experiments (DOE) enable the evaluation of the impact of several parameters on a system while keeping a reasonable number of experiments. As we saw in chapter II, there are several issues to avoid while designing a DOE. First, the choice of the influent variables and their interval of variation for the study, as well as the choice of the output responses should be carefully chosen. Last but not least is the choice of the design itself. Indeed, several designs can be used for response surface modeling and optimization (full factorial design, box-Benhken design. . .). We chose Doehlert design: a quadratic design which allows the estimation of all main effects, all first-order interactions and all quadratic effects. The geometry of the design is based on a uniform space-filling property, since the points are distributed along spheres and one (or more) center point(s). Figure 71 is, for example, the schematic representation of a 2 and 3 factor Doehlert design. One of the advantages of such a design is the possibility to perform the experiments sequentially: the design can be expanded to produce an upgraded design which is added to the initial experiments.

If we write x_i the inputs of the design and y_i the output responses, then after calculation the responses can be represented as a polynomial equation (equation 4.1). Such equations are valid only in the definition intervals of x_i in the study.

$$y_j = \beta_{j0} + \sum_{i=1}^n \beta_{ji}x_i + \sum_{i=1}^n \beta_{jii}x_i^2 + \sum_{i=1}^{n-1} \sum_{k=i+1}^n \beta_{jik}x_ix_k \quad (4.1)$$

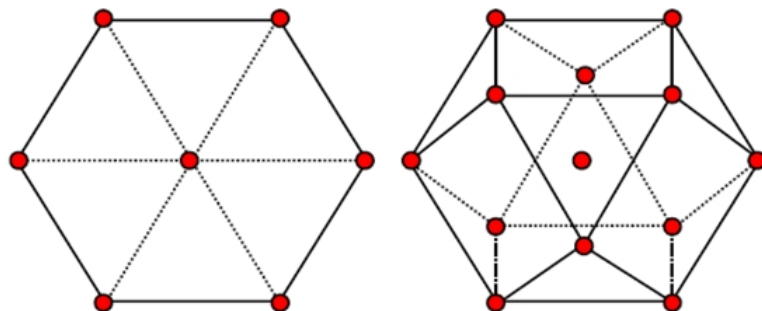


Figure 71: Schematic representation of a 2 and 3 factors Doehlert design.

where: y_j is a response, x_i are the input factors (n is the number of inputs), β_{j0} is the constant term, β_{ji} are the linear coefficients of first order, β_{jii} are the quadratic terms and β_{jik} are the interaction terms.

These coefficients highlight the most influencing factors and the interactions between factors. When a coefficient is positive, then the attached factor has a positive influence on the answer. On the opposite, when a coefficient is negative then the factor has a negative influence. A subsequent analysis of variance (ANOVA) treatment evaluates the significance of the factors. The statistical significance is the computational study of means and variances. It is determined by a ratio of two variances (variation between groups and within groups), which is compared to a handbook value to determine the significance (F-test). A large value of F is undesirable. It is evaluated by p , the level of significance. In this thesis, if $p \leq 0.05$, then the test is significant.

We selected three variables supposed to be influencing factors on our polymers, while keeping the same solvent (dichloromethane):

- The molar equivalent of monomer to the template
- The molar equivalent of cross-linker to the template (equivalent to cross-linking degree)
- The amount of initiator (a mole percentage of double bonds involved in the polymerization reaction).

We decided to keep a constant volume of solvent. Thus, 13 formulations (table 11) of polymer were obtained that we all synthesized twice to evaluate the reproducibility.

After synthesis (initiated by UV at 5 °C, overnight), polymers were manually and mechanically grounded, washed and then characterized.

Polymer	ratio MAA ^a 5 levels	ratio EDMA ^b 7 levels	% AIBN ^b 3 levels
M _{co} ^{a,b} 8	7.0	45.0	2.1
M _{co} ^{a,b} 9	12.0	45.0	2.1
M _{co} ^{a,b} 10	9.5	75.3	2.1
M _{co} ^{a,b} 11	4.5	75.3	2.1
M _{co} ^{a,b} 12	2.0	45.0	2.1
M _{co} ^{a,b} 13	4.5	14.7	2.1
M _{co} ^{a,b} 14	9.5	14.7	2.1
M _{co} ^{a,b} 15	4.5	34.9	0.5
M _{co} ^{a,b} 16	7.0	65.2	0.5
M _{co} ^{a,b} 17	9.5	34.9	0.5
M _{co} ^{a,b} 18	4.5	55.1	3.7
M _{co} ^{a,b} 19	7.0	24.8	3.7
M _{co} ^{a,b} 20	9.5	55.1	3.7

^a molar ratios are expressed compared to cortisol

^b concentration expressed in molar percentage compared to the polymerizable groups

Table 11: Formulations of polymers following a Doehlert design of experiments. a and b refer respectively to the first and second synthesis. The molar ratios of MAA and EDMA to template intervals are respectively 4.5 - 12 and 14.7 - 65.2, the amount of AIBN being between 0.5 and 3.7%. The starting point of this DOE was M_{co}6 with molar ratios cortisol/MAA/EDMA of 1/8/25 and 0.65mol% of AIBN.

4.2 Characterizations

4.2.1 Affinity responses

The first characterization is the affinity of the imprinted polymer (and the corresponding non imprinted reference polymer) for the template cortisol. Here, a binding assay with a constant concentration of analyte (10 μ M) and a growing concentration of polymer in dichloromethane was performed. A first and simple screening of the polymers was done with only two different concentrations of polymer (5 and 20 mg/mL). Then, we chose the polymers that seemed the most promising to test them up to 40 mg/mL. Binding isotherms are shown in appendix F. They represent the average molecular uptake by M_{co}^a and M_{co}^b and the error bars are the standard deviation. Some polymers showed very low binding of cortisol (for example see figure 72a). Some polymers presented a better adsorption of cortisol but no specificity (figure 72b), reference NIP binding almost the same quantity of cortisol than MIP. In other cases, we could observe a bigger amount of cortisol retained by MIP than by the reference, proving an imprinting effect (figure 72c).

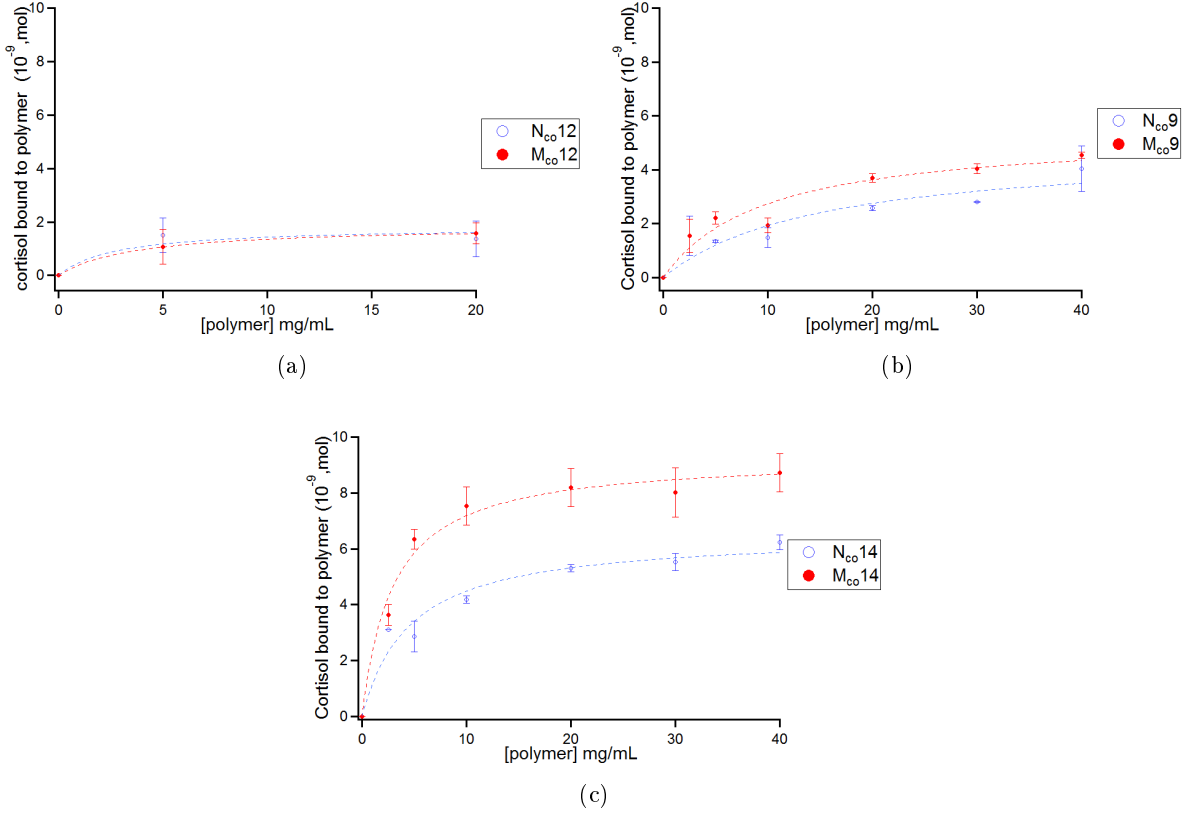


Figure 72: Three different types of adsorption isotherms observed in the design of experiments. (a) M_{co12} , N_{co12} , (b) M_{co9} , N_{co9} and (c) M_{co14} , N_{co14} . Error bars represent the standard deviation between polymers *a* and *b*.

We focused on the maximum of molecules bound to the polymer, B_{max} , the polymer concentration required to bind half of the maximum target K_{50} , and the imprinting factor IF calculated for the maximum polymer concentration tested (20 or 40 mg/mL) and these binding parameters are summarized in table 12.

B_{max} , K_{50} and IF are the responses of the design. The coefficients of the modeled polynomial equations are reported in table 13. These coefficients are calculated for the average results of M_{co}^a and M_{co}^b (with all the variability that polymer synthesis can create). The determination coefficients ($R^{2(a,b)}$) for K_{50} and IF are quite low. R^{2a} and R^{2b} are also specified in the table, and show that each design modeled well the experiments. The two designs studied together introduce some variability in the results. However, we observed that the inputs have the strongest influence on B_{max} , which presents a good determination coefficient, and the most influencing input will present the same optimum for the designs studied separately or together.

Polymer	K_{50} (mg/mL)	B_{max} (nmol)	IF
$M_{co}^{a,b}8$	6.3	3.9	2.3
$M_{co}^{a,b}9$	6.8	4.4	1.3
$M_{co}^{a,b}10$	0.4	1.1	1.1
$M_{co}^{a,b}11$	3.0	1.8	1.1
$M_{co}^{a,b}12$	2.8	1.6	1.1
$M_{co}^{a,b}13$	6.9	8.1	2.5
$M_{co}^{a,b}14$	2.6	8.7	1.5
$M_{co}^{a,b}15$	5.8	3.9	1.1
$M_{co}^{a,b}16$	0.8	2.6	1.4
$M_{co}^{a,b}17$	7.6	4.4	1.3
$M_{co}^{a,b}18$	2.5	2.2	1.6
$M_{co}^{a,b}19$	8.2	7.0	1.9
$M_{co}^{a,b}20$	12.7	4.9	2.6

Table 12: Binding parameters measured for the polymers synthesized according to the DOE. Binding assays were led in dichloromethane with an initial concentration of cortisol at 10 μ M.

	$y_1=K_{50}$	$y_2=B_{max}$	$y_3=IF$
j	1	2	3
β_{j0}	6.00	3.60	2.00
β_{j1} (MAA)	0.13	1.12*	0.019
β_{j2} (EDMA)	-1.28	-3.40*	-0.26
β_{j3} (AIBN)	1.84	0.50	0.30
β_{j11}	0.13	-0.65	-0.40
β_{j22}	-3.74	1.85	-0.69
β_{j33}	0.43	0.24	-0.50
β_{j12}	0.009	-0.005	0.002
β_{j13}	-0.20	0.72	0.09
β_{j23}	0.09	-1.17	-0.30
	$R^{2(a,b)}=0.26$ $R^{2(a)}=0.50$ $R^{2(b)}=0.95$	$R^{2(a,b)}=0.87$ $R^{2(a)}=0.98$ $R^{2(b)}=0.99$	$R^{2(a,b)}=0.34$ $R^{2(a)}=0.65$ $R^{2(b)}=0.76$

Table 13: Normalized coefficients of the polynomial responses calculated for the design of experiments. *are the coefficients for which $p \leq 0.05$.

Data analysis can be simplified by the plot of the responses. The surface representation of y_i as function of the MAA and EDMA ratios for a fixed value of AIBN mole% are plotted. Plots are then superimposed for the three different levels of AIBN mole%, covering then the interval of AIBN values.

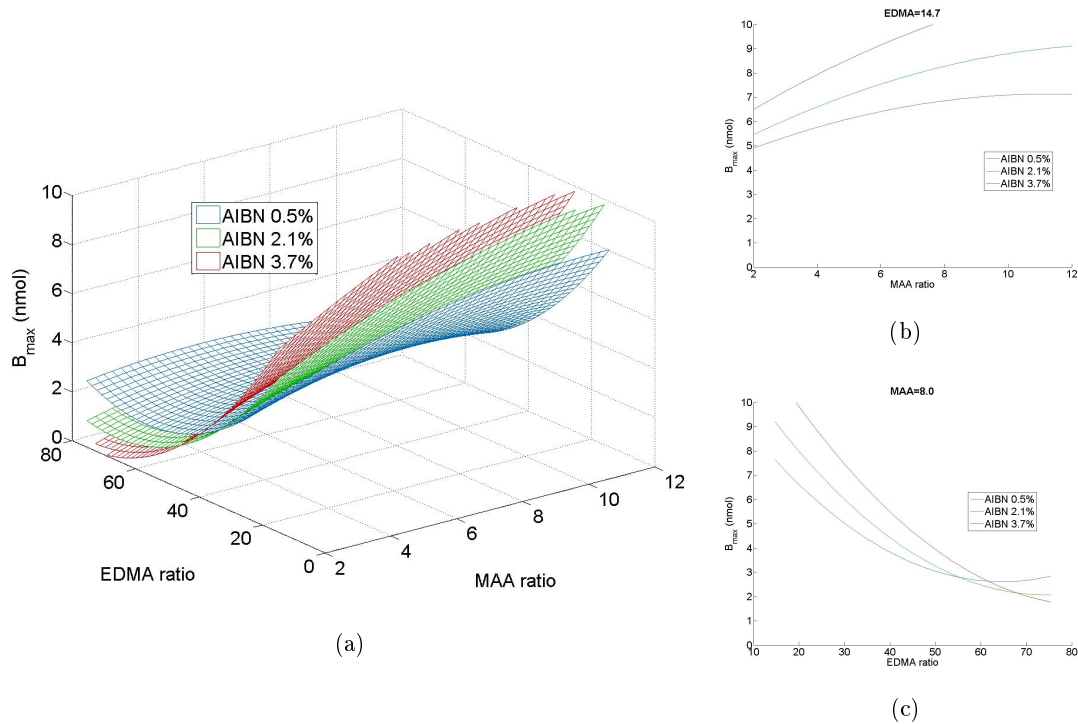


Figure 73: Plot of the response B_{max} as a function of MAA and EDMA ratios. (b) and (c) are cutting planes of the surface response (a).

The B_{max} response is observed on figure 73. Figures 73b and 73c are cutting planes for fixed values of MAA and EDMA. A high ratio of MAA with a low ratio of EDMA tends to increase the value of B_{max} . The quantity of AIBN should be fixed at its highest value. The surface plots are non parallel, this indicates a non linear effect of the parameters. The cross-linker and functional monomer ratios present significant coefficients with the treatment of both polymers M_{co}^a and M_{co}^b . To explain their joint role, B_{max} was plotted as a function of the cross-linking density (CL%). This variable takes into account both the MAA and EDMA quantities (equation 4.2, where n_i is the mole number of component i).

$$CL\% = \frac{n_{EDMA}}{n_{EDMA} + n_{MAA}} \quad (4.2)$$

The plots of B_{max} as a function of the cross-linking density of MIPs and NIPs are represented in figure 74. The quantity of cortisol retained by the polymer decreases with high densities of cross-linking. This is not surprising because the quantity of functional monomer is lower and the polymer networks are very rigid. When the cross-linking decreases, NIPs bind cortisol by non specific

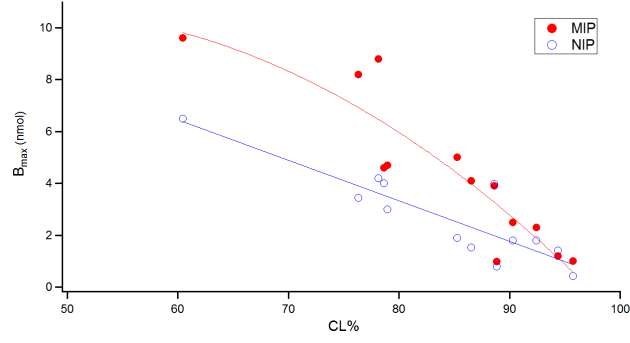


Figure 74: Evolution of B_{max} versus the cross-linking density for polymers of the Doehlert design.

adsorption and the B_{max} rises steadily. MIPs, however, present both non specific adsorption and imprinting effect. Their B_{max} increases faster than NIPs ones. A potential optimum may appear for a cross-linking density around 60%. If the cross-linking density is further decreased, the polymer would be too flexible to favor imprinting. Thus, a decrease in cross-linking to 60% would optimize B_{max} , but this should not be at the expense of the imprinting effect.

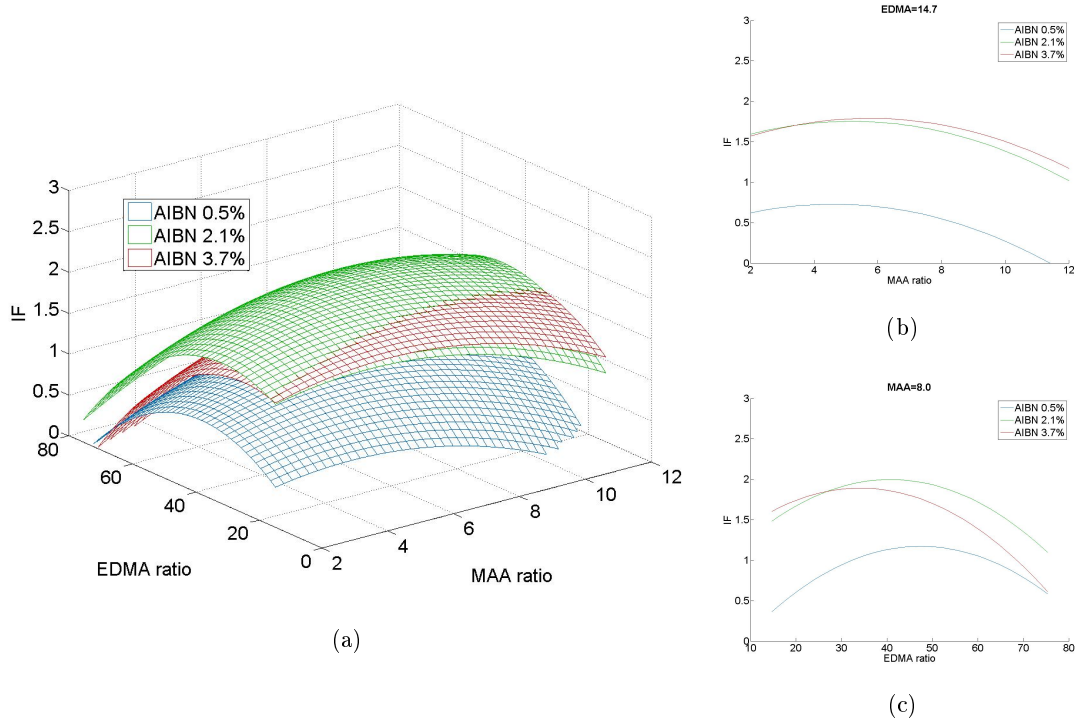


Figure 75: Plot of the IF response as a function of MAA and EDMA ratios. (b) and (c) are cutting planes of the surface response (a).

The imprinting factor, IF, is represented in figure 75. We observed that the effects of the parameters are less important than for B_{max} . The initiator should be incorporated in a higher amount than 2.1%, because low quantities lead to an imprinting factor under or around 1. As for MAA and EDMA, a small optimum appears in the middle of their ranges of variation.

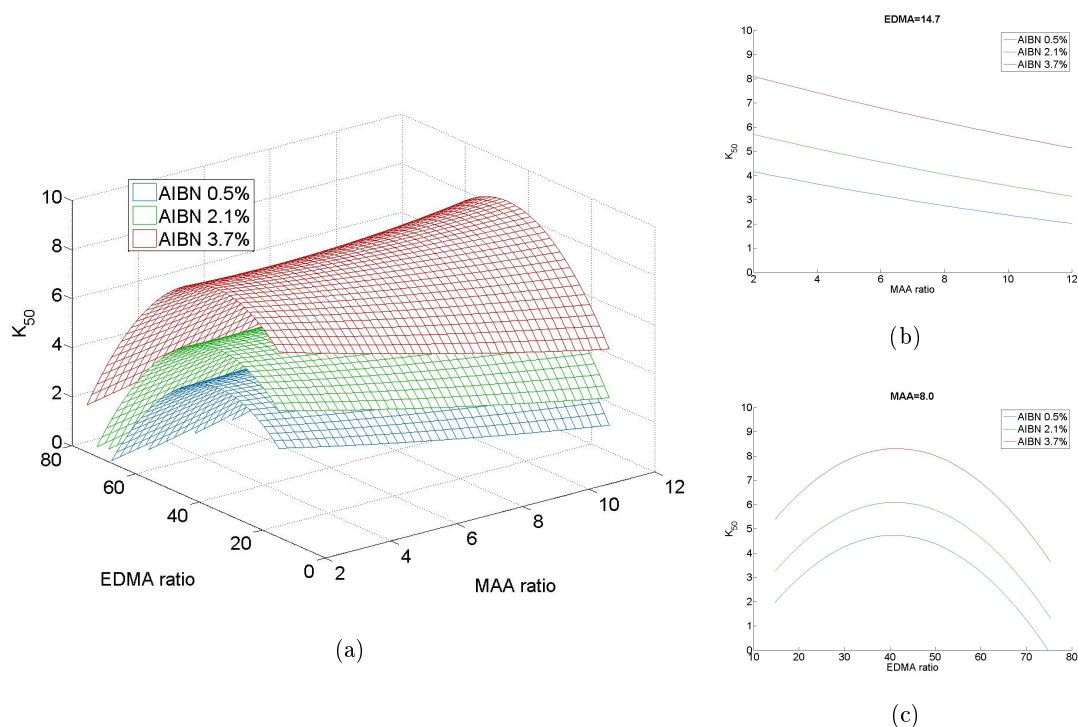


Figure 76: Plot of the K_{50} response as a function of MAA and EDMA ratios. (b) and (c) are cutting planes of the surface response (a).

Figure 76 is the representation of the K_{50} response. K_{50} reflects both the specificity and the capacity of the polymer (as we don't know the number of imprinted sites). K_{50} should be minimized to improve the selectivity and capacity of the polymer. The response plot shows that either a high or low ratio of EDMA leads to a small K_{50} with an optimum around 40. The higher the amount of MAA, the lower is K_{50} , *idem* for AIBN. Indeed, a high ratio of MAA offers numerous binding sites and subsequently a lower K_{50} . With higher quantities of AIBN, the polymerization reaction is launched faster and the polymer chains are shorter, which may improve the selectivity of the polymer.

These first analyses set some tendencies for the ratios of MAA and EDMA and the quantity of AIBN, but some of them are contradictory or do not lead to a clear optimum. Thus, multiobjective optimization (MOO) was used to clarify the results and determine the best compromise.

The MOO consists in setting the desirability of the responses (*i.e.* what is good). The performance of a MIP formulation is measured with respect to the objectives. In this design, they were: the lowest K_{50} and the highest B_{max} and IF. The optimized formulation of polymer should compromise all the parameters (with their modeled influences) to get close to the objectives. The calculated optimal formulation is the molar ratio of **template/MAA/EDMA 1/8/14.7** and 3.0 mol% of polymerizable bonds for AIBN. That's why we chose these values to fix the MAA and EDMA ratios in the onset plots of figures 73, 75 and 76. The separate studies of design *a* and design *b* give an

optimum formulation of a 14.7 ratio for EDMA too. The ratio of MAA and the quantity of AIBN are a bit different, but we saw previously that they had a weak significance. The best modeled response is B_{max} and this is also the only response where the MAA ratio is significant.

Finally, this design and the study of the affinity responses, showed that the cross-linker plays an important role in the formulation of cortisol imprinted polymers and should be optimized with a molar ratio template/cross-linker 1/14.7.

4.2.2 Porosity responses

Polymers synthesized for the second time (M_{co}^b) were also characterized by porosimetry. This study was performed to evaluate the evolution of the pore structures in a panel of polymers synthesized in the same solvent (with a constant solvent volume) and its potential effect on imprinting efficiency.

The pores of a solid material are described by their geometry, their size and size distribution. Three types of pores are distinguished by their size: macropores (width ≥ 50 nm), mesopores ($2 \leq \text{width} \leq 50$ nm) and micropores (width ≤ 2 nm). In the case of MIPs, polymers have large permanent pores and a high specific area that ensure the cavities formed by the imprinting (0.5-1.5 nm) to be accessible [30]. SEM images of a polymer MAA-co-EDMA show the difference of pores sizes (figure 77).

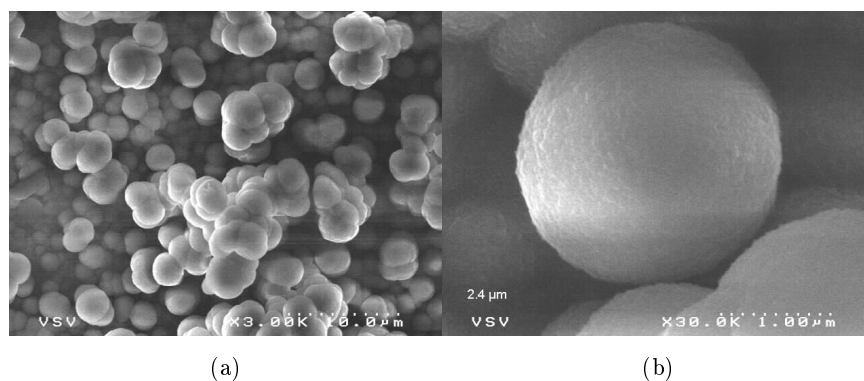


Figure 77: SEM images of a poly(MAA-co-EDMA). (a) Macropores, (b) mesopores in the sphere.

Pores are formed during the polymerization process, it starts with the decomposition of the radical initiator. Polymer chains then grow and progressively form a gel, called nuclei, that precipitates (either because of high cross-linking or because of its low solubility in the solvent). Polymerization continues and the growing nuclei collapse and form globules. Globules can get in contact and cross-link together, forming clusters. At the end of polymerization, globules and clusters form the units of the macroporous polymer. The voids between globules are filled with solvent and become the pores. Larger pores are therefore obtained with poor solvent (earlier precipitation) and smaller pores with

good solvent (solubilize longer polymers chains and delays precipitation and nuclei formation).

In the Doehlert design, the specific surface areas were determined by BET measurements (Brunauer-Emmett-Teller). Further adsorption isotherms of N_2 led us to the evaluation of pore size and volume with the BJH method (Barret-Joyner-Halenda) applied on the desorption branch of the isotherm. Several types of isotherms were observed. For example, in figure 78a, it is a type IV (according to the IUPAC classification): the polymer is mesoporous and a big hysteresis is displayed between the adsorption and the desorption, due to capillary condensation. In figure 78b, the isotherm is a type II: it is still a mesoporous material but there is no hysteresis and adsorption is multimolecular. Data collected by these porosity analyses are summarized in table 14 and all the isotherms are in appendix G. Specific area varied in a large interval, from 4.8 to 236.7 m^2/g . Pores size went from 3.55 to 13.88 nm and pore volume from 0.01 to 0.66 cm^3/g . To interpret these results, the data were studied as output responses of the Doehlert's design.

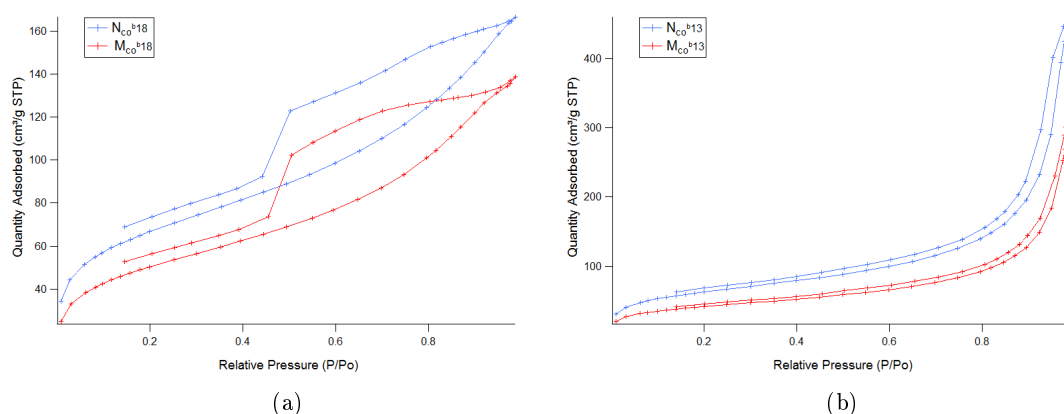


Figure 78: Adsorption and desorption isotherms of N_2 . (a) $M_{co}18$ and $N_{co}18$, (b) $M_{co}13$ and $N_{co}13$.

Modelized data give the coefficients of the polynomial responses (summarized in table 15). This time again, the data were analyzed thanks to response plots. Specific area, pore sizes and pore volume were plotted, for MIPs and NIPs, as functions of MAA ratio, EDMA ratio and were superimposed for the three levels of AIBN quantity.

Surface areas are slightly higher for NIPs than for MIPs. The presence of the template molecule can affect the polarity of the mixture, and thus, influence the surface area. Surface areas increase with increasing ratio of cross-linker (cf figure 79a and 79b). This phenomenon was also observed by Gagne and coll. [31]. The quantity of cross-linker may influence the solubility of the polymer chains and thus modify the surface area. MAA has a negative influence on the specific area, in particularly for the NIPs ($\beta_{11}(NIP) = -43.8$ and $\beta_{21}(MIP) = -2.7$). We assume that MAA monomers swell the nuclei during polymerization (they have a better affinity for the nuclei than for the solvent). Thus,

Polymer	Specific area (m ² /g)	Pore size (nm)	Pore Volume (cm ³ /g)
M _{co} 8 ^b	132.6	4.25	0.14
N _{co} 8 ^b	162.4	3.92	0.15
M _{co} 9 ^b	89.3	5.6	0.13
N _{co} 9 ^b	125.5	4.66	0.16
M _{co} 10 ^b	176.2	4.48	0.13
N _{co} 10 ^b	196.7	4.16	0.15
M _{co} 11 ^b	4.84	8.52	0.01
N _{co} 11 ^b	156.3	3.55	0.11
M _{co} 12 ^b	117.8	4.08	0.10
N _{co} 12 ^b	189.3	3.59	0.12
M _{co} 13 ^b	151.3	13.88	0.45
N _{co} 13 ^b	227.9	13.56	0.66
M _{co} 14 ^b	42.9	13.39	0.13
N _{co} 14 ^b	58.7	12.73	0.22
M _{co} 15 ^b	85.2	4.72	0.1
N _{co} 15 ^b	111.7	4.01	0.03
M _{co} 16 ^b	13.8	3.99	0.02
N _{co} 16 ^b	147.2	3.67	0.09
M _{co} 17 ^b	39.2	6.76	0.09
N _{co} 17 ^b	91.6	13.5	0.04
M _{co} 18 ^b	180.3	4.47	0.19
N _{co} 18 ^b	236.7	4.48	0.22
M _{co} 19 ^b	157.6	10.88	0.39
N _{co} 19 ^b	164.0	9.80	0.34
M _{co} 20 ^b	198.8	6.04	0.26
N _{co} 20 ^b	162.6	3.93	0.14

Table 14: Porosity parameters measured for the polymers synthesized according to the design of experiments.

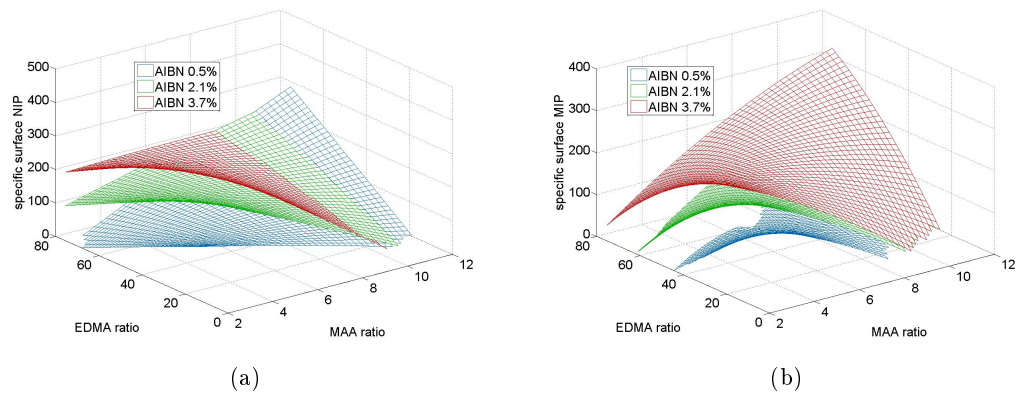


Figure 79: Plot of the specific area as a function of EDMA and MAA molar ratios for (a) NIPs and (b) MIPs.

	y₁=spec surf NIP	y₂=spec surf MIP	y₃=pore size NIP	y₄=pore size MIP	y₅=pore volume NIP	y₆=pore volume MIP
j	1	2	3	4	5	6
β_{j0}	162.4	132.59	3.92	4.25	0.15	0.14
β_{j1} (MAA)	-43.83	-2.71	0.85	0.27	-0.05	-0.01
β_{j2} (EDMA)	26.07	-5.21	-5.85	-4.15	-0.15	-0.13
β_{j3} (AIBN)	43.48	81.38	-1.42	1.21	0.11	0.13
β_{j11}	-5.01	-29.02	0.21	0.59	-0.01	-0.03
β_{j22}	-1.70	-42.03	6.04	7.56	0.18	0.06
β_{j33}	-13.49	-12.45	3.41	0.80	-0.05	0.04
β_{j12}	121.00	161.59	0.83	-2.05	0.28	0.25
β_{j13}	-75.92	-17.71	-3.93	0.44	-0.15	-0.04
β_{j23}	-5.84	52.23	3.11	-0.28	-0.08	-0.03
	R ² =0.96	R ² =0.97	R ² =0.97	R ² =0.94	R ² =0.87	R ² =0.95

Table 15: Normalized coefficients of the polynomial responses calculated for the porosity of polymers from the design of experiments.

once the nuclei are swollen, they are larger and the specific surface is smaller. In case of the MIPs, MAA monomers form complexes with cortisol and may be less available for diffusion in the nuclei. The greatest specific areas were observed for the highest ratios of both EDMA and MAA, which is explained by the quantity of material involved. The quantity of AIBN enhances the specific area of the MIPs. A higher amount of initiator leads to shorter polymer chains, and thus they precipitate later in the polymerization process, creating smaller globules and larger specific areas. The plots of NIPs specific surface display a different role of AIBN, this is not a linear influence of AIBN but rather a crossed influence of MAA-AIBN and EDMA-AIBN. Here again, the presence or absence of the template seems to be important.

The evolution of the pore volume is very similar for both NIPs and MIPs (figure 80a and 80b). Higher quantities of MAA decrease the cumulative pore volume. EDMA has the same effect. Polymers were synthesized with a constant solvent volume, thus while MAA and/or EDMA increase, the porosity decreases. AIBN has a positive effect on the pore volume. A larger quantity of AIBN launches more polymer chains and this rhymes with larger specific areas and porosity volume.

The last porosity response is pore size (figure 81a and 81b). It seems to strongly depend on the cross-linker ratio and to be quite independent of the MAA ratio and the quantity of AIBN, at least for MIPs. It is easier to explain evolution of pore size with cross-linking density. Pore size was plotted against the cross-linking density (figure 82). It displays a sudden decrease for the pore size: around 80% pore size decreases from 14 nm to 5 nm. Frechet and coll. explained that, as soon

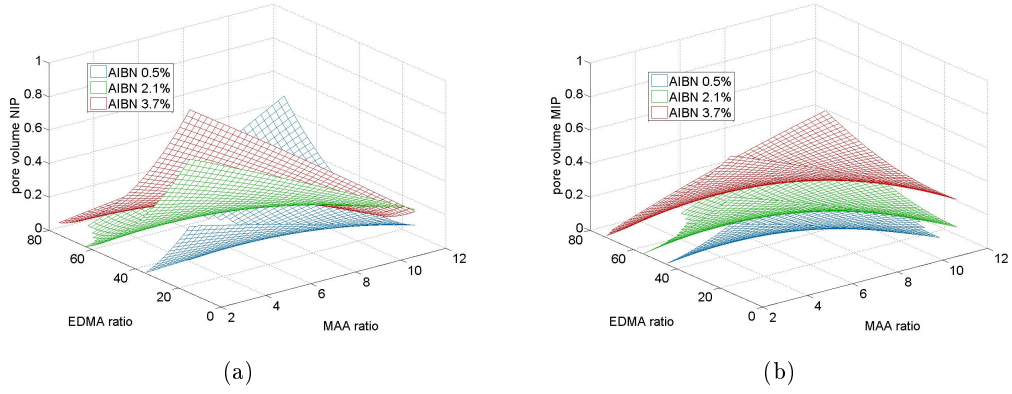


Figure 80: Plot of the pore volume as a function of EDMA and MAA molar ratios for (a) NIPs and (b) MIPs.

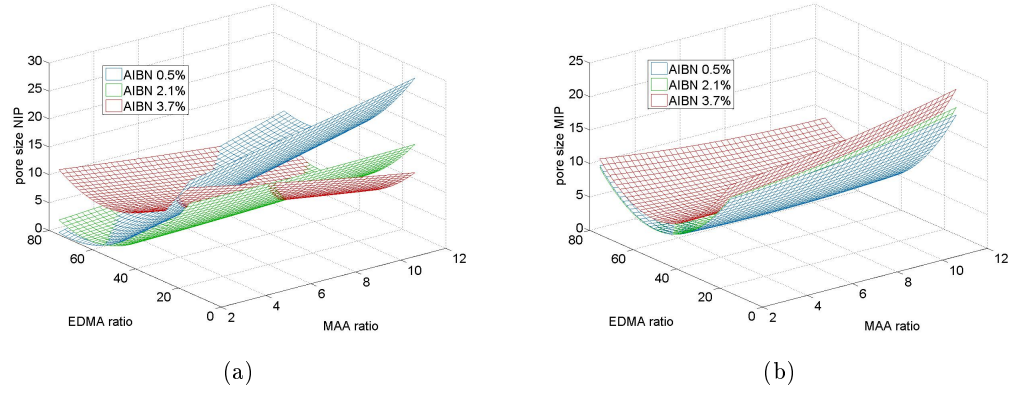


Figure 81: Plot of the pore size as a function of EDMA and MAA molar ratios for (a) NIPs and (b) MIPs.

as the polymerization starts, cross-linking density is already high in the nuclei and leads to early phase separation [32]. As nuclei are more cross-linked, they don't swell much with surrounding non polymerized monomers and are relatively small. The final polymer structure is therefore made of small globules and consequently smaller pores. It is tempting to think that a threshold appears in the pore size around 80% of cross-linking.

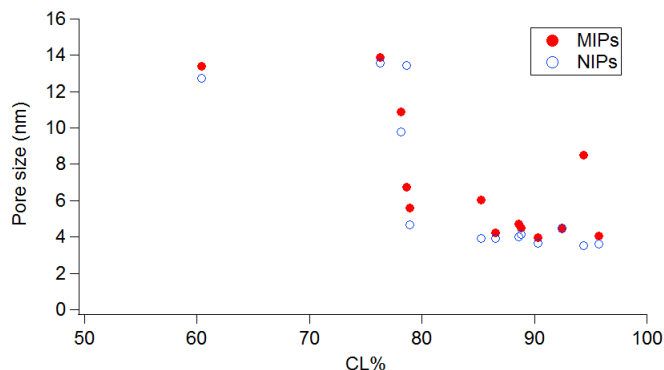


Figure 82: Evolution of the pore size against the cross-linking density for polymers of the Doehlert design.

4.2.3 Correlations between porosity and affinity responses

Physical characterization of the polymers was also performed to understand the morphological effects on molecular recognition. It consists in studying the correlations between binding affinity responses and porosity responses. M_{co}^b responses were only used here, since porosity measurements were only done for these polymers.

To study the evolution of the imprinting factor with specific area, IF was plotted as a function of the difference between the specific areas of NIPs and MIPs (figure 83). With a large difference in specific areas between the MIP and its corresponding non imprinted reference polymer, the imprinting factor is likely to be small. On the opposite, the greatest imprinting factors are observed for polymers with similar specific areas. We first assume, that the template plays a role in polymer morphology, which explains the differences in specific areas between MIPs and NIPs. Thus, a small difference between the specific areas could be a necessary but insufficient condition to observe an imprinting effect. This is represented by the dotted line on figure 83.

Pores size does not show any influence on the imprinting factor. On the contrary, an increase in

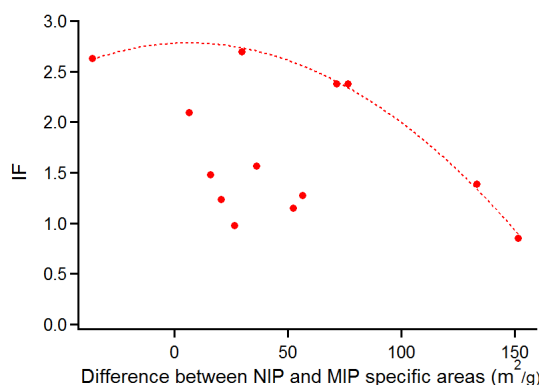


Figure 83: Evolution of the imprinting factor against the difference between NIPs and MIPs specific area for the polymers of the Doehlert design.

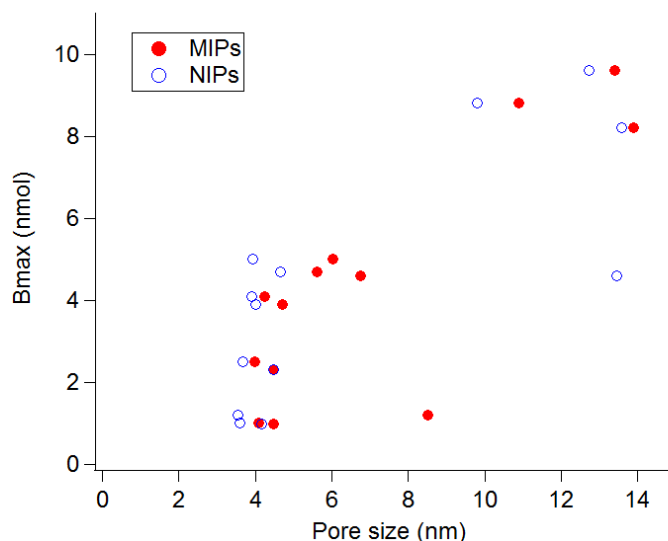


Figure 84: Evolution of B_{max} against the pore size for the polymers of the Doehlert design. Filled red symbols represent MIPs, blue empty symbols represent NIPs, identical symbols represent a MIP and its reference NIP.

the total pore volume is logically linked to a higher IF.

The maximum quantity of cortisol retained by the polymers is linked to pore size (figure 84). The class of pores with a size around 4 nm has moderate B_{max} (1-5 nmol); with bigger pores, B_{max} increases, up to 9.5 nmol ($M_{co}^b 14$). There is a threshold for pores between 4.5 nm and 10 nm. It is observed for both MIPs and NIPs. Larger pores may enable penetration of solvated cortisol and leads to a better molecule adsorption.

Porosity properties of the imprinted polymers may give hints to optimize polymer formulations. Indeed, the maximum amount of template recognized by the polymer can be increased with a higher porosity and particularly with larger pores sizes. The imprinting factor seems to be enhanced with MIPs and NIPs presenting close specific areas. In conclusion, a combination of optimized porosity properties has a positive influence on the binding parameters of MIPs.

4.3 Validation of the study

The multi-objective optimization combined with the experimental design drove us to synthesize the polymer $M_{co}21$ with molar ratios of cortisol/MAA/EDMA of 1/8/14.7 and with AIBN at a concentration of 3.0 mol% of polymerizable groups. The cross-linking density is of 64%. As expected, the pores are large (16.3 nm) and this is correlated to a very good binding ability ($B_{max}=9.6$ nmol). On figure 85, we compare the binding isotherm for this polymer and the first polymer, $M_{co}6$, synthesized prior to the design (molar ratios cortisol/MAA/EDMA of 1/8/25 and AIBN 0.65 mol%). B_{max} is higher for the optimized formulation and the K_{50} is also better. The imprinting factor is smaller

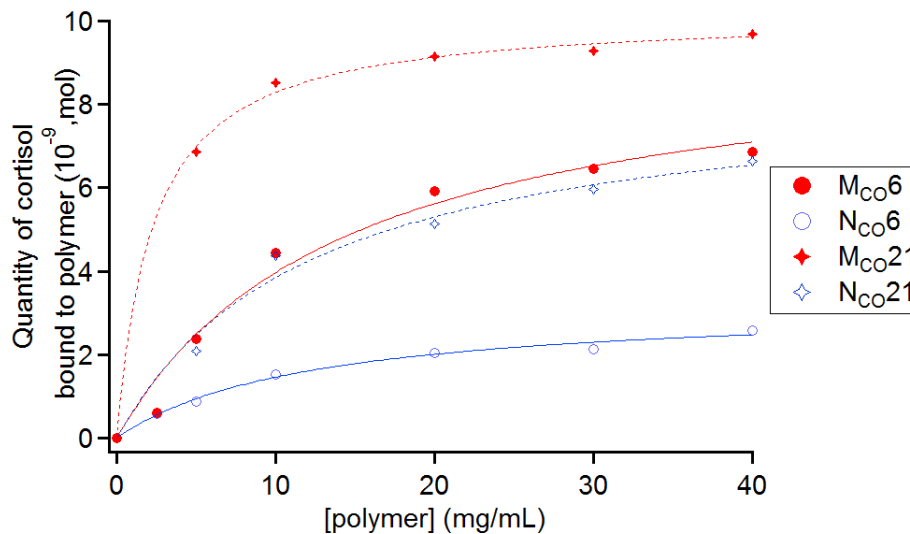


Figure 85: Binding isotherm of cortisol ($10 \mu\text{M}$) to the polymers in dichloromethane. Comparison of the first polymer developed (M_{co6}) and the optimized formulation (M_{co21}).

	M_{co6}	M_{co21}	Predicted response
K_{50} (mg/mL)	7.8	2.0	5.2
B_{max} (nmol)	7.7	9.6	9.3
IF	2.7	1.5	1.8

Table 16: Parameters for the binding affinity of the polymers prior (M_{co6}) and after (M_{co21}) optimization and the predicted values.

however. We resume the parameters in table 16. The values that were predicted by the model are close to the values obtained with the optimized formulation, except for K_{50} which is much smaller than predicted.

The design of experiments that we performed led us to a formulation with a good template recognition and an improved selectivity. Even if the imprinting factor is smaller than the initial value, B_{max} was slightly increased and we obtained a K_{50} four times smaller.

5 Conclusion

In order to monitor stress and prevent its consequences on human health and behaviour, we proposed in this chapter to detect adrenaline and cortisol, two hormonal biomarkers of stress. Polymers imprinted with adrenaline did not show any interesting imprinting. Indeed, the molecule appears to degrade really fast. Other types of polymers, such as sol-gel, could be tested to imprint adrenaline but this would not be compatible with the sensor we want to elaborate. As we were not sure that adrenaline can be detected in sweat, we mainly focused on the glucocorticoid cortisol, a steroid that had already been imprinted by others. A few papers relate formulations of MIPs for cortisol but none of the ones tested were satisfying as they did not display a good imprinting. First, basic trial-and-error tests were used for new formulations. This drove us to synthesize a poly-MAA-co-EDMA in dichloromethane. The formation of a complex between cortisol and the functional monomer in dichloromethane was proved with NMR interaction studies. The Job's plots attested the complex formation. Then, starting from the first formulation of MIP, the influence of the quantities of monomers and initiator in the formulations were investigated, thanks to a Doehlert design of experiments. This drove us to minimize the quantity of cross-linker, which appeared to be the most significant factor in the study. We worked further with the design of experiments by studying the porosity of the polymers. Here, the influence of pore size was highlighted, since larger pores foster adsorption in the cavities. We also underlined that MIPs and NIPs have different morphologies, due to the presence of the template. As cortisol forms a complex with methacrylic acid, it makes MAA less available to swell the nuclei during the polymerization process, driving to greater specific areas in NIPs than MIPs. Finally, an optimized formulation for an imprinted polymer was obtained for cortisol, a pertinent stress biomarker.

Bibliography

- [1] L. T. (Fraunhofer Institute), “A vest to measure stress,” 2008.
- [2] D. Talbot, “Wrist sensor tells you how stressed out you are,” 2012.
- [3] H. Selye, *The Stress of Life*. Schaum Outline Series, new york: ed., 1956.
- [4] W. B. Cannon, *Bodily changes in pain, hunger, fear and rage, an account of recent researches into the function of emotional excitement*. New-York and London D.Appleton company, 1915.
- [5] M. Pruessner, “Self-Reported Depressive Symptoms and Stress Levels in Healthy Young Men: Associations With the Cortisol Response to Awakening,” *Psychosomatic Medicine*, vol. 65, pp. 92–99, Jan. 2003.
- [6] A. Taylor and S. Schatz, “Measuring the Effectiveness of Stress Prevention Programs in Military Personnel,” in *Foundations of Augmented Cognition. Directing the Future of Adaptive Systems* (D. D. Schmorow and C. M. Fidopiastis, eds.), vol. 6780 of *Lecture Notes in Computer Science*, pp. 636–646, Berlin, Heidelberg: Springer Berlin Heidelberg, 2011.
- [7] E. D. Weitzman, D. Fukushima, C. Nogueira, H. Roffwarg, T. F. Gallagher, and L. Hellman, “Twenty-four Hour Pattern of the Episodic Secretion of Cortisol in Normal Subjects,” *Journal of Clinical Endocrinology & Metabolism*, vol. 33, pp. 14–22, July 1971.
- [8] K. J. Collins, J. D. Few, T. J. Forward, and L. A. Giec, “Stimulation of adrenal glucocorticoid secretion in man by raising the body temperature,” *The Journal of physiology*, vol. 202, pp. 645–60, June 1969.
- [9] M. Schedlowski, R. Jacobs, G. Stratmann, S. Richter, A. Hädicke, U. Tewes, T. O. Wagner, and R. E. Schmidt, “Changes of natural killer cells during acute psychological stress,” *Journal of clinical immunology*, vol. 13, pp. 119–26, Mar. 1993.
- [10] R. F. Walker, D. Riad-Fahmy, and G. F. Read, “Adrenal status assessed by direct radioimmunoassay of cortisol in whole saliva or parotid saliva,” *Clinical chemistry*, vol. 24, pp. 1460–3, Sept. 1978.
- [11] S. T. Trifonova, M. Gantenbein, J. D. Turner, and C. P. Muller, “The use of saliva for assessment of cortisol pulsatile secretion by deconvolution analysis,” *Psychoneuroendocrinology*, vol. 38, pp. 1090–101, July 2013.
- [12] J. Smyth, “Stressors and mood measured on a momentary basis are associated with salivary cortisol secretion,” *Psychoneuroendocrinology*, vol. 23, pp. 353–370, May 1998.
- [13] P. Moleman, J. H. Tulen, P. J. Blankestijn, A. J. Man in ’t Veld, and F. Boomsma, “Urinary excretion of catecholamines and their metabolites in relation to circulating catecholamines. Six-hour infusion of epinephrine and norepinephrine in healthy volunteers,” *Archives of general psychiatry*, vol. 49, pp. 568–72, July 1992.
- [14] R. P. Nikolajsen and A. s. M. Hansen, “Analytical methods for determining urinary catecholamines in healthy subjects,” *Analytica Chimica Acta*, vol. 449, pp. 1–15, Dec. 2001.
- [15] M. M. Kushnir, A. L. Rockwood, G. J. Nelson, A. H. Terry, and a. W. Meikle, “Liquid chromatography-tandem mass spectrometry analysis of urinary free cortisol,” *Clinical chemistry*, vol. 49, pp. 965–7, June 2003.
- [16] J. Nichols and A. T. Miller, “Excretion of Adrenal Corticoids in the Sweat,” *Experimental Biology and Medicine*, vol. 69, pp. 448–449, Dec. 1948.

- [17] M. E. Jenkins, M. A. Rivarola, S. W. Brusilow, and C. J. Migeon, "Excretion of 4-14C-cortisol and 1,2-3H-D-aldosterone in Human Thermal Sweat," *Journal of Clinical Endocrinology & Metabolism*, vol. 29, pp. 1102–1106, Aug. 1969.
- [18] A. García-cortés, J. Martí, I. Sayago, J. P. Santos, J. Gutiérrez, and M. C. Horrillo, "Detection of stress through sweat analysis with an electronic nose," in *Spanish conference on electron devices*, (santiago de compostela), pp. 1–4, 2009.
- [19] J. Matsui, K. Akamatsu, S. Nishiguchi, D. Miyoshi, H. Nawafune, K. Tamaki, and N. Sugimoto, "Composite of Au nanoparticles and molecularly imprinted polymer as a sensing material.," *Analytical chemistry*, vol. 76, pp. 1310–5, Mar. 2004.
- [20] R. Suedee, V. Seechamnaturakit, B. Canyuk, C. Ovatlarnporn, and G. P. Martin, "Temperature sensitive dopamine-imprinted (N,N-methylene-bis-acrylamide cross-linked) polymer and its potential application to the selective extraction of adrenergic drugs from urine.," *Journal of chromatography. A*, vol. 1114, pp. 239–49, May 2006.
- [21] M. Bouri, M. J. Lerma-García, R. Salghi, M. Zougagh, and A. Ríos, "Selective extraction and determination of catecholamines in urine samples by using a dopamine magnetic molecularly imprinted polymer and capillary electrophoresis," *Talanta*, vol. 99, pp. 897–903, Sept. 2012.
- [22] C. Liang, H. Peng, A. Zhou, L. Nie, and S. Yao, "Molecular imprinting polymer coated BAW bio-mimic sensor for direct determination of epinephrine," *Analytica Chimica Acta*, vol. 415, pp. 135–141, June 2000.
- [23] G. B. West, "Oxidation of adrenaline in alkaline solution," *British Journal of Pharmacology and Chemotherapy*, vol. 2, pp. 121–130, June 1947.
- [24] A. S. Al-Ayed, H. A. Al-Lohedan, M. Z. A. Rafiquee, M. S. Ali, and Z. A. Issa, "Kinetics of the autoxidation of adrenaline and [copper(II)(adrenaline)]²⁺ in alkaline aqueous and micellar media," *Transition Metal Chemistry*, vol. 38, pp. 173–181, Dec. 2012.
- [25] M. Lasakova, D. Thiébaud, P. Jandera, and V. Pichon, "Molecularly imprinted polymer for solid-phase extraction of ephedrine and analogs for human plasma," *Journal of separation science*, vol. 32, no. 7, pp. 1036–1042, 2009.
- [26] O. Ramström, L. Ye, and K. Mosbach, "Artificial antibodies to corticosteroids prepared by molecular imprinting.," *Chemistry & biology*, vol. 3, pp. 471–7, June 1996.
- [27] C. Baggiani, P. Baravalle, C. Giovannoli, L. Anfossi, and G. Giraudi, "Molecularly imprinted polymers for corticosteroids: analysis of binding selectivity.," *Biosensors & bioelectronics*, vol. 26, pp. 590–5, Oct. 2010.
- [28] C. Baggiani, "Chromatographic characterization of a molecular imprinted polymer binding cortisol," *Talanta*, vol. 51, pp. 71–75, Jan. 2000.
- [29] K. Sreenivasan, "On the Application of Molecularly Imprinted Poly (HEMA)," *Journal of applied Polymer Science*, vol. 71, pp. 1819–1821, 1999.
- [30] S. Wei and B. Mizaikoff, "Binding site characteristics of 17beta-estradiol imprinted polymers.," *Biosensors & bioelectronics*, vol. 23, pp. 201–9, Oct. 2007.
- [31] C.-l. Effects, B. P. Santora, and M. R. Gagne, "Porogen and Cross-Linking Effects on the Surface Area, Pore Volume Distribution, and Morphology of Macroporous Polymers Obtained by Bulk Polymerization," *Macromolecules*, vol. 34, pp. 658–661, 2001.
- [32] C. Viklund, F. Svec, and J. M. J. Fre, "Monolithic , " Molded ", Porous Materials with High Flow Characteristics for Separations , Catalysis , or Solid-Phase Chemistry : Control of Porous Properties during Polymerization," *Chem. Mater.*, vol. 8, no. 5, pp. 744–750, 1996.

CHAPTER IV

Elaboration of an optical biosensor

1 Towards a new optical sensor

In this chapter, we aim at combining a MIP as the specific recognition element with a mean of optical transduction in order to develop a sensor for analyte detection in body fluids. Several possibilities were considered for transduction. Photonic crystals are interesting candidates as they do not require labeling or a specific optical property of the target analyte. Inverse opals are well-known photonic crystal materials, and a MIP in the form of an inverse opal will offer large specific surface area with an optimized accessibility to the recognition sites and thus they optimize the sensitivity of the sensor. At the same time direct label-free analyte detection is possible, and thus we chose this combination to develop a device. The principles of the sensor are represented in figure 86. Upon recognition of the solvated analyte, the structure swells and this leads to a shift in the reflected and transmitted wavelengths.

As a support material for the inverse opal structure, for the preliminary studies within this thesis, we chose polymethylmethacrylate (PMMA) sheets. These substrates can be easily cut in a required size (in our case, 0.9×4 cm, to fit in a spectrophotometric cell), they are transparent and enable measurements in transmission and last but not least, they resist the hydrofluoric acid treatment during inverse opal manufacturing. Unfortunately, PMMA does not resist to many solvents, and in particular not to dichloromethane and toluene used to synthesize MIPs for cortisol and cyproterone acetate respectively. We chose to demonstrate the principle of our sensor using a MIP imprinted

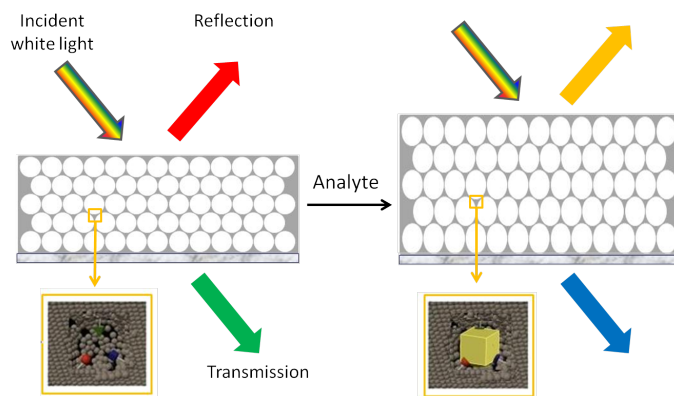


Figure 86: Principles of a sensor based on an imprinted polymeric inverse opal.

with 2,4-dichlorophenoxyacetic acid (2,4-D), a herbicide. A MIP for this molecule can be synthesized in methanol/water 4/1 (v/v), and can be used in aqueous media aswell [1]. This molecule is still of interest because it is a commonly used herbicide which rises environmental concerns, is associated to health risks and can be detected in body fluids [2] [3].

We will focus in the next sections on the different necessary steps to elaborate the sensor and on their optimization. Finally, we will test it in the presence of 2,4-D.

2 Opal formation

Opals are a natural example of photonic crystals whose main supplier in the world is Australia. The gemstones are deposited at relatively low temperature and may occur in fissures of many rocks. Opals show a large panel of colors, depending on their inner structure (figure 87a). They are composed of silica spheres in a hexagonal or cubic close-packed lattice. A SEM image of a volcanic opal shows the stacking of microspheres responsible for the stone color (figure 87b).

Synthetic opals have been fabricated by chemists. The first process was developed by Pierre Gilson in 1974 and is still used. The process takes up to 18 months but the opals really have different colors and the size of the stone can be chosen. Nowadays, it is also possible to imitate opals for different research fields at a laboratory scale. Indeed, monodisperse silica spheres have the particularity to self-assemble. These opals synthesized in research laboratories are called "imitation opals" since they are not made under the same temperature and pressure conditions as their natural counterparts. In the next sections, we will discuss some different possibilities to make the opals.

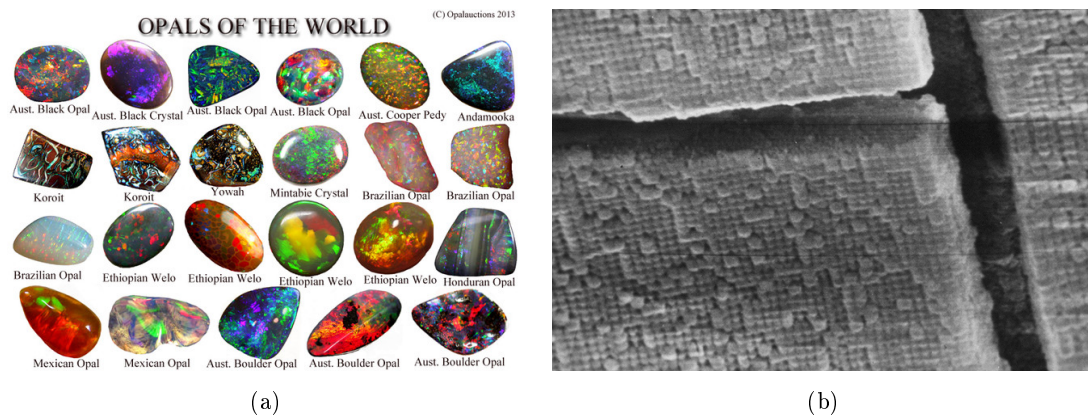
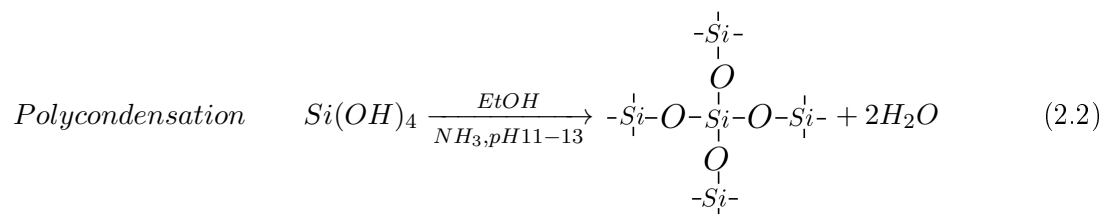
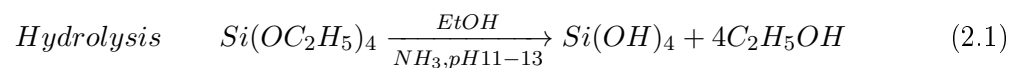


Figure 87: Natural opals. (a) Different opals found around the world [4] and (b) SEM image of a volcanic opal from Queensland where spheres have approximately a diameter of 300 nm.

2.1 Bead synthesis

Opals are basically a compact stack of silica spheres. Thanks to the process developed by Stöber, it is possible to synthesize monodisperse silica spheres [5]. The reaction comprises the basic hydrolysis of tetraethoxy silane (TEOS) leading to a tetrasilanol and a subsequent condensation to form solid germs of SiO_2 . This nucleation step is followed by their growth, *i.e.* the deposit of successive silica layers (equation 2.1 and 2.2). A short nucleation stage compared to the growth stage leads to more monodisperse particles.



When the synthesis is completed, the final diameter of the silica particles depends on the concentrations of TEOS/ NH_3 /water, the temperature, the solvent type and its ionic force [6]. Bogush and coll. demonstrated that it was also possible to pursue the growth stage by adding successive amounts of TEOS in a solution where silica particles are already formed. In this case, the diameter d of the particles is given by the initial amount of TEOS (n_0) and the added amounts (n), relatively to the initial size of the particles (d_0) (equation 2.3).

$$d = d_0 \left(\frac{n}{n_0} \right)^{\frac{1}{3}} \quad (2.3)$$

This synthesis is convenient for laboratory processes but is quite long and only produces small amounts. Other ways of synthesis have been developed for industrial production. During the thesis, the particles were synthesized by this method for producing opals by evaporation and dip-coating, but they were bought for the Boostream[®] process (outlined below).

The beads diameters were determined by light scattering with a zetasizer and a further confirmation was obtained by SEM images. Particles were also characterized by their size distribution, evaluated by polydispersity (PDI, it is the width of the particle size distribution, indices less than 0.1 are referred to as "monodisperse"). Particles synthesis and size measurements are summarized in table 17. An example of SEM image of P2 is given in figure 88.

With these silica beads, opals can be fabricated. Several ways of synthesis are commonly used in the literature and were explored in this thesis.

Particles	TEOS	NH ₃	Water	EtOH	Particle size	PDI
P1	7.29 mL	4.5 mL	16.97 mL	150 mL	120 nm	0.03
P2	0.67 mL	2.1 mL	3.94 mL	23.3 mL	290 nm	0.12
P3	0.67 mL	3.95 mL	1.55 mL	23.8 mL	670 nm	0.2
P4	3.35 mL	2.72 mL	6.2 mL	37.8 mL	420 nm	0.1

Table 17: Silica beads formulations and size characterization.

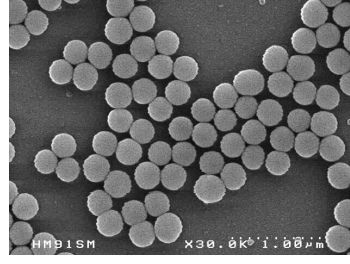


Figure 88: SEM image of synthesized silica beads P2. Their diameter is around 290 nm.

2.2 Evaporation

Historically, the silica beads stack was obtained by sedimentation. However, this yielded irregular, polycrystalline photonic crystals. Norris and coll. showed how to create a photonic crystal from a colloidal suspension of spheres *via* evaporation [7]. In this approach, a substrate is placed vertically in the colloidal suspension and, as the solvent evaporates, the meniscus is swept downwards and the particles are ordered on the surface. They developed this process for beads with a diameter up to 1 μm thanks to a temperature gradient which counteracts sedimentation. This technique is represented in figure 89.

Evaporation is nowadays the most common way of imitating opals at a laboratory scale. Scientists have developed their own techniques with a substrate placed at 45°, at a particular evaporation

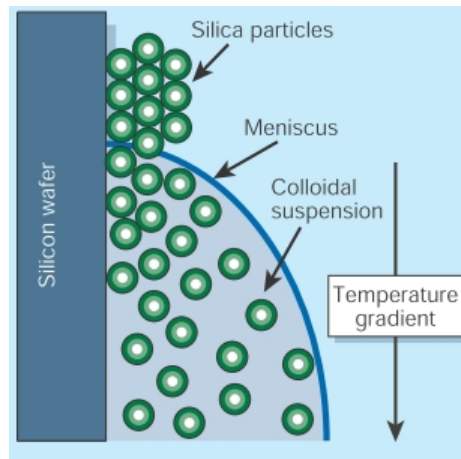


Figure 89: Schematical representation of opal synthesis performed by evaporation. Figure from [8].

temperature and in the absence of vibrations.

Several imitations of opals were made in this thesis by evaporation. Beads were dispersed in ethanol with a mass ratio of 1%, and were left to deposit on a vertical silicon substrate at 46 °C. After one night, all the solvent was evaporated and the substrates were placed in an oven at 180 °C for annealing. It consists in the condensation of surfacic silanol, thus forming covalent bounds between the particles and solidifying the structure. Optical and SEM images are given in figure 90. Concerning their macroscopic aspects, the deposits were often brittle. However, under normal incidence of white light, the substrates reflect only certain wavelengths and look slightly colored. Moreover, the SEM images confirm the self-assembly of silica spheres into a compact stack. Unfortunately, the samples are not uniform and two types of cracks were observed on all the samples:

- lines parallel to the solvent limit with a gradient in the density of the beads (as it can be observed in figures 90a and 90b). A change of color is clearly visible in parallel bands and the SEM image shows a dense area close to a few lonely spheres on the upper right corner. This is probably due to a fast evaporation. A lower temperature may help to suppress these bands.
- big parallelepipeds giving a snake skin aspect to the deposit (figure 90d). It seems that during drying, the structure shrinks. This is confirmed by the observation of the crystal domains around the cracks: they are continuous from one side of the cracks to the other. Inside those local areas, color is quite homogeneous (figure 90c).

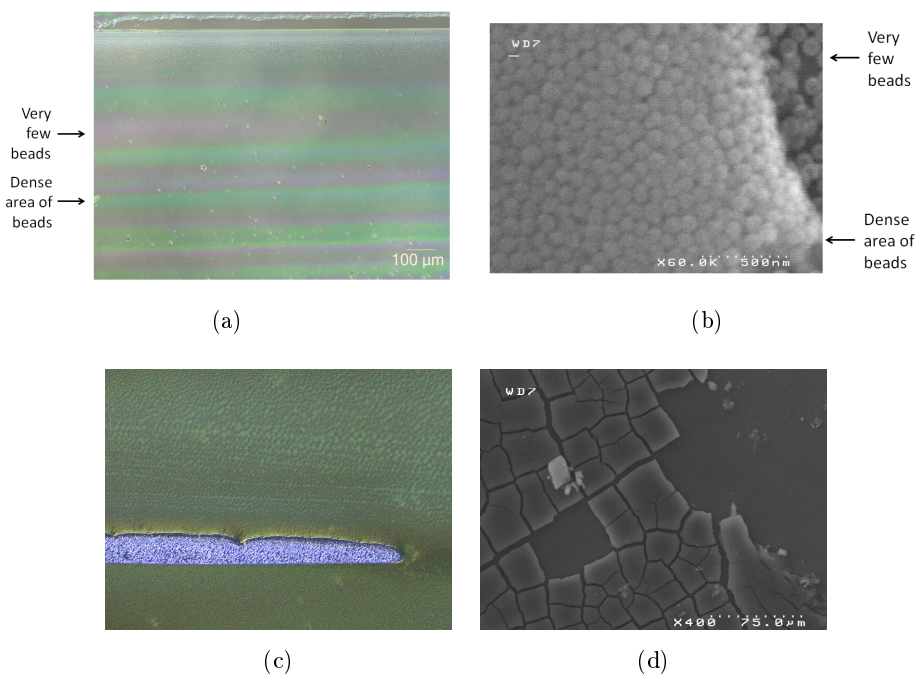


Figure 90: Imitation opals synthesized by evaporation: (a) and (c) microscope images of respectively P1 and P4 deposits, (b) and (d) SEM images of P1 and P4 respectively.

Solvent evaporation was also performed under vacuum and gave similar results in a much shorter time. It was also possible to deposit beads with a $1\ \mu\text{m}$ diameter, whereas they sediment too fast during classical evaporation deposit. This technique is a good alternative to evaporation in an oven but the drawbacks of heterogeneity are still the same.

Others have reported better results with evaporation. They optimize the deposit conditions but it is mainly a question of duration of evaporation and absence of vibrations. Other approaches were tested in the thesis, in order to overcome these deposit defaults.

2.3 Dip-coating

Another way to obtain silica spheres deposit is to use a Langmuir-Blodgett process. This technique was elaborated with amphiphilic molecules dispersed at a water/air interface. Molecules arrange themselves so as to reduce surface energy. They are compressed on the surface until they reach the critical micellar concentration, and then, they are deposited layer-by-layer on a solid substrate inserted in or extracted from the liquid. The process was also used with silica spheres [9], [10]. Spheres are dispersed on the surface of a liquid and compressed until a "transfer pressure" (a surface pressure) is reached. Then the substrate is immersed rapidly in the liquid and the transfer takes place during the slow emersion. With such a technique, the number of layers is uniform on the substrate. Nevertheless, fabrication is time-consuming due to this layer-by-layer technique and samples have to be fabricated one-by-one.

Dip-coating is a similar approach and represents an alternative to Langmuir-Blodgett technique. It consists in immersing a solid substrate in a suspension of silica particles in a suitable liquid. The substrate is then emerged very slowly, at a constant speed, from the liquid and several layers of beads are deposited. We used this technique for opal formation. Particles P1 were suspended in ethanol with a mass ratio of 1%. A PMMA substrate was immersed in the solution during 1 minute and then emerged with a mechanic plate at $1\ \mu\text{m/s}$. One hour after total emersion, the process is repeated a second time to thicken the deposit. The obtained deposit is macroscopically homogeneous. A SEM image shows the compact order of the particles (figure 91). The thickness is more or less controlled by the number of immersions in the suspension and the number of layers is homogenous on large surfaces.

This approach presented interesting properties. However, samples can be made only one-by-one and it is consequently very long to obtain a dozen or so substrates for our experiments. Moreover, it is difficult to scale up the fabrication, which would make a sensor based on this technique rather costly.



Figure 91: SEM image of an opal deposited by dip-coating (particles P1).

2.4 Boostream[®] equipment

A laboratory of the CEA-Liten has developed an equipment comparable to a Langmuir-Blodgett equipment at large scales. The technology is called Boostream[®] (for "Bottom-up/top-down technique based on a smart stream"). It aims at forming a compact monolayer of silica beads on large areas, solar panels for example. The equipment is made of several modules represented in figure 92.

The particles are suspended in a solvent and injected on a liquid carrier. Beads stay at the liquid/air interface thanks to a well-controlled balance between the surface energies. The particles are then compacted on a retention area thanks to hydrodynamic forces, then they order themselves under the influence of different phenomena such as dipole moments, partial positive charges and hydrophobicity. Above the transfer zone, a camera pictures the surface. The camera is connected to a dedicated software. The latter evaluates the order of the beads and the compacity of their arrangement: the macroscopic aspect of the surface is correlated to the microscale assembly. Thus, the deposit is launched when beads compacity is optimal. The difference of reflection color according to the order of $1\ \mu\text{m}$ beads is represented in figure 93. With a standard deposit by the equipment, the reflected color is much less intense than with a deposit assisted by the software monitoring.

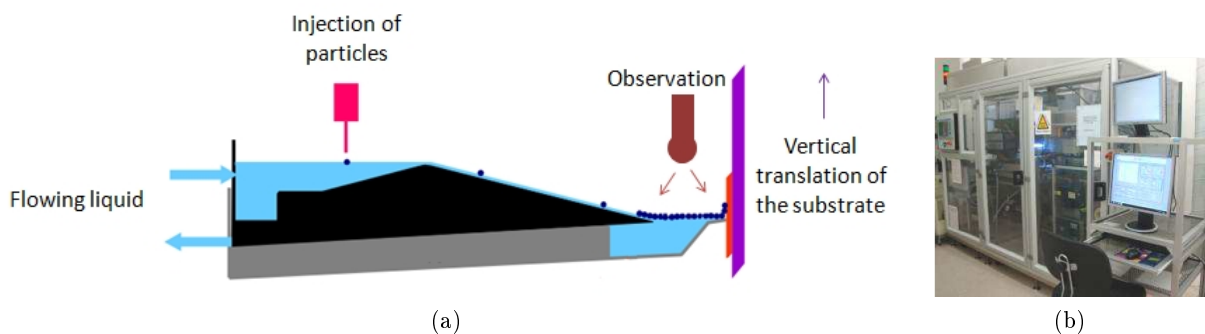


Figure 92: The Boostream[®] equipment. (a) Schematic representation and (b) picture of the equipment.

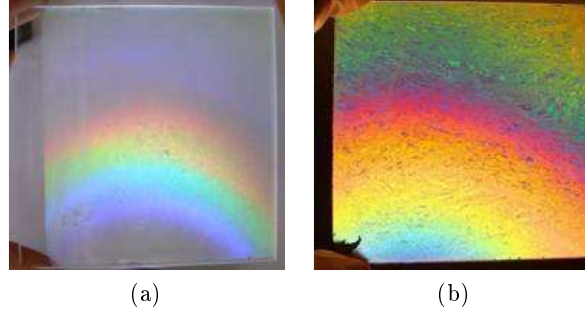


Figure 93: Pictures of a monolayer of 1 μm silica beads deposited by the Boostream[®] equipment. (a) Standard deposit and (b) deposit assisted by the software giving a highly compact monolayer and thus a high intensity of reflection.

At the start of the thesis, this equipment seemed promising for the compacity control and the large areas of deposit. However, it was only defined to deposit monolayers. Then, we performed several assays to develop a process leading to the obtention of multilayers. Finally, 5 or 10 layers of silica beads could be transferred on a substrate by a layer-by-layer technique with a 30 minutes drying by an infrared lamp heater between each layer. In the developed process, the solid substrates are immersed in the carrier fluid and the transfer of the particles takes place when the solid is pulled out of the liquid. Silica particles with a diameter of 300, 500 or 1000 nm were used. Pictures and SEM images of the opals are represented in figure 94. Each layer has a good compacity but the crystalline arrangement between layers is not optimum. Several parameters play a role, such as the angle and the speed of the substrate during the particle transfer. In figure 94c, we can see that the number of layers is uniform and the result is similar to a Langmuir-Blodgett opal.

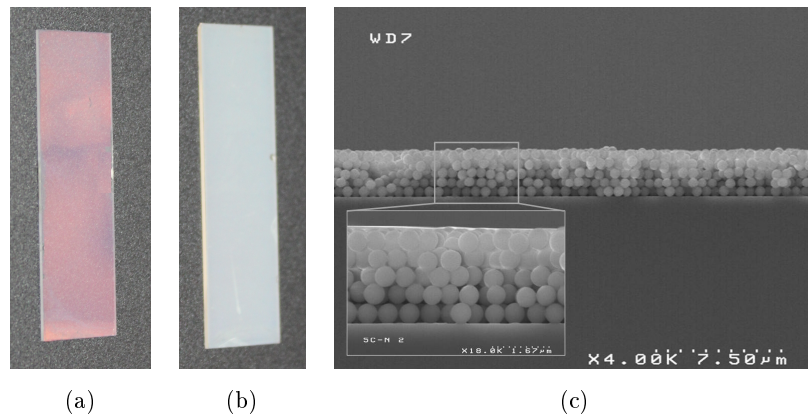


Figure 94: 5 layers of silica beads, deposited by the Boostream[®] process. (a) picture of 5 layers of 300 nm spheres, (b) picture of 5 layers of 500 nm spheres, (c) SEM image of 5 layers of 500 nm spheres.

Several characterizations of the opals will be performed in section 4. This process developed for opal formation has a high potential. Indeed, the particles are assembled in compact layers, the

number of layers is uniform, and large substrates can be coated or several substrates simultaneously. With optimization of the crystallinity of the opals, such a process would enable the industrialization of opal fabrication. This would be of high interest since the main obstacle of opal devices is the scale of fabrication.

3 Inverse opal synthesis

Inverse opals are obtained by filling the interstitial space in opals with a different material, such as a polymer, followed by the dissolution of the beads forming the original opal. The obtained inverse structure, presents a large specific surface area. Indeed, for a compact stack of spheres, the compacity is 74%. Thus, in perfect inverse opals, there is 74% of air and 26% of material, and this leads to a high specific area. The difficulties in the synthesis of inverse opals reside in the molding process. Indeed, inverse opals should present the same crystallinity as their masters and have the same thickness. Thus, the infiltration between the beads, the further solidification and the beads dissolution have a great influence on the final result. We will discuss in the next sections the different possibilities tested during this thesis to make inverse opals.

3.1 Sandwich

As outlined in chapter I, inverse opals based on MIPs are often synthesized with a "sandwich" technique (figure 95). After infiltration of the precursor mixture in the opal, a PMMA cover is laid on the structure and polymerization is launched by UV illumination. After 1 hour, the so-called "sandwich" is made of a glass (or silicon) substrate, an opal embedded in polymer and a PMMA substrate. A bath of hydrofluoric acid dissolves the beads and the oxide layer of the silicon/glass substrate. The inverse opal is therefore transferred on the PMMA substrate.

This technique was tested on glass and oxidized silicon substrates with 5 layers of beads. The films showed heterogeneous results. A few films were uniform and colored as expected, others were white and brittle whereas the great majority of films displayed both a white film with colored edges (figure 96). These white films are probably due to an excess of precursor mixture which gives after polymerization a thick layer of amorphous polymer on top of the inverse opal.

SEM images illustrate these macroscopic observations. Figure 97a shows a SEM image of a colored inverse opal. The small holes in the uniform polymeric matrix represent the ex-contact points of the silica beads on the glass substrate. They are distributed in the former beads pattern, in a hexagonal lattice. The inverse opal structure of the film can be observed thanks to a laceration of the polymer. The polymer molded the bead shape and holes can be distinguished, as evidence

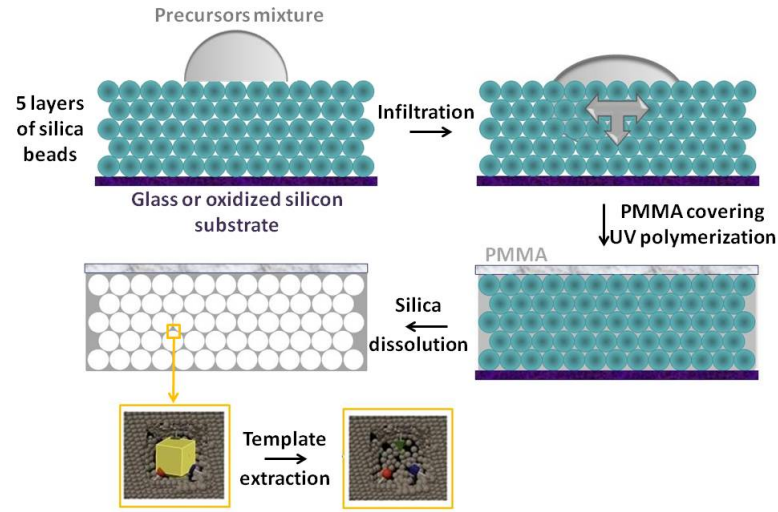


Figure 95: Schematic representation of inverse opal formation by the "sandwich" technique. The inverse opal is synthesized by a transfer on PMMA substrate.

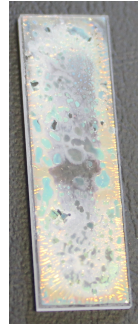


Figure 96: Picture of an inverse opal on a PMMA substrate made by "sandwich".

of the previous tangent points between the beads. The period of the structure is the same for the molded beads and for the holes on the plane surface, as proved by the intensity profile in figure 97b and measured as 545 nm. The same observations can be made on AFM images, figure 98 displays small contact holes ordered in a hexagonal structure. Figure 97c is a SEM image of a white film. Some contact points are visible but many are obstructed and particularly at the center of the picture. Even if the film seems to be planar, there is excess of polymer. This assumption is verified by the figure 97d, a SEM image of a white film. Here, the polymer surface is not planar but rather bumpy. Some spherical cavities appear on the surface but not with the expected crystalline order.

To avoid such failures, a pressure could be applied on the top of the sandwich to eliminate the excess of precursor mixture. This approach was not convenient in this study, though, since the UV illumination was performed on the top of the sandwich. We therefore worked on alternatives, using opals directly deposited on PMMA substrates, as described in the next sections.

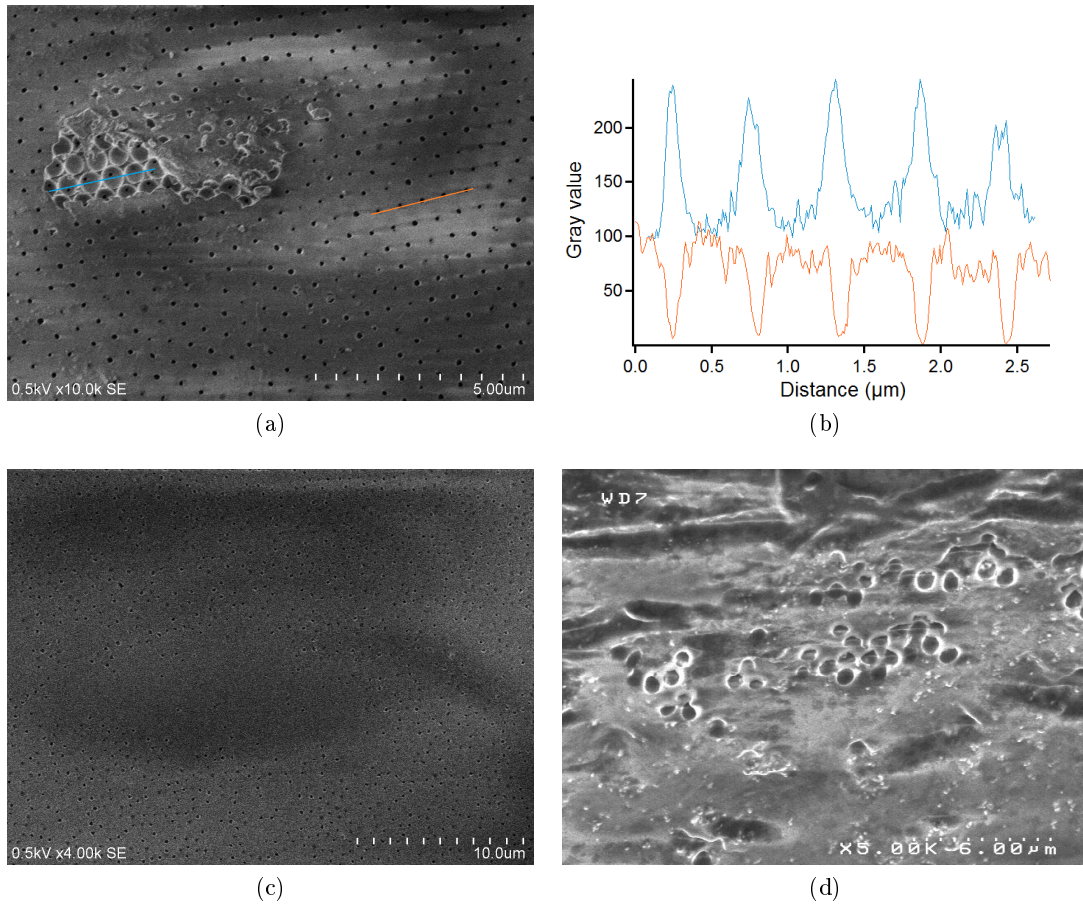


Figure 97: SEM images of inverse opals made by the "sandwich" technique. (a) A film displaying a color, (b) intensity profiles of the lines displayed on (a), (c) and (d) white brittle films.

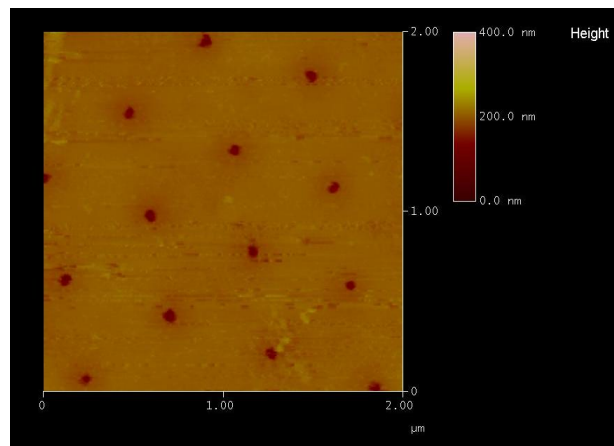


Figure 98: AFM image of an inverse opal fabricated by the "sandwich" technique.

3.2 Spin-coating

With opals on PMMA substrates, a direct synthesis of inverse opal was attempted by spin-coating (figure 99). The modified substrate is fixed in a spin-coater under inert atmosphere. A drop of the precursor mixture is applied on the substrate and the solution infiltrates the opal by capillary driven force. When the whole sample is transparent (completely infiltrated by the precursors mixture), the spin-coater is turned on to eliminate the excess of liquid (500 rpm, 30 s), in order to avoid the formation of an unstructured polymer layer. Polymerization is then launched inside the spin-coater with an optical-fiber connected to a UV lamp (15 min, 4.5 W/cm^2). It is important to notice that the beads keep their opal configuration and do not seem to move despite the rotation.

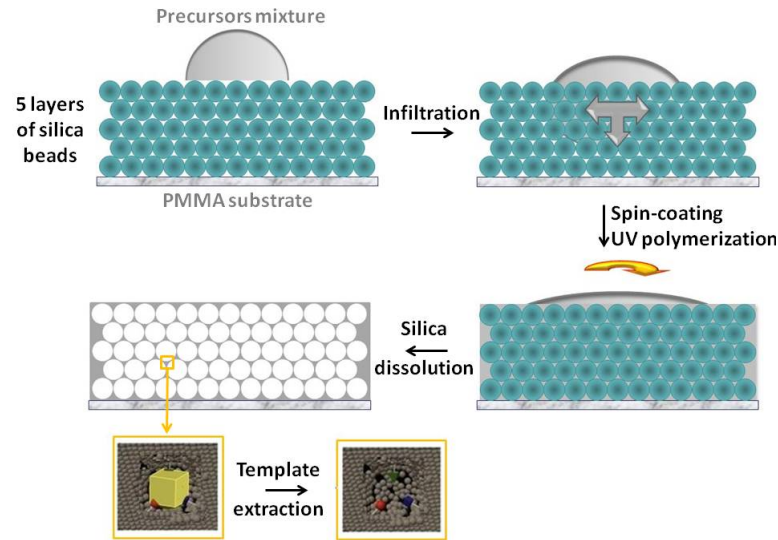


Figure 99: Schematic representation of inverse opal formation by spin-coating.

After dissolution of the silica beads, the obtained inverse opals presented a heterogeneous aspect (figure 100). A circular area is noticeable which corresponds to the spread of the initial drop. White and colored areas are evidences for different thicknesses for the polymer film.

SEM images of the colored areas exhibit a uniform periodic structure with a structure periodicity

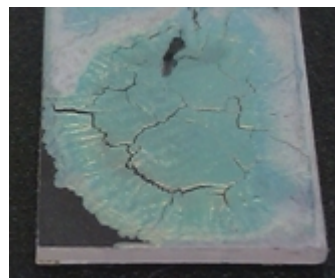


Figure 100: Picture of an inverse opal on a PMMA substrate made by spin-coating.

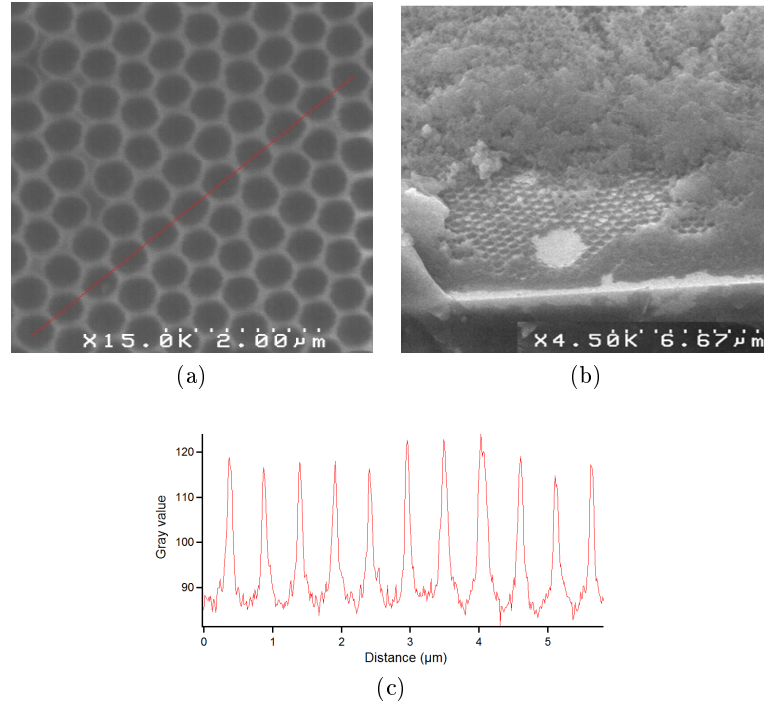


Figure 101: SEM images of inverse opals, made by spin-coating. (a) A film displaying a color, (b) edge of the film and (c) the intensity profile of the red-line on (a) displaying the period's measurement of 527 nm.

of 527 nm (figure 101a and 101c). On the opposite, the edges of the sample have different thicknesses (figure 101b). It is not sure whether the lack of inverse opal is due to the absence of beads (possibly ejected by spin-coating) or to the bad distribution of the precursor mixture. Another drawback is the evaporation of the solvent during the rotation. Acting as a porogen, it has an important role in the imprinting process, and thus, its evaporation should be avoided during polymerization.

Finally, this technique leads to inverse opals whose uniformity is better than with the sandwich technique but still not optimal. The evaporation of the solvent during spin-coating is moreover difficult to avoid. We thus tested a third technique to see if certain of these drawbacks could be avoided.

3.3 Dip-coating

Dip-coating is an alternative to spin-coating (figure 102). Forces involved are much weaker and may not alter the opal structure.

The dip-coating equipment is set up in a glove box under inert atmosphere (figure 103). The PMMA substrate with the opal is fixed on a translation plate and immersed in the precursor mixture. After one minute, it is slowly emerged (0.1 mm/s). Polymerization is then launched with a UV

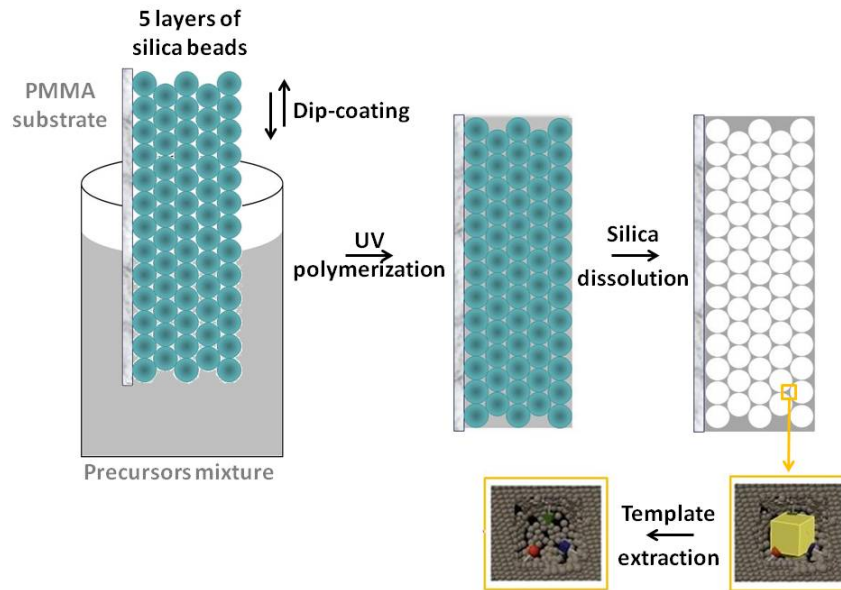


Figure 102: Inverse opal formation by dip-coating.

lamp (15 minutes, 4.5 W/cm^2) connected to an optical fiber. Because of the limited aperture of the optical fiber, the illumination cone is too small to cover the whole sample. That's why the sample is periodically agitated (up and down) in front of the optical fiber during the translation stage.

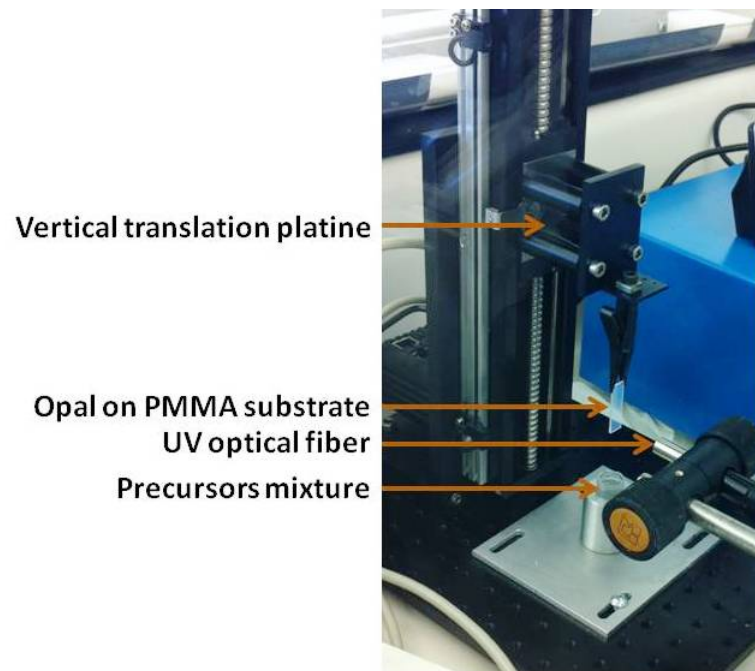


Figure 103: Picture of the dip-coating equipment.

After dissolution of beads, the inverse opal was macroscopically non uniform: it was more colored in its bottom part than in its upper part (figure 104). We assume that under the gravity effect,

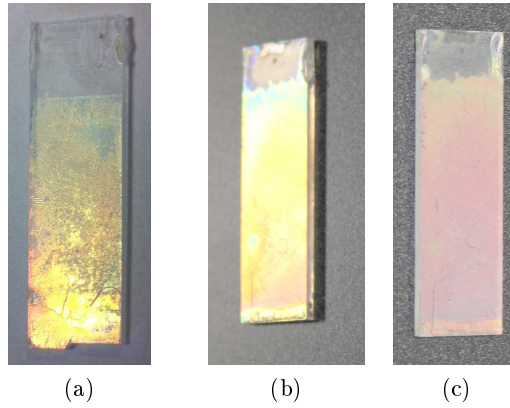


Figure 104: Pictures of inverse opal obtained by dip-coating. (a) One dip-coating and accumulation of polymer at the bottom of the sample, (b) two successive dip-coatings (white light reflected is intense and its color homogeneous), (c) same sample as (b) but the light is not reflected directly on the sample.

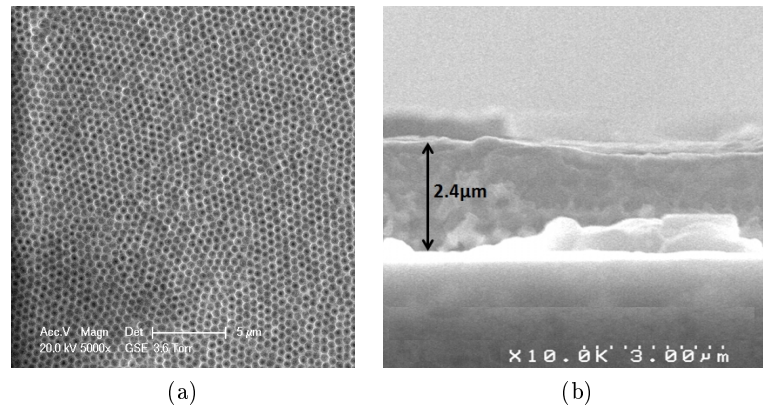


Figure 105: SEM images of inverse opals, made by one dip-coating. (a) Top view of uniform inverse opal, (b) side view of an inverse opal.

more precursor mixture was accumulated at the bottom part. As the upper part of the sample was just slightly colored, it means that not enough precursor mixture was infiltrated and polymerized there. SEM images confirmed the production of inverse opals (figure 105a) and a side view of the bottom part confirmed the thickness of the bottom-film (figure 105b): 5 layers of 500 nm beads give an inverse opal with a thickness around $2.4 \mu\text{m}$. In order to obtain inverse opal macroscopically uniform, we tried to apply a second dip-coating followed by a new polymerization to the sample. Inverse opal films were then much more colored (figure 104b and 104c). SEM and AFM images of inverse opal, made from $1 \mu\text{m}$ spheres, confirm that the upper layer of beads was covered by polymer (figure 106). Some polymeric spheres can be observed, neighbouring spheres that seem to be collapsed.

Dip-coating technique of gave the best results over all the tested methods. Homogeneous surfaces

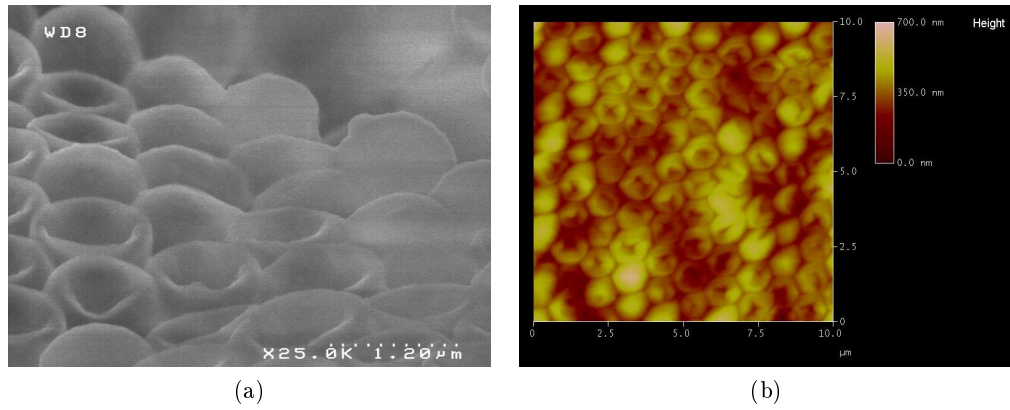


Figure 106: Images of inverse opals, made by two dip-coatings. Spherical shapes can be observed on (a) a SEM image and (b) an AFM image.

(or areas) are obtained and the films display an intense color. We will therefore use this technique for further inverse opal fabrication and characterization.

4 Opals and inverse opals characterization

Opals and inverse opals were synthesized and optimized (as much as possible) for the development of a sensor. The elaboration of the sensor also went through several optical characterizations.

Three types of opals, listed below, were synthesized and characterized by different means according to their optical properties.

- Layers of **300 nm** spheres: these are classical photonic crystals, showing a colored reflection typical of a photonic stop band.
- Layers of **500 nm** spheres: this is a limit case as the diameter of the spheres is big but the samples display a color and are semi-opaque.
- Layers of **1000 nm** spheres: this is a scale for diffraction in the visible wavelength.

The layer-by-layer process used by the Boostream[®] equipment was applied for all the samples studied in the following sections. If not otherwise indicated, opals have five layers of beads. This number of layers was chosen because 5 layers are enough to complete the formation of the optical stop band resembling that of an infinite crystal [11].

4.1 Diffraction figure and evaluation of $n_{grating}$

Diffraction is the result of the light splitting into different directions after reflection or transmission through a periodic structure. This phenomenon appears for a periodic grating with a period bigger than the wavelength of interest. Thus, a monolayer of 1 μm silica beads diffract a white light beam with the diffraction figure pictured on figure 107.

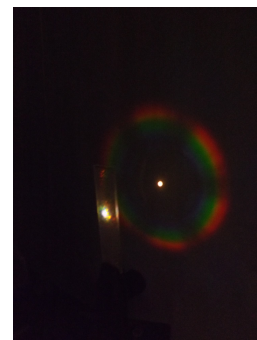


Figure 107: Diffraction of light by a monolayer of 1 μm silica spheres.

4.1.1 Opals

Opal structures have a hexagonal lattice (figure 108) and the diffraction figure for such crystals is composed of six points around the transmitted beam. Thus, with a single or multilayer of silica beads with $1\ \mu\text{m}$ diameter, a laser beam splits into this diffraction figure, which can be observed on a screen (figure 109a). Higher orders of diffraction are more deviated from the transmitted beam and are thus more difficult to project on a planar screen. That's why in figure 109b, the diffraction orders are observed on a spherical screen. In this picture, the diffraction spots are not points but rather large bands that tend to join and form complete circles. It means that the laser beam hits several crystal domains.

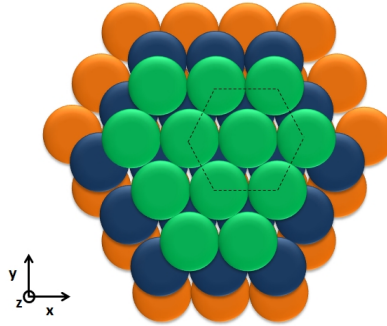


Figure 108: Schema of an opal stack, viewed from the $[111]$ direction and with hexagonal face in dashed line.

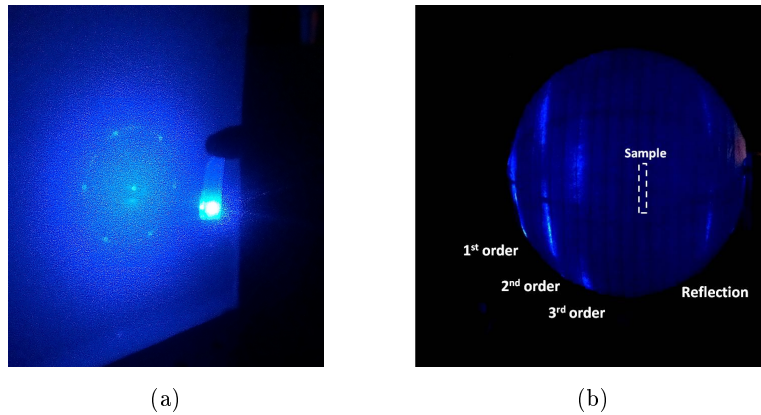


Figure 109: Diffraction figure for 5 layers of $1\ \mu\text{m}$ particles. (a) Six points for the first order of diffraction, (b) the second and third orders are visible on a spherical screen.

The diffraction pattern is wider with smaller beads. Thus, for 5 layers of $500\ \text{nm}$ spheres, the first order of diffraction is almost perpendicular to the sample and is difficult to observe.

To simplify the detection of the diffraction spots, a detector holder was fabricated (figure 110). This holder enabled the measurement of diffraction intensity for small beads. Indeed, thanks to a

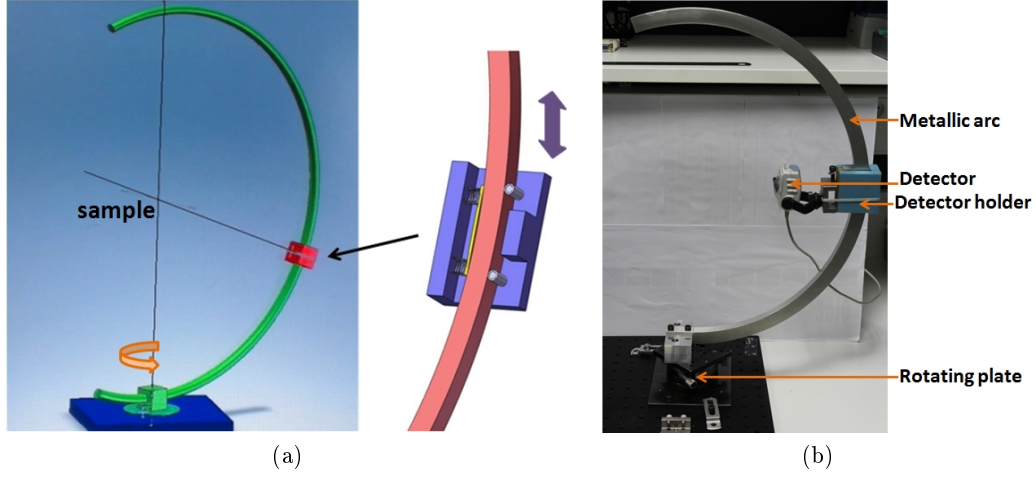


Figure 110: A new detector support for 3D measurements of diffraction intensities: (a) the solidworks model and (b) picture of the realized prototype.

graduated metallic arc fixed on a pivot, the detector can move along a sphere. A powermeter or a camera can be fixed on the support and measure intensities of the diffraction orders.

In chapter I section 2.3.5, a method to determine the refraction index of the polymer was detailed. The diffraction efficiency (η) is correlated to the refractive index of the surrounding medium (n_{medium}) and to the refractive index of the periodical material ($n_{grating}$, equation 4.1 where C is a constant and e the thickness of the grating). The silica spheres are deposited periodically and thus the diffraction efficiency can be studied. However, this is not a thin grating as the light's wavelength is 488 nm and the grating is 1 μ m-periodic. Despite this approximation, the model was still applied and the measurement of the diffraction efficiency for 5 layers of 1 μ m particles in different solvents gave a linear plot (figure 111). The linear fit presents a correlation coefficient of $R^2 > 0.99$. Every measurement was performed 5 times and was very reproducible (the standard deviations were too small to appear on the graph, inferior to $5 \cdot 10^{-3}$). By extrapolating the fit, the refractive index of the beads was evaluated: $n_{beads} = 1.46$. The value of the beads refractive index is not available from the supplier but the value obtained in this experiment is coherent with other non porous commercial silica beads.

$$\eta = C \left(\frac{e(n_{grating} - n_{medium})}{\lambda} \right)^2 \quad (4.1)$$

The same experiment performed with a monolayer of 1 μ m silica spheres also gave a linear fit with $R^2 > 0.99$ and $n_{beads} = 1.46$. This confirms the reproducibility of the measurement. Even if the application of equation 4.1 is outside its validity area, this result is coherent with common silica refractive indices. The value of n_{beads} will therefore be used in further optical characterizations.

Thanks to the special detector holder, it was also possible to measure the intensity of the first

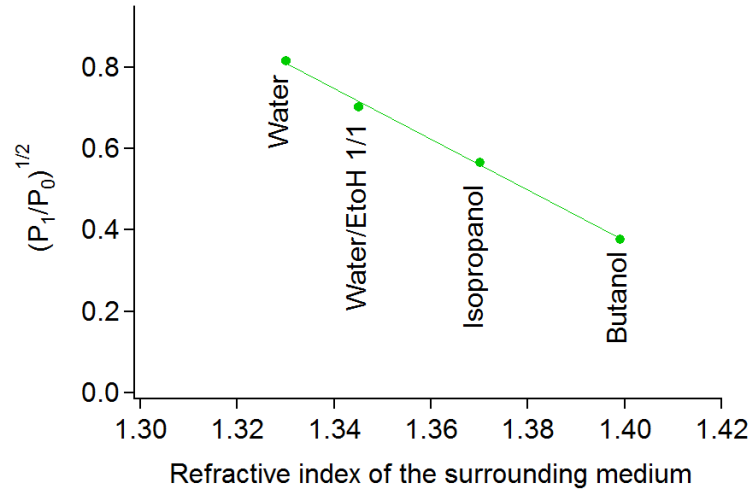


Figure 111: Evaluation of the refractive efficiency of an opal with 1 μm silica spheres in different solvents. The extrapolation of the linear plot gives the refractive index of the grating.

diffraction order for 500 nm beads (figure 112). Indeed, the intensities of the first order of diffraction with beads of 1 μm could be measured on a planar surface (detector on a rail, the curvature of the pattern is neglected), whereas it is not possible with 500 nm beads. The plot of the diffraction efficiency is linear with $R^2 > 0.99$ and gives $n_{beads} = 1.50$. The refraction indices of the 1 μm and 500 nm beads are in the same range but slightly different. This difference may be explained by measurement errors or by a difference of porosity of the beads, since then a more porous bead would have a lower refractive index.

Diffraction figures of opals proved their good spatial organization. Moreover, the diffraction efficiency allowed for an evaluation of the beads refractive index.

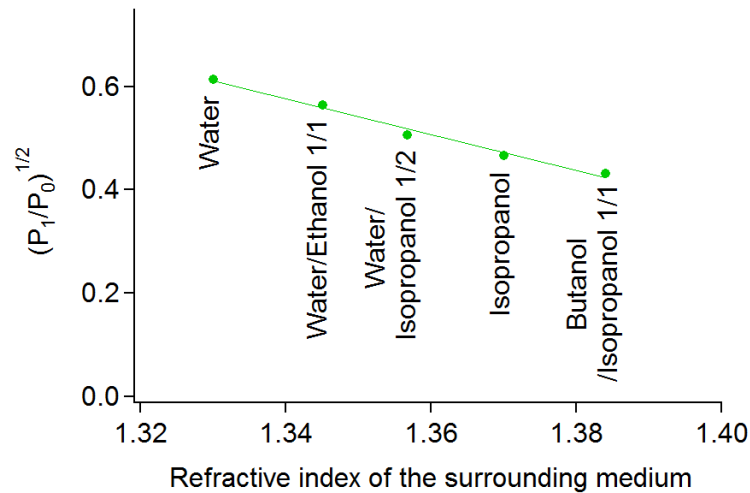


Figure 112: Evaluation of the refractive efficiency of an opal with 500 nm silica spheres in different solvents. The extrapolation of the linear plot gives the refractive index of the grating.

4.1.2 Inverse opals

Imprinted inverse opals synthesized for 2,4-D were also studied by diffraction. In this case, the thin grating approximation is made once again but yet once again respected. However, the model used for opals still works and the fit of the diffraction efficiency as a function of the refractive index is linear (figure 113). The correlation coefficient is $R^2 > 0.99$ for both the NIPs and MIPs. Refractive indices are measured and give $n_{grating}^{NIP} = n_{grating}^{MIP} = 1.53$. If we consider the quantities of reactants (monomers 4-vp and EDMA, initiator ABDV) and their respective refractive indices, with a total polymerization of all the monomers, the expected refractive index is given by equation 4.2, where $\%_i$ is the quantity of component i and n_i its refractive index. The calculation gives $n_{polymer} = 1.47$. The expected and evaluated values are in the same range and several assumptions can explain their difference. First, the model used is at the boundaries of its validity area. Then, the polymers may have a difference of porosity (due to evaporation speed of the solvent during polymerization). Finally, it is also possible that polymerization was incomplete and thus the ratio of 4-vp higher than expected (and $n_{4-vp} > n_{EDMA}$).

$$n_{polymer} = \%_{(4-vp)}n_{4-vp} + \%_{(EDMA)}n_{EDMA} + \%_{(ABDV)}n_{ABDV} \quad (4.2)$$

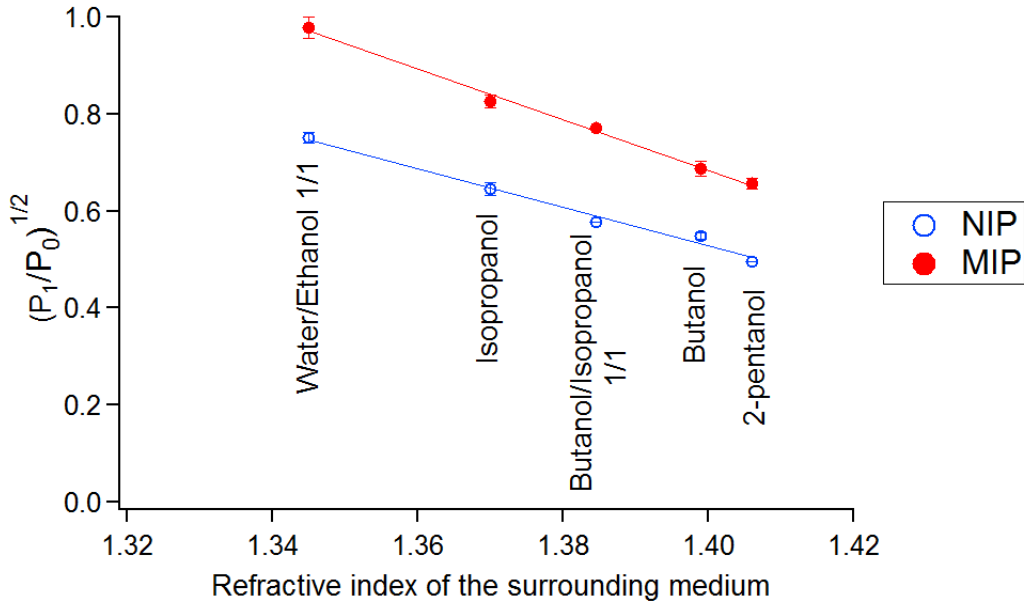


Figure 113: Evaluation of the refractive efficiency of an inverse opal built from $1 \mu\text{m}$ silica spheres in different solvents. The extrapolation of the linear plot gives the refractive index of the grating.

Diffraction figures of inverse opals proved that the structure of opals was conserved. Thus, inverse opals are periodic with a hexagonal lattice. Measurement of the diffraction efficiency in different solvents gave an evaluation of $n_{grating}$ which will be used in the next sections.

4.2 Spectrophotometry and evaluation of n_{eff}

Reflection and transmission measurements are commonly used to probe the crystalline structure of photonic crystals. Structured samples are illuminated with white light and the reflected or transmitted light is collected. The spectra have a diffraction resonance whose energy is given by a combination of the laws of Bragg and Snell (equation 4.3, where λ_{max} is the wavelength of the absorption maximum, d_{111} is the period of the crystal -represented in figure 114- along the direction [111] -i.e. normal to the substrate-, if d is the bead diameter $d_{111} = \frac{\sqrt{3}}{2}d$, n_{eff} is the effective refractive index of the film and θ is the incidence angle of the light).

$$\lambda_{max} = 2d_{111}\sqrt{n_{eff}^2 - \sin^2\theta} \quad (4.3)$$

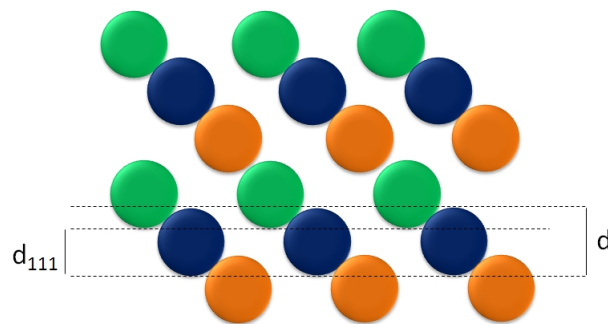


Figure 114: Schematic representation of d and d_{111} for opals.

4.2.1 Opals

If an opal is illuminated by a white light spot, the reflected light will appear as a colored spot. In figure 115, the reflected spot by an opal of 300 nm diameter beads is pictured for different angles of rotation of the sample. The reflected color is clearly dependent of the light incidence.

Characterization of the samples by spectrophotometry requires angle measurements since the Bragg equation depends on the angle of light incidence. Thus, a specific optical bench was elaborated (figure 116). The principle is the same as a goniometer but with reduced size and precision. The sample is fixed at the center of the equipment. The source of light arrives by an optical fiber and is focused on the substrate over a spot surface of about 1 mm^2 . Light collection is achieved by an optical fiber connected to a spectrophotometer. This detection part can move around the sample thanks to an automated rotative support (precision of 1°). It can measure reflected light with angles from 10 to 180° . The sample is fixed on a rotation plate and can also turn along the vertical axis.

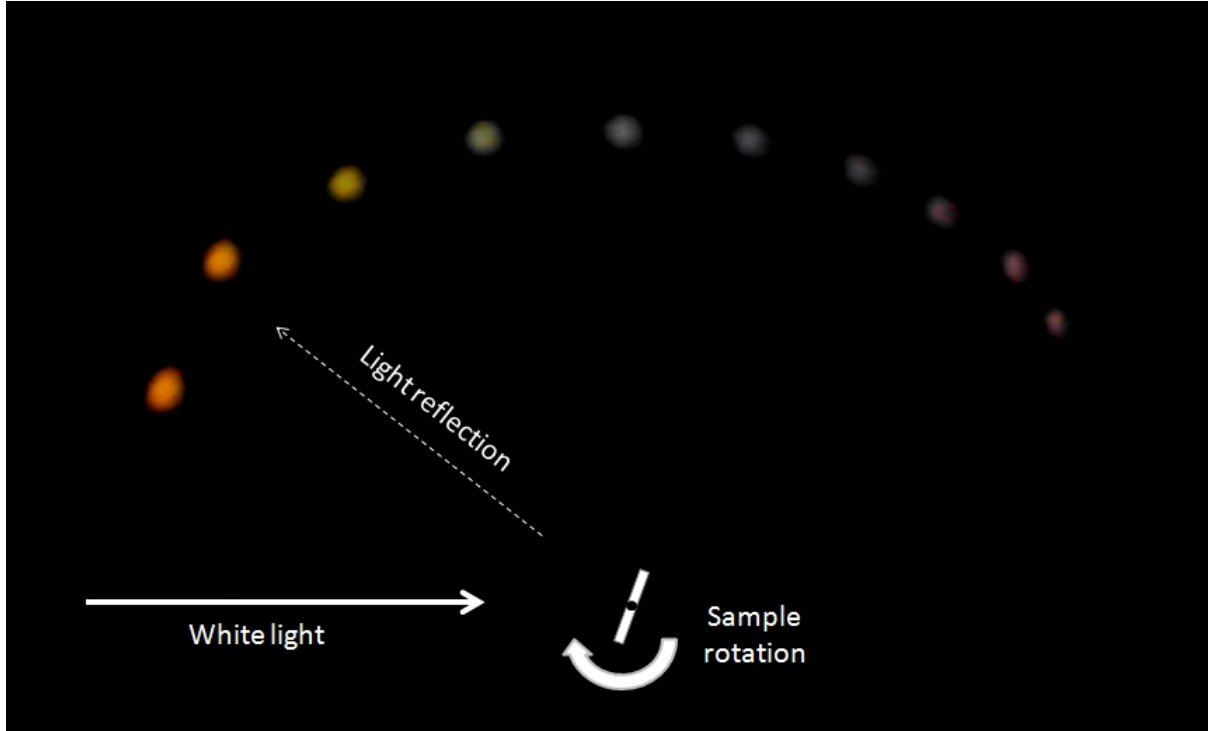


Figure 115: Reflection of white light by an opal - 5 layers of 300 nm spheres on a PMMA substrate - for different angles of incidence. This illustrates equation 4.3.

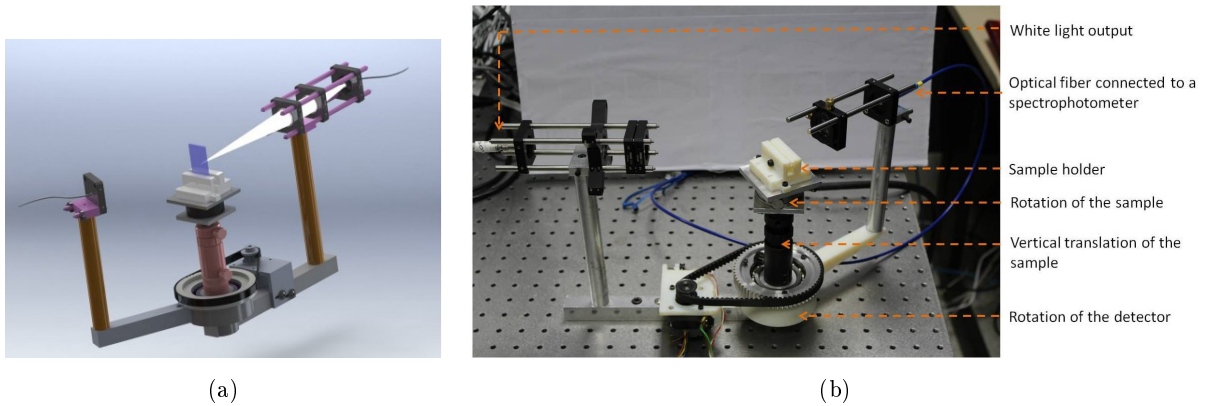


Figure 116: The developed optical bench for angle resolved spectroscopy: (a) 3D model and (b) picture of the prototype.

This bench can be used for reflection and transmission spectrophotometric measurements. Indeed, photonic crystals can be studied either in transmission or in reflection. Thus, with 20° incident light, spectra for a 5 layer opal (300 nm) in transmission and reflection are reported in figure 117. The maximum of absorption corresponds to the maximum of reflection. We chose to perform reflection measurements for the next optical characterizations.

A 5 layer opal of 300 nm beads was studied. The reflection spectra were recorded for different angles of light incidence and we observed that the maximum of absorption shifts (figure 118a) as

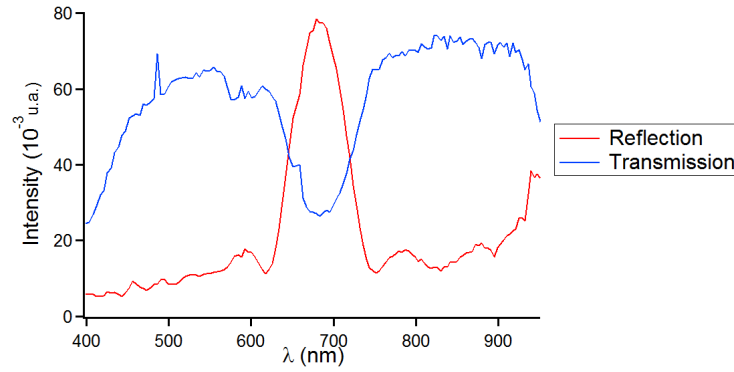


Figure 117: Transmission and reflection spectra for an opal with 5 layers of 300 nm beads and 20° incident light.

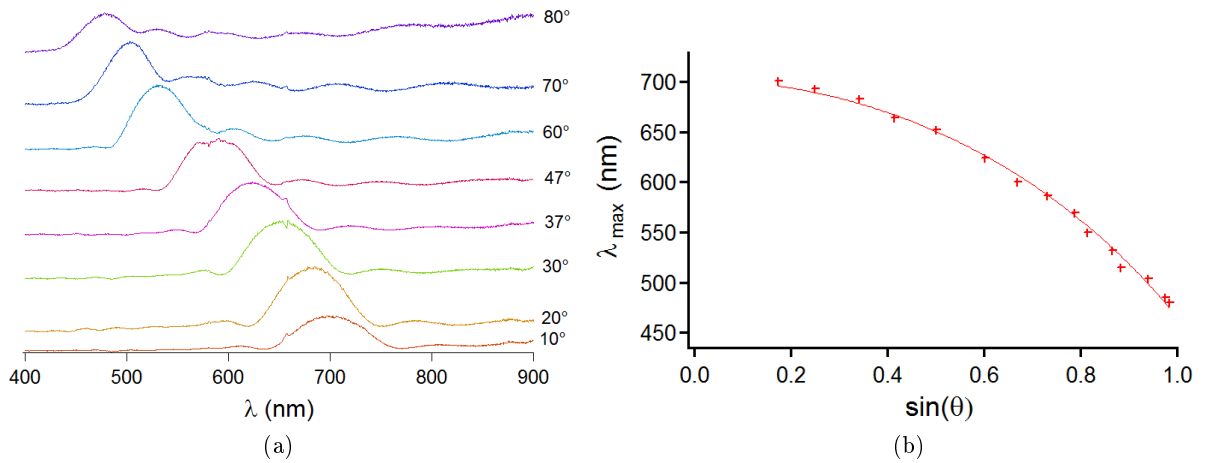


Figure 118: Spectrophotometric study of an opal with 5 layers of 300nm beads. (a) Reflection spectra for different angles of light incidence and (b) modelization of the Bragg law.

expected from the dependence of the Bragg law to light incidence.

The plot of the maximum of reflection is fitted with the Bragg law (figure 118b). The fitting coefficients (d and n_{eff}) were evaluated as $d = 303 \pm 3 \text{ nm}$ and $n_{eff} = 1.33$. The diameter of the beads was therefore consistent with the value obtained by the fit. The effective refractive index is the refractive index of the complete structure including air and material grating. This index can be calculated with equation 4.4, where f is a filling factor and n_i is the refractive index of the medium i (in this case, 1 and 2 are silica beads and air)¹ [12].

$$n_{eff}^2 = f n_1^2 + (1 - f) n_2^2 \quad (4.4)$$

The equation is used with the following assertion/assumptions:

- $n_2 = n_{air} = 1$
- $f = 0.74$. For compact sphere stacking, the optimal filling factor of the beads is 0.74.

¹ Another possibility is $n_{eff} = f n_1 + (1 - f) n_2$ but this is less frequent in literature.

- $n_{eff} = 1.33$, value obtained from the fit of the Bragg law.

Thus, we obtain $n_1 = n_{beads\ 300nm} = 1.43$. This value is coherent with the expected value for silica and in particular with the value measured in diffraction for $1\ \mu m$ beads ($n_{beads\ 1\mu m} = 1.46$). However, the assumption for the value of f is not accurate. Indeed, as we underlined in a previous section, the beads were compact in each layer but not between layers. Nevertheless, this assumption will be kept and next measurements will allow for relative comparison between the values.

On several spectra, one can distinguish interference fringes (figure 119) which are local maxima of reflection. These maxima appear for thin opal films of good quality [11]. Usually, their existence is explained by Fabry-Perot oscillations related to the interference of light on opposite surfaces of the opal. If the thickness of the opal is not homogeneous, then the interferences vanish.

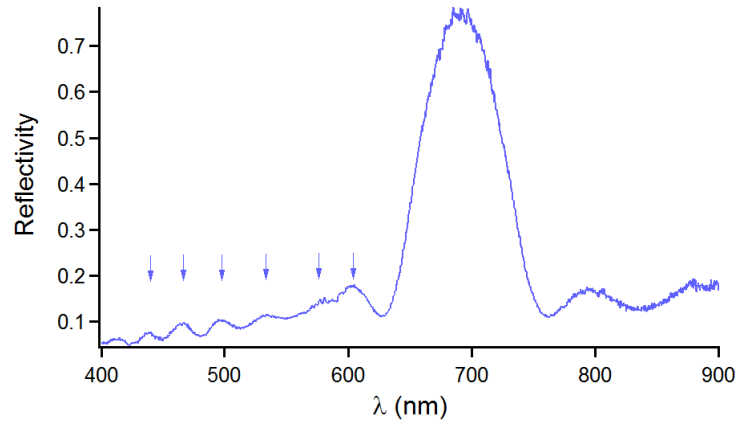


Figure 119: A reflection spectrum for an opal with 5 layers of 300 nm beads and 15° incident light. Fabry-Perot interferences appear as local maxima evidenced by arrows.

Figure 120 exposes the principle of a Fabry-Perot cavity. It is made of two reflecting parallel surfaces. The cavity exhibits a resonance in the transmission spectrum as a function of the wavelength. The multiple reflections of light between the two surfaces interfere constructively when the beams are in phase. Thus maxima of transmission are given by equation 4.5.

$$m\lambda_m = 2n_{eff}l\cos(\theta') \quad (4.5)$$

where m is the diffraction order (an integer), λ_m is the wavelength of the maxima, n_{eff} is the effective refractive index of the cavity, l its thickness and θ' the angle of the light travelling through the cavity.

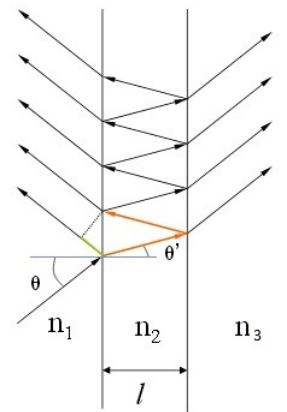


Figure 120: A Fabry-Perot cavity. n_1 is the refractive index of air and n_2 the effective refractive index of the cavity, l its thickness, θ the incidence of light and θ' the angle of light in the cavity.

Surfaces of the opal act as a Fabry-Perot cavity. The maxima respect the equation 4.5, where $n_2 = n_{eff}$, the effective refractive index of the opal. If we consider two opal films (of1 and of2) with the same angle for light incidence and the same refractive index, and such as $l_{of1} = 2l_{of2}$, then the maxima occur at $\lambda_{of1} = 2\lambda_{of2}$. This is effectively observed for opals with 5 and 10 layers of 300 nm beads, observed with a light incidence of 77° for example (figure 121).

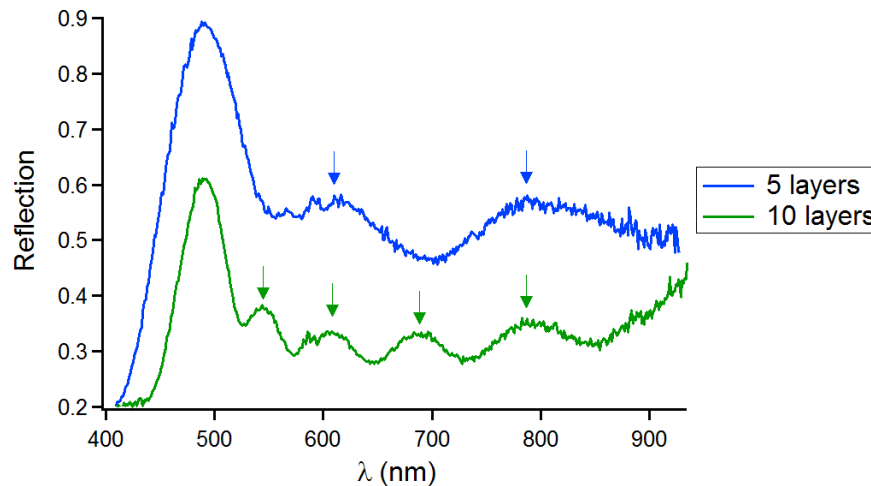


Figure 121: Reflection spectra for opals with 5 and 10 layers of 300 nm beads and light incidence of 77° . Fabry-Perot interferences appear as local maxima evidenced by arrows.

Opals made with beads of 300 nm diameter can therefore be characterized by spectrophotometry. The Bragg law can be applied to the reflection peaks. Moreover, the opals made by the Boostream[®] equipment displayed a high quality, highlighted by Fabry-Perot interferences.

4.2.2 Inverse opals

Inverse opals made from opals with 300 nm beads can also be characterized by spectrophotometry. Indeed, if the structure is periodic, a Bragg's diffraction peak is observed. The maximum of reflection respects the Bragg law and depends on light incidence (figure 122).

The plot of the maximum of reflection is fitted by the Bragg law (figure 122b) and the fitting coefficients were evaluated as $d = 410 \pm 4 \text{ nm}$ and $n_{eff} = 1.34$. The size of the "air beads" is much bigger than the molded silica beads. The shape of the structure may have changed, for example the polymer could have widened the space between bead layers. This is not really consistent with the SEM images presented earlier in this chapter which display contact holes between the air beads (figure 105a). However, the period of the lattice is $d_{111} = 336 \text{ nm}$ and this is coherent with the periods measured on the SEM images.

Equation 4.4 was used with $n_2 = n_{air} = 1$, $f = 0.26$ and $n_{eff} = 1.34$ the value evaluated by the fit. The calculation gives $n_1 = n_{polymer} = 2.0$. This value is really far from the value evaluated by

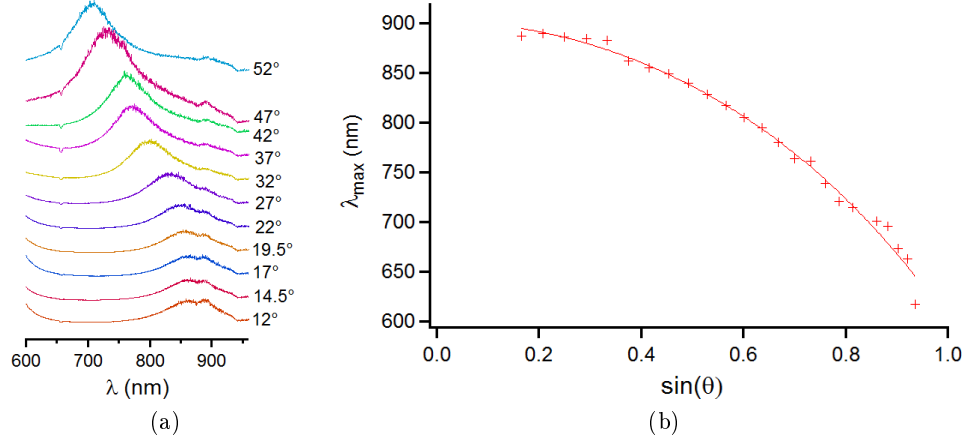


Figure 122: Spectrophotometric study of an inverse opal made from 5 layers of 300 nm beads. (a) Reflection spectra for different angles of light incidence and (b) modelization with the Bragg law.

diffraction ($n_{\text{polymer}} = 1.53$). In this case, the model may encounter too many hypothesis (such as the compacity of the structure) to give correct results. To be completely evaluated, the sensor should undergo a compacity evaluation. In the next section, we will use spectrophotometric measurements for sensing and thus rather use comparisons of Bragg's peaks than of the fitted coefficients.

5 Sensing with inverse opals and MIPs

The elaboration of the sensors based on inverse opals was not possible with cortisol and CPA imprinted polymers. Indeed, these polymers display their binding in dichloromethane and toluene respectively, and both these solvents dissolve PMMA. Unfortunately, the opals were deposited on PMMA substrate and this prevented any formulation of MIPs in dichloromethane and toluene. To develop a proof of concept of the sensor, we decided to work with a MIP for 2,4-dichlorophenoxy acetic acid, a well-known MIP working in aqueous media.

5.1 Imprinting 2,4-dichlorophenoxyacetic acid

The herbicide 2,4-D possesses two chlorides and one carboxylic functions (figure 123). A first formulation from literature was tested in a bulk format (table 18). The NIP was prepared exactly as the corresponding MIP, but without the template.

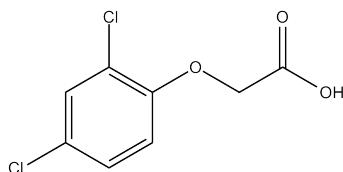


Figure 123: The chemical structure of 2,4-dichlorophenoxyacetic acid.

Refs.	Polymer	Template	Functional monomer, cross-linker and molar ratios ^a	Initiator ^b	Solvent	Polymerization conditions
[1]	M _{24D} ¹	2,4-D 0.75 mmol	4-vp, EDMA 1/3/30	ABDV 0.6 mol%	MeOH/H ₂ O 4/1 3.75 mL	50 °C overnight

^a molar ratio of template/functional monomer/cross-linker

^b concentration expressed in molar percentage compared to the polymerizable groups

Table 18: Formulation of a 2,4-D imprinted polymers.

To evaluate the binding of 2,4-D to the polymer, the concentration of 2,4-D needs to be determined. A calibration is thus performed by measuring the areas of HPLC peaks as a function of 2,4-D concentration (method detailed in appendix C). As the binding test was carried out at a concentration of 100 μM , the calibration curve was done between 100 μM and 5 μM with a correlation coefficient $R^2 > 0.99$ (figure 124).

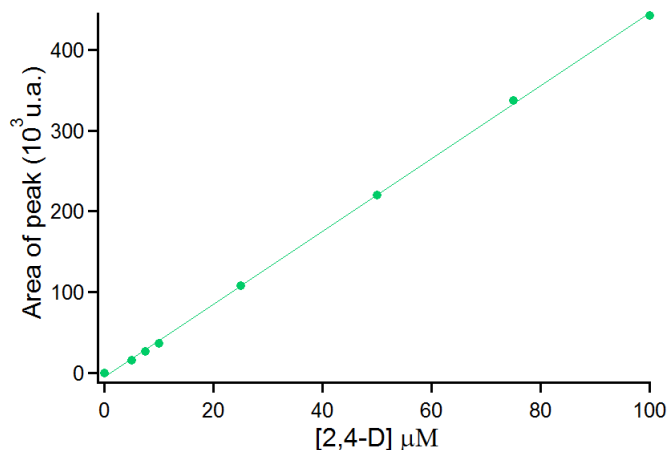


Figure 124: Calibration curve for 2,4-dichlorophenoxyacetic acid obtained by integration of area chromatograms peaks (HPLC), $R^2 > 0.99$.

The binding assay was performed on ground polymers with a constant concentration of 2,4-D (100 μM) in methanol/water 4/1 (v/v). M_{24D}^1 was successfully imprinted. Indeed, the binding isotherm represented in figure 125 displays more 2,4-D binding by the MIP than its reference. The K_{50} is about 1.3 mg/mL, and for a polymer concentration of 10 mg/mL, the imprinting factor is $\text{IF} = 3.6$. Thus, the tested formulation was satisfying, as it displays a good IF in a solvent which does not dissolve PMMA, and kept for the synthesis of inverse opals.

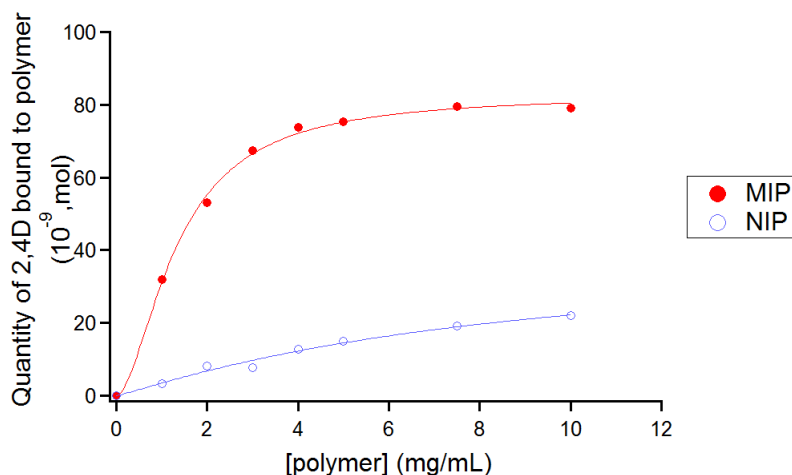


Figure 125: Binding isotherm of 2,4-dichlorophenoxyacetic acid (100 μM) in methanol/water 4/1, for NIP and MIP.

5.2 Diffraction studies

Diffraction was used to characterize the opals and inverse opals in the previous section. However, the equation 4.1 is also dependent of the lattice of the structure. Moreover, we assume that when the polymer recognizes the target it undergoes conformation changes and swell. Consequently, it is possible to monitor the polymer swelling by measuring the diffraction efficiency (for 1 μm beads). The plot of the relative diffraction efficiency against time should put in evidence the swelling of the inverse opal (equation 5.1).

$$\eta_r = \frac{\eta(t) - \eta_0}{\eta_0} \approx \frac{(d\Delta n)^2 - (d_0\Delta n_0)^2}{(d_0\Delta n_0)^2} \quad (5.1)$$

where η_r is the relative diffraction efficiency, $\eta(t)$ and η_0 are the diffraction efficiencies at a t time and for $t = 0$, d and d_0 are the periods of the grating at t and $t = 0$, Δn and Δn_0 are the differences of refractive index at t and $t = 0$.

Such real-time monitoring required an optical bench with several particularities (figure 126). First, a laser beam is aligned with the substrate. An electrical beam stop shutter was set to avoid sample illumination (and deterioration) between measurements. The diffraction figure is then projected on a semi-opaque screen. Finally, two cameras recorded respectively the images of transmitted beam and the first order of diffraction with a determined frequency. Further image treatment¹ gave a measurement of the diffraction efficiency.

Particular attention was drawn to the sample holder (figure 127). For real time monitoring, the inverse opal should be immersed in a liquid phase. The sample was fixed in a spectrophotometric cell with the substrate turned towards the inside of the cell. Then, a cover was applied to close the cell and avoid evaporation. The latter was made with particular specificities. Indeed, a needle could be inserted so as to inject either the solvent or an analyte during measurements. Magnetic stirring could not be achieved in the cell because of the fixation of the holder on a rail. That's why a space was also dedicated in the cover for the insertion of a plastic cone connected to a peristaltic pump. The other input of the pump was in contact with the air and the pump was connected to alternative voltages so as to suck and blow small quantities of air in the cell and assure homogenization in the liquid phase. Finally, the cell was inserted in an aluminum holder with fluidic channels that enable a temperature control of the cell.

Measurements of the intensity of diffracted beams, P_1 and P_0 , were performed every 30 seconds, starting before solvent (water) injection and until the relative diffraction efficiency was stabilized, then measurements were done every minute (figure 128). The diffraction efficiency rised during the first ten minutes and stabilized at 3.3%. The degree of swelling is the ratio $\frac{d}{d_0}$, as we know the

¹thanks to the software ImageJ, a public domain java-based image processing program.

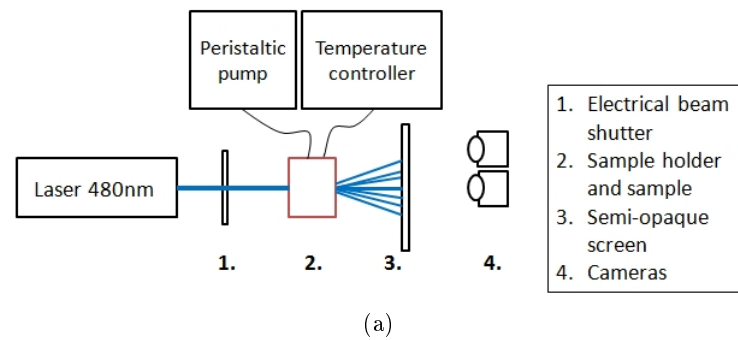


Figure 126: Optical bench for the diffraction monitoring. (a) Schematic representation and (b) picture of the bench.

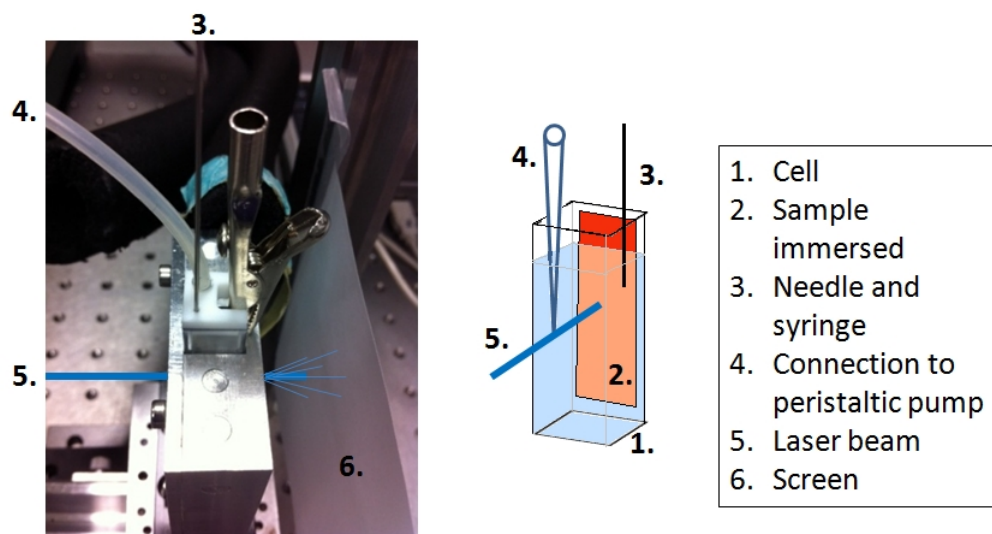


Figure 127: Picture and schematic representation of the sample holder.

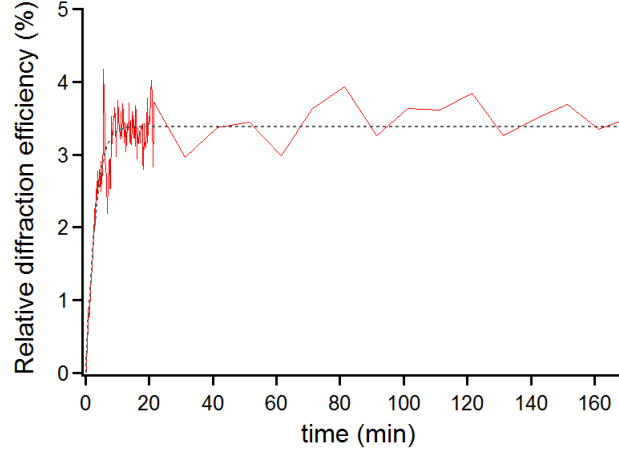


Figure 128: Relative diffraction efficiency as a function of time after solvent injection.

values of $\Delta n = n_{grating} - n_{medium}$ at an instant t and at $t=0$, we can deduce from equation 5.2 (obtained from equation 5.1), that the degree of swelling is 5%. Compared to hydrogels, this is quite a low value for swelling. This is due to the high degree of cross-linking of the polymer, as the bulk formulation of the polymer was used. We thought this would however preserve the recognition process of the inverse opal for 2,4-D: the polymer is too rigid to swell a lot, but still rigid enough to recognize the analyte.

$$\left[\frac{d\Delta n}{d_0 \Delta n_0} \right]_{max} = \sqrt{\eta_{r,max} + 1} \quad (5.2)$$

It is important to notice that figure 128 was obtained for NIPs only. Unexpected behaviors were observed with MIPs yielding irreproducible plots of the diffraction efficiency. We first focused on the study of the NIP and injected 2,4-D in the cell after stabilization of the swelling in solvent during one hour. The diffraction efficiency remained constant which shows that the polymer did not swell nor shrink due to analyte binding. This is also a proof that the refractive index is virtually not affected by the injection of 2,4-D. However, after washing in different solvent baths, when a second experiment was led, the diffraction efficiency was unstable and displayed irreproducible behavior. A measure of the 2,4-D concentration by HPLC evidenced that the solution contained 2,4-D whereas the polymer was supposedly washed and the solvent pure. Further experiments with a nude PMMA substrate showed that the PMMA had a high affinity for 2,4D (hydrophobic substrate). Thus, during the washing steps of the MIPs and the regeneration of the NIPs in solvent baths, it appears that 2,4-D is absorbed by PMMA. As a consequence, during experiments, the substrate released variable amounts of 2,4-D, biased measurements.

This issue stopped the diffraction experiments as the solution would have been to change the substrate, which would require a new optimization of the opal and inverse opal synthesis. It is possible, for example, to use a cyclo olefin copolymer that would resist to HF and to certain organic

solvents. We rather focused our efforts on spectrophotometry.

5.3 Spectrophotometry studies

Opals with 300 nm beads were used to mold NIPs and MIPs inverse opals for 2,4-D. Right after dissolution and a first washing in water, spectrophotometric reflection studies were performed with angles between 5° and 20° of light incidence. To avoid similar issues to the previous section, the washing steps were performed with a dropwise system (figure 129). Drops arrive on the inverse opal inclined of 45° and gravity expulses them from the film with a reduced contact with the PMMA substrate.

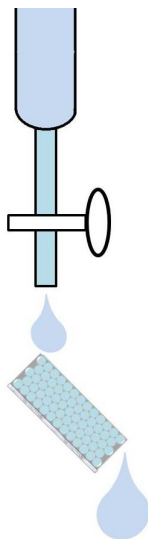


Figure 129: Washing the inverse opal with a dropwise system.

Reflection spectra were recorded after these washing steps, on dried films. Bragg's reflection peak showed a blue-shift for MIPs of 40 nm (spectra with 5° of light incidence are represented on figure 130). For NIPs, a red-shift of 63 nm was observed.

Incubation was then performed with a dropwise system so as to fill all the cavities of the MIP and still avoid the PMMA absorption of 2,4-D. The molecule was dissolved in 200 mL of MeOH/H₂O 4/1 (v/v) at a concentration of 1 mM and the solution passed through the inverse opals in about one hour. Reflection spectra were recorded after incubation (figure 130). One can observe red-shifts for both NIP and MIP structures, synonymous with a swelling of the polymers. For MIP, Bragg's peak shifts of 28 nm, whereas for NIP, it is only 5 nm. This preliminary experiment proves the recognition capability of the MIP and the transduction efficiency of the inverse opal.

If we consider the Bragg law, for $\Delta\lambda = 28$ nm, with $n_{eff} = 1.53$, it gives $\Delta d = 9.8$ nm, that is to say a swelling ratio of 3.5%, whereas for the NIP, $\Delta d = 1.6$ nm. The recognition of the analyte by the MIP is confirmed by spectra with 10, 15 and 20° of light incidence, since the shifts after washing and

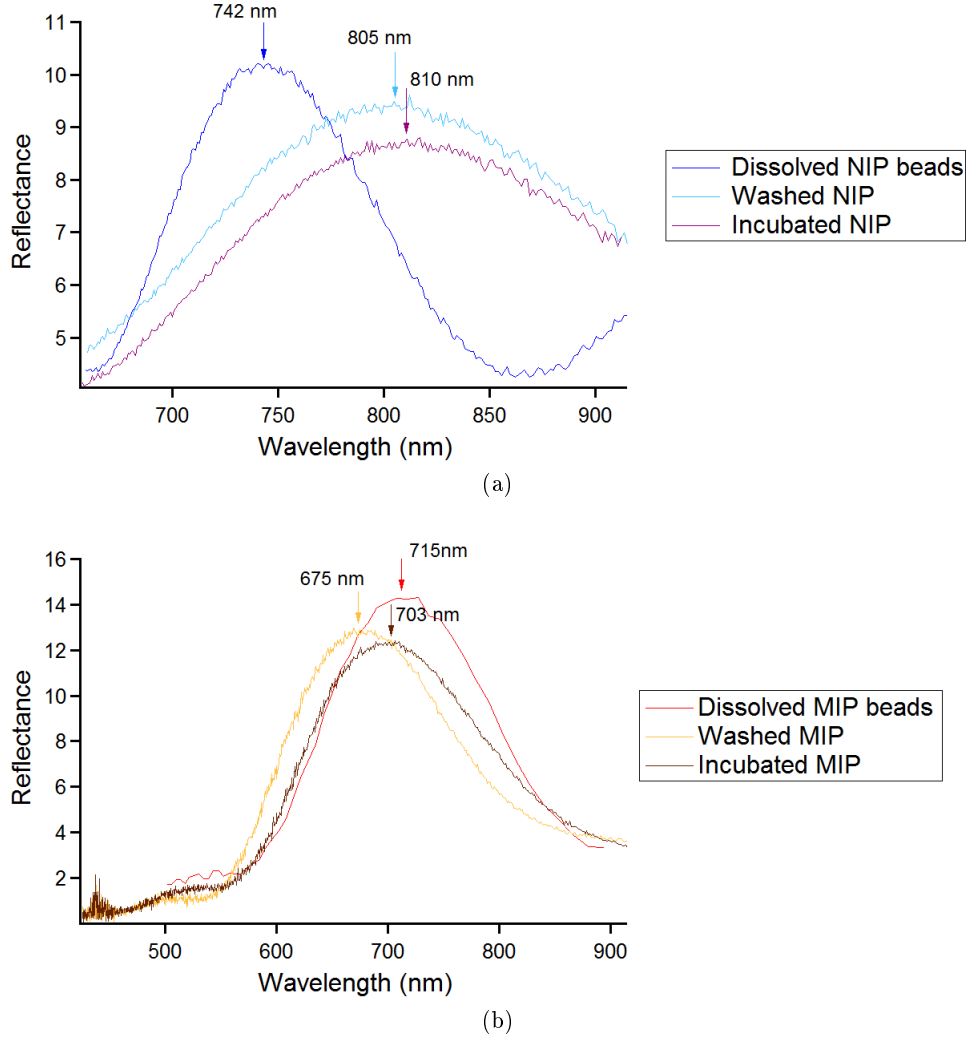


Figure 130: Reflection spectra for NIP and MIP inverse opals before and after incubation with 2,4-D, with light incidence of 5° . Arrows indicate the wavelengths of the maxima. (a) NIP and (b) MIP.

after incubation are similar. Further tests with more angles of incidence would enable a modelization by the Bragg law of the lattice evolution, and thus, confirm the sensing ability of the MIP inverse opal. This preliminary result was reproduced twice and displayed a good reproducibility. The sensitivity of the sensor is not optimal, since the shift observed is the maximum (if all the cavities are really filled with the template) but this is due to the high cross-linking degree of the polymer. A compromise should therefore be found between the swellability and the selectivity of the polymer in order to develop a reliable sensor.

5.4 Conclusion

In this chapter, we focused on an original optical transduction for MIPs-based sensors. This technique is a label free approach, easy to handle and which could be spread to numerous other com-

pounds. We successfully synthesized opals thanks to a new technique. Compared to any other opal synthesis, the Boostream[®] equipment offers a possibility to manufacture opal at an industrial scale. Furthermore, several approaches were tested for inverse opals. The sandwich and spin-coating techniques gave heterogeneous surfaces and results difficult to reproduce. However, once optimized, the dip-coating approach gave satisfying results. Characterization was performed by diffraction and spectrophotometry. Concerning the sensing ability of the device, several issues were encountered with the opal substrate (PMMA) which absorbed the analyte. We proposed to overcome this issue by washing the inverse opal with a dropwise system and performed spectrophotometry analyses in air before and after incubation. This solution gave a preliminary promising result. Indeed, we observed a small shift of Bragg's peak upon recognition of 2,4-D by the MIP. It supports the concept of the sensor for further optimizations. Bigger shifts could be observed with polymers less cross-linked, as already published in several papers. This may, though, reduce the MIP specificity. Finally, we developed an optical sensor for 2,4-D and as far as we know, this is the first time that such an inverse opal is used to detect 2,4-D and that a highly cross-linked polymer displays a Bragg's peak shift.

Bibliography

- [1] K. Haupt, A. Dzgoev, and K. Mosbach, "Assay system for the Herbicide 2,4-Dichlorophenoxyacetic Acid Using a Molecularly Imprinted Polymer as an Artificial Recognition Element," *Analytical chemistry*, vol. 70, no. 3, pp. 628–631, 1998.
- [2] N. M. Rosenberg, R. M. Queen, and J. H. Stamper, "Sweat-patch test for monitoring pesticide absorption by airblast applicators," *Bulletin of Environmental Contamination and Toxicology*, vol. 35, no. 1, pp. 68–72, 1985.
- [3] P. P. Egeghy, E. A. C. Hubal, N. S. Tulve, L. J. Melnyk, M. K. Morgan, R. C. Fortmann, and L. S. Sheldon, "Review of Pesticide Urinary Biomarker Measurements from Selected US EPA Children ' s Observational Exposure Studies," *Int. J. Environ. Res. Public Health*, vol. 8, pp. 1727–1754, 2011.
- [4] O. Auctions, "www.opalauctions.com."
- [5] W. Stober and A. Fink, "Controlled Growth of Monodisperse Silica Spheres in the Micron Size Range," *Journal of colloid and interface science*, vol. 26, pp. 62–69, 1968.
- [6] G. Bogush and C. Zukoski, "Studies of the kinetics of the precipitation of uniform silica particles through the hydrolysis and condensation of silicon alkoxides," *Journal of Colloid and Interface Science*, vol. 142, pp. 1–18, Mar. 1991.
- [7] Y. a. Vlasov, X. Z. Bo, J. C. Sturm, and D. J. Norris, "On-chip natural assembly of silicon photonic bandgap crystals," *Nature*, vol. 414, pp. 289–93, Nov. 2001.
- [8] J. D. Joannopoulos, "Self-assembly lights up," *Nature*, vol. 414, pp. 257–8, Nov. 2001.
- [9] M. Bardosova, P. Hodge, L. Pach, M. E. Pemble, V. Smatko, R. H. Tredgold, and D. Whitehead, "Synthetic opals made by the Langmuir – Blodgett method," *Thin Solid Films*, vol. 437, pp. 276–279, 2003.
- [10] N. Griffete, H. Frederich, A. Maitre, S. Ravaine, M. M. Chehimi, and C. Mangeney, "Inverse opals of molecularly imprinted hydrogels for the detection of bisphenol A and pH sensing," *Langmuir : the ACS journal of surfaces and colloids*, vol. 28, pp. 1005–12, Jan. 2012.
- [11] T. Maka, D. N. Chigrin, S. G. Romanov, and C. M. Sotomayor Torres, "Three dimensional photonic crystal in the visible regime," *Progress in Electromagnetics Research*, pp. 307–335, 2003.
- [12] H. Peng, S. Wang, Z. Zhang, H. Xiong, J. Li, L. Chen, and Y. Li, "Molecularly Imprinted Photonic Hydrogels as Colorimetric Sensors for Rapid and Label-free Detection of Vanillin," *Journal of Agricultural and Food Chemistry*, vol. 60, pp. 1921–1928, 2012.

Conclusion

This manuscript described the elaboration of a label-free optical sensor based on Molecular Imprinted Polymers (MIPs). The underlying goal was to provide new non invasive biosensors able to monitor some analytes in physiological fluids, notably in sweat. Indeed, this kind of sensors -non invasive, easy to integrate in a comfortable patch and easy to read- would allow a personalized monitoring of subjects health. Thus, in order to realize the proof of concept, we selected three molecules of interest, two steroid molecules secreted in some physiological fluids and one xenobiotic:

- Cyproterone acetate, a synthetic molecule, mainly used in the treatment of prostate cancer and paraphilia.
- Cortisol, a biomarker of stress, which secretion in too large amounts can lead to a paralysis or be a source of errors in crucial conditions.
- 2,4-dichlorophenoxyacetic acid, a pesticide used worldwide and which rises environmental and health concerns.

First developed building blocks for the elaboration of these sensors were MIPs, targeting specifically these two steroids and pesticide. MIPs present the advantages of being stable, selective, producible at an industrial scale and cheap. They are referred to as tailor made synthetic receptors and offer a good alternative to biomolecules for recognition in sensors.

Cyproterone acetate was first imprinted in a polymer using toluene as solvent. NMR studies in the latter proved the formation of interactions between CPA and monomer methacrylic acid. A design of experiments (DOE) was subsequently undertaken in order to lead to a formulation optimization and maybe to the discovery of a formulation efficient in aqueous media. In this DOE, binding parameters (quantity of CPA bound to 5 and 20 mg/mL of polymer) were considered as output responses. However, the obtained results were not those expected. The choices of the design and its input factors were unsuitable and these issues were amplified by the fact that washing steps needed much more time than predicted. That's why we proposed a critical review of the work as well as several ways of improvement. One of them was to separate the DOE into independent bricks, according to the solvent, for example. This approach was therefore chosen to develop a MIP specific to cortisol. Indeed, once a first formulation of MIP for cortisol was found and once the formation of a complex was demonstrated in liquid by NMR, we performed a new DOE. This time, the parameters were limited and only one solvent was used. The statistical analysis of the results, completed by porosity studies, gave an optimized formulation. The morphologies of the polymer displayed an important role in the binding affinity, and the study particularly highlighted that bigger pores foster adsorption. Finally, a bulk polymer imprinted by 2,4-dichlorophenoxyacetic acid was also tested, based on a formulation used in the laboratory of Compiègne.

After the development of these polymers, the second building block, that is the transduction part of the sensor, was implemented. The developed transduction is an optical approach thanks to an inverse opal structure. Indeed, the recognition of the analyte by structured MIP leads to a polymer swelling, which changes the network lattice and therefore the sensor color (which may, in certain cases, be read by naked eye).

In order to build this inverse opal, the first needed step is the realization of imitation opals. They were synthesized with silica beads deposited by a unique equipment (Boostream[®]), able to work at an industrial scale. The obtained opals were homogeneous and uniform. Inverse opals were then molded by injection of 2,4-D MIP inside the photonic crystals, followed by beads dissolution. Inverse opals are structures which possess a high specific area and this gives an easy access to the imprinted cavities by the analyte. Several techniques were explored and dip-coating was selected since it gave uniform and reproducible inverse opals. Structures were characterized by diffraction and spectrophotometry. Spectrophotometry studies were performed before and after incubation of the sensor with 2,4-D. Thus, we demonstrated the functionality of this kind of sensor. Polymers less cross-linked should display bigger changes of color than those observed upon sensing as already described in the literature. This should not, however, be at the expense of the recognition ability and the specificity of the sensor. In order to work with formulations developed for CPA and cortisol, an opal of latex beads could be deposited on a glass substrate. Indeed, latex beads would be dissolved in tetrahydrofuran and glass substrates would resist to toluene and dichloromethane. Moreover, in the case of 2,4-D, there would be no absorption of the analyte in the substrate and thus, the sensor could be tested for different concentrations of analyte.

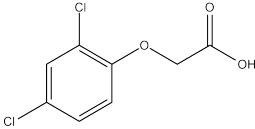
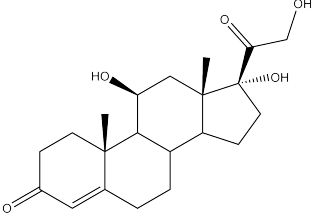
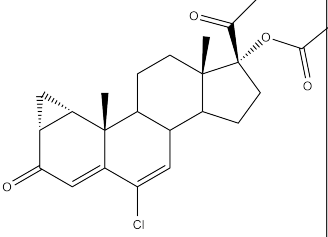
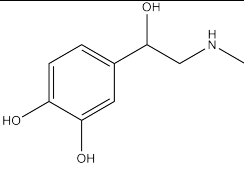
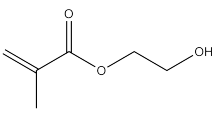
As a conclusion, this work, dedicated to the elaboration of a new sensor, proved the concept of the sensor and evidenced the need to optimize MIPs formulations for their use in inverse opal sensors. Furthermore, techniques employed created new opportunities for the development of opals and inverse opals (industrial equipment). This opens new ways of optimization for biosensors.

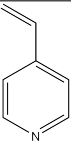
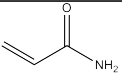
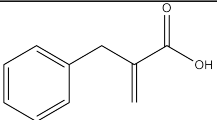
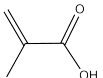
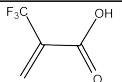
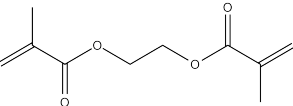
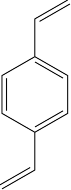
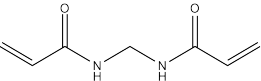
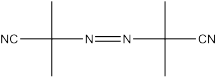
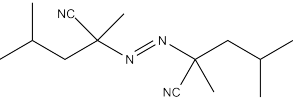
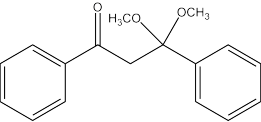
APPENDICES

A Materials

A.1 Chemicals

Chemicals used in the thesis are listed in table 19, with the supplier, the molecular representation and physical characteristics.

Reagent	Supplier	Representation	Molecular mass (g/mol)	Density (g/mL)
2,4-dichlorophenoxyacetic acid (2,4-D)	Sigma Aldrich		221	-
Cortisol	Sigma Aldrich		362.5	-
Cyproterone acetate (CPA)	Molekula		417	-
Epinephrine	Sigma Aldrich		183	-
2-hydroxyethyl methacrylate (HEMA)	Sigma Aldrich		130.1	1.07

4-vinylpyridine (4-vp)	Sigma Aldrich		105.1	0.98
Acrylamide (AM)	Sigma Aldrich		71.1	-
Benzylmethacrylate (BMA)	Sigma Aldrich		176.2	1.04
Methacrylic acid (MAA)	Sigma Aldrich		86,09	1.015
Trifluoromethylacrylic acid (TFMAA)	Sigma Aldrich		140.1	-
Ethylene glycol dimethacrylate (EDMA)	Sigma Aldrich		198.22	1.051
Divinylbenzene (DVB)	Sigma Aldrich		130.19	0.914
Methylene-bis- acrylamide (MbAAM)	Sigma Aldrich		154.2	-
2,2'-Azobis(2- methylpropionitrile) (AIBN)	Sigma Aldrich		164.21	-
2,2'-azo-bis-(2,4- dimethylvaleronitrile) (ABDV)	Dupont (Vazo52)		242	-
Dimethoxyphenyl acetophenone (DMPA)	Sigma-Aldrich		256.3	-

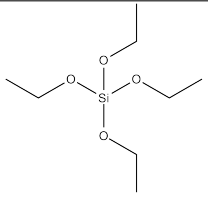
Tetraethoxysilane (TEOS)	Sigma Aldrich		208.3	0.93
Ammonium hydroxide	Sigma Aldrich	NH ₄ OH	35.1	0.9
Hydrofluoric acid	38%, Wako, Tamapure	HF	20.0	1.15

Table 19: Chemical products used in the thesis.

Solvents used in the thesis are listed in table 20.

Solvent	Supplier	Density (g/mL)
Acetonitrile (ACN) anhydrous 99.8%	Sigma Aldrich	0.786
Acetonitrile (ACN) chromasolv gradient grade for HPLC >99.9%	Sigma Aldrich	0.786
Chloroform anhydrous >99%	Sigma Aldrich	1.48
Dichloromethane anhydrous >99.8%	Sigma Aldrich	1.325
d2-dichloromethane	Aldrich	1.362
Ethanol absolute anhydrous	Carlo Erba	0.79
Ethyl acetate puriss p.a. ACS reagent	Sigma aldrich	0.90
Heptane	Sigma Aldrich	0.684
Isopropanol 99.5% HPLC grade	Sigma Aldrich	0.785
Butanol	Sigma Aldrich	0.81
2-Pentanol	Sigma Aldrich	0.81

Methanol puriss p.a. >99.8%	Sigma Aldrich	0.791
Tetrahydrofuran (THF) puriss p.a. >99.9%	Sigma Aldrich	72.11
Toluene puriss p.a. >99.7%	Sigma Aldrich	0.865
d8-toluene	Aldrich	0.943

Table 20: Solvents used in the thesis.

A.2 Equipments

Equipments used in the thesis are listed in table 21.

Material	Supplier and properties
UV lamp table for bulk polymers	Vilbert Lourmat TFX-20.M P=180W
Precellys 24 homonegizer	Bertin Technologies
BET ASAP2420	Micromeritics, Norcross, USA.
HPLC	Waters2695 coupled to a Waters2487 Dual λ Absorbance Detector
96-well filter plates	AcroPrep. 2mL, PTFE membrane (0.2 μ m)
NMR spectrometer Bruker Avance III 400MHz	Bruker GmbH, Germany
Zeta Sizer NanoZS	Malvern, United Kingdom
PMMA substrates	Technicoplast

Spin-coater Laurell	WS 400B 8NPP/LITE
UV lamp with optical fiber	HONLE UV Technology bluepoint 2 easycure, 4.5 W/cm ²
Lamp	Deuterium-Halogen Melles Griot 13HLS103
USB spectrometer USB2000+ XR_{ES}	OceanOptics
Laser	Argon, SPectra-Physics Lasers
USB camera	Moticam1000
SEM	Hitachi S.4000
AFM Dimension 5000A	Bruker. Tapping Mode. Tips RTESP (MPP 11100-10)
Optical microscope	Zeiss Axio Imager 2 A2M, Carl Zeiss Microimaging GmbH

Table 21: Equipments used in the thesis.

B Protocols

B.1 Polymer bulk

B.1.1 Synthesis

We report here a general bulk synthesis. Ranges of material quantities are indicated but exact amounts are specified in chapters.

Initiator was weighed in a small glass vial (0.1 mol% of template), closed by a septum. Solvent was added (1-3 mL), followed by functional monomer (1-12 times of template quantity) and cross-linker¹ (10-50 times of template quantity). Finally, exclusively for MIPs, the template was dissolved in the mixture (0.1-1 mmol). The so called precursor mixture was purged with inert gas (Argon or N₂), for 4 minutes.

Polymerization was then carried out either by thermal initiation (in a graphite bath, at least overnight and 45 °C) or by UV (UV table, in a refrigerated room or at room temperature, overnight).

B.1.2 Binding evaluation

After polymerization, bulk polymers were collected and crushed in a mortar. Polymers were finely ground in micro-centrifuge tubes, in solvent², with ceramic beads in a Precellys[®] homogenizer (2*20 s, 5000 rpm).

Particles were subsequently washed:

- 5 times in 10 mL of a mixture solvent²/acetic acid (4/1 in volume)
- 5 times in a mixture of solvent²/acetic acid (9/1 in volume)
- 5 times in pure solvent².

If leaching issues were encountered, polymers were then washed 5 more times in solvent²/acetic acid 9/1 and as many times as needed in pure solvent² so as to observe less than 0.5 μ M of template in the supernatant. Each washing step consists in agitation on a tubes rotator, during at least one

¹DVB was passed through an alumina column before use to remove the polymerization inhibitor

²Methanol for cortisol and 2,4-D, acetonitrile for CPA

hour, in centrifuge tubes. Afterwards, polymer particles were sedimented and separated from the solvent by centrifugation. The template content of the pure solvent supernatants was measured by HPLC, every 2 to 5 washes. Finally, after complete washing, the polymers were vacuum-dried overnight.

Binding assays for MIPs and NIPs were then performed. Solvent selected for the test was, most of the time, the solvent porogen of the synthesis.

Increasing concentrations of polymer (NIP or MIP) were suspended in solvent (from 0 to 40 mg/mL, complete volume of 1 mL), in 2 mL centrifuge tubes, and incubated with the template at the desired concentration, for a complete volume of 1 mL. Incubation occurs during 4 h, in obscurity, on a tubes rotator. The tubes were then centrifuged and next steps depend on the solvent used for incubation:

- for dichloromethane, toluene, tetrahydrofuran: these solvents were not recommended for HPLC and had to be removed. So, 300 μ L of supernatant were transferred in new tubes and subsequently evaporated under vacuum. Then, 300 μ L of solvent³ were added and the tube was well agitated to re-dissolve the template. The template concentration was then measured by HPLC (appendix C).
- for any other solvents, such as acetonitrile and methanol, the template concentration was directly measured by HPLC. The HPLC measurements gave the concentration of unbound template.

B.1.3 Porosity measurements

The surface areas were calculated using the Brunauer-Emmett-Teller (BET) equation and data from nitrogen adsorption/desorption isotherms at 77 K obtained with a ASAP2420 (Micromeritics, Norcross, USA). Approximately 0.2 g of samples was used. Prior to analysis, the samples were degassed at elevated temperatures (1 hour 90 °C, 16 hours 120 °C).

B.1.4 Designs of experiments

The design of experiments for CPA was an optimal design, to study the binding affinities of several MIPs formulations. The influence of seven factors was studied (solvent, volume of solvent, polymerization temperature, functional monomer, ratio of functional monomer, cross-linker, ratio of cross-linker) on the binding affinity (B_5^{NIP} , B_5^{MIP} , B_{20}^{NIP} and B_{20}^{MIP}). The software Design Expert 07[®] was used to define the set of experiments.

The Doehlert design of experiments was used for cortisol to optimize the MIP formulation. The influence of three factors was studied (ratios of functional monomer and cross-linker, amount of initiator) on some binding parameters (K_{50} , B_{max} and IF) and on the porosity of the polymers. The software JMP 7.0[®] (SAS institute) was used to define and analyze the results of the DOE.

³Acetonitrile for cyproterone acetate template and methanol for cortisol template

B.2 NMR ^1H and ^{13}C

NMR spectra ^1H and ^{13}C were obtained on a spectrometer (Bruker Avance III), at 400.2 MHz for proton; 100.6 MHz for carbon. Solvent were d6-toluene (CPA) or d2-dichloromethane (cortisol). The spectra were then analyzed with the MestReNova v8.1.2 software.

B.3 Silica spheres

B.3.1 Synthesis

We report here a general synthesis. Ranges of material quantities are indicated but exact amounts are specified in chapter IV.

All the glasswares were thoroughly washed with sodium hydroxyde (1.4 g) in water (150 mL) and ethanol (200 mL), in an ultrasonica bath for 10 min. They were then rinsed with distilled water.

Ethanol (20-200 mL), water (1-20 mL) and ammonia (2-5 mL) were mixed in an erlenmeyer and stirred to create a vortex. All TEOS (0.5-8 mL) was added at once. The solution was then agitated during 24 h.

If a subsequent growth stage was needed, new amounts of TEOS could be added. The amounts of TEOS added were equivalent to $\frac{1}{3}$ of the quantity previously introduced so as to avoid particles aggregation. For 1 mole of TEOS added, one should also add 2 moles of water. Water was always introduced first and TEOS was added at once. The solution was agitated during 12 hours between each addition of reagents. Beads were centrifuged and washed several time in ethanol. Finally, they were dried under vacuum.

B.3.2 Evaluation of the silica particles diameter

The size of silica particles was measured by dynamic light scattering with a Zeta Sizer NanoZS (Malvern, United Kingdom). Measurements are performed at a constant angle 173° , with a laser (633 nm) and each measurement is the average of three independent measurements, determined automatically (> 20 sequences of 10 s measurements).

The silica particles were suspended in ethanol (0.1% w/w). The size and polydispersity are given by the cumulants analysis of the autocorrelation function. Size distribution is an intensity distribution, this can be converted, thanks to Mie theory, to a volume and number distribution.

B.4 Opals

Silica particles were suspended in a solution of butanol (35 mg/mL). They were dispersed in an ultrasonic bath (30 min). Particles were then injected on a carrier fluid (water) and brought, thanks

to hydrodynamic forces, to form a compact film on the liquid surface. This area is called "transfer area". Its surface was controlled by a camera connected to a unique software (image processing). When the software detected an optimal compacity of the beads, substrates were emerged from the fluid (a few cm/min) and a monolayer of beads was transferred on PMMA substrates. The layer was then dried under a infrared lamp heater (1200W, around 30 min). The substrates were immersed back in the fluid and the process was repeated as many times as needed.

B.5 Inverse opals

B.5.1 Polymer synthesis

The precursor mixture was prepared and purged in a flask, in the same way as bulk polymers.

- Sandwich

A drop of the precursor mixture was deposited on the opal. A subsequent PMMA cover was carefully added on the opal. Polymerization was then launched by UV illumination, during 15 minutes.

- Spin-coating

The substrate with the opal was immobilized in the spin-coater, under inert atmosphere (N_2). One or two drops of precursor mixture was deposited on the opal. The liquid spread into the opal by capillarity. Once the opal became transparent, the spin-coater was turned on (500 rpm, 30 seconds). Next, polymerization was launched under UV light thanks to a optical fiber inserted in the spin-coater (15 minutes).

- Dip-coating

The equipment was set in a glove box under N_2 atmosphere. The substrate was clipped on a vertical translation plate and immersed in the precursor mixture (5 mm/s). After 1 minute, the substrate was emersed (0.1mm/s). After total emersion, the polymerization was launched thanks to a UV lamp connected to an optical fiber. During polymerization (15 minutes), the substrate was periodically agitated in front of the UV cone (up and down).

B.5.2 Beads dissolution

PMMA substrates with opals embedded in polymer were immersed in a hydrofluoric acid bath (4%) and the beads dissolution took place overnight. The substrates were then thoroughly rinsed with water and dried with a N_2 flow.

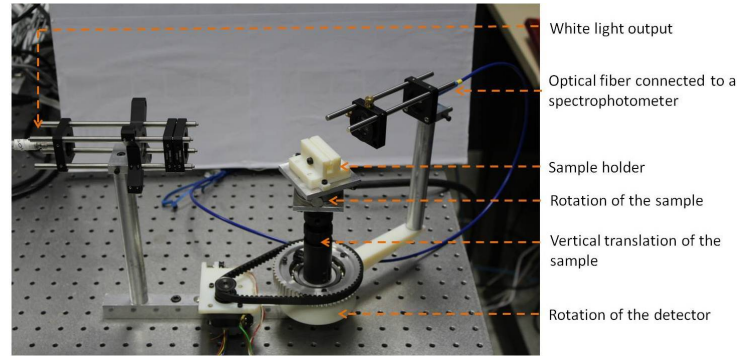


Figure 131: Picture of the developed optical bench for angle resolved spectroscopy.

B.5.3 Characterizations

Spectrophotometry

Spectrophotometric spectra were recorded with a USB2000+*XR_{ES}* spectrometer (OceanOptics, Netherlands) and registered either by the software SpectraSuite or with a home made Labview software. We used the developed goniometer bench (figure 131), light source was immobile and the detector could rotate. The sample was immobilized in the middle of the circular bench and could rotate along the vertical axis. Reflection and transmission spectra were then recorded.

Diffraction

- Evaluation of the refractive index

The PMMA substrate was immobilized in a plastic spectrometer cell. The cell was filled with a solvent (water, isopropanol, butanol, or 2-pentanol) and after 15 minutes, the laser beam (488 nm) hit the sample and a powermeter measured the intensities of the direct beam and the first order of diffraction, more than 5 measurements were made for each. The average was then used to trace the plot of the squareroot diffraction efficiency against the solvent refractive index. A linear plot enabled the evaluation of the grating refractive index (equation B.1).

$$\eta = C \left(\frac{e\Delta n}{\lambda} \right)^2 \quad (\text{B.1})$$

where: η is the diffraction efficiency, λ is the probing wavelength, $\Delta n = n_{\text{grating}} - n_{\text{medium}}$, the difference between refractive index of grating and surrounding medium, C is a constant and e the thickness of the grating.

- Monitoring the swelling

The PMMA substrate was immobilized in a plastic spectrometer cell. The cell was introduced in a specific support whose temperature is controlled. Thanks to a Teflon machined cover, a needle could be inserted in the cell, along with a pipette tip connected to a peristaltic pump (for agitation).

Once the laser turned on, the diffraction figure was projected on a semi-opaque screen behind which usb cameras (Moticam1000) pictured the beam and the first order of diffraction (every 30 seconds). After a few seconds, the solvent was injected in the cell. After 20 minutes the picture frequency was slowed down to every minute. Further injections of a stock solution of template could be performed. The pictures were then analyzed by the software ImageJ⁴, so as to evaluate the intensities of the diffracted orders and plot the effective diffraction efficiency against time (equation B.2).

$$\eta_r = \frac{\eta(t) - \eta_0}{\eta_0} \approx \frac{(d\Delta n)^2 - (d_0\Delta n_0)^2}{(d_0\Delta n_0)^2} \quad (\text{B.2})$$

where η_r is the relative diffraction efficiency, $\eta(t)$ and η_0 are the diffraction efficiencies at a t time and for $t=0$, d and d_0 are the periods of the grating at t and $t=0$, Δn and Δn_0 are the differences of refractive index at t and $t=0$.

⁴A public domain java-based image processing program

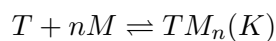
C Cyproterone acetate, cortisol and 2,4-dichlorophenoxyacetic acid dosage by HPLC

The HPLC system used for the HPLC studies was a Waters2695 coupled to a Waters2487 Dual λ Absorbance Detector. The HPLC column used was a Supelcosil LC-18 (25 cm x 4.6 mm x 5 μ m). The flow rate was 1mL/min, the injection volume was 10 μ m. The elution was carried out in isocratic mode.

Molecule	Mobile phase	Detection wavelength	Retention time	Limit of detection
Cyproterone acetate	water/acetonitrile 30/70	280 nm	5.56 min	0.5 μ M
Cortisol	water/acetonitrile 60/40	254 nm	4.6 min	0.5 μ M
2,4-dichlophenoxy acetic acid	water/acetonitrile (with 0.05% of trifluoroacetic acid) 30/70	220 nm	3.7 min	1 μ M

D Job plot - method of continuous variations

Let's consider the complex formation of the template (T) and a monomer (M).



The association constant is: $K = \frac{C_{TM_n}}{C_T C_M^n}$ with C_T , C_M and C_{TM_n} , the equilibrium concentrations of T, M and TM_n respectively.

To study the complex formation and stoichiometry, we perform NMR spectra of a series of solutions where the mole fraction of the template and the monomer vary but the total concentration and the volume remain constants. We monitor the chemical shift of several protons that changes with the formation of a complex.

We write V_T as the template's solution volume and V_M as the monomer's solution volume, and $V = V_T + V_M$

The total concentration C_{tot} is given by:

$$C_{tot} = \frac{1}{V} (V_T C_T^i + V_M C_M^i) = \frac{1}{V} ((V - V_M) C_T^i + V_M C_M^i)$$

where i refers to stock solution concentrations.

We write C_T^0 and C_M^0 the initial concentrations of template and monomer in the solutions. Thus, $C_T = C_T^0 - C_{TM_n}$ and $C_M = C_M^0 - nC_{TM_n}$

$$K = \frac{C_{TM_n}}{(C_T^0 - C_{TM_n})(C_M^0 - nC_{TM_n})^n}$$

$$\begin{aligned}
 C_{TM_n} &= K (C_T^0 - C_{TM_n}) (C_M^0 - nC_{TM_n})^n \\
 C_{TM_n} &= K \left(C_T^i \frac{V_T}{V} - C_{TM_n} \right) \left(C_M^i \frac{V_M}{V} - nC_{TM_n} \right)^n \\
 C_{TM_n} &= K \left(C_T^i \frac{V_T}{V} - C_{TM_n} \right) \left(\left(1 - \frac{V_T}{V}\right) C_M^i - nC_{TM_n} \right)^n
 \end{aligned}$$

We note $v = \frac{V_T}{V}$ and $r = \frac{C_M^i}{C_T^i}$

$$C_{TM_n} = K (C_T^i v - C_{TM_n}) ((1-v)rC_T^i - nC_{TM_n})^n$$

We look for the maximum of C_{TM_n} with v varying. Let's derive the function in $\frac{\partial C_{TM_n}}{\partial v}$

$$\begin{aligned}
 \frac{\partial C_{TM_n}}{\partial v} &= K \left[\left(C_T^i - \frac{\partial C_{TM_n}}{\partial v} \right) ((1-v)rC_T^i - nC_{TM_n})^n \right. \\
 &\quad \left. + n (C_T^i v - C_{TM_n}) \left(-rC_T^i - n \frac{\partial C_{TM_n}}{\partial v} \right) ((1-v)rC_T^i - nC_{TM_n})^{n-1} \right] \\
 \frac{\partial C_{TM_n}}{\partial v} &= C_{TM_n} \left[\frac{C_T^i - \frac{\partial C_{TM_n}}{\partial v}}{C_T^i v - C_{TM_n}} + \frac{n \left(-rC_T^i - n \frac{\partial C_{TM_n}}{\partial v} \right)}{(1-v)rC_T^i - nC_{TM_n}} \right]
 \end{aligned}$$

The maximum of C_{TM_n} is obtained for $\frac{\partial C_{TM_n}}{\partial v} = 0$

$$(1-v)rC_T^i - nC_{TM_n} = nr (C_T^i v - C_{TM_n})$$

we work in such conditions that $r = 1$, so:

$$\begin{aligned}
 C_T^i [r(1-v-nrv)] &= 0 \\
 v &= \frac{1}{1+n}
 \end{aligned}$$

If we vary the molar ratio of the template and monomers, while keeping a constant molecularity, the maximum of the complex concentration will occur for a template molar fraction of $\frac{1}{1+n}$

In NMR spectra, we can follow the chemical shift (δ_{obs}) of protons close to chemical function that are aken to form a complex. In fast exchange systems, this shift is the average of the complex chemical shift (δ_{TM_n}) and the free form chemical shift (δ_T).

$$\begin{aligned}\delta_{obs} &= \frac{C_{TM_n}}{C_T^0} \delta_{TM_n} + \frac{C_T}{C_T^0} \delta_T \\ \delta_{obs} &= \frac{C_{TM_n}}{C_T^0} \delta_{TM_n} + \frac{C_T^0 - C_{TM_n}}{C_T^0} \delta_T \\ \delta_{obs} - \delta_T &= \frac{C_{TM_n}}{C_T^0} (\delta_{TM_n} - \delta_T)\end{aligned}$$

We write $\Delta = \delta_{obs} - \delta_T$ and $\Delta^0 = \delta_{TM_n} - \delta_T$

$$\begin{aligned}\frac{C_{TM_n}}{C_T^0} &= \frac{\Delta}{\Delta^0} \\ \Delta C_T^0 &= \Delta^0 K (C_T^i v - C_{TM_n}) ((1-v)rC_T^i - nC_{TM_n})^n\end{aligned}$$

where $v = \frac{V_T}{V} = \frac{C_T}{C_{tot}}$

$$\Delta v = \frac{\Delta^0}{C_{tot}} K (C_T^i v - C_{TM_n}) ((1-v)rC_T^i - nC_{TM_n})^n$$

During the studies we will note $v = \chi_T$, the mole fraction of template when $r = 1$. We can therefore plot $\Delta\chi_T$ as a function of χ_T . The maximum for $\chi_T = \frac{1}{1+n}$ gives the complex stoichiometry.

E Formulations of polymers for the CPA design of experiments

Table 23: Formulations of polymers for the CPA DOE.

Run	Functional monomer ratio	Cross linker ratio	Solvent volume (mL)	Polymerization temperature (°C)	Solvent	Functional monomer	Cross linker
1	2	44,2	3,48	44	Acetonitrile	MAA	EDMA
2	11,3	14,4	1	53	Acetonitrile	MAA	EDMA
3	12	26	4	40	Toluene	MAA	EDMA
4	2	16	5	70	Ethanol	MAA	EDMA
5	8,1	16	2,38	63	Ethanol/Water 4/1	MAA	EDMA
6	8,1	16	2,38	63	Ethanol/Water 4/1	MAA	EDMA

Run	Functional monomer ratio	Cross linker ratio	Solvent volume (mL)	Polymerization temperature (°C)	Solvent	Functional monomer	Cross linker
7	10,25	38,6	4	45	Acetonitrile/Water 4/1	MAA	EDMA
8	12	10	1,23	70	Acetonitrile/Water 4/1	MAA	EDMA
9	2	10	4	40	Ethyle acetate	MAA	EDMA
10	12	50	4	69	Ethyle acetate	MAA	EDMA
11	3,5	36	1	70	Ethyle acetate	MAA	EDMA
12	2	50	1	62	Acetonitrile	TFMAA	EDMA
13	5,9	50	2,41	45	Toluene	TFMAA	EDMA
14	2	10	4	46	Toluene	TFMAA	EDMA
15	12	48,6	1,24	70	Toluene	TFMAA	EDMA
16	12	22,31	2,77	53	Ethanol	TFMAA	EDMA
17	12	10	1	40	Ethanol/Water 4/1	TFMAA	EDMA
18	11,3	50	3,85	40	Ethanol/Water 4/1	TFMAA	EDMA
19	7,85	26	2,91	70	Acetonitrile/Water 4/1	TFMAA	EDMA

Run	Functional monomer ratio	Cross linker ratio	Solvent volume (mL)	Polymerization temperature (°C)	Solvent	Functional monomer	Cross linker
20	7,85	26	2,91	70	Acetonitrile/Water 4/1	TFMAA	EDMA
21	4,85	17,8	1,75	45	Ethyle acetate	TFMAA	EDMA
22	10,2	10	3,25	40	Acetonitrile	MAA/HEMA 1/1	EDMA
23	3,2	23,8	1	43	Toluene	MAA/HEMA 1/1	EDMA
24	2	50	3,48	70	Toluene	MAA/HEMA 1/1	EDMA
25	4,6	44,4	3,7	42	Ethanol	MAA/HEMA 1/1	EDMA
26	12	50	1	55	Ethanol/Water 4/1	MAA/HEMA 1/1	EDMA
27	2	10	1	70	Ethanol/Water 4/1	MAA/HEMA 1/1	EDMA
28	4,4	49,2	1,35	59	Acetonitrile/Water 4/1	MAA/HEMA 1/1	EDMA
29	12	20,2	3,88	70	Ethyle acetate	MAA/HEMA 1/1	EDMA

Run	Functional monomer ratio	Cross linker ratio	Solvent volume (mL)	Polymerization temperature (°C)	Solvent	Functional monomer	Cross linker
30	8,45	38	3,93	70	Acetonitrile	BMA	EDMA
31	4,75	19,8	1,5	56	Toluene	BMA	EDMA
32	8	10	1	40	Ethanol	BMA	EDMA
33	10,5	50	2,5	70	Ethanol	BMA	EDMA
34	2	42,8	1	40	Ethanol/Water 4/1	BMA	EDMA
35	12	40,4	4	60	Ethanol/Water 4/1	BMA	EDMA
36	2	23,8	1,75	40	Acetonitrile/Water 4/1	BMA	EDMA
37	10,45	23,4	2,85	52	Ethyle acetate	BMA	EDMA
38	10,4	10	4	48	Acetonitrile	MAA	DVB
39	4,25	50	1,45	70	Acetonitrile	MAA	DVB
40	2	12,4	2,05	63	Toluene	MAA	DVB
41	12	30,6	1,3	59	Ethanol	MAA	DVB
42	2	45,2	3,93	50	Ethanol/Water 4/1	MAA	DVB
43	4,8	44,2	3,22	70	Acetonitrile/Water 4/1	MAA	DVB

Run	Functional monomer ratio	Cross linker ratio	Solvent volume (mL)	Polymerization temperature (°C)	Solvent	Functional monomer	Cross linker
44	4,8	44,2	3,22	70	Acetonitrile/Water 4/1	MAA	DVB
45	10,35	20,84	1	40	Ethyle acetate	MAA	DVB
46	2	10	3,03	70	Ethyle acetate	MAA	DVB
47	3,55	13	2,8	61	Acetonitrile	TFMAA	DVB
48	3,55	13	2,8	61	Acetonitrile	TFMAA	DVB
49	12	20,2	3,66	57	Toluene	TFMAA	DVB
50	9,5	50	4	70	Toluene	TFMAA	DVB
51	7,85	25,4	2,2	40	Ethanol	TFMAA	DVB
52	7,85	25,4	2,2	40	Ethanol	TFMAA	DVB
53	2	50	1,08	70	Ethanol/Water 4/1	TFMAA	DVB
54	11,25	50	1	40	Acetonitrile/Water 4/1	TFMAA	DVB
55	2	10	3,55	48	Acetonitrile/Water 4/1	TFMAA	DVB
56	2	45,2	4	40	Ethyle acetate	TFMAA	DVB
57	12	50	1,39	70	Ethyle acetate	TFMAA	DVB

Run	Functional monomer ratio	Cross linker ratio	Solvent volume (mL)	Polymerization temperature (°C)	Solvent	Functional monomer	Cross linker
58	8,95	50	4	40	Acetonitrile	MAA/HEMA 1/1	DVB
59	4,67	47,6	2,08	50	Acetonitrile	MAA/HEMA 1/1	DVB
60	6	24,8	1	67	Acetonitrile	MAA/HEMA 1/1	DVB
61	2	13,2	3,46	40	Toluene	MAA/HEMA 1/1	DVB
62	10	50	1	65	Toluene	MAA/HEMA 1/1	DVB
63	9,65	10	4	70	Ethanol	MAA/HEMA 1/1	DVB
64	9,45	12	1,8	55	Ethanol/Water 4/1	MAA/HEMA 1/1	DVB
65	11,5	32,8	2,65	40	Acetonitrile/Water 4/1	MAA/HEMA 1/1	DVB
66	9,7	21	4	54	Ethyle acetate	MAA/HEMA 1/1	DVB
67	12	24,6	2,05	41	Acetonitrile	BMA	DVB

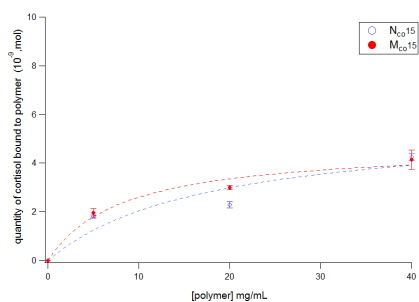
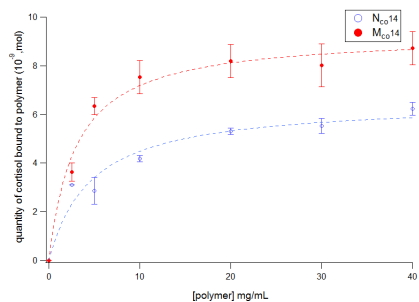
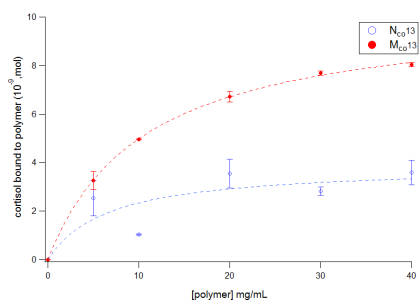
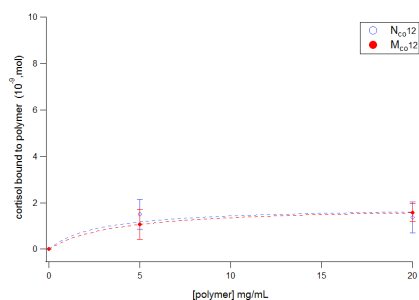
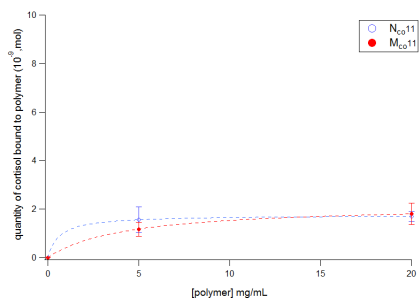
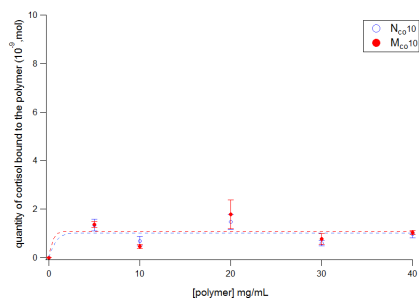
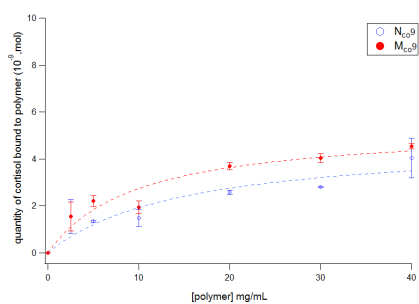
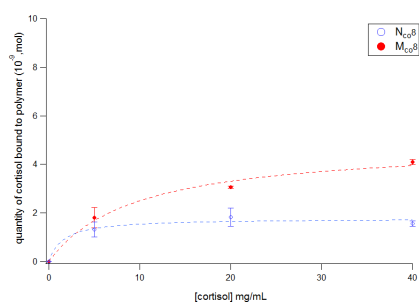
Run	Functional monomer ratio	Cross linker ratio	Solvent volume (mL)	Polymerization temperature (°C)	Solvent	Functional monomer	Cross linker
68	2	50	2,62	53	Ethanol	BMA	DVB
69	10,5	50	2,58	40	Ethanol/Water 4/1	BMA	DVB
70	12	40,8	1	70	Ethanol/Water 4/1	BMA	DVB
71	3,5	10	4	70	Ethanol/Water 4/1	BMA	DVB
72	6,9	11	1	55	Acetonitrile/Water 4/1	BMA	DVB
73	10	50	1	48	Toluene	MAA	MbAam
74	2	50	1,9	40	Ethanol	MAA	MbAam
75	11,6	37,6	4	70	Ethanol	MAA	MbAam
76	12	47	4	40	Ethanol/Water 4/1	MAA	MbAam
77	2	10	1	70	Ethanol/Water 4/1	MAA	MbAam
78	7	24,4	1	40	Acetonitrile/Water 4/1	MAA	MbAam

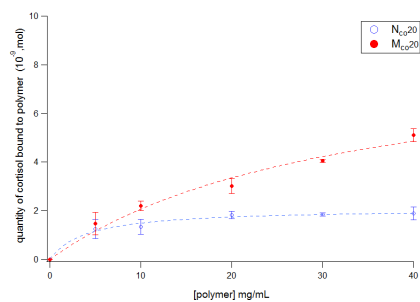
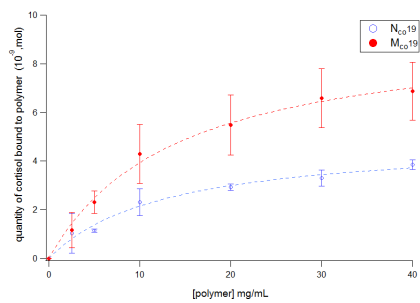
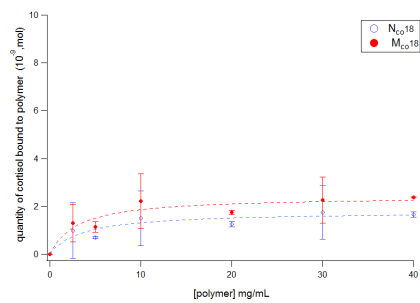
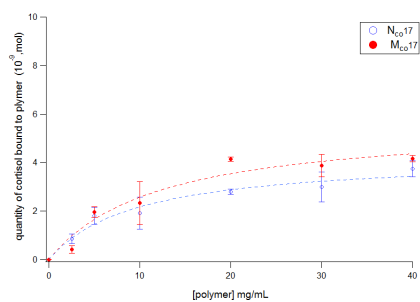
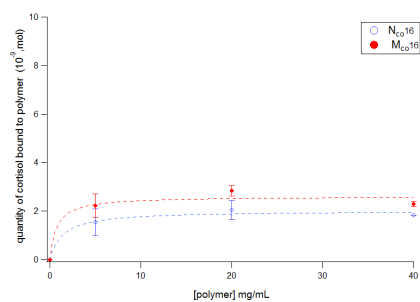
Run	Functional monomer ratio	Cross linker ratio	Solvent volume (mL)	Polymerization temperature (°C)	Solvent	Functional monomer	Cross linker
79	2	50	4	61	Acetonitrile/Water 4/1	MAA	MbAam
80	7,6	22,4	2,95	52	Ethyle acetate	MAA	MbAam
81	11	46,4	3	48	Acetonitrile	TFMAA	MbAam
82	12	10	2,44	40	Toluene	TFMAA	MbAam
83	2	37,66	1,59	64	Toluene	TFMAA	MbAam
84	2	50	4	66	Ethanol	TFMAA	MbAam
85	7,25	10	1	70	Ethanol	TFMAA	MbAam
86	7	19	4	40	Ethanol/Water 4/1	TFMAA	MbAam
87	7,5	44,4	1,2	50	Ethanol/Water 4/1	TFMAA	MbAam
88	4,75	10	4	65	Ethanol/Water 4/1	TFMAA	MbAam
89	12	24,8	1,32	58	Ethyle acetate	TFMAA	MbAam
90	12	10	4	70	Ethyle acetate	TFMAA	MbAam
91	10,95	19,6	2,8	70	Acetonitrile	MAA/HEMA 1/1	MbAam

Run	Functional monomer ratio	Cross linker ratio	Solvent volume (mL)	Polymerization temperature (°C)	Solvent	Functional monomer	Cross linker
92	12	48,8	4	51	Toluene	MAA/HEMA 1/1	MbAam
93	8,5	10	1	70	Toluene	MAA/HEMA 1/1	MbAam
94	11,5	10	1,08	40	Ethanol	MAA/HEMA 1/1	MbAam
95	2,8	39,2	1,27	70	Ethanol	MAA/HEMA 1/1	MbAam
96	3,2	46,2	4	40	Ethanol/Water 4/1	MAA/HEMA 1/1	MbAam
97	7	47,2	4	69	Ethanol/Water 4/1	MAA/HEMA 1/1	MbAam
98	6,15	10	4	70	Acetonitrile/Water 4/1	MAA/HEMA 1/1	MbAam
99	2,5	50	1,39	42	Ethyle acetate	MAA/HEMA 1/1	MbAam
100	2,05	17,6	1,3	46	Acetonitrile	BMA	MbAam
101	2	25,8	3,82	64	Acetonitrile	BMA	MbAam
102	4,5	50	4	40	Toluene	BMA	MbAam

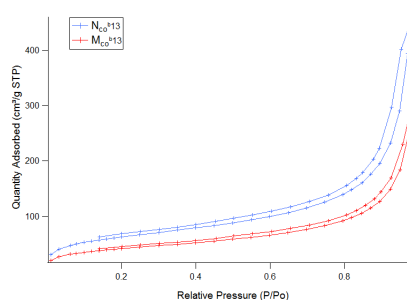
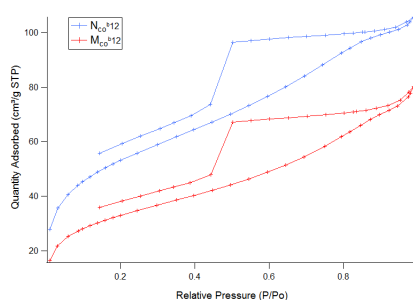
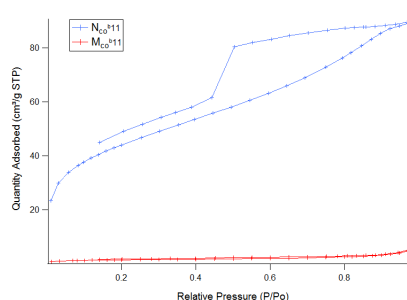
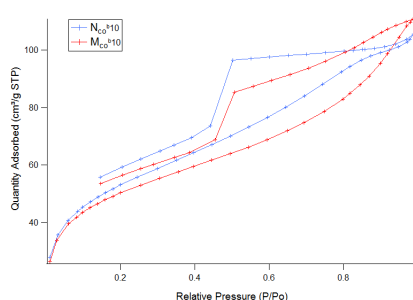
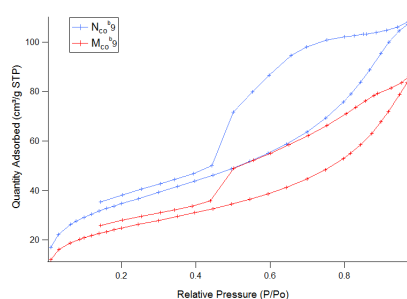
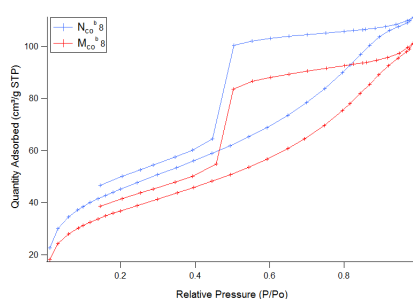
Run	Functional monomer ratio	Cross linker ratio	Solvent volume (mL)	Polymerization temperature (°C)	Solvent	Functional monomer	Cross linker
103	12	12,2	4	70	Toluene	BMA	MbAam
104	12	50	1	40	Ethanol	BMA	MbAam
105	2	12	3,93	46	Ethanol	BMA	MbAam
106	9,63	10	2,34	53	Ethanol	BMA	MbAam
107	7,25	10	1,84	70	Ethanol/Water 4/1	BMA	MbAam
108	12	50	2,31	62	Acetonitrile/Water 4/1	BMA	MbAam
109	2	10	1	40	Ethyle acetate	BMA	MbAam
110	2,85	50	3,1	70	Ethyle acetate	BMA	MbAam

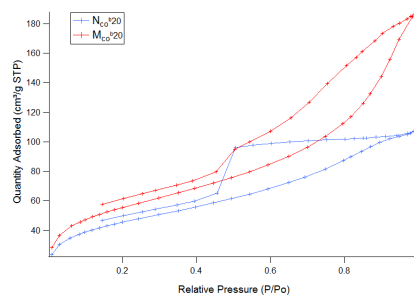
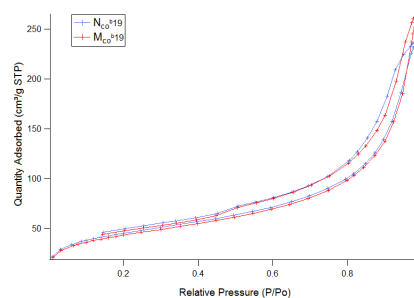
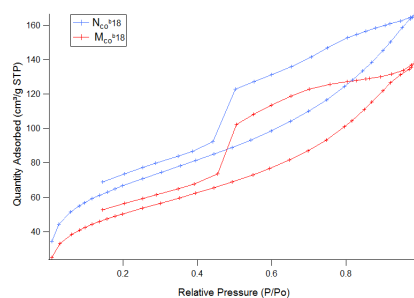
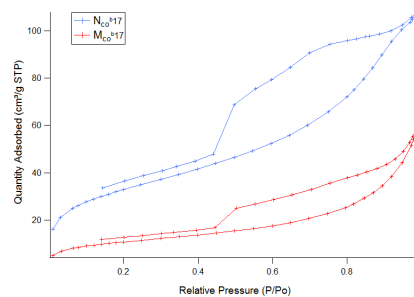
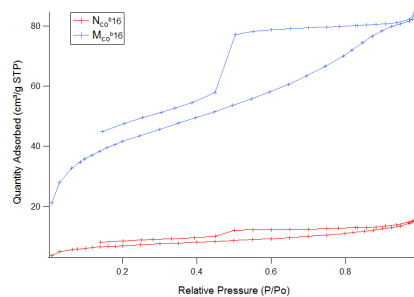
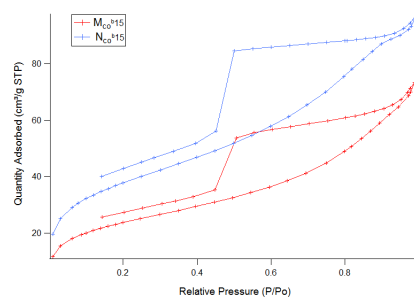
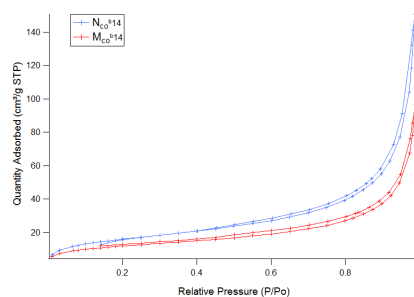
F Binding assays isotherm for polymers of the cortisol design of experiments





G BET measurements: isotherms of N₂ adsorption and desorption for polymers of the cortisol design of experiments





Abstract: This thesis aimed at elaborating an optical sensor to detect molecules in a biological fluid. Two steroids and a xenobiotic were identified as biomarkers released in some body fluids: cyproterone acetate, cortisol and 2,4-dichlorophenoxyacetic acid respectively.

On one hand, detection was performed by Molecularly Imprinted Polymers (MIPs). These tailor-made synthetic receptors display numerous qualities that foster their integration in sensors. MIPs were therefore developed against the targetted analytes. Formulation optimization was led thanks to experimental designs.

On the other hand, optical transduction was made possible thanks to the structuring of a polymer into a photonic crystal. Opals were manufactured with a new process suitable for large scales and were used to mold MIPs in inverse opals. Thus, submicron structures of the polymer are responsible for the color of the sensor. A change of color is triggered by the recognition of the analyte by the polymer (upon swelling). Polymers studied displayed sufficient swelling observed by spectrophotometry.

Finally, the work of this thesis consisted in elaborating polymer formulations and their integration in a sensor so as to detect an analyte with direct, rapid and unobtrusive means.

Key words: Molecularly imprinted polymers, MIPs, steroids, herbicide, biosensor, optical transduction, photonic crystal, body fluids.

Résumé: Ce travail de thèse avait pour objectif l'élaboration d'un capteur optique pour la détection directe de molécules d'intérêt dans un fluide biologique. Deux stéroïdes et un xéniobiotique (herbicide) ont été choisis en tant que biomarqueurs apparaissant dans des fluides corporels: respectivement l'acétate de cyprotérone, le cortisol et l'acide 2,4-dichlorophénoxyacétique.

La partie détection, d'une part, est assurée par les polymères à empreintes moléculaires (MIPs, de l'anglais *Molecularly Imprinted Polymers*). Ces récepteurs synthétiques sur mesure présentent en effet de nombreuses qualités pour l'intégration dans un capteur. Des polymères à empreintes moléculaires ont ainsi été développés pour les analytes visés. L'optimisation des formulations de polymère a été basée sur des plans d'expériences.

La transduction optique, d'autre part, est basée sur la structuration du polymère sous la forme d'un cristal photonique. Des opales ont été fabriquées avec un procédé industrialisable pour permettre la mise en forme du MIP en opale inverse. Ainsi structuré à l'échelle submicronique, le matériau présente une couleur susceptible d'évoluer lors de la détection de l'analyte, et ce, grâce à un changement de conformation (gonflement). Les formulations polymères étudiées ont généré des gonflements réduits mais visibles en spectrophotométrie.

Le travail rapporté dans cette thèse consiste donc en l'élaboration de polymères à empreintes moléculaires et leur intégration dans un capteur afin de détecter un analyte de façon directe, rapide et ne nécessitant que des équipements transportables, voire portables.

Mots clés: Polymères à empreintes moléculaires, MIPs, stéroïde, pesticide, capteur, transduction optique, cristal photonique, fluides corporels.